Experimental and Theoretical Studies of the Atomic Structure of Platinum-based Nanoclusters

By

Caroline Elizabeth Blackmore

A thesis submitted to the
University of Birmingham
for the degree of
DOCTOR OF PHILOSOPHY

Centre for Doctoral Training in Fuel Cells and Their Fuels
School of Chemical Engineering
College of Engineering and Physical Sciences
University of Birmingham

September 2016

UNIVERSITY OF BIRMINGHAM

University of Birmingham Research Archive

e-theses repository

This unpublished thesis/dissertation is copyright of the author and/or third parties. The intellectual property rights of the author or third parties in respect of this work are as defined by The Copyright Designs and Patents Act 1988 or as modified by any successor legislation.

Any use made of information contained in this thesis/dissertation must be in accordance with that legislation and must be properly acknowledged. Further distribution or reproduction in any format is prohibited without the permission of the copyright holder.

Abstract

This thesis focuses on the atomic structure of platinum-based nanoclusters, and covers two main areas: Binary platinum-titanium clusters, and pure platinum clusters. In both cases, the nanoclusters were produced with a magnetron sputtering, gas-aggregation cluster beam source, and imaged with an aberration-corrected Scanning Transmission Electron Microscope (STEM) with detailed image analysis.

The key issue in the study of the Pt-Ti clusters is in identifying their overall morphology. For oxidised clusters a Pt core with a TiO_x shell is found for smaller clusters, whereas for larger clusters multiple Pt cores are seen within the TiO_x shell. The Pt cores, for all sizes of nanoclusters, exhibit a preferred core size of 30 $\pm$ 6 Pt atoms. The Pt-Ti clusters have also been transferred between the cluster source and the STEM in a nitrogen environment, in order to reduce oxidation. Here, the morphology of the clusters is more amorphous in nature than for the core-shell structure of their counterparts transferred in air, with the Pt and Ti atoms forming an alloy core within the cluster. A small amount of oxidation seems to allow a thin shell of TiO_x to form around these clusters.

The study of the pure Pt nanoclusters was motivated by the Pt cores found in the binary nanoclusters transferred in air. Experimentally, clusters were produced containing between 10 and 600 Pt atoms. The structural motif of these clusters was identified through aberration-corrected STEM imaging, showing that the large clusters ($>$ 250 Pt atoms) typically present with a cubic structure which matches that of bulk FCC Pt. The smaller clusters do not display such a distinct structure, although some have been identified as icosahedral or decahedral in motif. Additional investigation of the pure Pt nanoclusters has been performed by examining the structure of the magic number sized clusters of 55, 147, and 309 Pt atoms. This experimental work has been complemented by theoretical modelling of the most stable structures, to identify dominant motifs within a large size range from 55 to 10,000 Pt atoms. Empirical potentials were used to study the dominant motifs of symmetric clusters within this size range. An interpolation scheme, which predicts the energies of asymmetric clusters, was used to investigate this size regime in

further detail. The results show that there is a persistent switching between the decahedral and octahedral motifs, with the decahedral having broadly greater dominance at smaller sizes, and the octahedral becoming dominant at larger sizes. This work was complemented by performing global optimisations on the magic number clusters, including a 2% size bracket. This has allowed a detailed study of the small clusters, showing that for 55 atoms the icosahedral and decahedral motifs are dominant, whereas for 147 atoms the decahedral motif is dominant, and for 309 atoms the octahedral motif is broadly dominant.

Several papers are emerging from this thesis work. The Pt-Ti multiple-core work has been published in PCCP journal 'Modular Construction of Size-Selected Multiple-Core Pt-TiO_2 Nanoclusters for Electro-Catalysis' by Caroline E. Blackmore, Neil V. Rees, and Richard E. Palmer. The latter part of the Pt-Ti chapter is currently being converted into a manuscript, with collaborative theory work from Keith McKenna's group at the University of York. The pure Pt experimental and theory work is due to be combined into a paper discussing the FCC motif evolution. This paper will contrast the Pt results with previous work on gold nanoclusters performed by Richard E. Palmer (University of Birmingham) and Anna L. Garden (University of Otago). A second paper, on the variations of motif dominance caused by the use of different empirical potentials, is also being drafted and will also include some of the work on Pt shown in this thesis.

Acknowledgement

I would like to thank my supervisor, Richard E. Palmer, for the opportunity to work within NPRL. The advice, motivation and support during my PhD has been invaluable.

I would like to thank Anna L. Garden for supervising the theoretical part of this PhD during my placement in New Zealand. Her support and inspiration has had a huge impact upon my thesis, as well as helping to develop my interpersonal skills.

I would also like to thank my second supervisor, Neil V. Rees, for helping with all areas of the preliminary electrochemistry.

Thanks also goes to the wider NPRL group, who have all helped me during my project. A special mention to Dawn, Scott, Tibo, and Will who have been particularly supportive. I would like to thank all of the people I worked with in New Zealand for their support, especially Steph.

The last a biggest thank you goes to my family for their unconditional support through out. Andy in particular has been my rock.

Author's Contribution

The author has performed all experimental work related with the production, characterisation and analysis of the platinum-titanium and pure platinum clusters. The gold temperature studies used for comparison in Chapters 3 and 4 was performed by Dawn Foster from the University of Birmingham. The theory calculations for the platinum-titanium clusters presented in Chapter 3 were conducted by Dr Keith McKenna at the University of York. All of the theoretical work presented in Chapter 5 was done by the author during a placement in New Zealand.

The work presented in Chapters 3 and 4 was conducted under the supervision of Prof Richard E. Palmer from the University of Birmingham, whilst the work presented in Chapter 5 was conducted under the supervision of Dr Anna L. Garden from the University of Otago.

Contents

Nomenclature **viii**

List of Figures **x**

1 Introduction **1**

1.1 Motivation for the Project 1

1.1.1 Sustainable Energy 1

1.1.2 The Hydrogen Economy - Fuel Cells and Water Splitting 3

1.1.3 Platinum and Titanium Dioxide - Materials for The Hydrogen Economy 8

1.2 Nanoclusters 13

1.2.1 Motivation for Studying Nanoclusters 13

1.2.2 Nanocluster Size and Structure 16

1.3 Cluster Production 18

1.3.1 Overview 18

1.3.2 Chemical Methods of Production 19

1.3.3 Physical Methods of Production 20

1.3.4 Characterisation of Clusters 25

2 Experimental Methods **29**

2.1 Cluster Source 29

2.1.1 Cluster Generation 30

2.1.2 Ion Optics 34
2.1.3 Mass Selection 34
2.1.4 Deposition 36
2.2 Imaging of Clusters 38
2.2.1 Scanning Transmission Electron Microscope 38
2.2.2 Number of Atoms in Each Cluster 49
2.2.3 Video Analysis of Clusters 53

3 Platinum-Titanium Clusters 54
3.1 Introduction 54
3.2 Pt-Ti Clusters Transferred in Air 55
3.3 Pt-Ti Clusters Transferred in Nitrogen 64
3.3.1 Nitrogen Transfer Method 64
3.3.2 Results for Pt-Ti Clusters Transferred in Nitrogen 66
3.4 STEM Beam Induced Structural Changes within Pt-Ti Clusters Transferred in Air and Nitrogen 72
3.5 Preliminary Electrochemistry Results 75
3.6 Conclusions and Further Work for Platinum-Titanium Clusters 77

4 Pure Platinum Clusters 81
4.1 Introduction 81
4.2 Intensity Measurements 82
4.2.1 Verification of the Number of Pt Atoms 82
4.3 Structure Identification 84
4.3.1 Alternative Methods of Structure Identification 87
4.3.2 Dominant Motif at Each Pt Cluster Size 90
4.3.3 QSTEM Simulations of Clusters with 55 and 147 Atoms 95
4.4 Electron Beam Heating of the Pt Samples 106

4.5 Comparison Between Experimental and Theoretical Pt Magic Number Clusters . . . 107
4.6 Conclusion and Further Work for Platinum Clusters . . . 109

5 Platinum Theory **110**
5.1 Introduction . . . 110
5.2 Computational Details . . . 111
5.3 Motif Dominance of Pt Clusters Between 55 and 10,000 Atoms . . . 113
5.3.1 Symmetric Clusters . . . 115
5.3.2 Asymmetric Clusters . . . 118
5.3.3 Influence of the Interaction Potential . . . 128
5.4 Explicit Modelling of Magic Number Clusters . . . 130
5.4.1 The Global Optimisation Problem . . . 130
5.4.2 Global Optimisation Methods for Clusters . . . 131
5.4.3 GOUST Algorithm . . . 133
5.4.4 Generation of the Low Energy Starting Guesses . . . 135
5.4.5 GOUST Results . . . 137
5.5 Conclusions and Further Work for Platinum Theory . . . 155

References **157**

Nomenclature

2D - Two Dimensional

3D - Three Dimensional

AKMC - Adaptive Kinetic Monte Carlo Simulation

AMU - Atomic Mass Units (equivalent to Da)

ASAP - As Soon As Possible calculator for ASE

ASE - Atomic Simulation Environment

BSE - Back Scattered Electrons

CEOS - Company Name - Corrected Electron Optical Systems

Da - Dalton (equivalent to AMU)

DFT - Density Functional Theory

EAM - Embedded Atom Model

EDX - Energy Dispersive X-ray

EELS - Electron Energy Loss Spectroscopy

EMT - Effective Medium Theory

EU - European Union

FCC - Face Centred Cubic

FEG - Field Emission Gun

FFT - Fast Fourier Transform

GC - Glassy Carbon

GOUST - Global Optimisation Using Saddle Traversal

HAADF - High Angular Annular Dark Field

PEC - Photo Electro-Chemical

PEM - Polymer Exchange Membrane

PEMFC - Polymer Exchange Membrane Fuel Cell

PES - Potential Energy Surface

QSTEM - Quantitative TEM / STEM Simulation Software

SE - Secondary Electron

SOFC - Solid Oxide Fuel Cell

STEM - Scanning Transmission Electron Microscope

TEM - Transmission Electron Microscope

UHV - Ultra High Vacuum

List of Figures

1.1 Schematic of a PEM fuel cell 5

1.2 Schematic of an electrolysis cell 6

1.3 Schematic of a PEC cell 7

1.4 Volcano plot showing molecular oxygen binding energy of pure metals . . . 10

1.5 Volcano plot showing molecular oxygen binding energy of bimetallic metals 11

1.6 Schematic of possible arrangements of Ti within a Pt cluster 12

1.7 Simulations of strain within clusters 17

1.8 Schematic of the {100} and {111} facets 18

1.9 Schematic of a supersonic expansion nozzle cluster beam source 21

1.10 Schematic of a laser ablation cluster beam source 22

1.11 Schematic of a gas evaporation liquid nitrogen condensation cluster beam source 23

1.12 Schematic of a magnetron sputtering gas condensation cluster beam source 24

1.13 Schematic of a scaled up cluster beam source, the matrix assembly cluster source 24

1.14 Combination of two STEM images to make a 3D visualisation of the cluster studied 28

2.1 Schematic of a magnetron sputtering gas-aggregation cluster beam setup used at the University of Birmingham 31

2.2 Effect of varying helium pressures on cluster current 32

2.3 Effect of varying power levels on cluster current 33

2.4 Schematic of the mass selector used within the cluster beam source at the University of Birmingham . . . 35
2.5 Photograph of STEM available at the University of Birmingham . . . 38
2.6 Schematic of detectors available for STEM . . . 39
2.7 Ray diagram for spherical aberration . . . 40
2.8 Image of STEM Cs corrector software . . . 40
2.9 STEM Cs corrector aberrations . . . 41
2.10 ADF efficacy . . . 47
2.11 Low magnification STEM image . . . 48
2.12 Median image for detector efficacy . . . 48
2.13 Threshold application for Pt-TiO_2 clusters . . . 50
2.14 Image of background subtraction method . . . 51
2.15 Comparison of methods . . . 52

3.1 Images of Pt-TiO_2 clusters at different sizes . . . 56
3.2 Histogram of the number of atoms contained within each cluster . . . 57
3.3 Histogram of number of atoms within each cluster for small clusters . . . 58
3.4 Histogram of number of atoms within each cluster for large clusters containing one core . . . 61
3.5 Histogram of number of atoms within each cluster for large clusters containing multiple cores . . . 61
3.6 EELs spectra for carbon, titanium and oxygen . . . 62
3.7 EELs spectra for Pt-Ti clusters transferred in air. . . . 62
3.8 Plot showing cluster intensity and projected Pt intensity . . . 63
3.9 Photo of the gas transfer glove box . . . 65
3.10 Images of Pt-Ti clusters transferred in an air or nitrogen atmosphere . . . 67
3.11 FFT of clusters transferred in air and in nitrogen . . . 68
3.12 Plot of the frequency of intensity for Pt-Ti clusters transferred under air and nitrogen . . . 69

3.13 Schematic of the intensity variations in the region of interest for analysis . 70
3.14 Images from a video of Pt-Ti clusters transferred in air 72
3.15 Images from a video of Pt-Ti clusters transferred in nitrogen 73
3.16 Images of the Pt-Ti sample transferred in nitrogen showing the area before and after the video has been taken 74
3.17 Plot of the intensity from clusters transferred in air 79
3.18 Plot of the intensity from clusters transferred in nitrogen 79
3.19 Preliminary electrochemistry results 80

4.1 Plot of the diameter of the 309 Pt atom cluster 83
4.2 Example octahedral, decahedral, and icosahedral atlases produced by QSTEM 86
4.3 FFT of example clusters 88
4.4 FFT of large gold clusters 89
4.5 Overview of the dominant motif for Pt clusters between 10 and 600 atoms 91
4.6 Representative images of 309 Pt atom clusters 93
4.7 Representative images of 147 Pt atom clusters 93
4.8 Representative images of 55 Pt atom clusters 93
4.9 Images of the unidentified / amorphous 309 Pt atom clusters 94
4.10 QSTEM simulation atlas of the icosahedral motif for 55 Pt atoms 96
4.11 QSTEM simulation atlas of the decahedral motif for 55 Pt atoms 97
4.12 QSTEM simulation atlas of the octahedral motif for 55 Pt atoms 98
4.13 STEM images of 55 Pt atom clusters identified as icosahedral 100
4.14 STEM images of 55 Pt atom clusters identified as decahedral 100
4.15 STEM images of 55 Pt atom clusters identified as octahedral 100
4.16 QSTEM simulation atlas of the decahedral motif for 147 Pt atoms 102
4.17 QSTEM simulation atlas of the octahedral motif for 147 Pt atoms 103
4.18 Twinned clusters seen in the simulation of the octahedral QSTEM atlas for 147 Pt atom clusters. 104
4.19 STEM images of 147 Pt atom clusters identified as decahedral 104

4.20 STEM images of 147 Pt atom clusters identified as octahedral 105

5.1 Schematic of (i,j) and (p,q,r) 112

5.2 Schematic of symmetric, asymmetric closed and asymmetric open shell clusters 114

5.3 Plot of the energy of symmetric Pt clusters calculated with the Gupta potential for 55 - 10,000 atom clusters 116

5.4 Plot of delta for symmetric Pt clusters calculated with the Gupta potential for 55 - 10,000 atom clusters 117

5.5 Schematic of octahedral removal mechanisms 119

5.6 Schematic of decahedral removal mechanisms 119

5.7 Plane removal orders from an octahedral cluster 120

5.8 Plane removal orders from a decahedral cluster 120

5.9 Plane removal orders from a decahedral corner 120

5.10 Atom removal orders from an octahedral cluster 123

5.11 Atom removal orders from a decahedral cluster 123

5.12 Atom removal orders from a decahedral corner 123

5.13 Optimal removal order for octahedral clusters 125

5.14 Optimal removal order for decahedral clusters 125

5.15 Plot of delta for symmetric and interpolated asymmetric Pt clusters, calculated with the Gupta potential for 55 - 10,000 atom clusters 127

5.16 Comparison of the Gupta and EMT potential for Pt clusters 129

5.17 Schematic of basin hopping algorithm 132

5.18 Plots of interpolation energy vs locally minimised energies 136

5.19 Local to globally optimised energies for 55 atom clusters 138

5.20 Schematic of lowest globally optimised structure for 55 atoms 138

5.21 Schematic of low energy globally optimised structures for 55 atoms 139

5.22 Schematic of low energy globally optimised structures for 54 atoms 143

5.23 Schematic of low energy globally optimised structures for 56 atoms 143

5.24 Local to globally optimised energies for 147 atom clusters 144
5.25 Schematic of low energy globally optimised structures for 147 atoms 145
5.26 Local to global optimisation energy for 144 - 147 Pt atom clusters including images 146
5.27 Local to global optimisation energy for 147 - 150 Pt atom clusters including images 147
5.28 Local to global optimisation energy for 309 Pt atom clusters 149
5.29 Local to global optimisation energy for 303 - 306 Pt atom clusters 150
5.30 Local to global optimisation energy for 306 - 309 Pt atom clusters 150
5.31 Local to global optimisation energy for 309 - 312 Pt atom clusters 151
5.32 Local to global optimisation energy for 312 - 315 Pt atom clusters 151
5.33 Schematic of low energy globally optimised structures for 303 - 315 decahedral clusters 154
5.34 Schematic of low energy globally optimised structures for 303 - 315 octahedral clusters 154

Chapter 1

Introduction

In this chapter, background material on the topics covered within this thesis is examined. This includes the motivation for the project as a whole, the limits with the current technology, and the role that platinum and platinum-based materials play within this setting. Pure platinum and platinum-titanium are the materials that are focused upon within this thesis. Nano structuring materials vastly changes their properties, which, when coupled with the reduction in material, offers a good way to use these materials. Below, the production, imaging and analysis methods of nanoclusters are discussed.

The background to the theoretical work is discussed in detail in Chapter 5.

1.1 Motivation for the Project

1.1.1 Sustainable Energy

Our planet's resources are limited, none more so than energy. Useful energy is predominantly produced from fossil fuels, but as these are limited, alternative methods of producing, storing, and transporting energy have to be developed. Conservative predictions of power consumption in 2050 show that 30 TW will be needed, with 40-70% being produced by renewable energy [1]. The two main renewable sources in the UK, solar and wind, have the capability to meet a lot of the human population's needs, but both

are often limited by intermittent supply. The nature of human power usage means that demand fluctuates second by second, hour by hour, and season by season. To address these fluctuations, technological developments in power production and storage are being sought. These include the building of hydroelectric dams, investment in battery technology, and the use of hydrogen as an energy storage medium. Hydrogen, as a gas or a liquid, has the ability to be stored and transported, which is key to many applications. The study of nanoclusters, relevant to the hydrogen economy is the focus of this thesis.

Hydrogen, when coupled with fuel cell technology, provides a compact energy source, particularly useful to the vehicular industry. Vehicles using petrol- or diesel- based engines not only deplete the limited fossil fuel supply, but also release harmful pollutants into the atmosphere [2]. The switch to hydrogen fuel for cars, lorries, and buses, offers a solution to both of these issues, provided that the hydrogen is produced in an environmentally friendly, green manner. To date, Transport for London runs eight hydrogen fuel cell buses [3], and is championing hydrogen fuel cell technology. The current fuel cell technology is well suited to use on buses, as they are capable of carrying large, heavy loads such as hydrogen canisters, and always return to a single station which can be used as a refilling point. However, improvements still need to be made to fuel cell technology and hydrogen production in order to make both practical and economically viable. This leads to two areas of research connected to this thesis: Improving the efficiency of hydrogen fuel cells used within small vehicles, and increasing the efficiency of the green production of hydrogen from water.

Hydrogen can be produced in a multitude of ways with steam reformation, partial oxidation, biomass gasification, and alkaline electrolyser being the four commercial options[4]. Whilst steam reformation is the most used and the most efficient at 80 % it is not an environmentally friendly process as it releases carbon, predominantly carbon dioxide, into the atmosphere and burns fossil fuels. To combat this, greener methods need to be sort for future hydrogen production. Electrolysis uses electricity to split water, producing hydrogen, and can be a green method if a renewable power source is used to generate the

electricity. It is approximately 60 % efficient, and a good way to store excess electrical energy from unpredictable renewable energy sources [4]. Photoelectrochemical cells are have an efficiency of approximately 13 % when turning sunlight in to hydrogen [4]. Hydrogen can also be produced from sunlight by photobiological material like algae, but this has an efficiency of less than 0.5 % [4].

The work of this thesis is concerned with materials that could help improve fuel cell reactions and water splitting efficiency. In-depth studies of these materials, specifically nanoclusters, allows us to explore novel production methods and the impact of particle size upon the overall morphology of the nanocluster. This in-turn, will improve their performance by offering the hope that we can improve the technology by controlling the materials, thus improving the economics of the hydrogen economy, ready for wider deployment. Platinum based materials are the main concern for this thesis, as it is currently widely used as a catalyst, but its high cost due to its rarity limits its future use.

1.1.2 The Hydrogen Economy - Fuel Cells and Water Splitting

Improvements within the hydrogen economy can be made in two areas: Fuel cell technology for vehicles, specifically cars, or the process of splitting water into hydrogen and oxygen.

Fuel cells are a technology that allows hydrogen to be used as a fuel to produce energy by chemical reactions rather than combustion. There are many types of fuel cells, but for this work Polymer Exchange Membrane Fuel Cells (PEMFC) will be the main focus. PEM fuel cells operate at low temperatures (<100 °C), and are typically used for mobile applications, such as vehicles. They react pure hydrogen with oxygen from the air as inputs, resulting in power and water as outputs. This makes it a very clean technology, as no pollutants are released. A schematic of a PEM fuel cell is shown in Figure 1.1. The fuel in, H_2, is split at the anode into hydrogen ions which pass through the polymer membrane to the cathode. At the cathode, O_2 is split into ions so that water can be formed with two hydrogen ions and an oxygen. The splitting of the O_2 and recombination into H_2O

is the slowest step within the process [5], so a catalyst, typically a layer of Pt, is used to speed up this reaction. The equations for PEM fuel cells are shown in Equations 1.1 and 1.2. Improving this rate-limiting step by improving the ability of platinum to catalyse the reaction forms a major part of the work investigated within this thesis.

$$H_2 \rightarrow 2H^+ + 2e^- \tag{1.1}$$

$$\frac{1}{2}O_2 + 2H^+ + 2e^- \rightarrow H_2O \tag{1.2}$$

The second main type of fuel cell is a Solid Oxide Fuel Cell (SOFC), which has a ceramic electrolyte, typically yttria-stabilised zirconia. This type of fuel cell avoids the need for a precious metal catalyst by running at high temperatures of 800°C. This high temperature means that the fuel cell can process impure hydrogen, but the increased temperature can lead to high levels of degradation within the fuel cell. SOFC are typically bulkier than PEMFCs, thus stationary applications are sought, rather than mobile applications. This includes setting up SOFC homes, where the fuel cell generates electricity from natural gas, utilising the excess heat produced to warm water and run the central heating [6, 7]. Other types of fuel cells include Direct Methanol, Phosphoric Acid, Alkaline, and Molten Carbonate, all of which have advantages and disadvantages.

Electrolysis can be used to split water into hydrogen and oxygen gas, a schematic of which is shown in Figure 1.2. A power supply is attached to two electrodes suspended in an electrolyte. A salt based electrolyte which is used to improve the conductivity of the solution. This electrical potential allows breakdown of the bonds within water molecules. At the cathode, the reduction reaction occurs, forming an alkali. This is where hydrogen ions are stripped from H_2O, forming H_2 gas and OH^- ions. At the anode, the oxidation reaction occurs, forming an acid. This is where oxygen ions are stripped from H_2O, releasing H^+ ions and O_2 gas. The H^+ and OH^- ions within the solution recombine to form water. The balanced half-cell equations for the cathode and anode are shown in

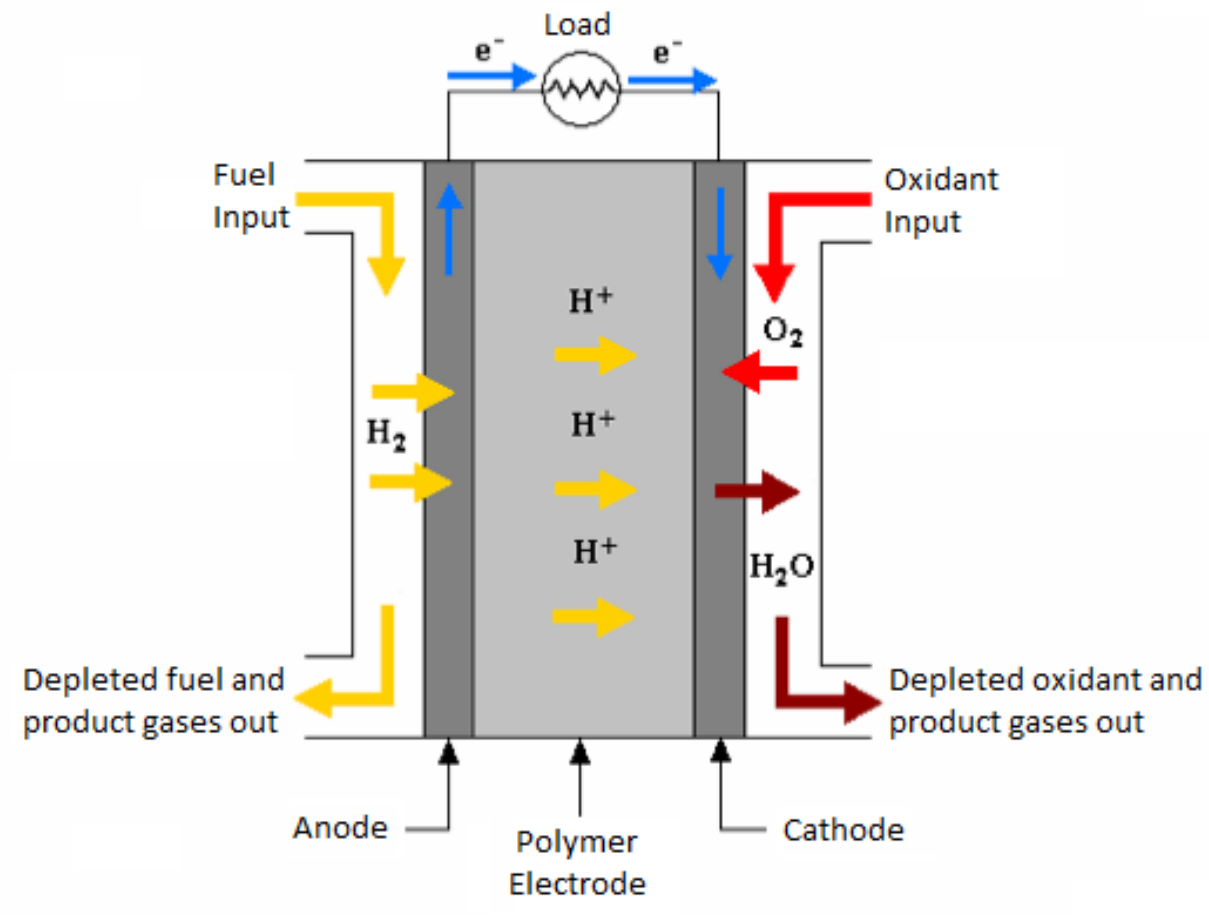

Figure 1.1: A schematic of a PEM fuel cell with hydrogen and oxygen inputs, and a water output, producing power through the flow of electrons. The catalyst particles are located on the anode and cathode. Reproduced from [8].

Equations 1.3 and 1.4.

$$4H_2O + 4e^- \rightarrow 2H_2 + 4OH^- \tag{1.3}$$

$$2H_2O \rightarrow O_2 + 4H^+ + 4e^- \tag{1.4}$$

The gaseous oxygen and hydrogen products form bubbles which rise to the surface of the solution. A gas separator is used to aid collection of the H_2 gas, which can then be purified before use within a PEM fuel cell. The PEM fuel cell and water-splitting electrolysis are in effect opposites of each other, with one using hydrogen to produce power and the other using power to produce hydrogen.

To make electrolysis a green technology for water splitting, the power used has to be generated by a renewable source, typically solar power via a photovoltaic array. The

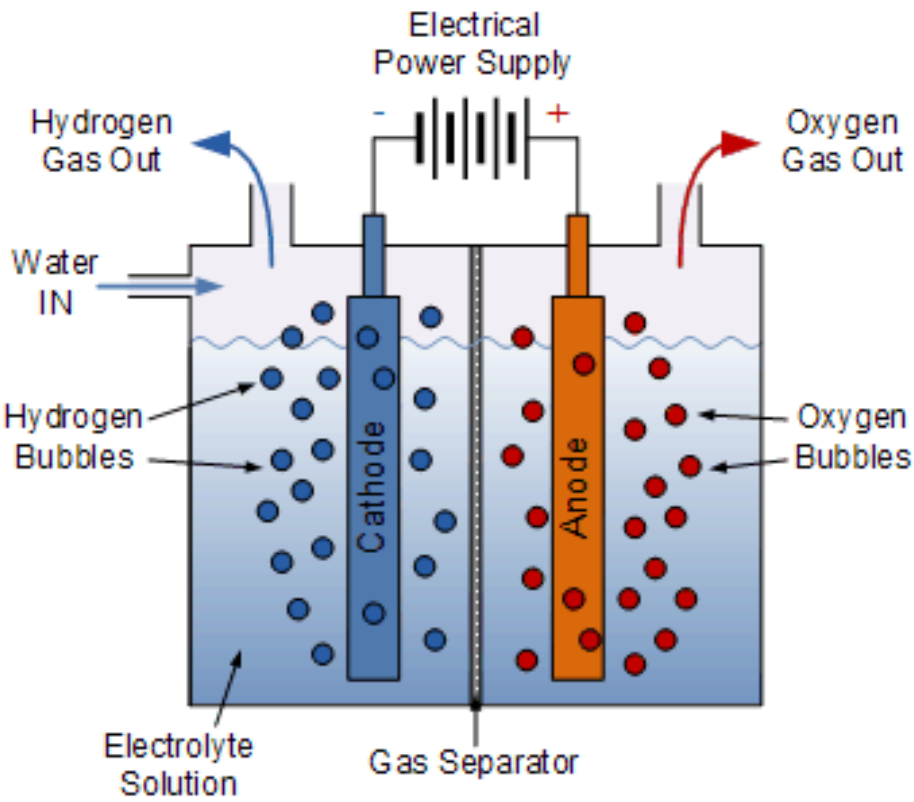

Figure 1.2: A schematic of an electrolysis cell used to split water and produce hydrogen and oxygen gas. Reproduced from [9].

alternative to using a solar array to produce electricity is to use Photo Electro-Chemical (PEC) water splitting, where a semiconducting material is used, in conjunction with sunlight, to directly split water.

Figure 1.3 shows a schematic of a PEC cell. Incident photons, with energy $h\nu$ (Plancks constant times the frequency of the photon), interact with the cell. The energy of the photon causes an electron to be promoted from the valance band into an excited state in the conduction band, leaving a positively charged quasi-particle called a hole. The choice of materials designate the energies at which the valance and conduction bands sit. The energy of the photon has to match the energy gap between the valance and conduction bands for it to be absorbed.

The electron released flows, via a circuit, to the counter electrode (cathode), whilst the hole acts as the positive anode. This potential difference provides the energy to split

water in the same way the power source does in Figure 1.2. Careful design of the cell allows for the two gasses to be collected independently, with the hydrogen ready for use within a fuel cell.

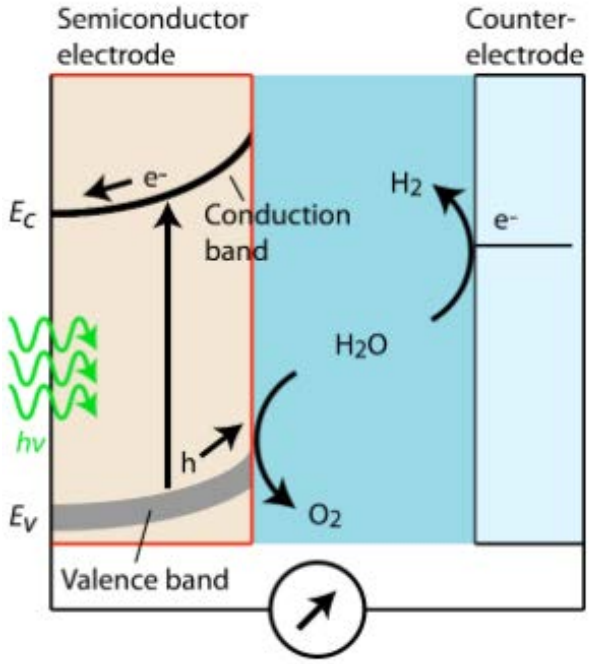

Figure 1.3: A schematic of a PEC cell using photons of light to split water and produce hydrogen and oxygen. Reproduced from [10].

Typically, TiO_2 is used as the semiconductor electrode material, but as it has a band gap of 3.0-3.2 eV it only absorbs in the ultraviolet area of the electromagnetic spectrum [11]. This means that a large proportion of the energy from sunlight is wasted. To collect more of the spectrum, dye-sensitised PEC cells are being developed. They often contain multiple materials, with different band gaps to absorb a wider range of photon energies, generating more electron hole pairs [12, 13].

TiO_2 has been shown to produce 0.011 mmol of hydrogen per gram of catalyst in a bulk form [14]. This improves to 0.36 mmol of hydrogen per gram for TiO_2 when it is nano structured[14]. The addition of Ag and Au improve the nanoclusters hydrogen production to 12.82 mmol per gram[14]. Pt and TiO_2 nano clusters show the highest rate for all materials studied at 18.6 mmol of hydrogen per gram of catalyst[14]. This study by

Ahmad *et al.*[14] shows how nanostructuring a material can vastly improve its reactivity per gram.

TiO_2 also has many properties well suited to the hydrogen economy. It is a relatively cheap metal, which is widely available. For example approximate metal prices from June 2017 show that gold costs 1250 USD/oz and silver costs 17 USD/oz[15]. Non precious metals are far cheaper, with tin costing 9 USD/lb, nickel costing 4 USD/lb, copper costing 2.5 USD/lb, and titanium costing 1.6 USD/lb [15]. The mechanical properties of TiO_2 are also very good as it is a strong, thermally stable and non-flammable, thus appropriate for use as a catalyst. TiO_2 is also a non-toxic and easy to handle material as it is regularly used in sun cream and paint [16, 17]. Another major benefit of using TiO_2 is that it is a well researched material[18, 19, 20].

Pt and TiO_2 stand out as being the main materials for research and improvement in the hydrogen economy. Section 1.1.3 details work investigating both materials and their impact upon the hydrogen economy.

1.1.3 Platinum and Titanium Dioxide - Materials for The Hydrogen Economy

Pt forms the base material of many catalysts. It is most commonly used in catalytic converters, enabling hydrocarbons leaving an engine to be converted into carbon dioxide and water vapour, reducing the harmful effect upon the environment. Pt is classed as a critical metal due to its many uses, but limited supply. The mining of platinum group metals is also a very dirty process using many chemicals to extract and process the ore [21, 22]. For this reason, reducing the quantity of Pt used within all applications is a key part of its future. Pt has a multitude of uses which means that research into understanding the material, particularly at the nanoscale, is very valuable, especially if improvements in catalysis, focusing upon the hydrogen economy, can be made. Below is detailed literature on recent studies of Pt, with the main focus being upon the hydrogen economy as an emerging area which Pt will benefit.

Pt nano clusters have been studied by a number of groups to further understand both the structure and chemical properties of these clusters. Theoretical studies by Kumar *et al.* have indicated that for Pt clusters of less than 9 atoms, a planar structure is most stable [23]. Between 10 and 20 atoms, these planar structures form into pyramids. The decahedral motif becomes dominant in the 21 to 24 Pt atom range, followed by an octahedral motif becoming dominant for all larger sizes. This study found that for Pt clusters, the triangle (3 atoms) and square (4 atoms) are key shapes for stable clusters being formed. For bimetallic Pt based clusters there has been work on comparing different minority metal materials [24, 25]. These alloys have shown promise for increasing activity, reducing Pt loading, and improving stability and durability of the clusters produced

For fuel cells, Pt is the typical catalyst used [26, 27], with a lot of work focussing upon reducing the Pt loading, whilst keeping the reactivity and durability high [28, 29].

To compare the activity of different metals, volcano plots are often used. A volcano plot shows the activity for each metal plotted against oxygen binding energy. There is a volcano shaped relationship between the two, with the peak being a sweet spot that balances the oxygen binding strength. If the oxygen binds too weakly to the material it does not attach to the catalyst surface at the cathode. If the oxygen is bound too strongly, it can not dissociate, ready for the reactions to produce water. Nørskov *et al.* [30] conducted a DFT study on different materials calculating the activity of each material, plotted as a function of oxygen binding energy. The results are shown in Figure 1.4. The tip of the peak represents the ideal binding energy. The left-hand side shows metals that bind too weakly with oxygen, whilst the right-hand side shows metals that bound too strongly with oxygen. Pt is therefore classified as the 'best' with Pd being a close second. Greeley *et al.* [31] showed that the activity and oxygen binding energy was also highly dependent upon the surface that was being studied. For example, for Pt the activity and oxygen binding energy for the (211) step edge site is far lower than for the (100) and (111) facets. These studies enable experimentalists to know which sites are catalytically most active and thus which structures to try to produce to maximise the

number of ideal facets. For Pt, with the above information, maximising the (100) and (111) facets is preferential, which means cuboctahedral structures are best.

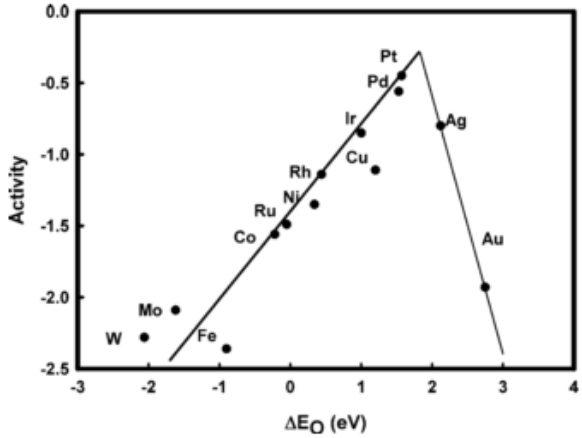

Figure 1.4: A volcano plot showing the activity of different metals as a function of molecular oxygen binding energy. Pt has the best balance of oxygen binding energy, which is neither too strong or too weak. Reproduced from [30].

To improve the catalyst, moving closer to the peak of the volcano plot is desirable. To move closer to the peak than pure Pt, bimetallic clusters can be formed. Figure 1.5 shows a volcano plot for bimetallic clusters, with Pt_3Ni (111) being classed as the best. Pt_3Y is a close second.

To gain the structural control, and preferentially make structures with (111) or (100) facets, the material has to be tailored at the nanoscale. Scaling the material to the nano size allows facets to be presented for catalytic reactions that are not present on the bulk materials surface. Reducing the size of the particle also makes the most efficient use of all of the material, as the surface to bulk ratio, explained in Section 1.2, is higher. Nanoclusters between 1 and 10 nm have been reviewed for use in fuel cells [33, 34, 35], focusing upon how the size and elemental make-up of the clusters influences the structure and reactivity of the cluster. By making clusters on the nanoscale, the structure does not always reflect that of the bulk, thus the facets of the clusters are different, with more or less of a particular facet being presented as a reaction site.

For Pt-Ti nanoclusters in fuel cells, Density Functional Theory (DFT) modelling has

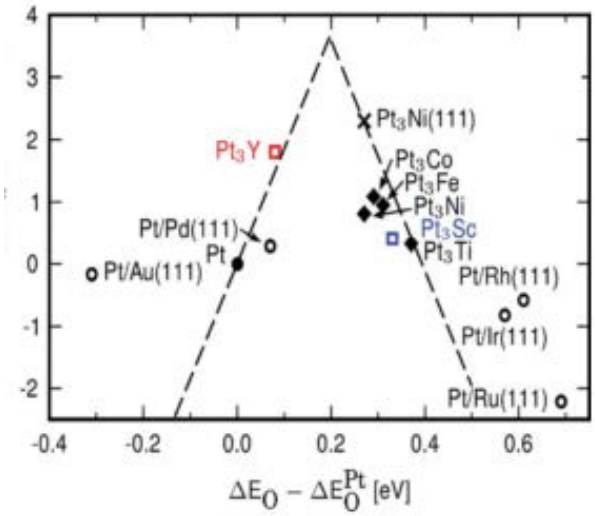

Figure 1.5: A volcano plot showing the activity of different bimetallic metals as a function of molecular oxygen binding energy, normalised so that pure Pt is at zero on both scales. $Pt_3Ni(111)$ and Pt_3Y have the best binding energies, as they are close to the volcano plot peak. Reproduced from [32].

been performed to investigate which arrangement of metal atoms is preferential [37, 36]. For this work, high symmetry clusters of $Pt_{32}Ti_6$ have been studied, with some possible arrangements shown in Figure 1.6. The high symmetry clusters shown are truncated octahedral, with core-shell, hex and centroid configurations. The figure shows three possible distributions of the Ti atoms within the Pt clusters. The two reactions studied were hydroxyl absorption and carbon monoxide adsorption. The DFT results show that the binding between the hydroxyl molecules and the Pt cluster with Ti was weaker than for a pure Pt cluster. This weaker binding is linked with a faster oxygen reduction reaction, which would be beneficial for fuel cell catalysts. The results also show a weaker bonding between the carbon monoxide molecule and the Pt cluster with Ti than for a pure Pt cluster. This suggests a lower level of poisoning within the fuel cell, which would also be very beneficial as it allows higher use of each catalytic site. Further work by Jennings *et al.* [37] shows similar trends for larger clusters, up to 201 atoms. The conclusions of both pieces of work show that a Ti cored cluster with a Pt skin 1 or 2 atoms thick would be more active as fuel cell catalyst than a pure Pt cluster of the same size. This would also have the added benefit of reducing the quantity of Pt used for the catalyst, as only the

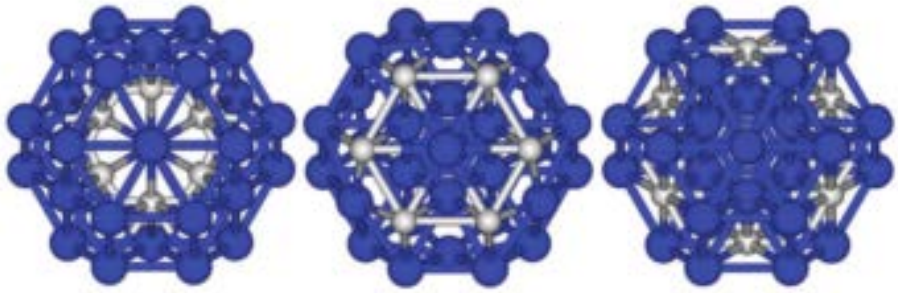

Figure 1.6: Slice through clusters showing possible arrangements of Ti atoms within a Pt cluster. 32 of the atoms are Pt(blue) and 6 are Ti(grey) in all cases. Reproduced from [36].

.

shell would contain Pt atoms.

The work by Jennings *et al.* [37, 36] also discusses the fact that if the shell of the cluster was Ti, the cluster would inhibit the fuel cell reactions. This is because the binding between Ti and carbon monoxide is far stronger, leading to high levels of poisoning of the catalyst.

TiO_2 is very useful for water splitting as described in Section 1.1.2, but the technology has a number of caveats: The probability of recombination of the electron hole pair, the low activation of TiO_2 by sunlight, and the backward reaction where hydrogen and oxygen return to water. Making this technology efficient is extremely important, as without the clean supply of fuel, hydrogen fuel cells have limited use. To combat these issues, developments in TiO_2 have been focussing upon adding noble metals to the TiO_2 [38]. For this work, noble metals are those which are either noble in chemistry terms (resistant to corrosion or oxidation), and those that are noble in physics terms (complete d-band shells). These metals include Pt [39], Au [39, 40, 41], Pd [42], Rh [43], Ni [44], Cu [45] and Ag [46]. Adding each of these materials to a Pt cluster can alter the absorption of the electromagnetic spectrum, reduce the recombination of electrons and holes, or inhibit the backward reaction where hydrogen and oxygen form water. The metal added changes the energy levels within the cluster, thus changing the electromagnetic wavelengths absorbed. Each additional metal changes the properties of the Pt cluster in differing ways.

A number of studies have shown that the inclusion of Pt atoms within TiO_2 can improve the production of H_2 if an electron donor is present, for example methanol [47, 48]. The presence of iodine can additionally suppress the backwards recombination of hydrogen and oxygen forming water. The backward reaction uses up hydrogen gas, so reducing this is beneficial for hydrogen production. In turn, this improves the economics of water splitting as it increases the yield of hydrogen. Yu *et al.* [49] found that TiO_2 loaded with Pt nanoparticles exhibited higher catalytic activity when compared with pure TiO_2 samples. Adding 2% by weight of Pt to the sample produced the highest catalytic activity for hydrogen production.

Developments in durability of the Pt catalyst have been demonstrated by Mohapatra *et al.* [50] who tested carbon doped Pt TiO_2 nano tubes. These displayed both a high reactivity and durability whilst being relatively inexpensive to produce, as the Pt loading was 0.4% by weight when compared with the total TiO_2 weight.

This work shows promise for fuel cell applications for Ti core Pt shell clusters, and mixed Pt TiO_2 clusters for water splitting. These two types of clusters form the basis for the work undertaken within this thesis. The reduction of the amount of Pt used within catalysts can thus be achieved in part by using a bimetallic material, for example Pt mixed with Ti. An alternative way to maximise the use of the Pt is to nano structure it, making the greater usage of all Pt atoms within a sample. The surface area of nano structured materials are far higher than that of the equivalent bulk material by weight.

1.2 Nanoclusters

1.2.1 Motivation for Studying Nanoclusters

From the literature it is clear that one way of improving the materials catalytic activity is to reduce the size of the material to the nanoscale. The properties that change by scaling to the nano size are the surface to bulk ratio, crystal structure, and quantum confinement which changes the melting temperature, magnetic properties, and reactivity

of the material. Nanoclusters are typically classed as a group of atoms which is between 1 and 100 nm.

Au is a prime example of how properties are influenced by the size of the material. As a bulk material, Au is known for being un-reactive [51], but when reduced to between 2 and 50 nm in size it becomes very useful for many reactions. Examples include Au being very selective (based on Au cluster size) for partial oxidation of propane to propene oxide, and for low-temperature CO oxidation [52].

Skulason *et al.* investigated the catalytic activity of Pt nanoclusters for the formation of H_2 [53]. The study performed showed that B-edges were far more catalytically active than A-edges for H_2 production. The A-edge is formed where a (111) and (100) facet meet, whilst a B-edge is formed where two (111) facets join. The differing catalytic activity is attributed to how the H_2 binds to different sites. These types of study help to identify the sites most useful for a specific reaction, thus experimentally cluster size and motif can be produced to maximise the reactivity. In this case clusters with many (111) surfaces and thus B-edges would be preferential, thus the fully octahedral structure is desirable. The desirability of a specific structure will be very dependent upon the specific catalytic reaction required, thus there is no generic rule for improving catalytic reactivity.

Controlling the size, as well as creating alloys by combining the main material with a dopant has a large effect upon the properties of the material. In the macro world many materials are alloyed to improve properties of strength, malleability, or corrosion resistance.

Using both of these methods, nano structuring and alloying of Pt and TiO_2, will allow us to investigate how the properties, specifically structure, varies. The sizes investigated experimentally will be between approximately 2 and 5 nm for the alloyed materials, and up to 600 atoms for the pure Pt clusters. Theoretical examination will focus upon the pure Pt clusters, predicting structural trends in clusters up to 10,000 Pt atoms. A larger size range for theoretical clusters is being used for two main reasons. A maximum size of 5 nm has been chosen for the experimental work as this is a practical upper limit of cluster

size for both production and structure identification given the available instrumentation at the University of Birmingham. For the theory work a far larger size can be investigated, and is, as it gives a good overview for larger cluster sizes.

Clusters of atoms are said to have magic numbers in the same way as there are magic numbers for the electronic shell of a single atom. For electronic magic numbers an atom is most stable with a complete nuclear shell of electrons, with the discrete number of electrons being classed as the magic number. For clusters, the magic numbers are based upon the arrangements of the atoms with the cluster, preferentially forming closed shell clusters. The magic numbers are dependant upon the base motif of the clusters and thus the material [54]. For example for icosahedral, decahedral, and octahedral motif clusters the magic number clusters below 1000 atoms are 55, 147, 309, 561, and 923 atoms. This means that during production of clusters these sizes are likely to be produced in a higher abundance than those of neighbouring sizes [55]. This is not unique to Pt and can be seen in other metals, e.g. Au, Ag, and others where the bulk material has a cubic structure.

Clusters of atoms form motifs based upon driving forces within the cluster. These include strain and surface tension. For each motif an internal strain is based upon the arrangements of atoms [56]. The icosahedral motif is typically favoured at small size ranges due to the low energy of the structure. This is typically followed by a region where the decahedral motif is dominant. This is because, as the icosahedral motif grows in size the strain contained within the cluster becomes too high. This can be released by changing to the decahedral motif, or by loosing the central atom within the icosahedral cluster. Growth of a decahedral cluster is typically followed by a transition to a cubic structure, to match that of most bulk materials.

For bimetallic clusters the strain contained within a cluster is based upon the materials used, thus the arrangement of these atoms aims to reduce the strain within the cluster as a whole [57]. Figure 1.7 shows an example of four bimetallic clusters with increasing number of minority metal atoms. To release the strain caused by more minority metal atoms the initially round core of atoms deforms to form an asymmetric core seen offset

towards one side of the cluster. The properties of the minority metal material impacts the size at which asymmetric cores start to form.

1.2.2 Nanocluster Size and Structure

The reactivity related to the structure of a particle is based both upon the cluster's overall shape, as well as the detailed atomic arrangement. Nanoclusters are produced in many shapes, including the traditional spherical [58, 59], nano wires [60] and platelets [61] to name a few. These shapes, along with varying the size, alters the nanoclusters characteristics changing the way it reacts. Castleman [62] describes a '3D periodic table' where the size of a material adds the third dimension, vastly changing the characteristics of a material. One of the main reasons for the changes in reactivity of nanoclusters when compared with bulk it due to the change in the surface to volume ratio. For example, for a cubic cluster with 64 atoms, 8 would be internal, and 56 would be on the surface, giving a surface to volume ratio of 7:1 (87%). For a larger cluster of 216 atoms, the ratio would be 19:8 (70%), whilst for a cluster of 1000 atoms, a ratio would be 61:64 (49%). This is still a relatively small cluster, thus the surface to bulk ratio tends towards 0% for very large clusters and the bulk. For catalysts, this means that most of the material in large clusters and the bulk has mostly inaccessible sites for reactions. Only the top few layers of the material are useful, thus, reducing the cluster's size, and increasing the number of surface atoms would increase the reactivity, whilst keeping the amount of material used constant. Alternatively, to keep the same surface area far less material would be needed if the material was nano structured.

When we look at the detailed structure of nanoclusters, the shape and size of the facets has to be taken into account. Nano structuring a material also results in deformation of the edges of the material. The majority of a cluster can have a bulk like structure, but subtle changes in the positions for edge atoms can change the reactivity of the material. Work by Skulason *et al.* [53] showed that theoretical, catalytic activity is highly dependent upon which facets meet along an edge of a cluster. Marks and Peng [63] discuss the fact

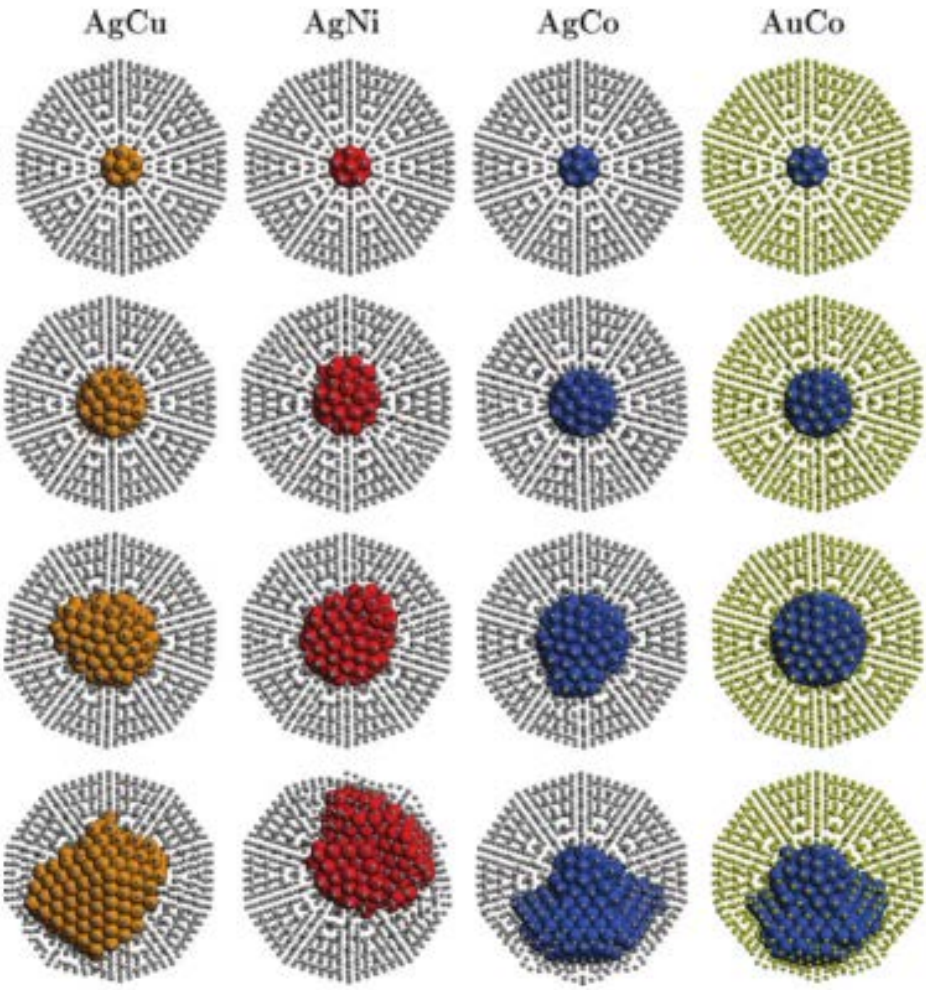

Figure 1.7: Simulations of the lowest strain arrangements of dopant atoms within an icosahedral cluster containing, 1415 atoms. The minority metal (shaded atoms) areas contain 13, 55, 147, or 309 atoms. These arrangements show how the cores become asymmetric to release the strain built up within the cluster, caused by increasing the number of dopant atoms. Reproduced from [57].

.

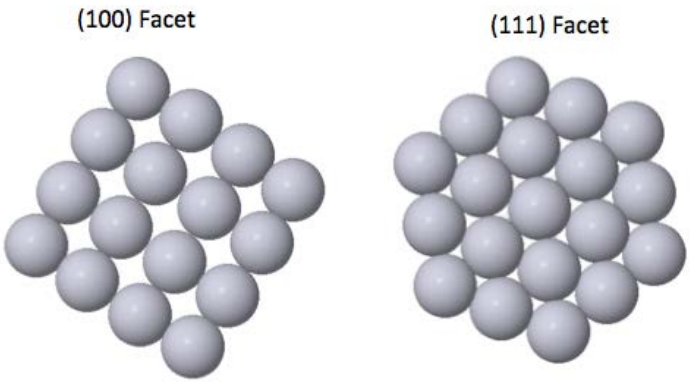

Figure 1.8: A 2D view of the atomic arrangement of the surface for {100} and {111} facets. Both facets are seen on the structural motifs of decahedral and octahedral clusters.

.

that different, but generally spherically shaped clusters, all contain different proportions of facet structures. For example, a complete cube contains only {100} facets, whilst a complete octahedron contains only {111} facets. A cuboctahedron therefore contains a mixture of {100} and {111} facets, dependent upon the size of the truncation. A 2D representation of the {100} and {111} facets are shown in Figure 1.8. Identifying the structure allows catalyst manufacturers to aim to preferentially produce the best cluster shape for their application.

Identifying the most stable structure of the clusters is thus important for knowing which reactions they are good for. Understanding how the clusters are formed during the production process, and how they are affected by their environment (storage time and conditions), helps in identifying possible uses of the clusters, both within and outside of the hydrogen economy.

1.3 Cluster Production

1.3.1 Overview

Nanoclusters can be produced in a number of ways, with most laboratory setups favouring chemical production. Some chemical methods are detailed in Section 1.3.2, but for

the work in this thesis physical preparation methods are preferred, mainly due to size control, detailed in Section 1.3.3. Chemical methods have the advantage of producing a high yield of clusters, and scaling up production tends to be simple. Disadvantages of chemical production includes the variation in the size distribution of the clusters, along with the varying elemental composition of each cluster, when bimetallic clusters are being produced. Physical production, in a beam cluster source environment, allows users to select the size of the clusters with additional mass selection apparatus. Using a mass selector gives a trade off between the size accuracy and output volume of the clusters. The total yield of clusters produced via physical methods is limited in comparison to chemical methods, as deposition on large areas is physically limited. Scale up of physically produced clusters can also be difficult, however there is ongoing research within this field [64]. The main reason for this is that by increasing cluster formation material, to produce more clusters, there is an increase in the average size of the cluster, thus scale up of the yield of clusters is directly linked to an increase in the average size of the clusters. There is also a limit to the physical size and power of the pieces of equipment used.

Chemically produced clusters are normally made in an aqueous solution, but physically produced clusters are typically deposited upon a solid substrate. The applications and the desired further testing of the clusters can determine the preferred preparation method, but wet clusters can be dried and dry clusters can be suspended within a solution.

1.3.2 Chemical Methods of Production

Liquid phase chemistry is the main method of producing nanoclusters. This involves adding specific chemicals to a reactor and typically heating the mixture to make certain particles precipitate out of the solution. The initial reactants, along with time and temperatures, define the characteristics of the particles that can be retrieved. The specifics of the procedure, vessel shape, and precursor quantities allow certain sizes or compositions of nanoclusters to be favoured. To precipitate Pt nano particles a starting material of H_2PtCl_6 was used with a reactant agent of potassium bitartrate by Cushing *et al.* [65].

This mixture was heated to 60 °C to form nanoclusters of a size less than 1.5 nm. To form PtO nanoclusters [66], $Pt_2(dba)_3$ (where dba = bis-dibenzylidene acetone) was used as a precursor and heated with hydrogen at 75 °C.

Variations on this method include radiation production, where γ radiation is used to induce the precipitation reaction. Belloni *et al.* [67] summarises achievements in producing silver based nanoclusters with the addition of elements like Au, Cu, Pd, Pt, and Pb.

The advantages of both of these methods is that they are typically very scalable in a lab or industrial setting. This could be done through the use of larger reactors, and more starting materials, or through the use of multiple reactors. Typically, the setup used is relatively inexpensive and has low running costs. The biggest disadvantage of chemically produced nanoclusters is the variation and uncontrollability of the size and composition of the clusters. The resulting clusters are poly-dispersed, often containing a very wide range of sizes. The nanoclusters are also typically made in an aqueous solution, thus there are issues of aggregation. If the material is dried, care has to be taken to prevent agglomeration of the clusters. For imaging with a microscope, the material has to be dried, ideally with the clusters well dispersed to enable high quality imaging.

1.3.3 Physical Methods of Production

There are a number of physical methods of production that can be used to generate nanoclusters. These typically produce 'dry' nanoclusters that can be easily studied within a microscope.

Ball milling involves grinding a material with ceramic balls until it reaches the desired size. This method has shown that nanoscale clusters can be produced, with reports of clusters with an average size of < 30 nm [68, 69]. Due to the high pressures created when milling, multiple materials that are not typically compatible, due to thermodynamic equilibrium, can be combined to produce clusters. The major issue with this production method is that the clusters produced have a wide range of sizes, so may need to be

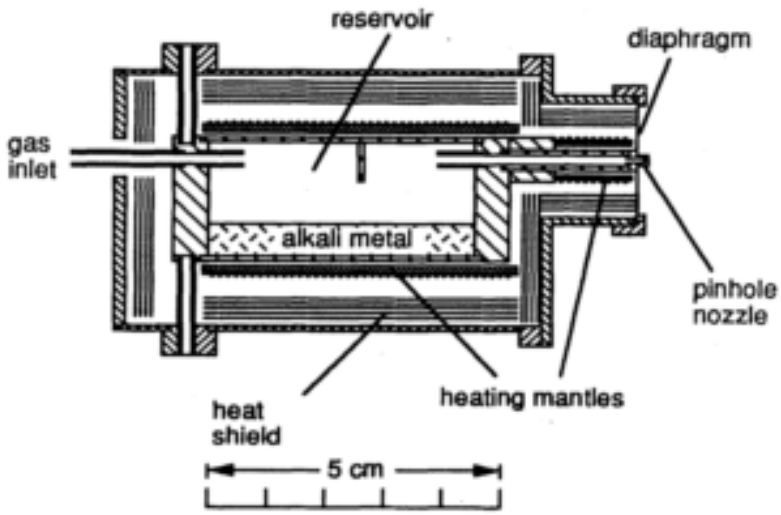

Figure 1.9: Schematic of a supersonic expansion nozzle designed by De Heer and Knight 1987. A metal is heated and evaporated so that the gas can carry the atoms through the pinhole nozzle, expanding, and forming a beam of clusters. Reproduced from [70].

.

filtered depending upon the desired usage. The clusters may also become contaminated with material from the milling balls or vessel.

Supersonic expansion nozzle sources [71, 72] use the fact that a gas rapidly expands upon entering a vacuum chamber to form a beam of clusters. The metal cluster material used has to initially be in a liquid form to be combined with the gas, prior to expansion. The supersonic expansion of this metal vapour, when it passes through the nozzle, generates a beam of clusters as shown in Figure 1.9. The pressure, temperature, nozzle size, and gas can be used to tune the size and flux of the clusters. The typical size of the clusters ranges between 1 and 1000 atoms [70]. As the clusters are in a beam, it is also possible to mass select them, thus improve their size distribution [73]. This type of source is limited in material that it can use for cluster generation, as the material needs to have a relatively low melting point so that it can be melted to a liquid state, without the chamber overheating.

To overcome the need for low melting point materials, laser ablation sources can be used. These sources uses a laser to vaporise a rod of the metal of the desired cluster

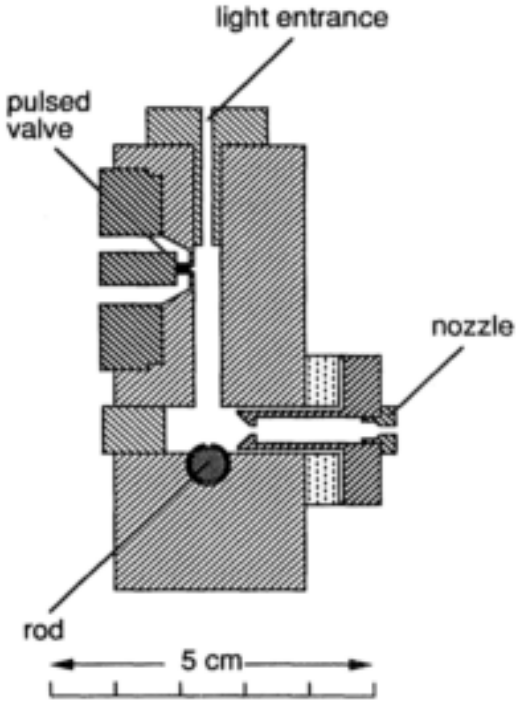

Figure 1.10: Schematic of a laser ablation cluster beam source. The laser enters at the top of the chamber generating an atomic vapour from the rod. This vapour exits the source via the nozzle with a pulse of gas from the pulsed valve. Reproduced from [70].

.

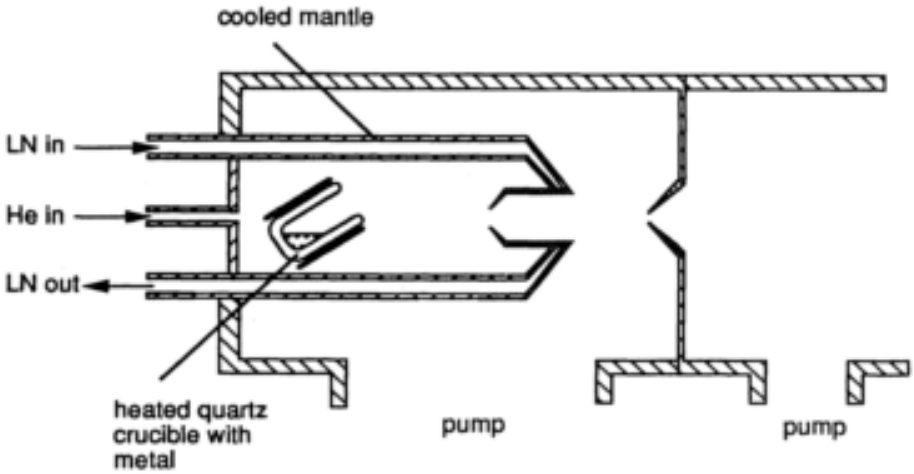

Figure 1.11: Schematic of a gas evaporation condensation cluster beam source. This source uses a crucible to heat a metal to evaporate atoms. These atoms then condense into clusters with the aid of liquid nitrogen. Reproduced from [70].

.

material. The vaporisation coincides with a burst of helium gas, to pulse the clusters away from the vaporisation site. The timing of the laser pulse and the helium gas jet allows the user to control the approximate size of the clusters to between 2 and 10 nm [74, 75]. A schematic of a laser vaporisation source is shown in Figure 1.10. For this source the laser enters the chamber at the top, vaporising the metal atoms from the rod. This atomic vapour is pulsed out of the source through the nozzle on the right-hand side.

Gas condensation cluster sources [77, 76] typically use a crucible of material that is heated until it evaporates or a magnetron to sputter the material. The evaporated or sputtered atoms are then condensed into clusters through the use of a cooled gas and high pressures. The gas acts as the third body for collisions, taking excess energy away from the atoms, allowing the formation of small clusters. This method enables the growth of clusters from two atoms up to many thousands of atoms, offering the widest scope of sizes of all cluster sources. A schematic of an evaporation source is shown in Figure 1.11 and a magnetron sputtering source in Figure 1.12. The main disadvantage of this type of source is that scaling up of production is difficult. This method has previously been used to produce 4 nm Pt clusters, which were deposited as a film [78].

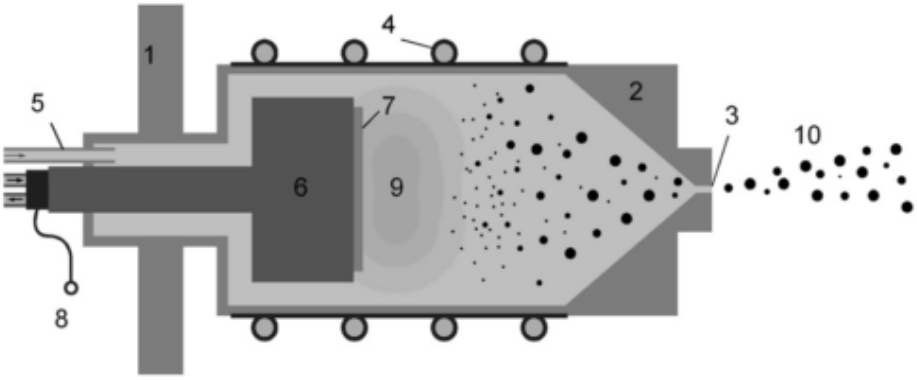

Figure 1.12: Schematic of a magnetron sputtering gas condensation cluster beam source. 1 and 2 are the chamber walls, 3 is the output nozzle, 4 is cooling, 5 gas inlet, 6 is a magnetron, 7 is a metal target, 8 is the power supply, 9 is the plasma, and 10 is the cluster beam output. Reproduced from [76].

.

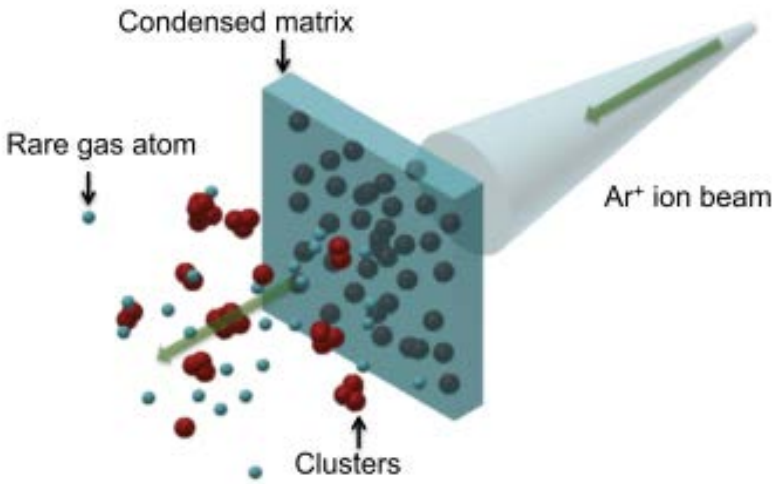

Figure 1.13: Schematic of a scaled up cluster beam source, the matrix assembly cluster source. A matrix of rare gas and metal atoms is condensed on to a matrix, with an argon beam used to sputter clusters from the matrix at a high flux. Reproduced from [64]

.

The scale up of cluster beam sources has been of focus for research in recent years as increased production is critical for real world applications. Keeping the size control with a high flux of clusters, along with careful deposition of these clusters to keep the integrity of each cluster is key for their study and uses. One method of scale up involves embedding metal atoms within a cooled rare gas matrix [64]. This metal gas matrix can then be sputtered with an ion gun to knock out clusters. A schematic is shown in Figure 1.13. This has shown promise for good size control along with higher cluster yields. The equipment is also very scalable, as the matrix can be made larger.

The gas condensation technique forms the basis of the machine used for this work, a magnetron sputtering gas-aggregation cluster source, and is described in detail in Section 2.1. This source has the benefit of producing a reasonably high flux of clusters, with fine size control, especially when coupled with a mass filter, making the clusters produced ideal for the study of cluster characteristics. The source is limited to producing thin samples (less than a mono-layer thick) as the time taken to deposit the clusters is prohibitive at large sample sizes or thicknesses.

1.3.4 Characterisation of Clusters

The clusters produced have to be characterised in a way that indicates useful properties such as their size and morphology. There are a number of ways of getting information from the clusters about their properties, with some main ones detailed below.

A Transmission Electron Microscope (TEM) utilises the same base machine as a Scanning Transmission Electron Microscope (STEM), but projects a diffraction pattern through a sample. The electrons from the electron gun interact with the planes within a crystal sample, interfering constructively and destructively. The spacing and arrangement of the diffraction pattern generated can be used to determine information about the crystals structure. For samples made of multiple materials there will be a doubling up of bright spots as each material has a unique diffraction pattern spacing, even if the structural motif is the same.

For higher resolution imaging a STEM microscope can be used. This works in a similar way to a scanning electron microscope, where a focused beam of electrons are swept across thin samples. Due to the thickness the majority of electrons pass through the sample. Secondary electrons (SE) and back scattered electrons (BSE) can be collected from a sample imaged in STEM, but, due to the thickness of the samples, electrons that pass through contain the most information about the sample. For the analysis of these electrons Bright Field (BF), Dark Field (DF) and High Angle Annular Dark Field (HAADF) can be used. These all involve the electrons that pass through the sample, being deflected by the atoms. In the BF imaging mode the majority of the signal comes from elastically scattered, and zero loss electrons. Areas of low atomic density appear as high intensity regions in the images, whilst the high atomic density areas appear as low intensity regions in the images. This is because the electrons that interact with the material are deflected, thus thicker areas deflect more electrons. For DF and HAADF the detectors collect the electrons that have been scattered by the atoms, thus the higher atomic density areas appear brighter in intensity. The HAADF detector collects the electrons scattered at high angles, where the scattering is related to the square of the atomic number of the atoms. This means the intensity of the electrons gives information about either the thickness or atomic weight of the material that the electrons have passed through. This is detailed further in Section 2.2.1.

Within the STEM there is also the chance to use spectroscopy techniques to gain more information. These include Energy Dispersive X-rays (EDX) and Electron Energy Loss Spectroscopy (EELS). For EELS, electrons that have undergone inelastic scattering, have an energy which is less than their original energy. This energy loss can be measured and is related to the material being studied, thus more compositional information can be generated.

The STEM has been used to image many materials, especially clusters, due to the thickness of the samples. Gold [79, 80, 81, 82, 83], MoS_2 [61], palladium [84], and platinum [85] have all been studied using the STEM available at the University of Birmingham.

The majority of these studies have focused upon examining the atomic structure of the clusters, thus the STEM has been used in HAADF mode. This has allowed for motif determination, and the study of how the structures have changed due to cluster source parameters, environmental factors, and chemical reactions.

Beyond the University of Birmingham, STEM microscopes are used to study many materials, including small clusters. The cluster work predominantly focuses upon gold as a material due to its high atomic number, which makes study in HAADF mode very accessible. Menard *et al.* used a STEM in HAADF mode to study samples of ligand covered gold particles, identifying that the particle core contained 13 gold atoms [86]. Al Qahtani *et al.* investigated the orientations of clusters formed with 9 gold atoms. This research showed that these clusters displayed in either a 3D core shape or a pseudo-2D shape [87]. Van Aert *et al.* studied larger gold clusters, using two HAADF STEM images of the same cluster to produce a 3D visualisation, as show in Figure 1.14 [88]. This enables study of clusters in a deeper way as it gives height information as well as atomic arrangement in the X and Y planes. The use of HAADF STEM to identify different atomic number materials has also been utilised by Di Vece *et al.*. In this study both gold and silver cluster of equal size were deposited upon a TEM grid, thus differentiation by intensity allowed both to be identified and studied individually. Through the use of the other detectors within STEM chemical information can be gained. For example EELS has been used by Browning *et al.* to study boundaries between two differing materials [89, 90]. Privitera *et al.* has utilised both HAADF STEM and EELS STEM to examine Hf, HfO_2 and TiN for resistive switching devices [91]. Reyren *et al.* also used a combination of HAADF STEM and EELS STEM to investigate the chemistry of the O-K and Ti-$L_{2,3}$ edges close and far from an interface [92].

Currently the most state of the art microscopes are housed in the SuperSTEM laboratory in Daresbury [93]. The machines has spatial resolution of less than 0.7Å at 100 kV, accompanied by very small energy spreads of the order of 0.3 eV. These machines are situated in temperature controlled, vibration stabilised rooms, with the user working in

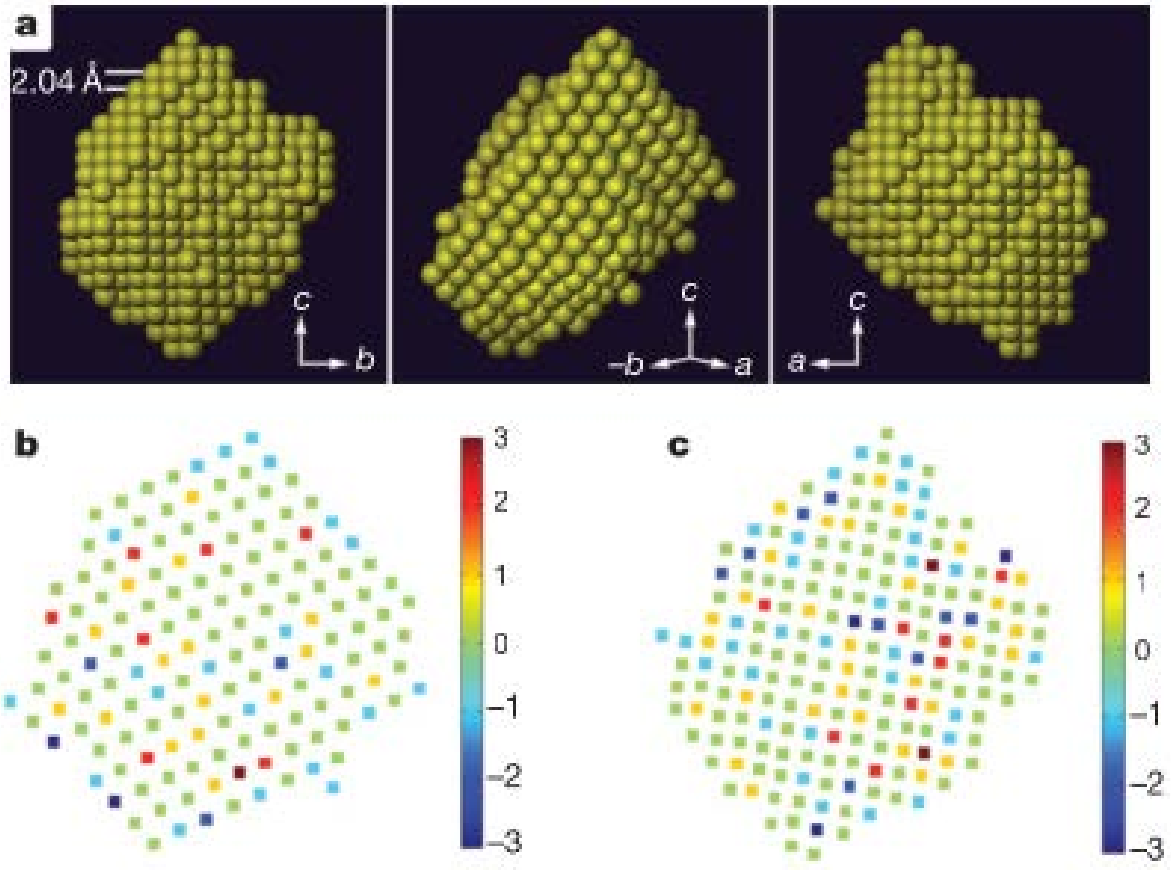

Figure 1.14: The left and the right-hand images in a have been used to produce a 3D representation of the gold cluster (centre image), utilising the fact that the intensity of each column is proportional to the number of atoms contained within the column. Reproduced from [88]

.

an adjacent room to maximise the resolution of the images. The addition of spectroscopy techniques like EELs and EDX give additional information about the samples.

These studies show the flexibility of a STEM microscope for identifying size, structure and compositional information about a sample. For the work within this thesis the main focus is upon the size and morphology of the clusters, rather than the chemical properties. The workings of the aberration-corrected STEM used is detailed further in Section 2.2.1.

Chapter 2

Experimental Methods

The experimental work presented in this thesis was performed predominantly using two pieces of equipment, a magnetron sputtering gas-aggregation cluster beam source and a scanning transmission electron microscope (STEM). These two machines were used to produce and then image the cluster samples before detailed image analysis was performed. This chapter outlines the way these pieces of equipment work, along with descriptions of the analysis used for the data.

2.1 Cluster Source

The magnetron sputtering gas-aggregation cluster source is used to produce clusters of both pure Pt and Pt-Ti for the experimental part of this thesis. Any material that can be sputtered can be used to produce clusters with such a cluster source. Previous work using this cluster source has been performed with many materials including gold, silver, copper, palladium, and molybdenum disulphide [79, 94, 95, 96, 97, 61]. The predecessor of the cluster source used within this work was developed in the early 1990s, and it was designed with an evaporator to produce a metal vapour that is condensed into clusters [98]. The high transmission mass selector was then developed to improve the size control of the cluster source [99]. The fine size control of clusters is participially useful for studying, with a microscope, size dependent structural variations. The system was subsequently

updated again to work with a magnetron sputtering source [100] and is described in more detail below. This development enables the clusters to be charged by the plasma ready for the mass selection.

The magnetron sputtering gas-aggregation cluster source is used to generate clusters from either a single metal or a mixed binary metal target. For this work targets of pure Pt, and mixed Pt-Ti have been used. The cluster source is split into three main areas as shown in the schematic in Figure 2.1. The first chamber, Generation, is used to produce the clusters by sputtering the target material. The second chamber, Ion Optics, is used to accelerate and collimate the beam of clusters, ready for mass selection. The third chamber, Mass Selection, is used to select the desired size of the clusters ready for deposition. The entire cluster source is a high vacuum system, with an average pressure of 10^{-7} torr. This pressure is attained through the use of rotary (generating 10^{-3} torr) and turbo pumps (generating 10^{-7} torr) and monitored with pirani and penning gauges. The entire system is vented with liquid nitrogen gas to change the target to either Pt or Pt-Ti. The liquid nitrogen gas helps to preserve the cleanliness of the chambers, as it reduces water contamination. After venting and changing the target, it takes upwards of five hours to pump the system down to a normal operating pressure. As this system is not required to operate at Ultra High Vacuum (UHV) pressures, the system is not baked. Although the system is not run at UHV pressures, maintaining a low contaminant environment is important, thus care is taken whilst performing target changes to minimise the time that the chambers are open and vented to atmosphere.

Figure 2.1 shows the cluster source schematic with the three sections marked. Each chamber will be discussed in detail in the following sections of the thesis.

2.1.1 Cluster Generation

The experimental work presented in this thesis includes the production and study of both pure Pt and mixed Pt-Ti clusters. The clusters are formed within the generation chamber of the cluster source before being accelerated and mass selected.

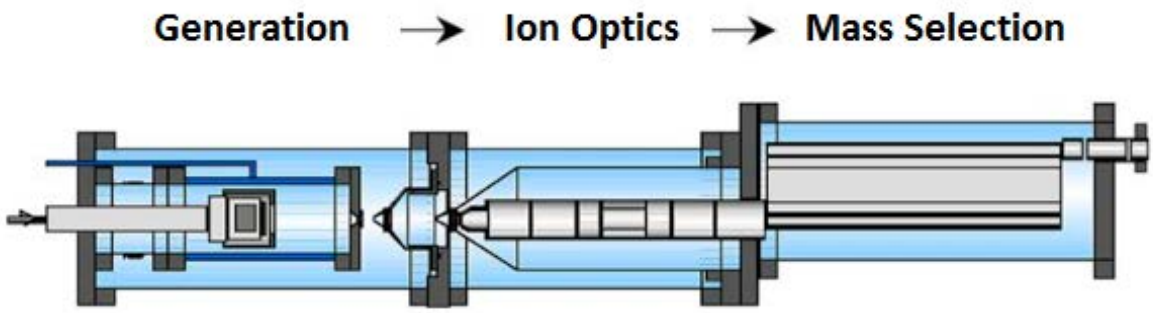

Figure 2.1: Schematic of the magnetron sputtering gas-aggregation cluster source setup, used to produce samples for this thesis. The source is split into three areas, each of which is described in detail in Section 2.1. Image adapted from [100]

The two targets used were a pure Pt target and a mixed Pt-Ti target, both 99.95% pure, supplied by PI KEM [101]. The mixed target was 25 weight percent Pt, 75 weight percent Ti, which is approximately equivalent to 1 in 13 atoms being Pt with the rest being Ti. The Pt-Ti target was normally stored in a vacuum to reduce the thickness of the TiO_2 layer which formed on the target's surface when exposed to air. The thin layer of TiO_2 that inevitably formed was removed through sputtering of the target prior to use.

Both targets are sputtered by a DC argon plasma making an ionised 'cloud' of atoms, some of which may have been sputtered as dimers or trimers instead of single atoms. Three body collisions occur between two metal atoms and a molecule of helium gas; the cooled helium gas acts as the third body, enabling the excess kinetic energy to be dissipated and the two metal atoms to bond. Liquid nitrogen cooling aids this process, by reducing the temperature of the atoms, and thus their kinetic energy. Without liquid nitrogen cooling only small clusters form, thus for large clusters cooling is necessary. The three body collisions form tiny clusters of a few atoms, which can then grow by the addition of single atoms or other tiny clusters. The sputtered atoms form charged clusters, due to the sputtered atoms being ionised by the plasma.

Figure 2.2 shows the effect of varying helium pressures upon the size and flux of the Pt-Ti clusters. As the pressure of He is increased, there is an increase in the flux of clusters

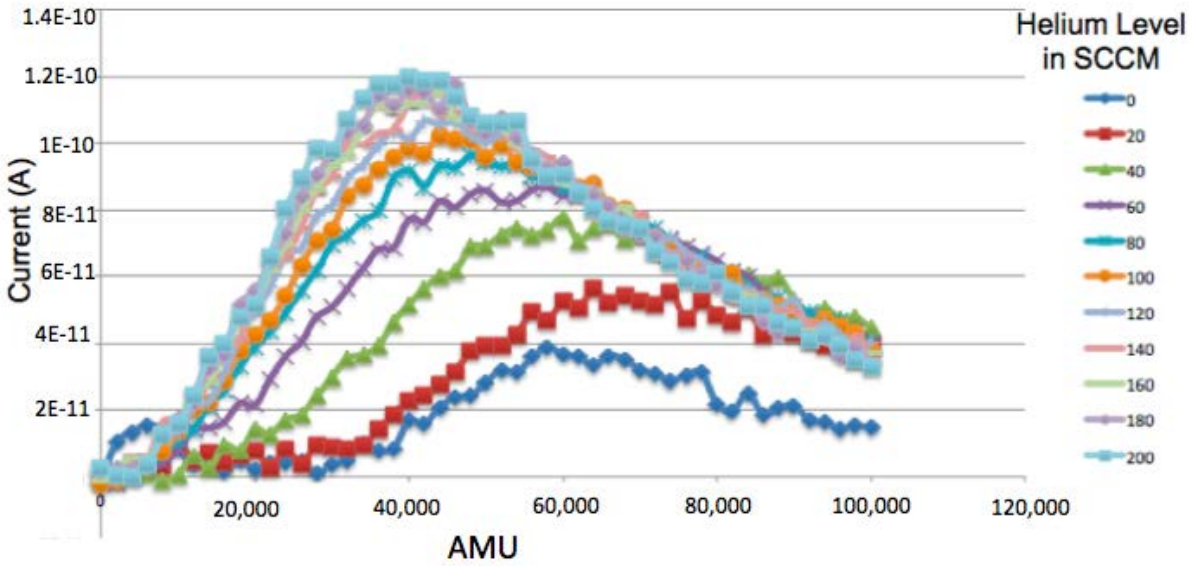

Figure 2.2: Effect of varying helium pressures on cluster current. As the helium level increases the cluster flux increases, but the average cluster size decreases.

produced, but a reduction in the average size of clusters from 6,000 to 4,000 Atomic Mass Units (AMU). The reduction in the size of the average cluster is due to the increased number of He collisions, causing an increase in cluster flux with a smaller average size. This reduces the amount by which the clusters can grow through addition of single atoms, forming more smaller clusters on average than at lower He levels. This also explains the increased current seen for higher He pressures: The number of sputtered atoms within the chamber remains constant, but as the size of clusters falls the quantity of clusters increases.

As well as controlling the He level, and adding enough Ar for the plasma to ignite and be maintained, the power level of the magnetron can be varied to increase the flux of clusters. Figure 2.3 demonstrates how varying the power level changes the flux of the clusters, as well as the average size of clusters produced. The higher the power level, the more atoms sputtered, and thus the larger the flux and size of clusters, as there are more collisions within the generation chamber. The cluster size stabilises, and then slightly shrinks, for power levels 90 W, 110 W and 130 W, due to a trade off between number of clusters and the size of cluster produced. As more atoms are available for cluster

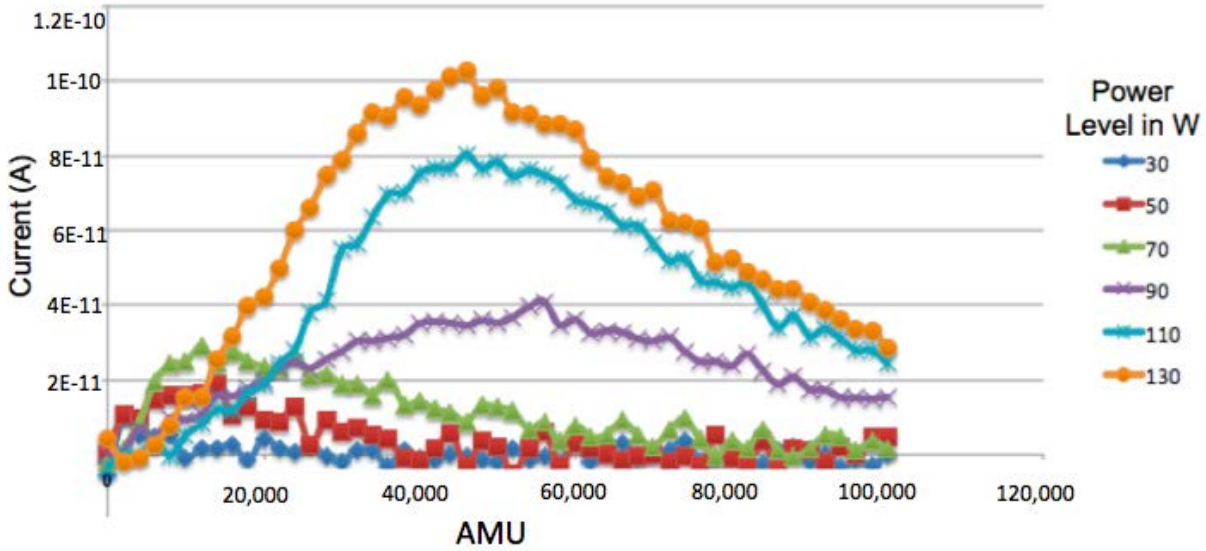

Figure 2.3: Effect of varying power levels on cluster current. As the power level is increased the cluster current increases, along with the average size of clusters.

nucleation events there is a decrease in the number of free atoms within the chamber. They are then not available for cluster growth, thus the size of the clusters start to decrease when the density of atoms within the chamber reaches this critical point.

Another parameter recorded was the overall pressure within the generation chamber. This could be varied using the Ar pressure or the nozzle size. The nozzle is the opening between the generation and ion optics chamber, and is fitted with an iris valve. Controlling the size of this opening changes the pressure within the generation chamber, with a smaller nozzle size increasing the pressure, causing more collisions and thus larger clusters. Contrary to this, if the nozzle was closed too far, the flux of clusters would dramatically reduce, as the clusters are prevented from leaving the generation chamber.

The condensation length of the generation chamber can also be varied. The condensation length gives the duration of time that the atoms can condense into clusters, before passing through the nozzle. A long condensation length has been shown to maximise stability within the clusters, whereas short condensation lengths lead to a higher proportion of unstable isomers [81]. This is because the clusters produced using a short condensation length tend to grow faster and thus are more prone to kinetic trapping effects. This is

where a cluster becomes stuck in a structural motif because that motif was dominant at a smaller cluster size. The larger condensation length, the slower the clusters from, giving each cluster a better chance of finding equilibrium and thus their most stable cluster structure. For the work within this thesis the maximum condensation length of 250 mm is used to favour the most stable clusters.

2.1.2 Ion Optics

The ion optics chamber, situated between the generation and the mass selection chambers, is used to accelerate and collimate the beam of clusters. The positively charged clusters from the generation chamber are guided with negatively biased plates and einzel lenses. These are controlled with software, so that the the maximum number of clusters can pass into the mass selector, and thus reach the deposition chamber and sample. For STEM samples, a relatively small cluster density is needed for imaging, so a trade off between time tuning the ion optic parameters and deposition duration has to be made. For low density samples, tuning is less important as the deposition time is already short, in the order of a minute. Conversely for very dense samples, approaching a mono-layer, it is very important to maximise the flux of clusters generated by the cluster source and ensure that the beam is propagated efficiently through the system.

The beam of clusters also needs to be travelling parallel to the central axis of the ion optics chamber when it enters the mass selector. This is important in order for the mass sector to be accurate, as any cluster with a vertical component of momentum initially, compared with the mass selector, may be incorrectly size selected. This is checked with a Faraday cup measuring the white beam current before mass selection, and adjusted with settings not typically varied by the cluster source user.

2.1.3 Mass Selection

The mass selector is situated after the ion optics chamber, and is used to isolate a small distribution of cluster masses ready for deposition. The mass selector works by acceler-

ating the clusters vertically, perpendicular to their initial travel direction, using a pulsed electrical field, seen in a schematic in Figure 2.4. The acceleration experienced by each cluster is proportional to its mass. The clusters, now travelling vertically and horizontally, then experience an acceleration free region between pulses which enables the clusters to spread according to mass in a vertical direction. A second opposite direction, but same period, pulsed electrical field, is then used to decelerate the clusters in the vertical direction, meaning only their initial horizontal component of motion remains. As the larger clusters are accelerated less than the smaller clusters, the clusters are distributed in a vertical direction once the second vertical pulse has been applied. The time between pulses and the duration of each pulse is used to control which mass of cluster passes through the aperture, and thus what size of clusters passes into the deposition chamber.

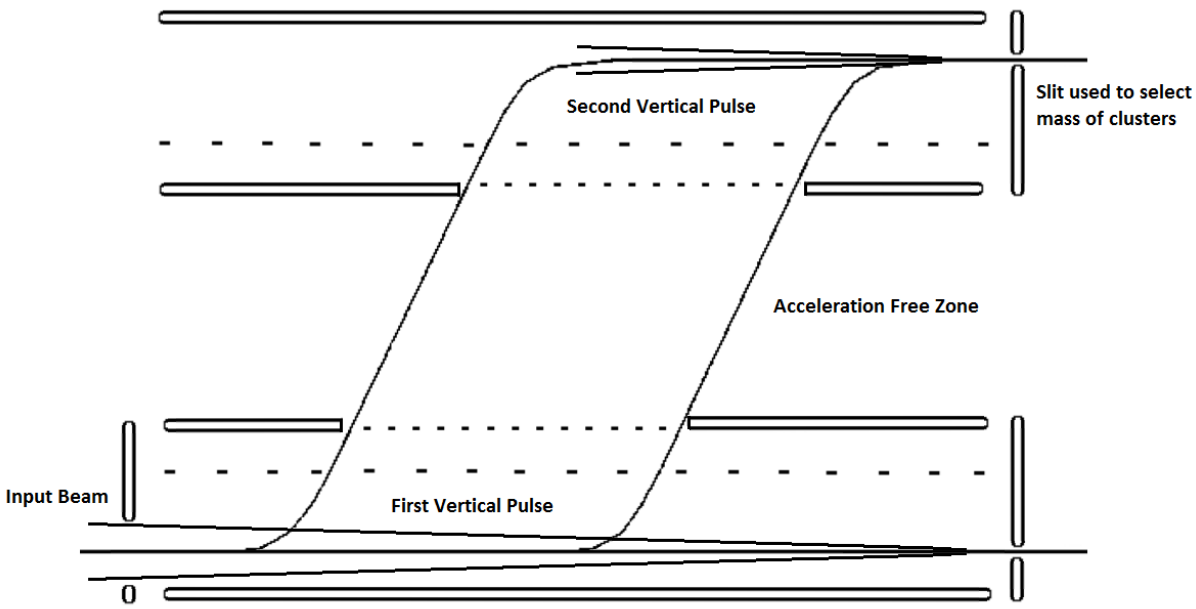

Figure 2.4: Schematic of the mass selector used within the cluster beam source. The beam enters from the lower left-hand side and is accelerated upwards by the first pulse. It then interacts with a field free region, before a second pulse is applied to counteract vertical motion. The cluster beam leaves the chamber via a slit at the top right-hand side. Timing and duration of the pulses are used to control which size of cluster passes through the slit. Image adapted from [99].

The mass resolution of the cluster source is based upon the convolution of the entrance and exit aperture, along with the vertical displacement between the apertures [99].

$$Mass\ Resolution = \frac{Vertical\ Displacement}{Convolution\ of\ Entrance\ and\ Exit\ Apertures} \tag{2.1}$$

Within our cluster source, the vertical displacement between the centre of the entrance and exit apertures is 180 mm. The size of the entrance and exit apertures can be varied between 2 mm and 8 mm, but typically for this work both apertures were set at 8 mm to maximise throughput of clusters.

$$Mass\ Resolution = \frac{M}{\Delta M} = \frac{180}{\sqrt{8^2 + 8^2}} = 16 \tag{2.2}$$

For a setting of 100 atoms, the size will range between 94 and 106 atoms. If both apertures had been set to 2 mm, the resolution would have been 64, thus for a setting of 100 atoms the clusters mass would range between 98.5 and 101.5 atoms.

If the mass selector is ramped across many masses, a plot like Figures 2.2 and 2.3 can be produced. If a single size is selected only the current from that size is measured or deposited upon the TEM grid.

2.1.4 Deposition

Once the clusters reach the deposition chamber, they are impacted upon a substrate using predominant the substrate acceleration voltage. If the substrate is grounded the clusters still have some kinetic energy, but soft land upon the substrate. The substrate acceleration voltage controls how the clusters sit upon the substrate surface, whether they are implanted, pinned, or soft landed [102]. For this work, 1 eV per atom was typically used so that the clusters were soft landed, but unlikely to move around the surface and grumose. This voltage also allowed the cluster to be deposited without breaking apart, which was verified with STEM imaging. Test experiments with small clusters deposited at higher voltages showed the break up of the cluster, with total disintegration as well as single atoms peppering the substrates surface. The clusters were also stored for many weeks and re-imaging showed that the clusters had not agglomeration, thus, the clusters

are adequately pinned.

The clusters were deposited upon nickel grids covered in a holey carbon film purchased, from Agar Scientific [103]. The holey carbon film is a good substrate for the clusters, as it has a low intensity when imaged in dark field STEM. This is because carbon has a low atomic number and thus does not scatter many electrons. The holey part of the film also provides a useful feature for easy focussing of the STEM. Clusters can also be deposited upon other samples within the cluster source, for example graphene oxide grids, graphite plates or glassy carbon disks, dependent upon the analysis method or further experimentation desired. The deposition of clusters on differing substrate materials may cause the clusters to form different shapes. For example, they may bind better or worse on a graphene oxide grid due to surface interactions between the cluster material and the graphene layer.

Once the clusters have been deposited upon the grids, they have to be removed from the cluster source. This is done through the use of a load lock, so that the entire system does not need venting. This allows multiple samples to be deposited in quick succession, which is ideal for depositing samples of multiple sizes with little variation within the cluster source parameters.

The load lock is also fundamental in the design of the nitrogen and argon transfer box, described in Section 3.3.1. This enables a user to move a sample from the deposition chamber into the load lock, vent the load lock with nitrogen or argon, and then transfer the sample into a glove box style setting, or gas bag with minimal air contamination. The sample grid can then be transferred to the STEM arm, and into the microscope with only a few seconds of air exposure. This has allowed for the study of the impact of oxidation upon the Pt-Ti clusters with low levels of air exposure.

Once the clusters had been deposited they were either imaged or stored under vacuum. This was to keep the samples as clean as possible, but as it was a communal vacuum storage system it was often vented, thus the samples were regularly exposed to air during storage. No change was seen between clusters imaged soon after production, and then im-

aged again after storage for many weeks, thus the storage conditions were determined not to have impacted the clusters. The only difference was a small increase in contamination of the carbon surface.

2.2 Imaging of Clusters

2.2.1 Scanning Transmission Electron Microscope

The probe corrected aberration-corrected STEM available for imaging the clusters at the University of Birmingham enables users to image samples with atomic resolution. Having both the STEM and the cluster source within one building allows for reasonably fast sample transfer, reducing contamination, which enables users to take the best possible images. The STEM used is an aberration-corrected JEOL 2100F STEM with Cs correction [104], a photo of which is shown in Figure 2.5.

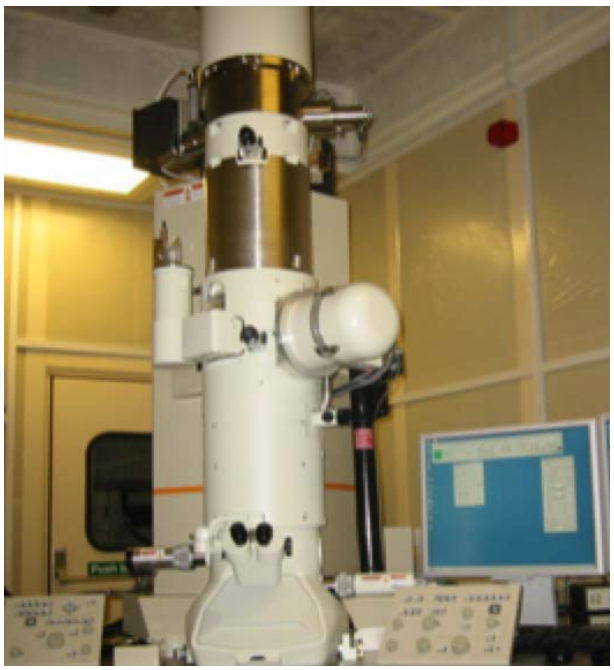

Figure 2.5: Photograph of the aberration-corrected JEOL 2100F STEM with Cs corrector used at the University of Birmingham.

The STEM is made up of an electron source, condenser lenses, apertures, aberration

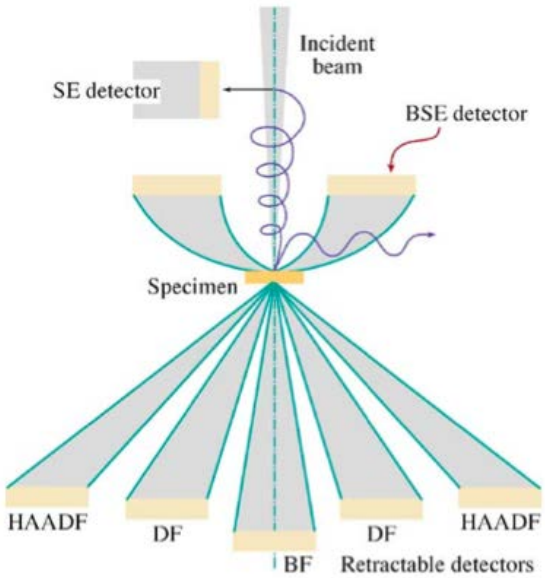

Figure 2.6: Detectors that can be used on STEM, including Dark Field (DF), Bright Field (BF), Secondary Electron (SE), Back Scattered Electron (BSE) and High Angular Annular Dark Field (HAADF). Reproduced from [105].

corrector, scanning coils, sample stage and detectors. The entire STEM is operated under a high vacuum, maintained by pumps and liquid nitrogen cooling. It is situated in a sound proof room to minimise vibrations which can affect the imaging resolution. The pumps and water cooling system are stored in a separate room, further reducing vibration. The electron source used in this STEM is a Field Emission Gun (FEG). This works by applying a strong electric field between a tungsten tip and an anode, situated just below the FEG, to generate a intense beam of electrons. These electrons are accelerated by a second anode up to 200 keV. They then pass through the condenser lens, which is used to focus the beam. An aperture is used at this point to balance the beam quality (inclusion or exclusion of edge electrons) with the intensity of the beam required.

The aberration corrector used within this STEM is a CEOS double hexapole spherical corrector. The spherical corrector is designed to compensate for the fact that all lenses cause rays passing through different areas of a lens to be focused at different points. Figure 2.7 shows that the rays pass through the outer edge of the lens focus before rays that passing through the centre of the lens. Correcting for this phenomenon produces a

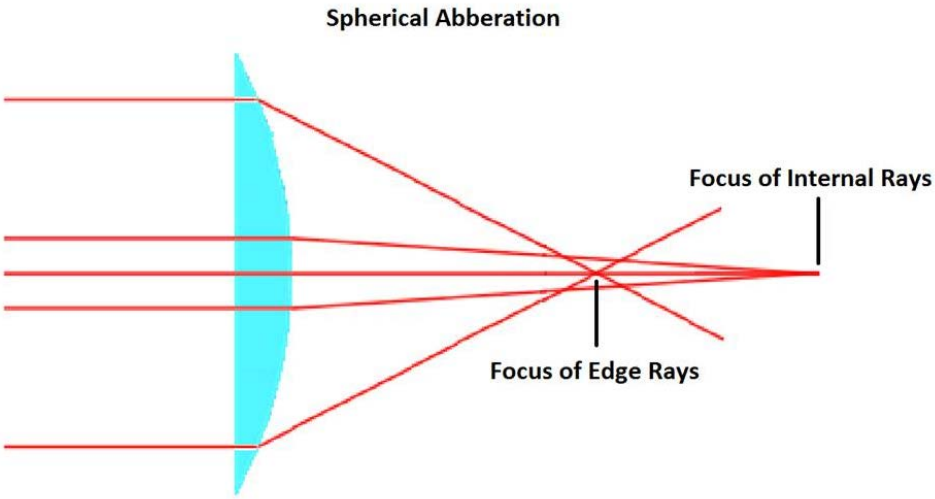

Figure 2.7: Ray diagram showing that external rays converge closer to the lens than internal rays. This leads to spherical aberration.

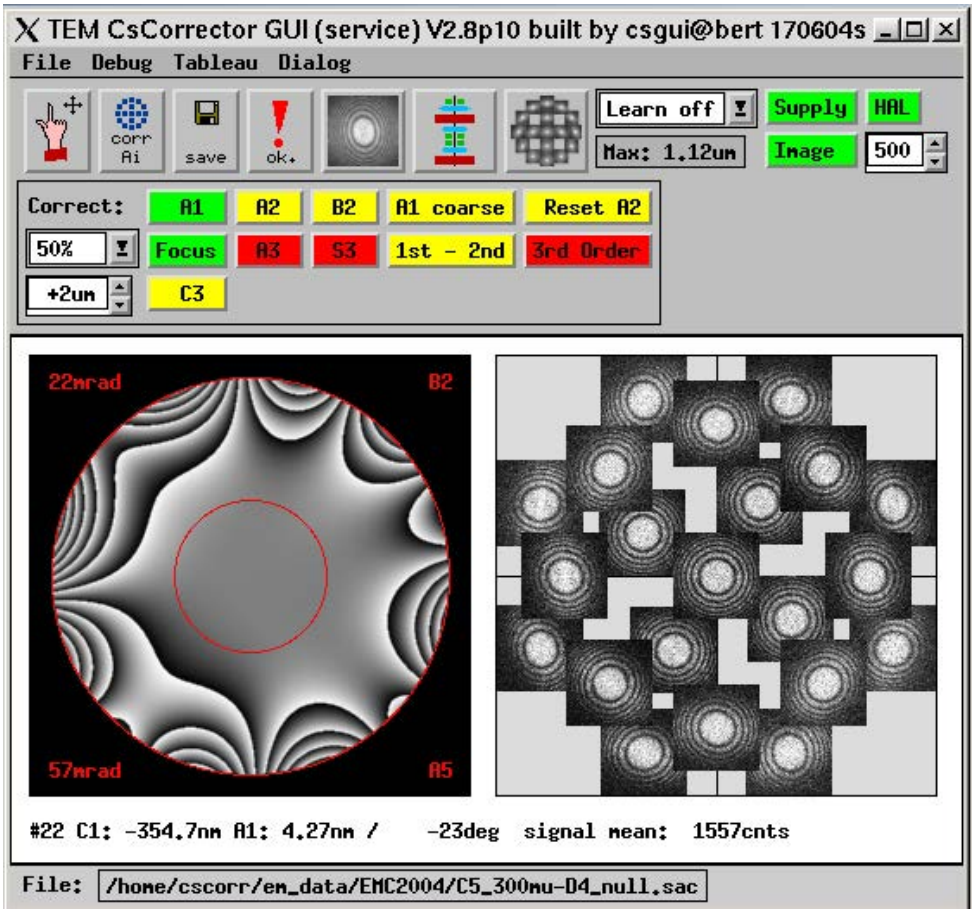

Figure 2.8: Image of the software used to correct the aberrations. Image reproduced from [106].

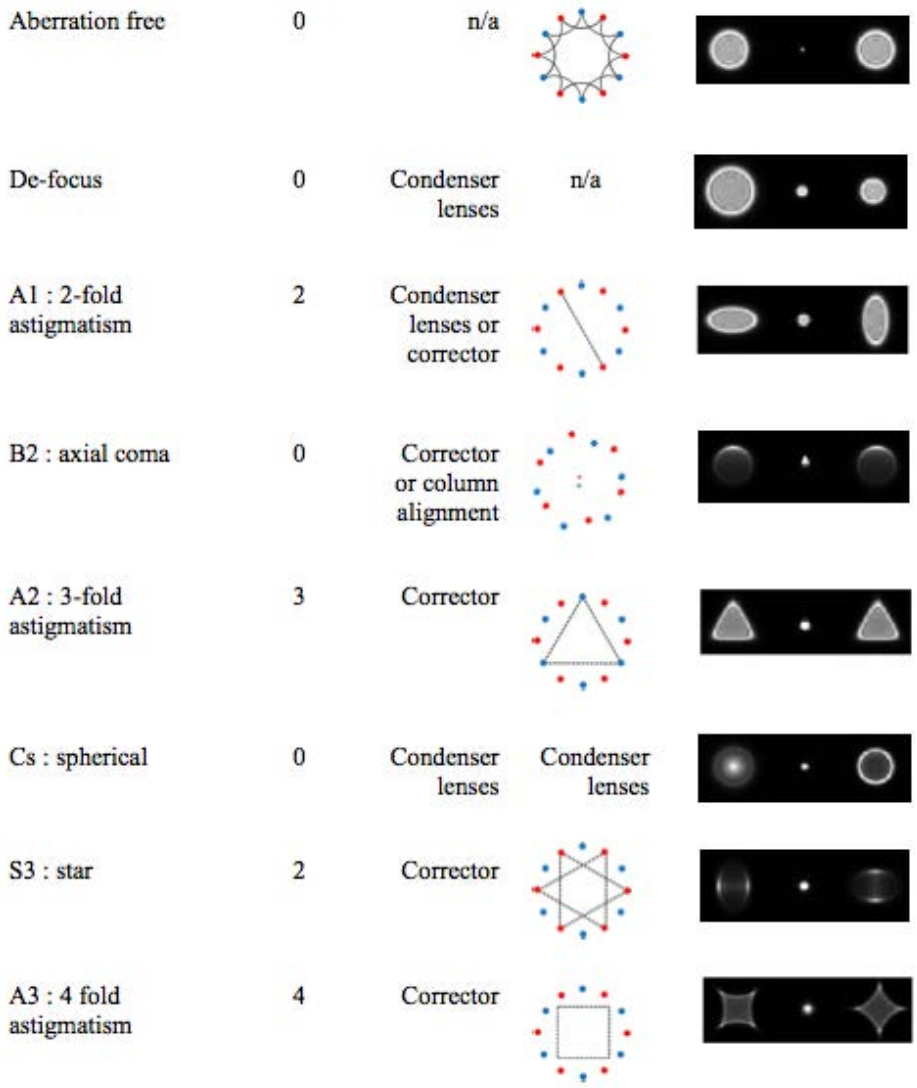

Figure 2.9: Diagram of principle aberrations experienced within the STEM, along with their cause and simulations of the image seen. The first column is the description of the aberration, the second is its symmetry, the third is the cause, the forth is the correction mechanism, and the fifth is the simulation of the aberration for an over, perfect, and under focused beam. Adapted from [107].

clearer image of the clusters, taking the resolution of the microscope from approximately 1 nm to 1 $\dot{A}$ for our microscope. State of the art microscopes can reach these limits prior to aberration correction. The hexapole corrector creates a negative spherical correction to compensate for the spherical aberration. Figure 2.8 shows the software used to change the hexapole corrector to correct for the aberrations, whilst Figure 2.9 shows the principle aberrations seen within the STEM. The tableau seen in Figure 2.8 is used by the software, in conjunction with the information in Figure 2.9, to recommend adjustments to the hexapole set-up. By making these adjustments the user can improve the images obtained from the microscope.

The scanning coils are used to raster the beam across the sample to build up an image. The sample stage is where the sample is inserted. For this work, TEM grids with clusters deposited upon the holey carbon film are used as they are thin enough for electrons to pass through. The detector used for this work is a HAADF detector, so that both elemental and structural information can be gathered. The collection angle for the University of Birmingham's STEM is 62 to 164 mrad. Other detectors that can be used are EELS and EDX, but they have not been utilised for this work. The schematic in Figure 2.6 shows where each detector ring is located, including Dark Field (DF), Bright Field (BF), Secondary Electron (SE), Back Scattered Electron (BSE) and High Angular Annular Dark Field (HAADF). The SE electrons have a particularly high resolution as they are produced very close to the samples surface, thus only contain information about a very localised area to a depth of less than 5 nm.

The images are taken on the STEM using Digital Micrograph software [108]. This allows for some analysis of data, but for this work the image, along with a scale bar are taken for post processing. All images are taken in grey scale, with false colours added for ease of interpretation.

The maximum resolution of the microscope is determined by the accelerating voltage of 200 keV [105]. For microscopes the resolution limit is:

$$Resolution \approx 0.61 * \lambda, \tag{2.3}$$

when the small angle approximation is used. For the electron microscope, λ is calculated using the De Broglie wavelength:

$$\lambda = \frac{h}{p} = \frac{h}{mv}, \tag{2.4}$$

where h is Planck's constant, m is the mass of the electron and v is its velocity of the electrons. The energy of the beam in electron volts is given by:

$$eV = \frac{1}{2}mv^2, \tag{2.5}$$

where V is the accelerating voltage and e is the elementary electron charge. This is rearranged to become:

$$v = \sqrt{\frac{2eV}{m}}. \tag{2.6}$$

It follows that

$$\lambda = \frac{h}{\sqrt{2meV}}. \tag{2.7}$$

Using this equation and an accelerating voltage of 100 keV gives a resolution of 3.88 pm. For 200 keV the resolution would be 2.74 pm, and for 300 keV the resolution would be 2.24 pm.

This calculation does not take into account the fact that the electrons are approaching the speed of light, thus relativistic effects have to be taken into account, giving:

$$\lambda = \frac{h}{\sqrt{2meV}} * \frac{1}{\sqrt{1 + \frac{eV}{2mc^2}}}. \tag{2.8}$$

Using this equation to calculate λ the resolution for 100 a keV accelerative voltage is

3.70 pm, for 200 keV it is 2.51 pm and for 300 keV it is 1.96 pm. These values are far smaller than the 1 $\dot{A}$ limit of the microscope as this is the theoretically smallest resolution, rather than the experimentally obtained resolution. The reality of aberrations within the microscope mean that this limit is never reached, but technology continuously develops, moving closer to this limit. These values also show that there is a trade off between resolution and damage to the sample; the higher the energy, the better the resolution, but the higher energy electrons damage the sample more. This is particularly important for clusters as the electrons can cause the cluster to morph between structural motifs or disintegrate.

The STEM is run in HAADF mode so that the intensity of the images produced relates to the atomic number of the sample. The large angle of the HAADF detector allow for almost exclusive collection of electrons scattered by Rutherford scattering. The equation for Rutherford scattering is shown in Equation 2.9

$$\sigma_r(\theta) = \frac{e^4 Z^2}{16(4\pi\varepsilon_0 E_0)} \frac{d\Omega}{sin^4 \frac{\theta}{2}} \tag{2.9}$$

where the scattering angle is θ, Z is the atomic number of the material, ε_0 is permittivity of free space and Ω is the solid collection angle. This equation shows that the cross sectional area of scattering is proportional to Z^2. In reality screening of electrons reduces the exponent so that the intensity is proportional to Z^α, where α has been experimentally verified to be 1.46 $\pm$ 0.18 for a collection angle of 62 to 164 mrad [97]. This calibration was done using clusters of gold and palladium atoms, both containing 923 atoms. The intensities of these two types of cluster could be related by Equation 2.10 where I indicates the intensity of each metal and Z indicates the atomic number. Larger collection angles result in an α value between 1.2 and 1.8 [109].

$$\frac{I_{Au}}{I_{Pd}} = (\frac{Z_{Au}}{Z_{Pd}})^\alpha \tag{2.10}$$

This relationship has been used to study a number of materials including gold [110,

111, 112], $SrTiO_3$ [113] and nickel bismuth [114].

The parameters used within STEM are also used later for the QSTEM simulations in Section 4.3.3. The QSTEM software is designed to simulate the scattering intensity for STEM images, or the diffraction pattern fo TEM samples. The key parameters are an accelerating voltage of 200 keV, convergence angle of 19 mrad, HAADF collection angle of 62 to 164 mrad, spherical aberration corrector of 0.001 mm and the temperature of 300 K.

For the STEM imaging the detector was assumed to be perfect. This includes the assumption that all electrons that are scattered towards the detector are captured, and the detector has a uniform collection efficiency. It also assumes that the response of the detector is linear with respect to increasing atomic number. These assumption have been made as characterising the response of the detector is complex; ideally, a totally uniform surface is imaged which should yield a uniform image. The discrepancy between the resultant image and a uniform surface would then be down to the detector. The uniform surface could be a surface with a very well known structure, but this means the comparison is performed with a simulation and thus would be less accurate [115]. As the STEM is imaging single atoms, creating a uniform surface that could be used to identify the efficiency of the detector is difficult. To minimise the variation in the detector between images, the same values for brightness and contrast were used for all studies done in this thesis. For annular detectors the variation in the detector efficiency should be radial as shown in Figure 2.10. This figure shows that if small or very large angles are used the detector efficiency is reduced towards the centre and very edge of the image. To reduce the chances of this impacting the images the HAADF set-up, with angles between 62 and 164 mrad, was used for this work.

A basic check of the detector efficiency was performed by comparing multiple low magnification images, to see if there is a regular pattern of bright/dark areas. For areas of poor efficiency, a dark patch was expected. 150 low magnification images were used for the calculation, an example of which is shown in Figure 2.11.

For each pixel the median value from the 150 images was taken. The median value was used to avoid any clusters present skewing the result (the median pixel is most likely to represent an image of the substrate). Images with clusters present were used as they proved that the microscope was set-up correctly and focused in the correct plane. The median would show a trend of darker/lighter patches as the areas would always measure a lower or higher value than expected. The median image is shown in Figure 2.12. The figure shows a reasonably uniform image with the maximum value of 224331 and a minimum value of 193422, thus the difference is 30909 arbitrary units. This is 13 % of the maximum intensity. This is reasonably consistent with the 10 % estimate from literature[116, 117], and would improve further if more images were used. This was shown to be true by performing the same analysis with only 10 images, which gave a bigger variation of 38 %.

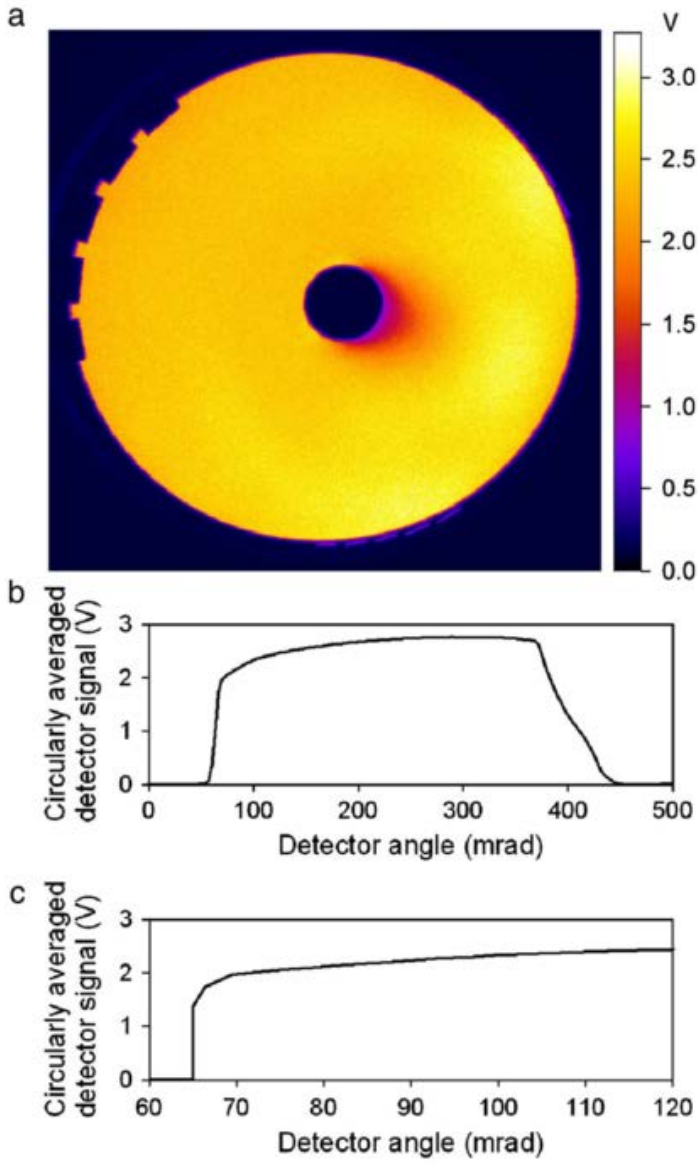

Figure 2.10: Image of a typical detector plot for a ADF detector. Reproduced from [115].

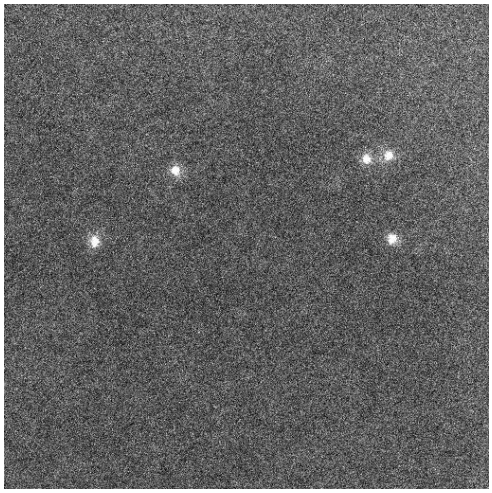

Figure 2.11: Low magnification image of 30,000AMU clusters for estimating the detector efficacy.

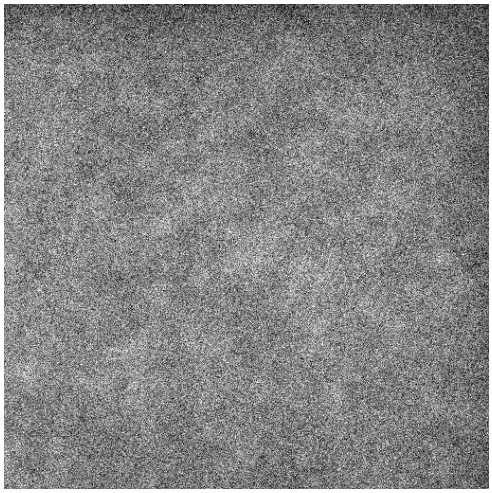

Figure 2.12: Median image calculated by taking the median value from 150 images on a per pixel basis.

From this analysis it is clear that there is variation across the image which can not be easily accounted for. If taken in to account this would effect the he intensity measured, and thus the number of atoms estimated to be within each cluster. From the median image it appears to be evenly distributed across the image, rather than in patches, so should not skew the results if some clusters are imaged with the cluster central, and some imaged with the cluster off centre. A background subtraction method described in Section 2.2.2 attempts to mitigate some of this error, and uses a ring to reduce the chance of a gradient across the image impacting the results. This source of error will only effect numbers of atoms calculated through the intensity method rather than through the area.

2.2.2 Number of Atoms in Each Cluster

The STEM images are taken in HAADF mode so that the intensity of each image can be converted into a number of atoms. This allows users to calibrate samples or use size selected clusters as a mass balance for clusters of unknown size, typically those produced chemically [112]. This is due to the fact that the scattering of electrons at high angles is proportional to the atomic number of the cluster [109], as described in Section 2.2.1.

There are two distinct methods used for calculating the number of Pt atoms within the mixed Pt-Ti (including Pt-TiO_2) and the pure Pt clusters. For the Pt-Ti clusters, a volume is calculated for the cores, whilst for the mixed 10-600 atom pure Pt clusters the intensity is used. Each is detailed with an example below, with each method forming the basis of analysis within the results chapters.

For the Pt-Ti samples transferred in air, the area of Pt in each core is used to predict a volume, from which the total number of Pt atoms is calculated. To perform this operation on many images a program was written that applies a threshold to each of the Pt-Ti cluster, highlighting all of the Pt atoms. The Pt atoms, which are bright in the black and white image, are encapsulated by blue outlines. The sum of the pixel value with its four nearest neighbours is used to determine the application of the threshold. This nearest neighbour calculation reduces the impact of noise on the threshold application for the

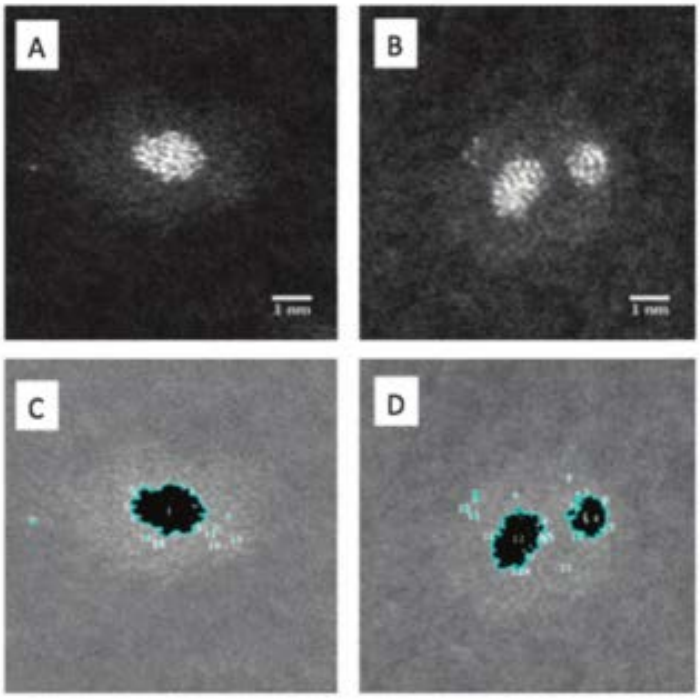

Figure 2.13: Images of Pt-Ti clusters transferred in air, before and after the application of the threshold. The Pt is contained within the blue outline, thus the area can be used to calculate the number of Pt atoms within each core. Reproduced from [85].

image. An example of the threshold application is shown in Figure 2.13, where images C and D are the result of applying the threshold to A and B respectively. The Pt atoms within the threshold application area have been coloured black for clarity. Images C and D both show extra small areas of black outlined in blue, where single atoms have been picked up. These are ignored by the program if they contain an area of less than two atoms. The area within the cores that have been outlined by the threshold are then projected into an equivalent circle. The radius of this circle is then used to calculate an equivalent volume of a sphere, working on the assumption that the cores are approximately spherical. The bulk properties of Pt can then be used to calculate the number of Pt atoms that would fit within the spherical volume, thus giving an approximation for the number of atoms within each of the Pt cores.

The equation for calculating the number of atoms within the volume is as follows.

$$Number\ of\ Atoms = \frac{Volume * Atoms\ in\ Unit\ Cell}{Volume\ of\ Unit\ Cell} \tag{2.11}$$

For Pt the number of atoms within the unit cell for the bulk is 4 as it is FCC in structure. The volume of the unit cell is 392.42 pm cubed as all of the lattice constants are the same.

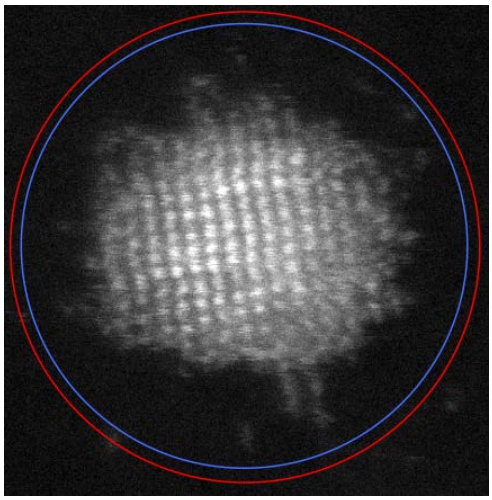

Figure 2.14: Example of background subtraction method used for each cluster. The average intensity between the two rings is used as the average background intensity. This can then be subtracted form the cluster intensity, leaving only the contribution from the metal atoms.

To calculate the number of atoms within each of the pure Pt clusters, the intensity of the cluster has to be taken without the contribution of any background intensity from the carbon substrate. Figure 2.14 shows an image with two concentric rings drawn around the cluster. The intensity contained within the rings, between the red and blue line, is due to the background carbon substrate, and can be divided by the number of pixels within this area to give an average background intensity. The diameter of the internal ring was determined manually for each cluster, and aimed to encompass all atoms within the cluster. This can then be subtracted from the intensity contained within the blue ring, after accounting for area, to give an intensity due to the Pt atoms only, excluding the background contribution. For the pure Pt samples, the intensity of known sized samples, (55, 147 and 309 atoms) was used to calibrate the mixed 10-600 atom samples. A check

was then performed by comparing the size distribution of the clusters imaged with the size distribution of the clusters deposited.

These two methods will give an approximation of the number of atoms contained within the clusters, but will be prone to some errors. For volume calculations approximating the cluster to an oval and projecting it to a 3D structure ignores variation in the cluster shape. Assuming a bulk structure for the cluster is only accurate if the clusters structure is bulk, which, for small clusters is not true. For the intensity measurements, although the background is subtracted, the intensity can be inaccurate as the substrate may not have been uniform. Many clusters have been imaged and analysed in this work to reduce the impact of these errors. Future work on very small clusters could look towards combining simulations of intensity and shape with experimental results directly.

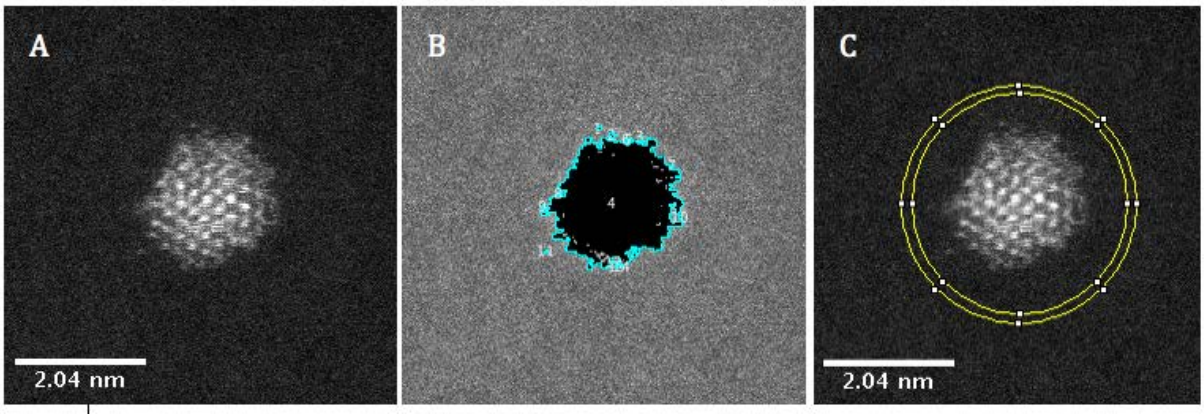

Figure 2.15: Images showing both analysis techniques performed on the same pure Pt cluster. A. original image, B. Image with threshold applied, C. rings for background subtraction.

To do a direct comparison of the two analysis methods a single Pt cluster was analysed both ways. These images are shown in Figure 2.15. Image A shows the original pure Pt cluster. Image B shows the threshold that was automatically applied to the cluster, with the cluster having an area of 2.97 nm^2. This converts to a projected volume of 4.003 nm^3 and 256 Pt atoms. Image C shows the two rings for background subtraction. The intensity after background subtraction was 14850306 arbitrary units, which gives 262 Pt atoms. These two values are remarkably close (2.5 % difference), thus both methods were

deemed appropriate for estimating the number of Pt atoms within each cluster.

2.2.3 Video Analysis of Clusters

Video analysis is used to investigate the impact of the electron beam upon the clusters. To do this many images were taken in the microscope, and combined to form a time lapse video, so that the changes could be easily seen.

The images were taken in 30 image sets, with a 2 minute beam shower separating each set. The beam showers were used to reduce sample contamination [105]. Each of the 30 images were taken as fast as possible, thus a 600 image video took approximately 200 minutes to take. Within this thesis, some images from the video are used to illustrate the data rather than all of the images from the videos.

To check that the changes seen were induced by the beam rather than by other factors, a lower magnification image of the area was taken before and after video imaging for comparison.

Chapter 3

Platinum-Titanium Clusters

3.1 Introduction

Within this chapter, we will investigate Pt-Ti clusters produced by the cluster source. They are transferred to the STEM in two distinct ways: With air exposure, and within a nitrogen atmosphere to minimise air exposure. This enables us to investigate the impact of oxygen within the air on the clusters, as Ti is a very reactive metal [118, 119]. With the samples transferred under nitrogen, two different phenomena are investigated: The influence of oxygen upon the clusters is studied by comparing samples of the same size transferred in air and nitrogen, whilst the impact of the beam is investigated by taking video images of the clusters.

The early work within this chapter, along with the preliminary electrochemistry has been published in PCCP 'Modular construction of size-selected multiple-core Pt-TiO_2 nano clusters for electro-catalysis' by Caroline E. Blackmore, Neil V. Rees and Richard E. Palmer [85]. The section 'Pt-Ti Clusters Transferred in Nitrogen' is forming part of a manuscript currently under development. The experimental work displayed here will be accompanied by results for the annealing of samples, as well as theoretical work conducted by the University of York.

3.2 Pt-Ti Clusters Transferred in Air

The Pt-Ti clusters are produced in the gas-aggregation magnetron sputtering cluster source (Section 2.1). They are removed from the cluster source and either transferred to STEM for imaging, or stored in a desiccator, at a vacuum pressure of 10^{-2} torr, until the STEM is available for imaging. A wide range of samples have been made which range in size between 20,000 and 90,000 AMU. Three repeats have been performed to check consistency, by producing new samples of the same size, and repeating the STEM imaging and analysis process. All repeats have shown the same results, independent of the settings used with in the cluster source. For each size, a minimum of 50 clusters have been imaged and analysed.

Once all of the images had been taken, analysis of the Pt core size was undertaken. This analysis was performed by applying a threshold to the image, and summing the Pt pixels within each core. This area was used to determine an approximate radius, from which a spherical volume can be calculated. The number of Pt atoms that fit within this volume is calculated using the lattice constants for bulk Pt. Assuming that these Pt cores have the same structure as bulk Pt is a source of error for this work, but will give the best approximation when the structure is unknown. The process is described in more detail in Section 2.2.2.

Figure 3.1 shows an overview of the appearance of the false coloured clusters. The yellow is the Pt (along with TiO_2 and background carbon), pink being TiO_2 (along with background carbon) and the purple is the background (a holey carbon film). Two magnifications are shown for each size of cluster, so that a detailed version can be seen as well as an overview of multiple clusters. A and E show the large, 120,000 AMU, clusters with 4 cores. The smaller clusters, D and H, 30,000 AMU, show that only a single Pt core is present in the TiO_2 shell. The lower magnification images show that the majority of larger clusters have multiple cores (E and F), whilst the smallest (H) all have a single core. These clusters were made and have been transferred directly to the STEM, although re-imaging of the samples after some weeks showed no change in structure seen. The Pt

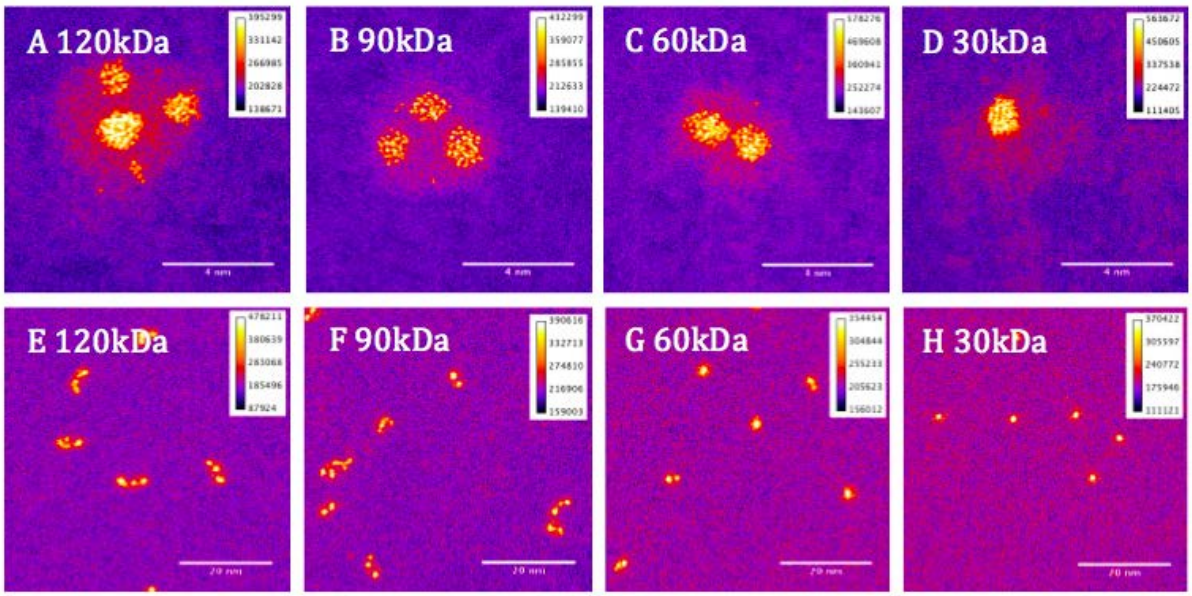

Figure 3.1: Pt-TiO_2 clusters are shown, with yellow being Pt (along with TiO_2 and background carbon), pink being TiO_2 (along with background carbon) and purple being the background carbon only. Two different magnifications of the clusters are shown with A and E, the largest clusters, showing 4 cores and D and H, the smallest clusters, showing a single core. Da are equivalent to AMU. The scale bar is 4 nm for images A to D and 20 nm for E to H.

cores were stable, and did not aggregate over time.

A software script was written to automatically process these images. The analysis method used means that the relative number of atoms between clusters is correct, but the absolute number may be incorrect. The majority of this error originates from the use of the bulk lattice constants for Pt, to calculate the number of atoms within each core. Being that the core is very small it may not have the bulk structure of cubic, thus the number of atoms could be inaccurate. The images have been examined to identify any structure in the Pt core, in a similar way to the identification process in Chapter 4, however, no structure has been positively identified. The second main cause of error is in using the assumption that the cores are approximately spherical, and that the projection seen is that of a sphere. An attempt to use the intensity of the Pt core was made, but the varying contribution from the TiO_2 shell made this very inaccurate.

The results of the number of Pt atoms within each core are plotted in Figure 3.2. The full width half maximum of the first Gaussian peak fit is approximately 45 atoms, and

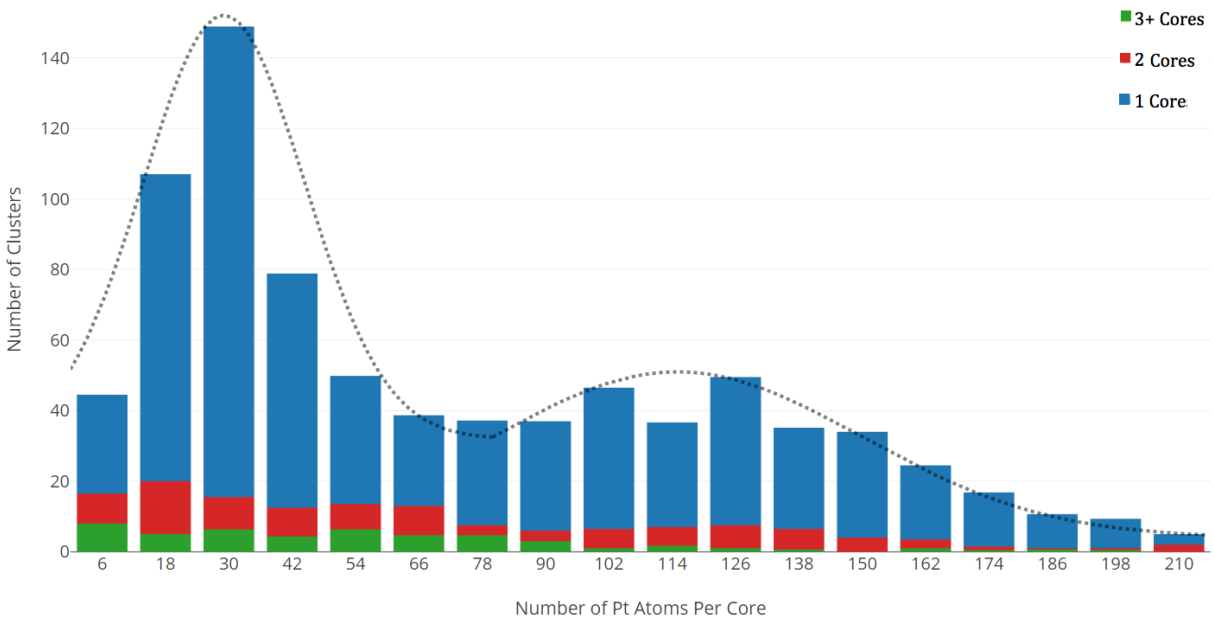

Figure 3.2: This histogram shows the number of Pt atoms contained within each core for all Pt-Ti clusters transferred in air. They are categorised based upon the number of cores present within the whole cluster.

for the second Gaussian in approximately 100 atoms. These results contain all sizes of clusters produced from 20,000 up to 90,000 AMU. Each core is analysed separately and categorised dependant upon the number of cores that the initial cluster contained. This means that the cluster observed in Figure 3.1D contained one core (categorised as blue) and each core observed in Figure 3.1B would be categorised green, as the cluster contained three cores. From the categorisation, it can be seen that the cores from multiple cored clusters (generally those deposited at a higher AMU) tend to be smaller. This is because the 2 and 3 cores (red/green) tend to be seen at a lower number of Pt atoms per core. It can also be seen from this figure that there are two peaks in the distribution, one at 30 $\pm$ 6 Pt atoms, and a second broader peak at 126 $\pm$ 6 Pt atoms.

To investigate this two peak distribution, the clusters were split into small and large clusters. Small clusters are classed as clusters between 20,000 and 50,000 AMU, whilst large clusters are those between 55,000 and 90,000 AMU. The crossover size of 50,000 AMU was chosen as the majority of clusters below this size contained a single core, whilst those above tended to contain two or more cores.

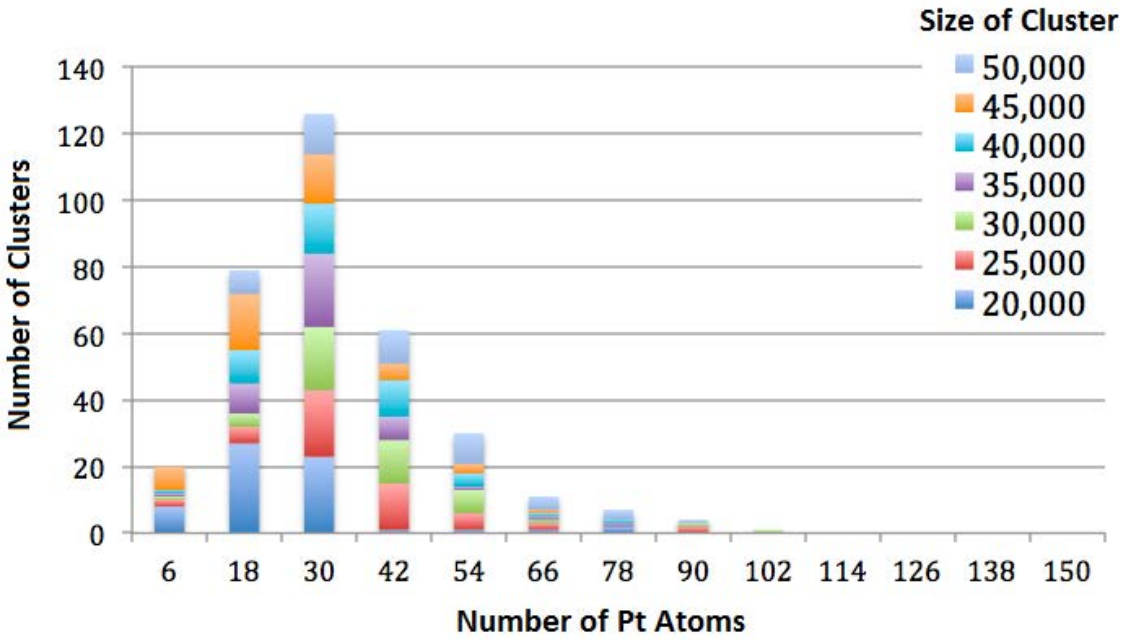

Figure 3.3: This histogram shows the number of Pt atoms within each of the cores for small clusters, those containing less than 50,000 AMU which typically a single core. They are categorised by the size of the original cluster.

Figure 3.3 shows the data for small clusters only, those that contained less than 50,000 AMU. 92% of these clusters were found to contain only a single core. The colours have been used to differentiate the deposited cluster sizes. From the overall plot it can be seen that the peak is at 30 ± 6 atoms, consistent with the results from Figure 3.2. The colours show that the peak core size for most of the cluster sizes is at 30 ± 6 Pt atoms. This data shows that the preferential core size of 30 ± 6 is forming independent of the overall cluster size.

To investigate the larger clusters, they were split into two categories: Ones with a single core and those with two or more cores, shown in Figures 3.4 and 3.5 respectively. Figure 3.4 shows us that the larger clusters contain a single larger core with 126 ± 6 Pt atoms, the same peak position as that seen in Figure 3.2. The colour coding on this figure also shows that the smaller clusters, 55,000 and 60,000 AMU tend to fall towards the left-hand side of the distribution, whilst the larger 75,000 and 90,000 AMU clusters tend to fall towards the right-hand size of the distribution. This may be caused by the

55,000 and 60,000 AMU cluster ideally containing 2 cores, whilst the 75,000 and 90,000 AMU cluster should ideally contain 3 cores. This would mean that the combined mass of the 75,000 or 90,000 AMU clusters cores would be greater than the combined mass of the 55,000 or 60,000 AMU cluster cores.

For the larger multi-cored clusters, show in Figure 3.5, the size of the Pt core is far smaller, peaking around 42 ± 6 Pt atoms, which is reasonably consistent with Figures 3.2 and 3.3, which show a peak at 30 ± 6 Pt atoms. For Figure 3.5, there is no correlation between cluster size and the peak core size. This is consistent with the preferential core size theory. This figure also shows a small peak at 126 ± 6 Pt atoms, where clusters that should have three cores actually contain two, one large (made of two cores) and one small core.

From these figures it is clear that a core size of 30 ± 6 Pt atoms is preferential for all cluster sizes. For small clusters, the single core is seen, whilst for larger clusters these cores either display as multiple individual or single aggregated cores. This preferential core size could be due to this size of cluster forming a structure that is very stable. This would mean that as a core grows to 30 ± 6 atoms a structure is reached, which is preferentially more stable than neighbouring sizes. It is thus energetically favourable for an atom to remain on its own, rather than join this stable core. These seed atoms are then likely to form a new core which can, in turn, repeat the process and grow to this critical size. This would generate multiple Pt clusters of approximately 30 atoms, which are then seeds for the Ti atoms to grow around. There is no conclusive literature that specifies that 30 Pt atoms would be more stable than that of its neighbours. Theory suggests that it would be decahedral in motif[23], but attempts to identify this motif within the clusters imaged has been unsuccessful. There has been no positive identification of any structure within the Pt cores, although they generally tend towards circular.

The Ti has been assumed to be TiO_2. This is because full oxidation of the sample is expected as it has been exposed to air for prolonged periods of time. It is possible that the clusters are not completely oxidised, and the oxidation state may not be TiO_2. An

attempt was made to perform EELs analysis on the sample, but the results for the small clusters was non-conclusive. An example EELs spectra for carbon and TiO_2 are shown in Figure 3.6. The C peak is at approximately 285 eV, the Ti is at approximately 455 eV and the O peak is at approximately 530 eV. Figure 3.7 shows the EELs spectra for a Pt-Ti cluster transferred in air. Peaks for C and Ti can be seen, but it is difficult to distinguish an O peak. This was repeated with a number of clusters on a number of samples, with similar results. Due to the fact that the O peak could not be identified, but the Ti atoms were expected to have undergone some oxidation during transfer, the oxidation state was assumed to be TiO_2.

A short study was also performed examining the quantity of Pt in the shell, and TiO_2 in the core. From the images it is clear that there was rarely any Pt present in the shell of the clusters, as bright spots were seldom observed. To analyse the percentage of Pt within the cores, a model of two concentric spheres was used. The inner sphere was modelled as containing Pt and TiO_2, and the outer sphere was modelled as containing only TiO_2. The theoretical intensity was calculated by taking an intensity profile through the spheres' centre. For the experimental data, a 5 pixel wide slice was taken across the imaged cluster. This gave an average pixel value in the x direction. Figure 3.8 shows an example of the experimental data, along with the calculated intensity for a cluster core with either 100 %, 80 %, and 60 % Pt, with the remained being TiO_2, along with an image of the cluster modelled. For all of the clusters that this analysis was performed upon, the best fit line was the 100 % Pt line. From this analysis it was concluded that the core was most likely pure Pt, and if there was TiO_2 present it was at a low percentage that was unlikely to effect the main results.

The following sections of this thesis investigate a further way that the multiple cores could form, by studying the oxidation of the Ti atoms of the clusters.

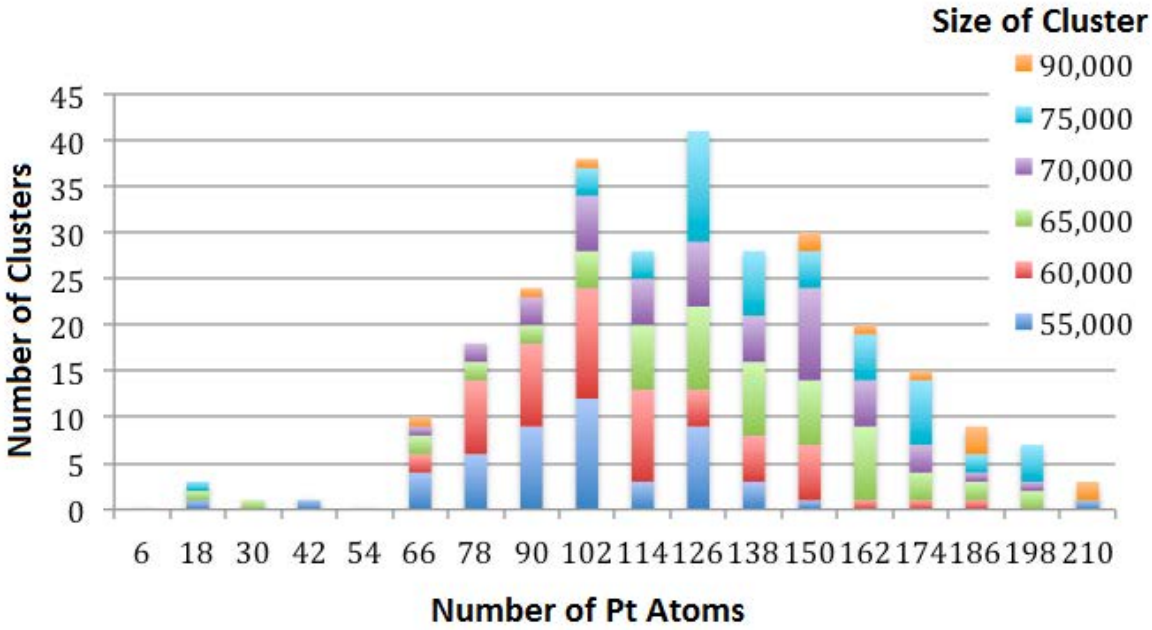

Figure 3.4: This histogram shows the number of Pt atoms within each of the cores for large clusters, those containing more than 55,000 AMU. These clusters all contained a single core, and are categorised by the size of the original cluster.

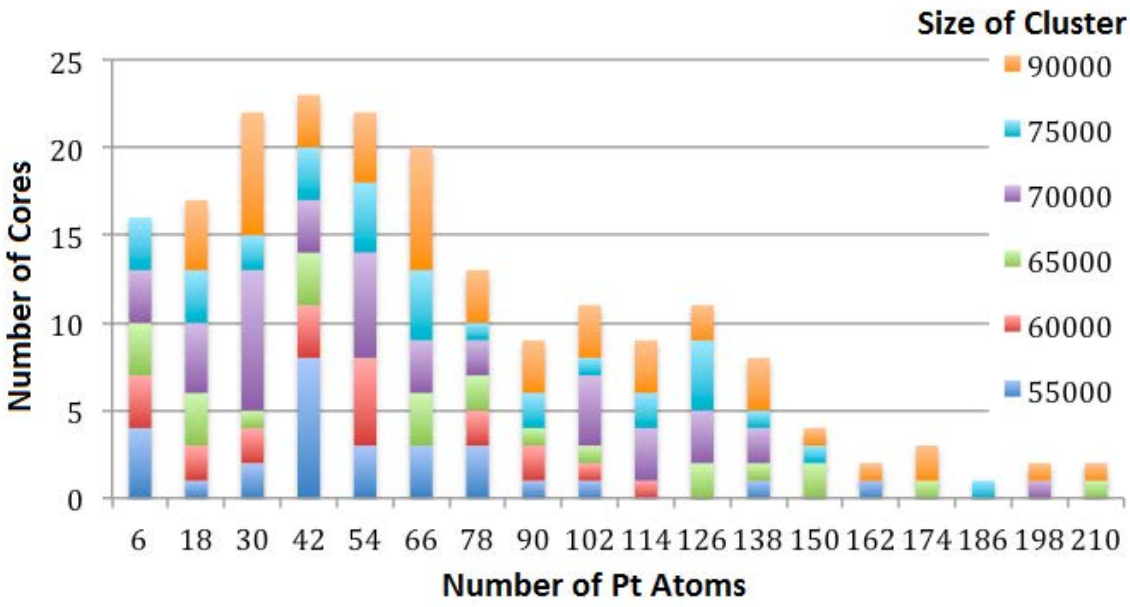

Figure 3.5: This histogram shows the number of Pt atoms within each of the cores for large clusters, those containing more than 55,000 AMU. These clusters all contained multiple cores, and are categorised by the size of the original cluster.

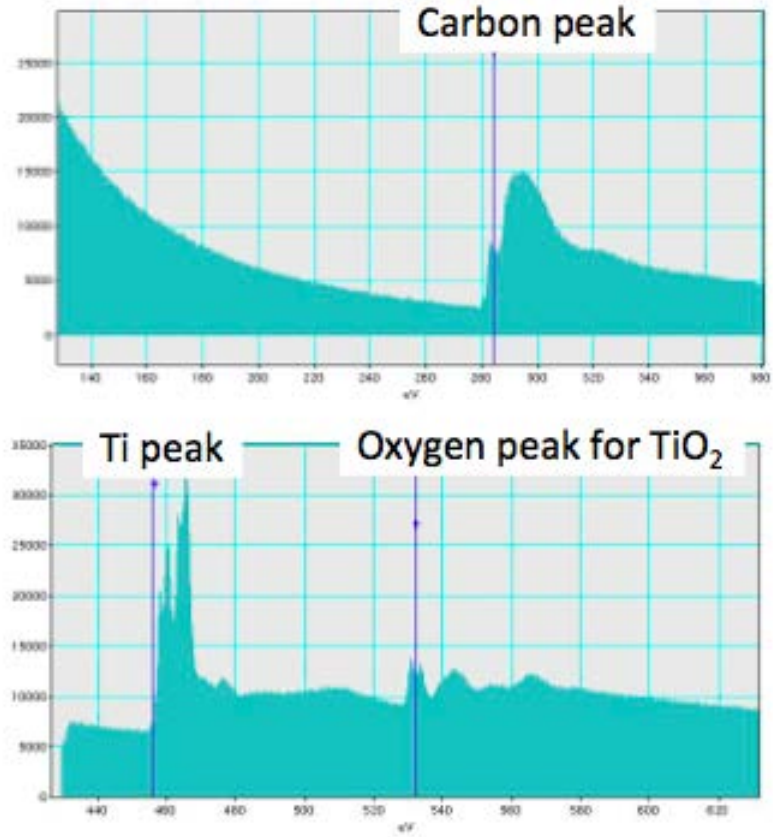

Figure 3.6: EELs spectra showing where different elements would be found. The C peak is at approximately 285 eV, the Ti is at approximately 455 eV and the O peak is at approximately 530 eV.

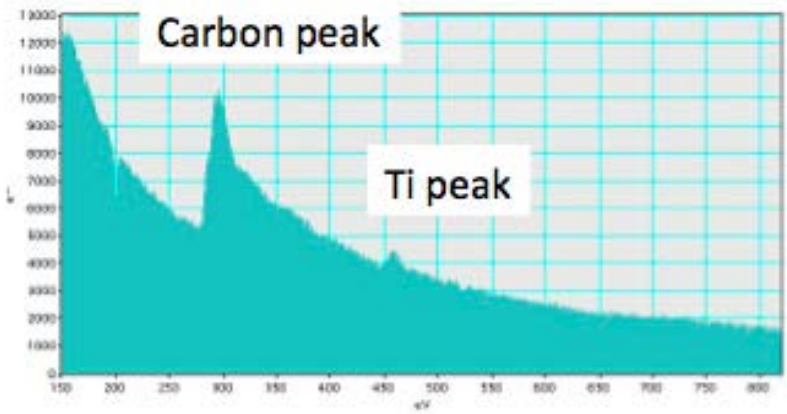

Figure 3.7: EELs spectra of a Pt-Ti cluster transferred in air. A carbon and titanium peak can be seen in the EELs spectra, but it is difficult to distinguish any oxygen peak.

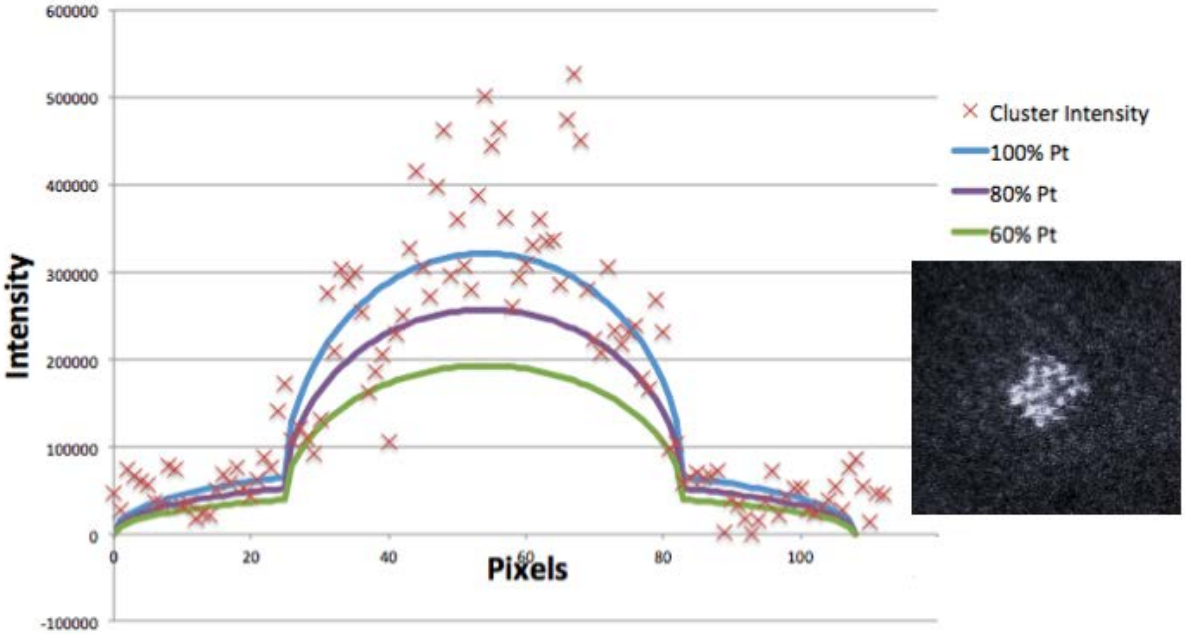

Figure 3.8: Plot of intensity of a cluster shown with crosses. The projected intensity of the cluster modelled as two concentric spheres with 60 %, 80 % or 100 % Pt in the core.

3.3 Pt-Ti Clusters Transferred in Nitrogen

3.3.1 Nitrogen Transfer Method

To investigate the effect of oxygen upon the Pt-Ti clusters, an oxygen reduced method of transporting the clusters from the cluster source to the STEM had to be designed. Initially, a glove bag was used to perform the transfer as it was flexible, easy to manoeuvre, and light weight. The large glove bag was filled with nitrogen and wrapped around the load lock opening on the cluster source, whilst the load lock was still closed. This allowed the load lock to be vented with nitrogen and the samples moved into the nitrogen filled gas bag with little oxygen exposure. The gas bag was then removed from the load lock and sealed for transportation between the two labs. Once it had been carried to the STEM room, the STEM arm was placed within the bag, minimising air ingress and nitrogen loss through the opening. After loading of the sample into the STEM arm, it was removed from the bag and inserted into the microscope, only exposing the sample directly to air for 1 to 2 seconds. Imaging then commenced as soon as the sample had settled sufficiently, approximately 15 minutes after loading. Attempts were made to image samples before this time, but the sample drifted in the X, Y and Z planes, resulting in poor quality images.

The gas bag worked reasonably well for transferring the samples, but had some limitations. It worked well as a proof of concept design, as the clusters seen in the microscope clearly showed a different morphology. The insertion of the STEM arm into the gas bag was difficult and always resulted in some air contamination and nitrogen loss. The bag was also quite cumbersome to manage, always requiring two people to work in close partnership. This was predominantly due to bag's gloves requiring the operator to don a second pair of latex gloves in order to preserve the original set. This meant that it was impractical to take them off during the transfer of the sample, and thus one user always had to have their hands within the glove bag. Through many uses, the bag also became damaged, which led to a number of temporary repairs being performed. The reducing

integrity of the bag led to increasing air exposure through small leaks. To overcome these limits, I designed a gas transfer box, which the physics workshop has built.

This gas transfer box, seen in Figure 3.9, allows for the transfer of samples in either a nitrogen or argon atmosphere between the cluster source and microscope. When the load lock is vented prior to use, the nitrogen box is attached rather than the typical flange cover, via a gate valve which is closed. The load lock is then pumped down to enable transfer of the sample from the deposition chamber to the load lock. Whilst this is happening, the STEM arm is placed inside the gas box and it is flooded with nitrogen (or argon). As nitrogen is slightly lighter than air, it will tend to rise, so the nitrogen is pumped in at the top of the box and the air is vented from the bottom. The opposite direction would be used for argon, as it is heavier than air.

Figure 3.9: A photo of the gas transfer box attached to the cluster source. On the left-hand side the box is connected to the cluster source by a gate valve. On the right-hand side there is the large opening for inserting and removing the STEM arm. The gas inlet and outlet can be seen at the top left and bottom right corners of the box.

Once the sample is in the load lock (with the load lock pumps turned off), and the gas box has been filled with nitrogen, the load lock can be vented with nitrogen and the sample transferred through the gate valve into the gas transfer box. The gate valve can

then be closed and disconnected from the load lock, ready for transporting to the STEM room. The box can be over-pressured with nitrogen or argon to reduce any flow of air into the box through any potentially leaky seals. Using the gloves, the sample can then be transferred into the STEM arm with no oxygen contamination as it is already inside the gas box. The very large opening on the right-hand side of the box can then be opened for the arm to be removed, and inserted into STEM. Currently, a tube with two large iris valves is being constructed to enable the STEM arm to be moved closer to the microscope before insertion, in order to further reduce air exposure. This method vastly reduces the oxygen contamination when compared with the gas bag, as the first contact with oxygen is when the STEM arm is being inserted into the microscope. Further developments of this method would include manufacturing a load lock for the microscope to further reduce air contamination and oxygen exposure.

3.3.2 Results for Pt-Ti Clusters Transferred in Nitrogen

To study the effect of oxygen from the air interacting with the Ti in the Pt-Ti nanocluster, a comparison was made between clusters of the same mass transferred through air and clusters transferred in the gas transfer box filled with nitrogen.

Example images are shown in Figure 3.10. The top row of images are the clusters transferred under nitrogen with minimal air exposure, whilst the bottom row of clusters have been exposed for at least 24 hours. The yellow is the Pt (along with TiO_2 and background carbon), pink being TiO_2 (along with background carbon) and purple being the background holey carbon film only.

It is clear from the images that the clusters that are transferred in the nitrogen atmosphere show a more dispersed distribution of Pt atoms when compared with the samples transferred in air. There is some air exposure during the transfer, which can be seen as a ring of TiO_2 around the amorphous core. This is particularly apparent in the 30,000 AMU sample, as it shows a mostly Pt core within a Ti shell very similar to the cluster transferred in air. The larger samples show a small amount of shell with a mixed Pt and

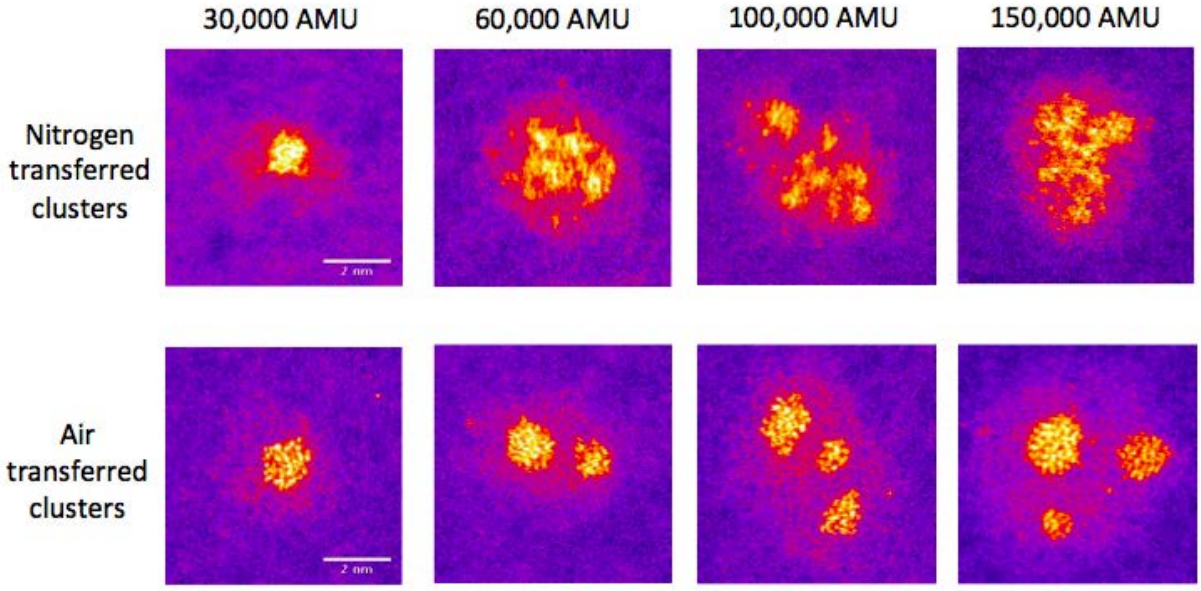

Figure 3.10: Comparison of multiple sizes of Pt-Ti clusters transferred in nitrogen and air. The yellow is the Pt (along with TiO_2 and background carbon), pink being TiO_2 (along with background carbon) and purple being the background holey carbon film only. The clusters transferred in air show a multiple Pt core within a TiO_2 shell, whilst the clusters transferred in nitrogen show a more amorphous core of mixed Pt and Ti atoms.

Ti core.

To investigate the amorphous nature of these clusters Fast Fourier Transforms (FFT) of some clusters have been performed. For clusters where structure is apparent the FFT shows pattern and structure, but for amorphous samples structure is not seen. Figure 3.11 shows example images, where A has structure and thus the resultant FFT in B has more structure than that of D, which is the FFT of image C. To quantise the amorphous nature of the core of the clusters an analysis method is described below.

To investigate the larger clusters in more detail, and compare the clusters transferred in air with those that have been transferred under nitrogen, a frequency histogram of intensity is produced. This is done by recording an average intensity of a 20 by 20 pixel region of interest in every position upon the image. In the histogram, the background intensity will show as the dominant peak (Figure 3.12). Above the background intensity peak, there is a region which shows the contribution from the titanium and platinum atoms (inset). The positioning and definition of these areas helps to identify whether the sample

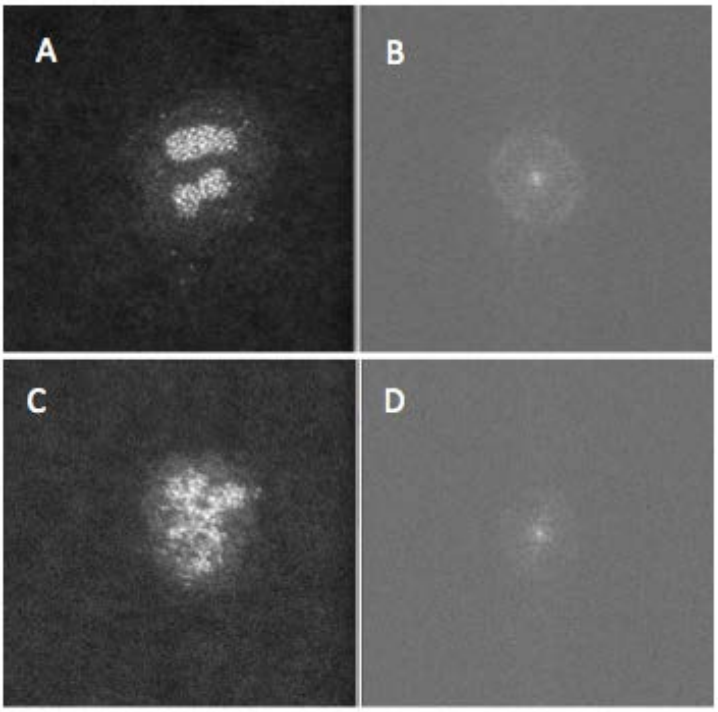

Figure 3.11: Images showing a cluster and its corresponding FFT. A is a cluster transferred in air, B is its FFT showing some structure, C is a cluster transferred in nitrogen, D is its FFT showing no identifiable pattern.

is predominantly mixed atoms of Pt and Ti, or if it is more segregated in structure. The absolute intensity values measured may be inaccurate due to variations between samples, particularly the carbon substrate thickness and the contamination experienced by each sample, and sample area. For this reason the main analysis is looking at the shapes of the curves and comparison over time of the same areas, aiming to minimise the impact of the beam damage and contamination. This analysis method does not take in to account the differing Ti oxidation states that may be present with the clusters. The varying quantity of O present would skew the intensity seen for the clusters. Further research determining the oxidation state would be very useful for direct comparison.

For samples transferred either in air or in nitrogen, the intensity from the background will generate similar profiles, but the contribution from the Pt and the Ti will produce different profiles at higher intensities. For the clusters transferred in air, which show multiple Pt cores within each TiO_2 shell, the intensity profile will contain contributions

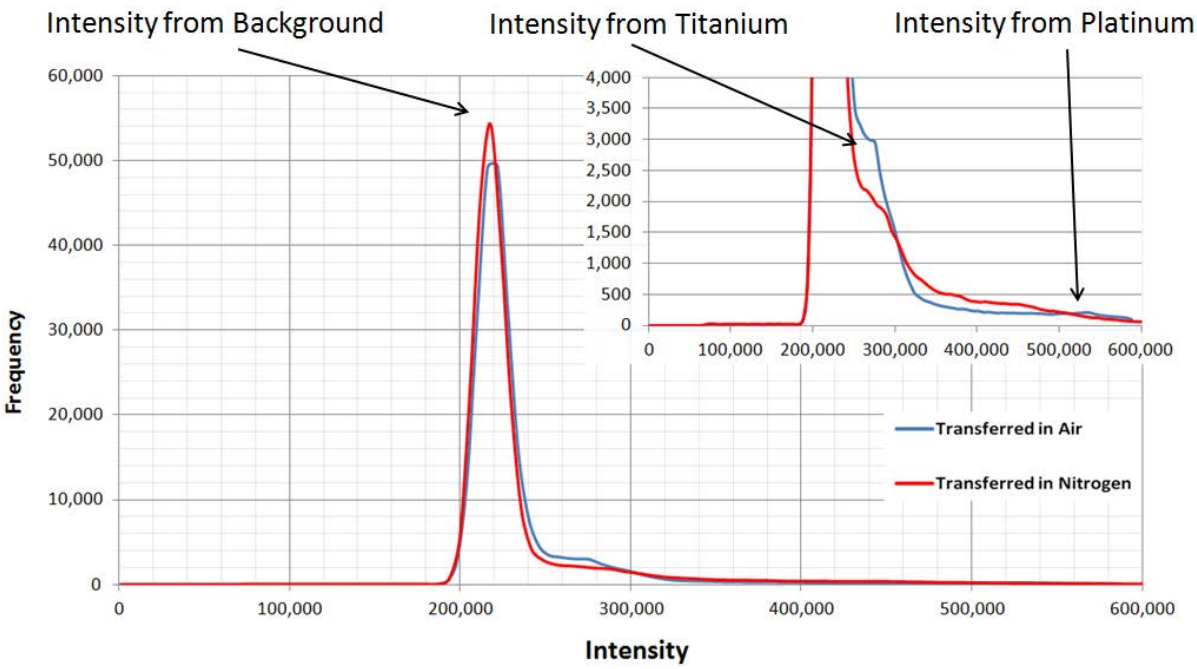

Figure 3.12: Plot of the intensity from Pt-Ti clusters transferred in air and nitrogen. The insert shows an enlarged version of the area of the graph dominated by Ti and Pt intensity. A large peak from the intensity due to the background can be seen.

predominantly from pure Ti and pure Pt as each region of interest typically only contains one type of atom. For the clusters transferred under nitrogen, the more amorphous structure will give rise to a range of intermediate intensities, consistent with the region of interest capturing both Pt and Ti atoms. This principle is illustrated in Figure 3.13.

This is seen to be true for the results shown in Figure 3.12, where the insert shows the intensity from the Pt and Ti in more detail. The sample transferred in air is shown in blue, whilst the sample transferred in nitrogen is shown in red. These results are the averaging of the intensities from 12 samples transferred in either air or nitrogen. These results match the expected profile for both types of cluster. This method allows for a more quantitative investigation of the dispersion of the Pt within the Ti/TiO_2 shell. This analysis method will be used in Section 3.4 for analysis of the videos taken from both types of clusters.

Research performed by a collaborator, Keith McKenna, from York University uses theoretical modelling to predict that for small clusters, there are different atomic ar-

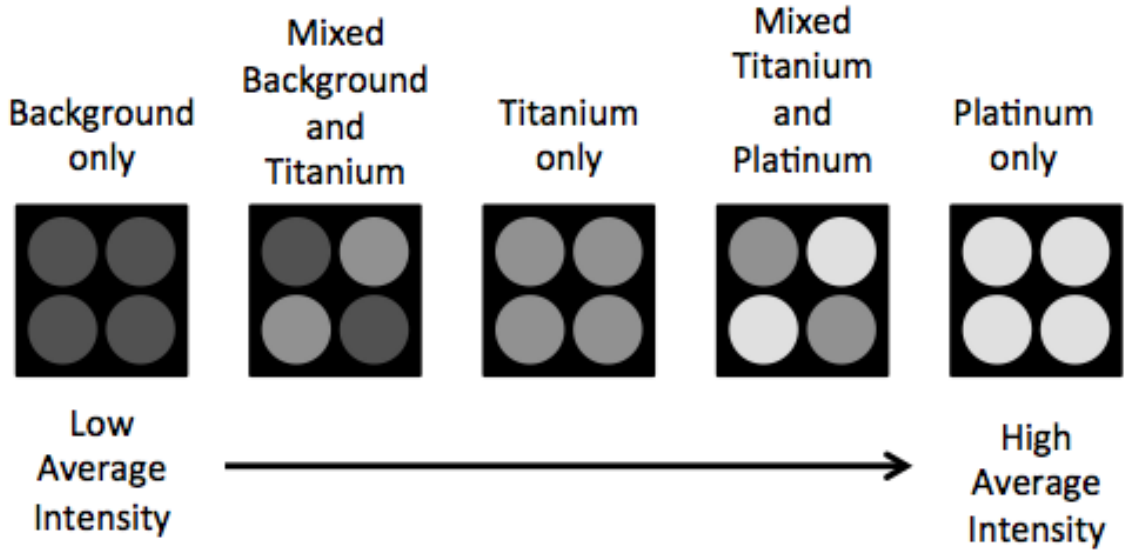

Figure 3.13: Schematic showing the intensity which occurs from different combinations of atoms within the region of interest. The high intensity seen in Figure 3.12 is generated by the 20 by 20 pixel region of interest containing predominantly Pt atoms, whilst the lower intensity peak is from predominantly background atoms. The combination of atoms within each region of interest indicated whether the region contains a mix of Pt and Ti atoms or if it is predominantly one element only.

rangements of the Pt and Ti dependent upon the amount of oxygen present [120]. For mixed Pt and Ti clusters, it is energetically favourable for the core to be Ti and the Pt atoms to be present on the outside corners of the modelled icosahedral cluster. For clusters with a single layer of oxygen present over the entire surface of the cluster, it is energetically favourable for the internal structure to be a random mixture of Pt and Ti atoms. For a fully oxidised cluster, the Pt aggregates together to form a core within the cluster. The clusters that have been modelled are very small, far less than the 30,000 AMU experimentally produced, thus this model matches favourably with the small clusters forming a single Pt core within a TiO_2 shell. Further theory work is being undertaken to investigate the possibility of the formation of multiple Pt cores to see if they have a similar energy to that of the single cored clusters. The model does not take into account the energy required to rearrange the atoms, thus this energy barrier could prevent a single Pt core forming in larger clusters within an experimental setting, if the single core is

theoretically preferential. The prediction of a single Pt core within the shell is consistent with calculations performed by Keith MeKenna[120].

3.4 STEM Beam Induced Structural Changes within Pt-Ti Clusters Transferred in Air and Nitrogen

During imaging of the Pt-Ti clusters transferred in a nitrogen atmosphere, changes in the structures were observed. To study this in more detail, videos were created by taking multiple images of the same cluster. This was undertaken for Pt-Ti clusters transferred in both air and nitrogen to study the similarities and differences.

Figure 3.14 shows representative images of the 100 image video taken over 30 minutes of a Pt-Ti cluster transferred in air, deposited at a size of 90,000 AMU. The video procedure, including beam showers, is described in Section 2.2.3. Six images from the 30 minute, 100 image, video are shown to give an overall impression of any of the cluster changes. From the stills and the video, the clusters do not to change significantly under the beam during imaging. The single cored examples remain as single cores, whilst the multiple cored clusters remain multiply cored. There are slight changes in the overall shape of each Pt core, with each tending towards a slightly more spherical shape. When higher magnifications are used, imparting more energy to the clusters, the clusters tended to disintegrate, with atoms dispersing across the surface of the holey carbon film.

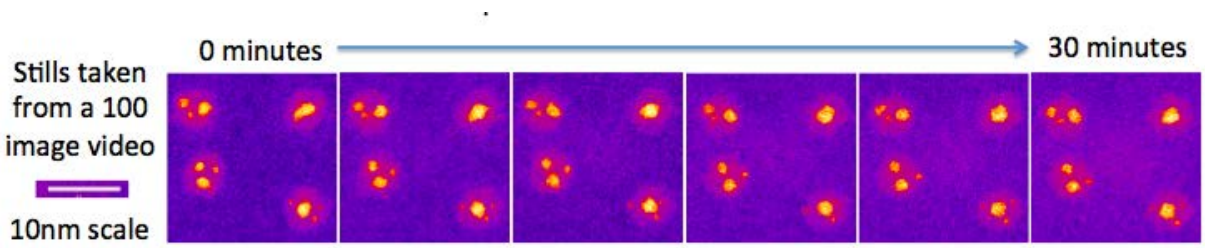

Figure 3.14: Stills from a video of the Pt-Ti clusters transferred in air, deposited at 90,000 AMU. The yellow is the Pt (along with Ti and background carbon), pink being TiO_2 (along with background carbon) and purple being the background holey carbon film only. No distinct change in the clusters is seen during the video.

Figure 3.15 shows a Pt-Ti cluster, transferred in nitrogen, at a size of 100,000 AMU. 600 images were taken over the course of 200 minutes, including beam showers. The images and video show that the clusters change from reasonably amorphous Pt-Ti distributions

to single Pt cored clusters. An image of the area before and after the video was taken, is shown in Figure 3.16. This shows that the area that has been irradiated displays single Pt cored clusters, whilst the external clusters show the amorphous starting structure. This leads us to conclude that it is the beam irradiation that is changing the morphology of the clusters. This could be occurring through the gentle annealing of the clusters as the electron beam imparts energy through collisions warming the sample. This would allow the atoms within the cluster to move around and reach a lower energy state, and as the lowest energy state would be a single Pt core within the shell (as shown theoretically) the Pt atoms start aggregating together forming tiny multiple clusters which tend to join into 'C' or 'U' shapes before rearranging to form the single core.

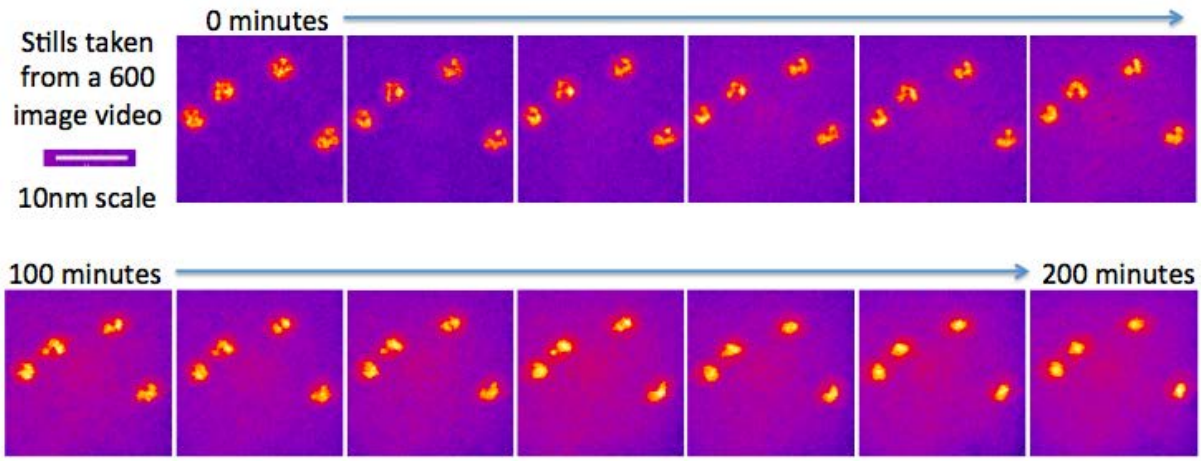

Figure 3.15: Stills from a video of clusters transferred in nitrogen, deposited at 100,000 AMU. The yellow is the Pt (along with Ti and background carbon), pink being TiO_2 (along with background carbon) and purple being the background holey carbon film only. During imaging the clusters have changed from an amorphous mix of Pt and TI to single Pt cores within a Ti shell.

The same analysis method can be used on the videos as described in Section 3.3.2. This allows for a plot to be made to see how the clusters are developing during imaging. Figure 3.17 shows that all 6 of the images appear to have very similar intensity for the Pt and Ti intensity (inset), thus the clusters change very little during imaging. This is in contrast to Figure 3.18, which shows that over time the shape of the Ti and Pt intensity areas of the plot changes quite dramatically. The first image (blue profile) shows a peak at

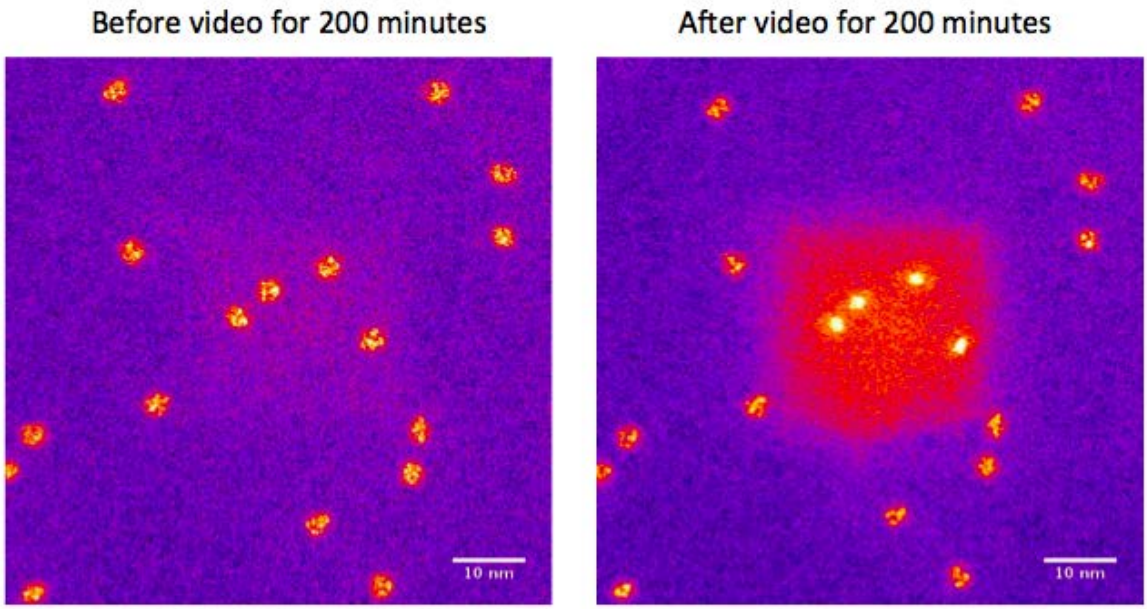

Figure 3.16: Images taken before and after the 200 minute video, for the 100,000 AMU Pt-Ti clusters transferred in nitrogen seen in Figure 3.15. The yellow is the Pt (along with TiO_2 and background carbon), pink being Ti (along with background carbon) and purple being the background holey carbon film only. The bright square in the right-hand image shows the beam damaged area where the video was taken at a higher magnification.

an intensity lower than the peak expected for Pt, but higher than the intensity expected for Ti alone. This is because the Pt is very dispersed within the clusters, thus the 20 by 20 pixels region of interest includes a mix of the Pt and Ti atoms, thus has an intensity between the two metals. As the Pt atoms form a core this peak disappears, and a peak for Pt becomes apparent. This is seen in the final image histogram (green profile), where there is an increase at an intensity of 450,000. The changes seen in the shape of the background peak are due to contamination and beam showers affecting the overall contrast of the images. This has the effect of reducing the height of the peak as well as broadening its distribution.

The changes in the clusters seen within the video of the Pt-Ti clusters transferred under nitrogen, show that the beam is imparting energy to the cluster. This electron beam energy is either gently annealing the cluster of causing a chemical reaction to happen within the cluster, altering its structure. Work in Section 4.4 discusses the impact of heating by the electron beam upon small Pt clusters. This work shows that the rise in

temperature for the clusters due to the STEM electron beam is unlikely to melt clusters of the size of the Pt-Ti clusters discussed here. At a temperature lower than that of melting, the electron beam could be warming the cluster to a level that allows atomic rearrangement towards energetically favourable cluster structures. This would be seen as atoms swapping positions within the clusters, with each swap aiming to reach a more favourable site. The electron beam could also be driving chemical reactions within the cluster. Due to the transfer method allowing some oxygen to reach the sample, there is always a low level of oxidation of the sample. The electron beam may be influencing this chemical reaction [121]. To investigate this possibility further an environmental STEM or an environmental cell attached to the STEM arm would be needed for experimentation. This would enable different gasses to come into contact with the sample during imaging, thus the reactions could be studied. If the same rearrangement of atoms happens with multiple gas types, the heating due to the electron beam is likely to be the cause of the rearrangement. If the rearrangement is unique to air contamination, a chemical reaction induced by the electron beam is driving the rearrangement. To totally rule out other possible causes of cluster changes the contamination and beam damage aspects of imaging method need to be removed. If the gently heating or exposure it to gases, didn't trigger the same rearrangement of atoms, it would point towards the beam damage or contamination being the driving forces for the changes. The contamination and the beam damage present could also change the quantitative results but it is unlikely to change the interpretation of the data.

3.5 Preliminary Electrochemistry Results

To study the catalytic properties of the Pt-TiO_2 nanoclusters preliminary electrochemistry was performed. The following results are used to indicate an improvement in catalytic reactivity, but far more research is needed to draw quantitative results for the catalytic nature of the particles.

The electrochemistry experiments were performed with a standard three electrode setup, with a glassy carbon (GC) working electrode, a saturated Ag/AgCl reference electrode, and a bright Pt mesh counter electrode. The clusters, TiO_2 and Pt-TiO_2, were deposited upon the GC electrode to give a coverage of less than 5 %. The potentiostat was an Autolab 128N from Metrohm[122], running Nova version 6.1. The solution used was 2.0 mM perchloric acid and 0.10 M sodium perchlorate dissolved in ultrapure water of resistivity not less than 18.2 MΩ cm.

The control experiment was performed by recording voltammograms at a scan rate of 25 mVs^{-1} with a clean GC electrode. The same scan rate was used for the electrodes with TiO_2 and Pt-TiO_2 clusters. The results of these scans are shown in Figure 3.19. This figure shows that the pure GC and the GC with TiO_2 nanoclusters show similar results, as both have the same position for the reduction peak (approximately 1.5 V). The Pt-TiO_2 clusters on GC show different behaviour, indicative of catalytic activity. They show a lower overpotential for both the onset of the reduction wave and peak position. Further work needs to be performed to unambiguously conclude that the shift seen is due to changed kinetics at the Pt-TiO_2 clusters and not due to subtle mass transport effects. However, these preliminary observations at such low cluster coverages strongly suggest that accelerated kinetics are the dominant reason for the changes in overpotential and indicate that these clusters would be useful for catalysis.

Further investigation would also be required for identifying the cluster structure upon the GC surface. These samples were deposited in the same way as those used within the microscope with an impact energy of 1 eV per atom. On this substrate that impact energy may have pinned the clusters or caused them to disintegrate. If the clusters had disintegrated the Pt atoms may be exposed, and could be changing the electrochemistry results.

Detailed studies of the size and morphology of the clusters with the highest catalytic activity would also help in identifying which structures or facets of a cluster is most catalytically active. The use of nano structuring these clusters offers hope that very small

quantities of Pt could be used for water splitting, making the process economically viable.

3.6 Conclusions and Further Work for Platinum-Titanium Clusters

Overall, a large number of Pt-Ti clusters have been produced with the gas-aggregation magnetron sputtering cluster source, with all the clusters imaged with STEM. These clusters have been transferred in air, forming Pt-TiO_2 clusters, or in nitrogen, as Pt-Ti clusters with a thin TiO_2 shell. The work shows that for air transferred clusters, a preferential Pt core of size 30 ± 6 atoms forms, whilst for nitrogen transferred clusters, a more amorphous cluster is seen. The larger clusters transferred in air often show multiple or agglomerated cores. Both types of clusters have been studied by taking multiple images to build up a video of the changes in structure induced by the STEM beam. This shows that the clusters transferred in air do not change, whilst the clusters transferred in nitrogen form Pt cored clusters. The STEM beam appears to either be slowly annealing the clusters, or inducing a chemical change. The annealing would be imparting enough energy to the clusters transferred in nitrogen to rearrange the atoms, but the amount of energy is too low to change the structure of the clusters transferred in air.

Continued work on Pt-Ti clusters could include further reductions in oxygen exposure during transfer of the samples. This could potentially be done with a graphene cell. Total oxygen prevention would enable comparison with the University of York prediction, that the clusters would form with a Ti core, with the Pt atoms upon the surface. It may be possible to do this by adding a protective layer to the clusters that would prevent oxygen reaching the cluster, but a material that does not change the structure of the cluster would need to be chosen. Alternatively, further development of the STEM arm insertion, so that it can be placed into the microscope through a load lock, would further reduce or prevent air exposure. The theoretical work could be developed to investigate larger clusters, or to model multiple Pt cores within the Ti and TiO_2 shell to see which is theoretically more

stable. This could answer the question as to whether the large Pt-TiO_2 clusters should have a single core or multiple cores. This would also show whether the clusters do not have enough energy to rearrange, or if the 30 $\pm$ 6 Pt atom core is very stable.

Experimentation with an environmental STEM or cell would allow further work to be done on the driving mechanism for atomic rearrangement under the electron beam. This would help differentiate whether the rearrangement is purely due to heating by the electron beam or if a chemical reaction was taking place.

Long term goals should include performing rigorous electrochemical testing upon the samples, investigating the impact of a TiO_2 shell on the Pt core. The electrochemistry results would prove what uses these clusters have for both fuel cells and water splitting. Preliminary testing has shown promise that these clusters are active, and that the TiO_2 shell acts as a protective layer around the Pt cores, thus making it a useful catalyst for PEM fuel cells [85].

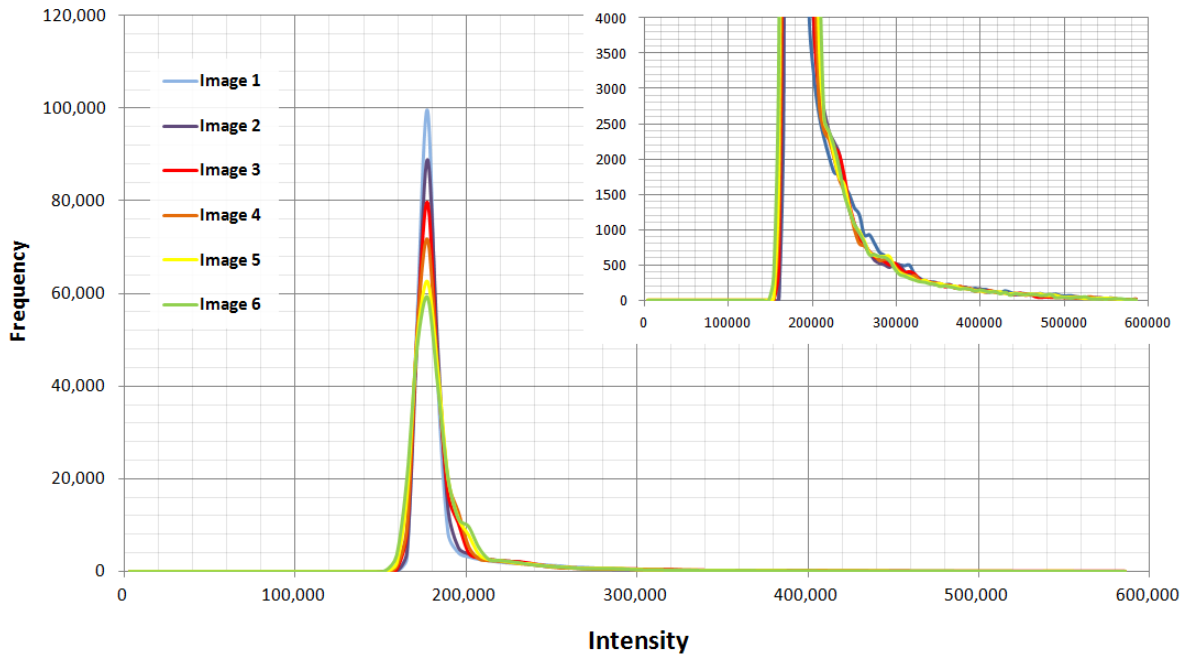

Figure 3.17: Plot of the intensity from the video images of Pt-Ti clusters transferred in air as seen in Figure 3.14. The insert shows an enlarged version of the area of the graph dominated by Ti and Pt intensity. Within this region, there is no change between image 1 and image 6.

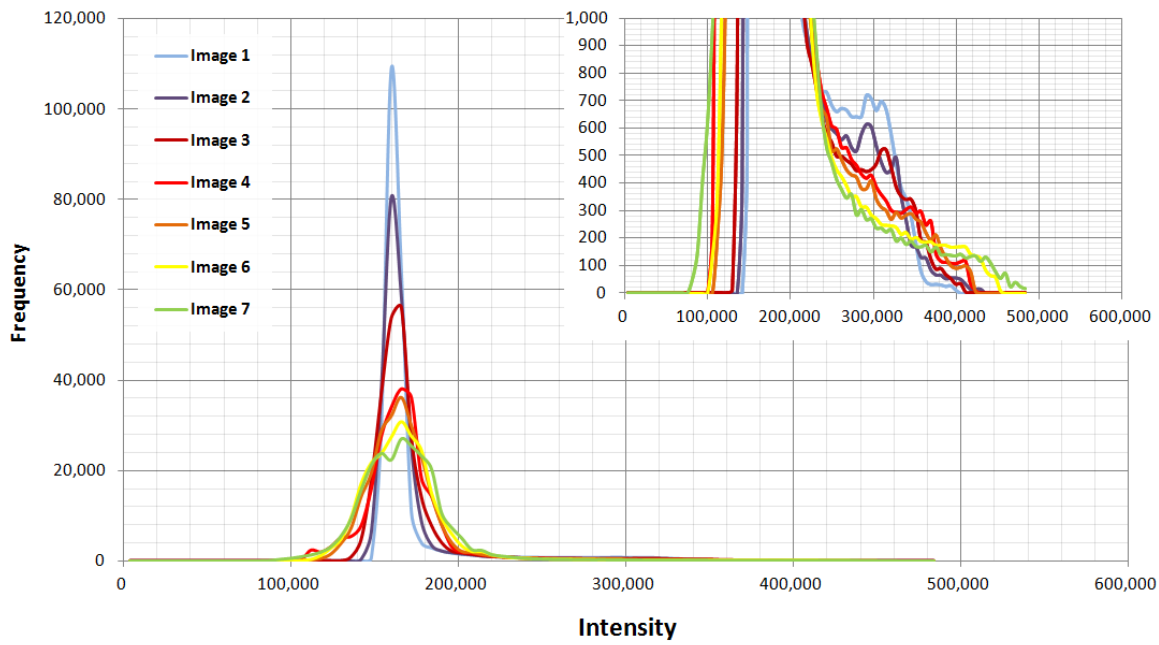

Figure 3.18: Plot of the intensity from the video images of Pt-Ti clusters transferred in nitrogen as seen in 3.15. The insert shows an enlarged version of the area of the graph dominated by Ti and Pt intensity. The change in profile seen within this region between image 1 and image 7 shows how the cluster has become less amorphous over time.

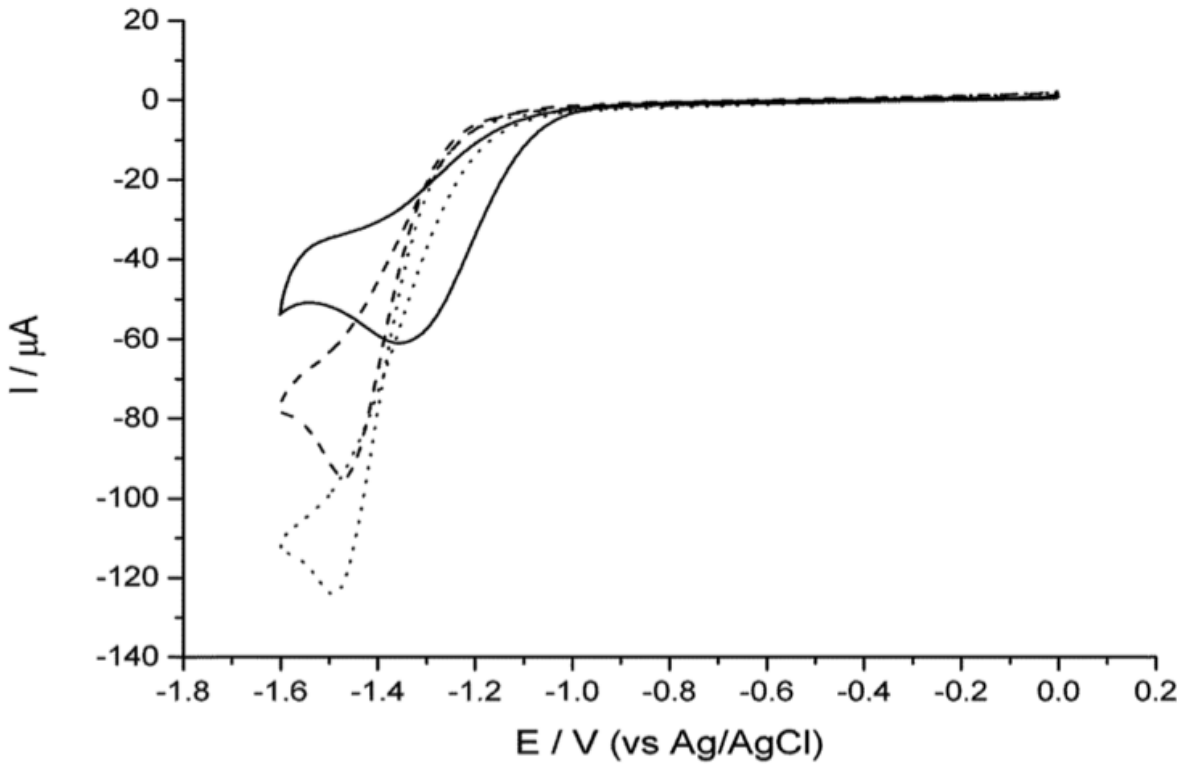

Figure 3.19: Preliminary electrochemistry results showing the results for clean GC (dots), GC with TiO_2 (dashes), and GC with Pt-TiO_2 (solid). The lower overpotential for both the onset of the reduction wave and peak indicates catalytic activity.

Chapter 4

Pure Platinum Clusters

4.1 Introduction

Within this chapter, experimental investigations into pure Pt nanoclusters will be performed to identify the dominant structure across a range of cluster sizes. This involves the production of clusters with the gas-aggregation magnetron sputtering cluster source, detailed in Section 2.1. Once deposited upon a nickel TEM grid, with a holey carbon film coating, the clusters are transferred to the STEM for imaging, as detailed in Section 2.2.1. Using the HAADF image intensity, corrected for background contributions, the number of atoms within the cluster can be calculated. This enables the clusters to be sorted by size, which, when combined with the structural information, allows for a broad look at the dominant structure trends. A detailed look at the 309, 147 and 55 atom Pt clusters allows us to further identify the cluster motifs, which is of particular use for clusters not initially identified as the traditional icosahedral, decahedral, or octahedral motif. The use of structures identified through global optimisations in Chapter 5 allows new simulations of HAADF STEM intensity to be made with QSTEM in order to aid identification of the structures.

Additionally the 309 atom Pt clusters are being used to verify that the clusters do not break up when they are landed upon the TEM grid within the cluster source. This

is done by using the radius of the clusters, then converting the radius into a number of atoms, as described in section 2.2.2.

4.2 Intensity Measurements

To calculate the number of atoms within each cluster, the STEM is used in HAADF mode. This enables us to use the intensity from the images as a way to calibrate the number of Pt atoms within each cluster (Section 2.2.1).

Once each image has been taken, two concentric rings are drawn around the cluster to enable calculation of the background intensity from the carbon film. This is then removed from the cluster intensity (Section 2.2.2), giving the intensity of the cluster without any background contribution. The background intensity, averaged over all clusters imaged, can be used to calibrate between samples. Combining this with the knowledge of what size of clusters were deposited on the grid allows the number of atoms within each cluster to be calibrated. This is particularly useful for the mixed sized samples. This allows the images of each cluster to be sorted by number of atoms within the cluster ready for identification.

4.2.1 Verification of the Number of Pt Atoms

To verify the number of Pt atoms within the clusters deposited at 309 atoms, the radius is used and compared with the bulk parameters for Pt. This helps to prove that the clusters are not breaking up when deposited upon the holey carbon TEM grid. It also serves as a check to see whether the clusters are deforming to a pancake shape when deposited within the cluster source.

The check is performed on the clusters deposited at 309 atoms as they tend to contain the cubic structure so will match most closely to the bulk parameters. Results showing that these clusters are predominantly cubic in structure are presented in Section 4.3.

To do this, two radius measurements were taken from each of the 100 images of 309

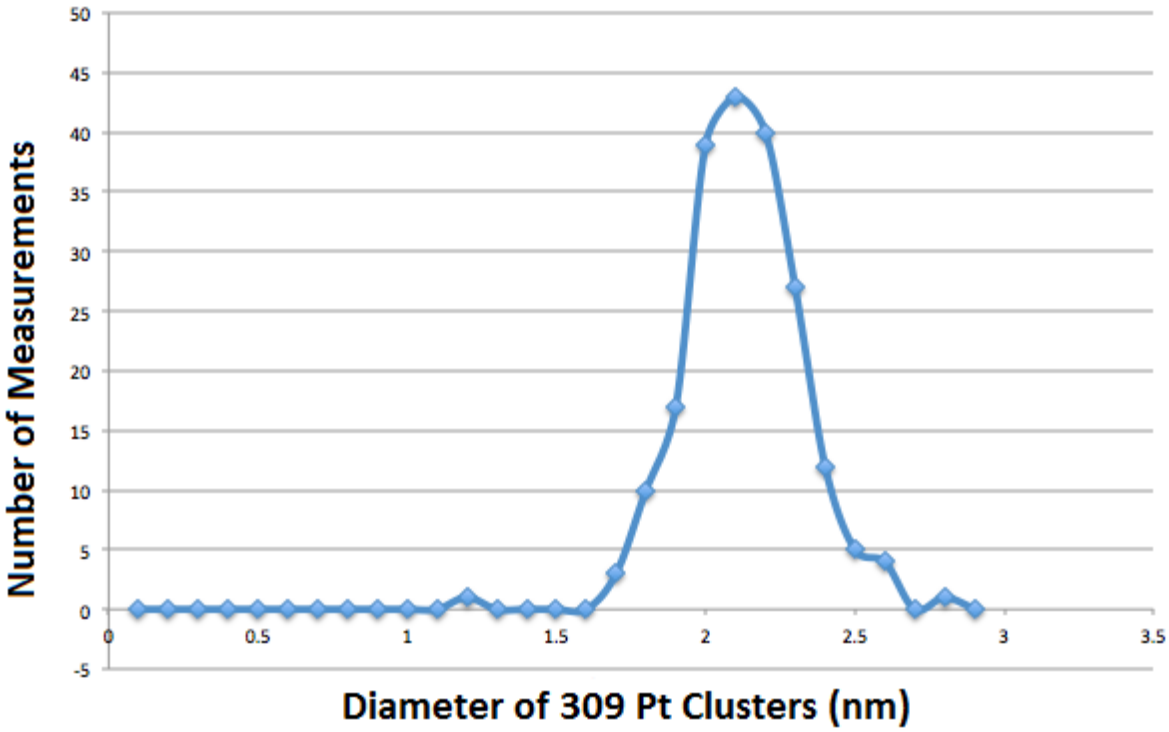

Figure 4.1: Plot showing the distribution of diameters of the Pt clusters deposited at 309 atoms. An average of 2.07 ± 0.2 nm is calculated.

atom clusters, the largest diameter and the smallest diameter. These results were then averaged to give a diameter of 2.07 ± 0.2 nm as seen in Figure 4.1. The error is calculated as the standard deviation of the data. This diameter is then used to calculate the spherical volume of 4.65 nm^3, which equates to 308.0 ± 0.28 atoms. This is remarkably close to the expected 309 atoms, and confirms that the clusters keep their shape when deposited. It is also notable that the distribution shows a single peak, rather than a double peak which would have been expected if the clusters tended to be oval in projection. This would have been caused by the largest and smallest diameters being taken and plotted, rather than the average of the pair of measurements being used. The emergence of two peaks would have indicated a big difference between the smallest and largest measurements, giving the cluster a high epitaxy. In this instance epitaxy refers to the difference in perpendicular directions e.g. the cluster would be oval. It is clear from the images and these results, shown in Figure 4.1, that this is not the case, and the clusters are mostly spherical.

If the clusters had lost their integrity when deposited upon the TEM grid surface

external atoms would have been seen and the calculation would have predicted a cluster with far less than 309 atoms. If the cluster had flattened as it impacted the TEM grid the radius measured would have been larger, and thus the cluster size calculated would have contained more than 309 atoms. This is good evidence that the carbon surface is not having a significant impact upon the shape of the cluster. If the cluster had been deforming due to interactions between the Pt and the carbon substrate atoms a flatter cluster would have been expected. Carbon is often used as the substrate material, and thus was used for this work [72, 123]. For growing nanoclusters and thin films the structure of the base substrate is very important for growing the structure, thus materials like quarts are used[124, 125].

4.3 Structure Identification

To identify the cluster's structure, QSTEM simulations were made for visual comparison. QSTEM v2.31 is an open source software package, released under the General Public Licence, used to simulate TEM and STEM intensities from clusters or bulk surfaces [126]. The atlases are produced by generating xyz co-ordinate files (text files that specify the element and the position of each atom within the cluster or surface) for each cluster structure and simulating an image. The parameters used by the QSTEM software replicate those used by the experimental STEM, detailed in Section 2.2.1. QSTEM simulations have previously been used to identify cluster structures for a number of metals [127, 84, 80]. The three base structures modelled are octahedral, decahedral and icosahedral.

For each simulation atlas, the clusters are rotated through multiple angles, so that a wide range of possible projections are generated. This means that the orientation of the real cluster upon the TEM grid is inconsequential in the identification process, as it can be matched with a simulated virtual cluster of a similar rotation. The rotation angles are limited to prevent duplicate simulations of the same cluster projection being made. We produce simulated intensity atlases for the magic number structures (147, 309 and 561

atoms) with the 147 example shown in Figure 4.2. After the real clusters are imaged with STEM, the intensity patterns seen are matched against the simulated QSTEM atlases.

The matching process involves picking out distinctive patterns or features of the cluster and atlas for comparison. For example, the octahedral atlases often show parallel planes of atoms, thus identifying parallel lines in a cluster implies that it is most likely to be octahedral. The decahedral clusters often show curved lines as well as areas of more distinct dots, while icosahedral clusters show more spherical contours often with the patterns radiating out from the centre of the cluster. These distinct patterns allow identification of clusters with an intermediate number of atoms, rather than solely the magic number sizes. If no positive identification can be made, the cluster is classed as unidentified / amorphous. Clusters that are unidentified / amorphous do not match any of the three typical structures, but occasionally have identifiable features.

Whilst imaging, care has to be taken to irradiate the clusters as little as possible, as the beam can alter the structures observed (similar to that seen in Section 3.4) [128, 129]. For the 55 atom clusters, prolonged imaging caused the cluster's atoms to disperse, therefore a 'one attempt' imaging policy was adopted. If the first image of the cluster taken was not in focus, or contained a scanning artefact (typically occurring when acoustic noise within the STEM room caused vibrations), the cluster was abandoned and a new cluster imaged. For consistency, the same process was followed for the 147 and 309 atom clusters, although these were less prone to damage from the beam. An alternative way of imaging would have been to take repeated images of the same cluster to study which structure motif was present in each frame. This would have allowed a picture to be built up about which motif was most stable. This would have been done either by calculating a percentage of time the cluster spent in each motif, or by looking at the final motif of each cluster, assuming it had morphed to the most stable configuration. This was not performed here as the damage to the 55 atom clusters caused them to disintegrate rather than morph between motifs.

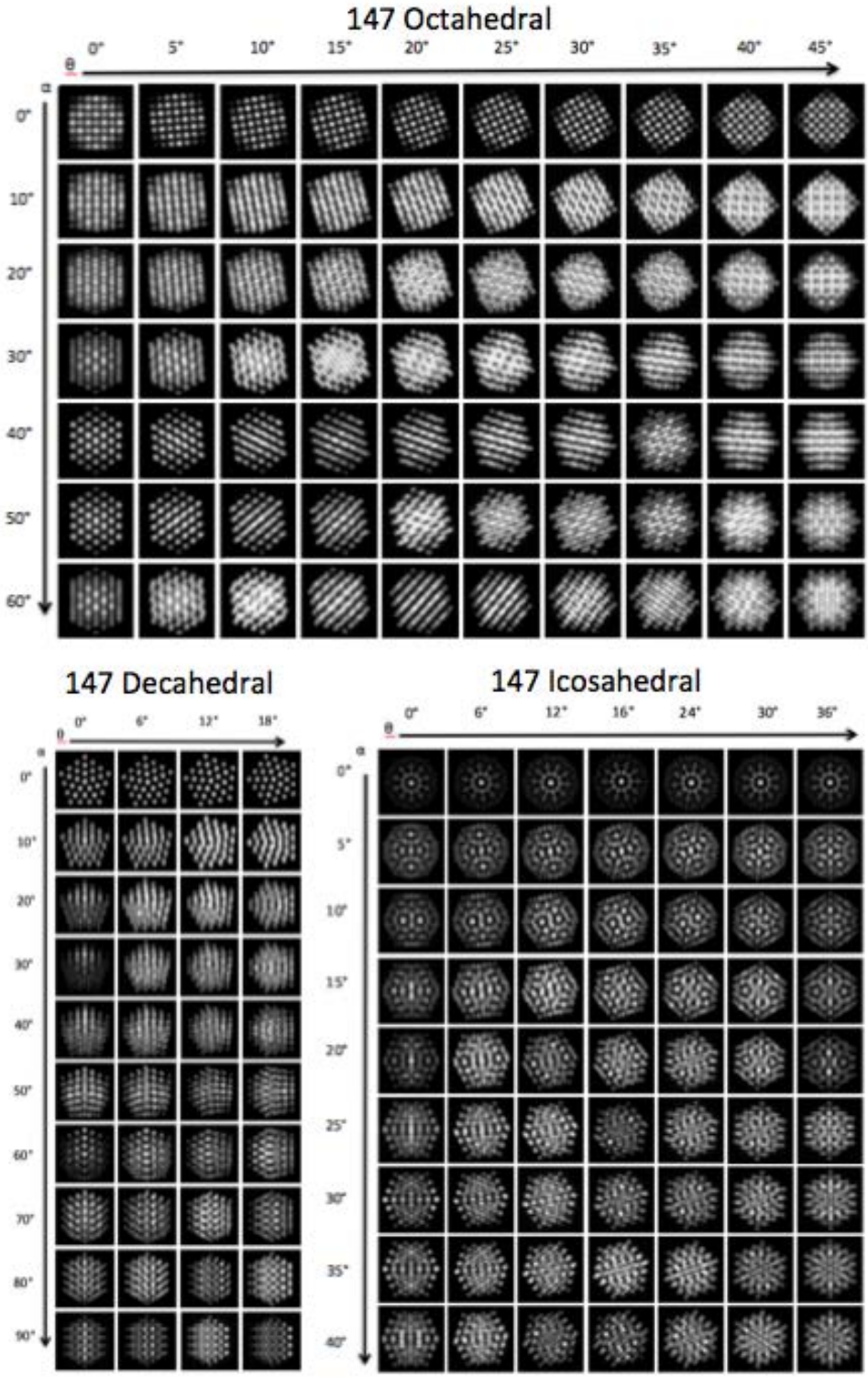

Figure 4.2: Example octahedral, decahedral and icosahedral QSTEM atlases for clusters with 147 Pt atoms, showing the rotation angles.

4.3.1 Alternative Methods of Structure Identification

The method used to identify the cluster structure within this work is identification by sight. It is done by directly comparing each cluster image with each simulated image, and the closet match chosen. This process is often repeated with each of the clusters, and positive matches are only made when the same identification was made repeatedly. This was further checked by a second person performing the same analysis. For these results Dawn Foster[130] was the second person.

Alternative methods of identification have been investigated by the group with little success. These include FFT, cross-correlation and learning algorithms. For these types of analysis to be used they need to identify the structure of clusters as reliably as a human, without a bias towards one motif over another. The first method tested was to use FFT on the clusters, with the hope that each cluster structure would show different symmetries. To test the methods a good example cluster of each motif was chosen and used as an example. A good cluster was chosen for its clarity and non ambiguity of structure. This gives the computerised methods the best chance of success.

Figure 4.3 shows an example of the FFTs generated from an octahedral, decahedral and unidentified/amorphous cluster. For the octahedral cluster the resultant FFT has some identifiable pattern which could make it distinct from a decahedral, icosahedral or unidentified/amorphous cluster. Looking at the resultant FFT images for the decahedral and unidentified/amorphous cluster there are very few features that would make them distinct. This is the main issue with trying to use FFTs to identify the cluster structures. In each FFT, a ring is formed reflecting the definition of each of the atoms, but the patterns seen within the FFT images are not identifiable with a cluster motif. This analysis was repeated with many clusters, showing the same trends, that identification of a motif was very difficult. For this reason it was decided that identification of the structure manually by eye was still the better method. It is possible that for large clusters, of 1000 atoms and more, this approach would be more successful as the patterning is more distinct. This is shown in Figure 4.4 where larger gold clusters were imaged, and clearly display

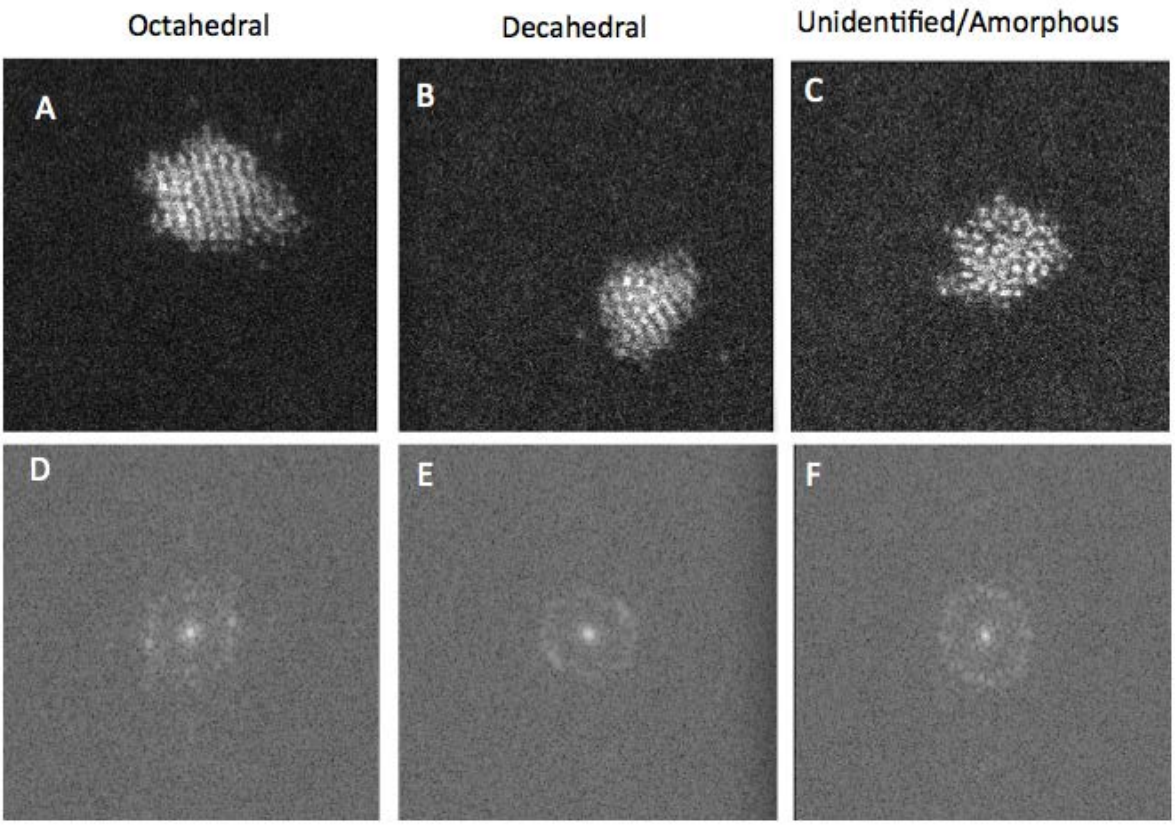

Figure 4.3: Images of 3 clusters with defined motif, octahedral, decahedral and unidentified/amorphous with their associated FFT image.

an octahedral or decahedral motif. The FFT's show more distinct patterning than for smaller clusters, but identifying the specific structure from the FFT alone may be difficult, especially identifying the subtle differences between octahedral and decahedral clusters.

A number of cross-correlation methods were attempted for the clusters. Initially clusters were cross-correlated with simulation images, but this proved unsuccessful for a number of reasons. The number of simulated images was in general small, thus inevitable there was never a simulation to perfectly match the rotation of the cluster imaged as the step size on the simulations is typically 10°. A possible improvement on the results may have been made if the simulation atlas was modelled with angle changes of 0.5°, but as simulating the atlases is very computer intensive, and would need repeating for each motif it was deemed not appropriate when matches could be made manually by eye.

The second attempt at cross-correlation was used to try and group similar clusters

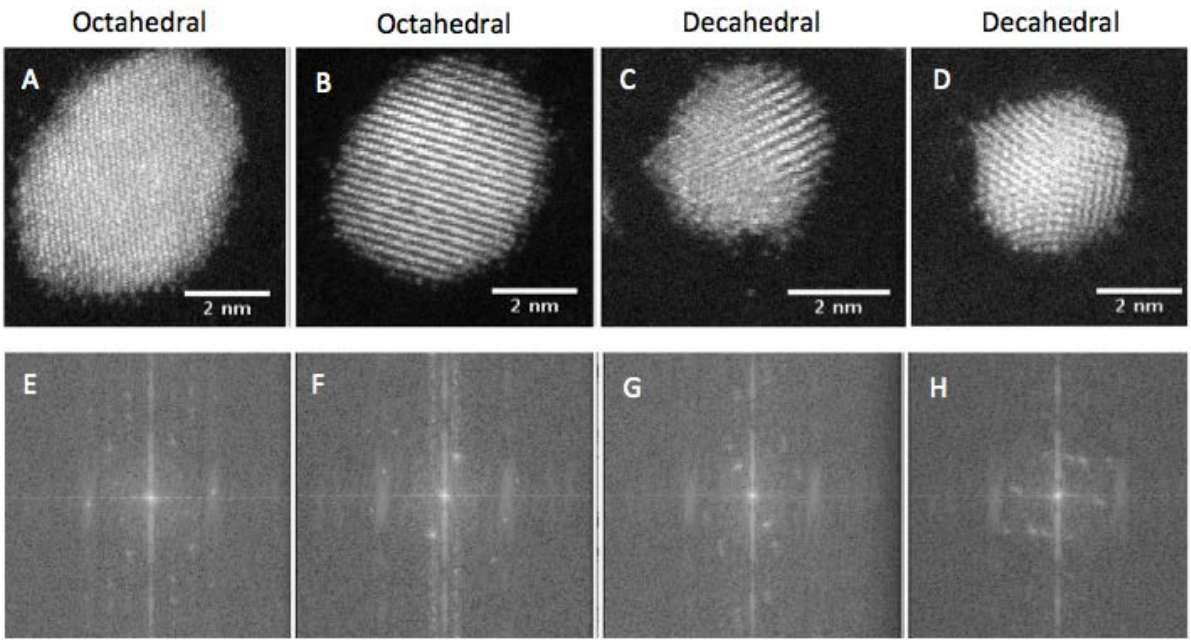

Figure 4.4: Images of 4 large gold clusters, two images with an octahedral motif, and two with a decahedral motif, with their associated FFT image.

together. For example, if a cluster was positively identified manually as octahedral it was then cross-correlated against all other clusters imaged to see if any similar clusters could be identified. This approach had some success, but only helped identify clusters which were easily identifiable manually by eye, and a large data set was needed. This still left many clusters without identifications, and, for clusters that were less distinguished in structure, made incorrect identifications. As all of the identifications made had to be manually checked it was also slower than doing the identification manually.

The learning algorithm method was attempted by a student, Alex Pattison[131], during a summer placement with the group. He used a method that attempted to match a new cluster to a close previous cluster to help with cluster identification. The method he attempted had little success and was very computer intensive.

The results from the above methods were deemed poor, thus the clusters were identified manually. I believe that for small clusters the presence of edge atoms has a huge impact on a computer's ability to identify the structure, whereas a human can look past these. Thus for larger clusters computerised methods may be more successful, but these clusters

tend to be easier to identify as they are more distinct in motif. Other possible methods of motif identification could include single particle analysis, where multiple similar images are used to build up a detailed image of a particle. This would generate a resultant image with higher signal to noise ratio that could help in identifying the structure. Alternatively the use of a 3-axis microscope arm would allow in-depth study of a single cluster, thus enabling better structure identification.

4.3.2 Dominant Motif at Each Pt Cluster Size

Initially, samples of mixed cluster sizes were made so that the distribution of cluster motifs could be investigated across a wide range of sizes. For this, three samples were made covering the 10 to 600 atom range. Three samples were made so that the density of clusters could be kept low, preventing aggregation, whilst still having enough clusters at each size to image. To do this, the cluster source was run with mass spectrum ramping across the size ranges, as opposed to single size mass selection. An equal amount of time was spent at each cluster size to help deposit an even number of each cluster size upon the grids. This meant that during imaging there was approximately an even distribution of each cluster size.

To analyse the data, 700 images of clusters were taken from the three samples. They were then individually identified as octahedral, decahedral, icosahedral or unidentified / amorphous. This was followed by the sorting of the clusters by size, and a histogram plotted with a bin width of 20 atoms. The results of this can be seen in Figure 4.5. The blue areas show the octahedral motif, red decahedral, and purple unidentified / amorphous. The green icosahedral motif was never seen, which is most likely due to icosahedral motifs being typically high [132] in energy, and is explored in more detail in Chapter 5. At large sizes of clusters, 250 atoms or more, the octahedral structure is seen as the dominant motif, whilst in the smaller size range, less than 250 atoms, most clusters are unidentified / amorphous. The decahedral motif is occasionally seen, but the icosahedral motif was not identified as present in any of the 700 clusters imaged. The

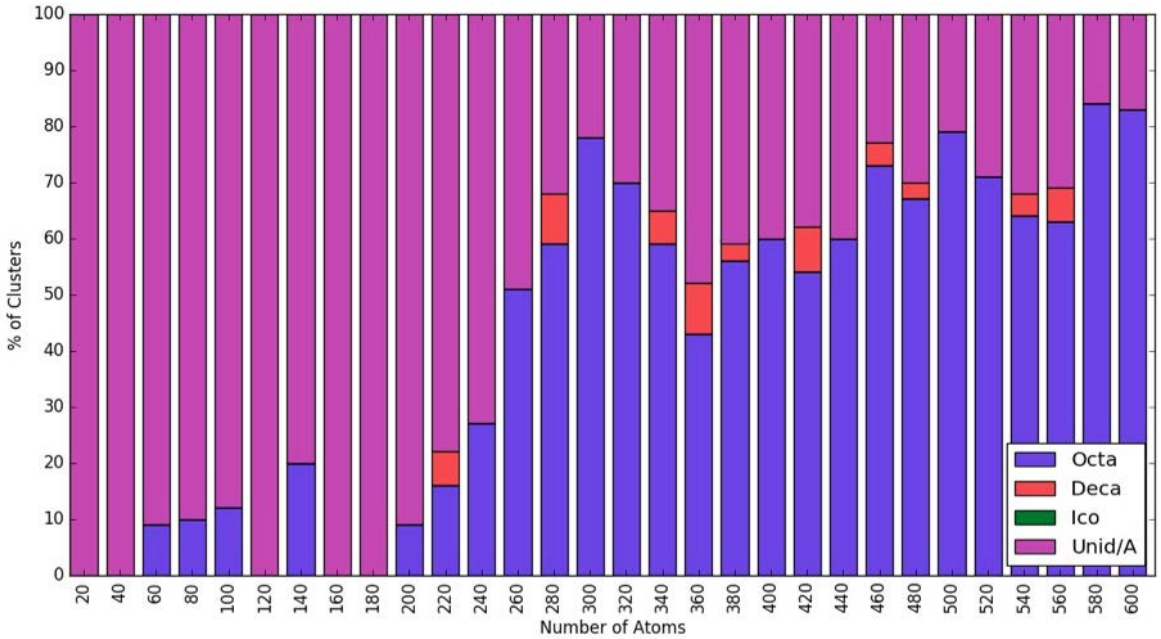

Figure 4.5: Overview of the dominant motif for Pt clusters between 10 and 600 atoms. At larger sizes > 250 atoms the octahedral motif is dominant, whilst at smaller sizes < 250 atoms there is no distinct motif easily identifiable, thus most are classified as unidentified / amorphous (Unid/A).

dominance of the octahedral motif at larger sizes is consistent with the bulk structure of Pt being FCC.

Figure 4.5 shows that there is a transition around 250 atoms to the cubic bulk structure of Pt from an unidentified / amorphous structure at lower sizes. To further investigate the unidentified / amorphous structures, magic number 55, 147, and 309 atom clusters were produced and imaged, ready for structural identification. These three sizes were chosen so that we could investigate two regions that were mostly unidentified / amorphous and a one region that was mostly octahedral in motif.

Figures 4.6, 4.7, and 4.8 show representative images from the 300 magic number clusters imaged (100 at each magic number size). The small inserts seen in Figure 4.6 are the QSTEM simulated images that best match the STEM images for 309 atom clusters. 66% of these clusters were identified as octahedral in structure, with 34% were categorise as unidentified / amorphous. Within this sample, no clusters were identified as decahedral or icosahedral in motif. For the 147 and 55 atom clusters, all were categorised as being

unidentified / amorphous, but some common distinct features could be seen. There are small areas of parallel lines and the appearance of rings with dots in both Figures 4.7 and 4.8. These features were noted when an area of a cluster could be identified manually by eye as having a pattern (rings, dots, or lines). These patterns are used to confirm that there may be the possibility of an underlying structure, but that this structure is not easily identifiable as the traditional octahedral, decahedral or icosahedral motif.

For 309 atoms, 34% of clusters have been assigned as amorphous / unidentified in structure. Figure 4.9 shows the two types of amorphous / unidentified clusters seen. These are possible twin clusters and clusters that have no distinctive structure. Twinned clusters are clusters which appear to be two FCC clusters that have joined together, thus their planes are non continuous. These have been studied previously for gold clusters [133, 134, 135]. These twin clusters could be forming in the growth phase of the clusters within the gas-aggregation magnetron cluster beam source. This could happen when two smaller clusters, of approximately 150 Pt atoms, collide and join to form a single cluster. If both initially had an FCC structure a twin structure like those seen in Figure 4.9 could be formed. An alternative to the twinned FCC based clusters is that the cluster has formed with a dislocation in one set of planes. An example of this (discussed in further detail in Section 4.3.3) where the octahedral 147 QSTEM atlas shows the projected STEM intensity from a dislocated octahedral cluster. The remaining amorphous / unidentified clusters seem to have no distinct identifiable structure, but may still be crystalline. These clusters may have melted under the STEM beam. This would be consistent with the 55 and 147 Pt atom clusters being all identified as amorphous / unidentified when compared with the traditional QSTEM simulations. Some of the 55 and 147 atom clusters are identified as distorted motifs in Section 4.3.3, but the proportion of clusters is still very low. Melting of the clusters is discussed in Section 4.4.

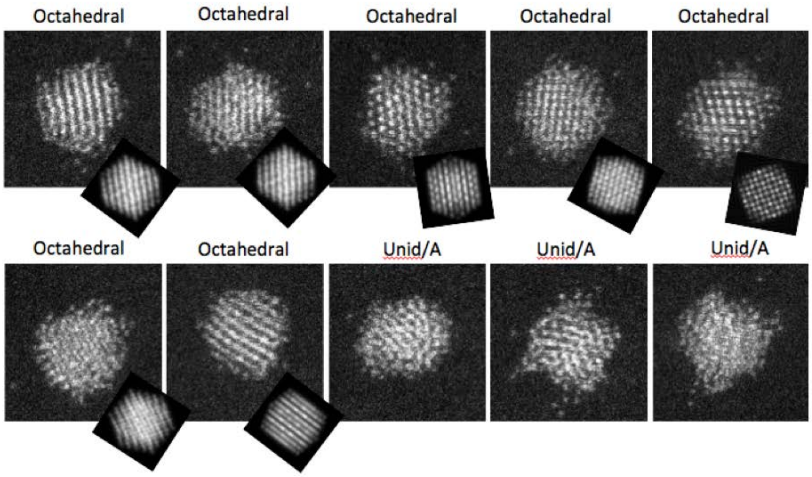

Figure 4.6: Ten experimental STEM images of clusters with 309 Pt atoms, accompanied by their QSTEM simulations. 66% of these clusters were identified as octahedral, whilst the remainder was categorised as unidentified / amorphous.

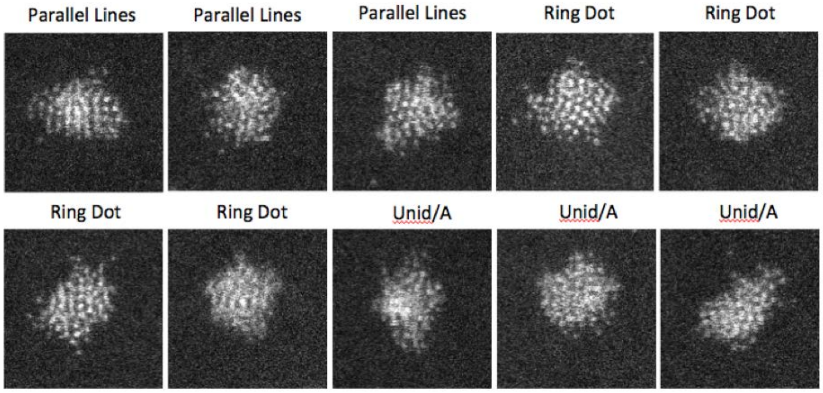

Figure 4.7: Ten experimental STEM images of clusters with 147 Pt atoms. All clusters of this size were identified as unidentified / amorphous.

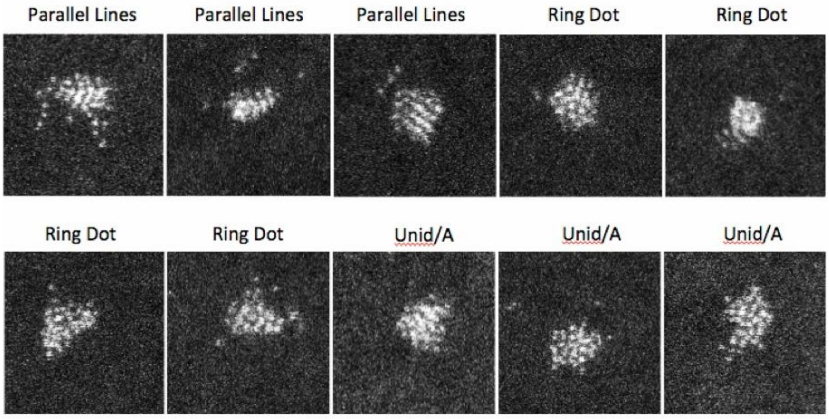

Figure 4.8: Ten experimental STEM images of clusters with 55 Pt atoms. All clusters of this size were identified as unidentified / amorphous.

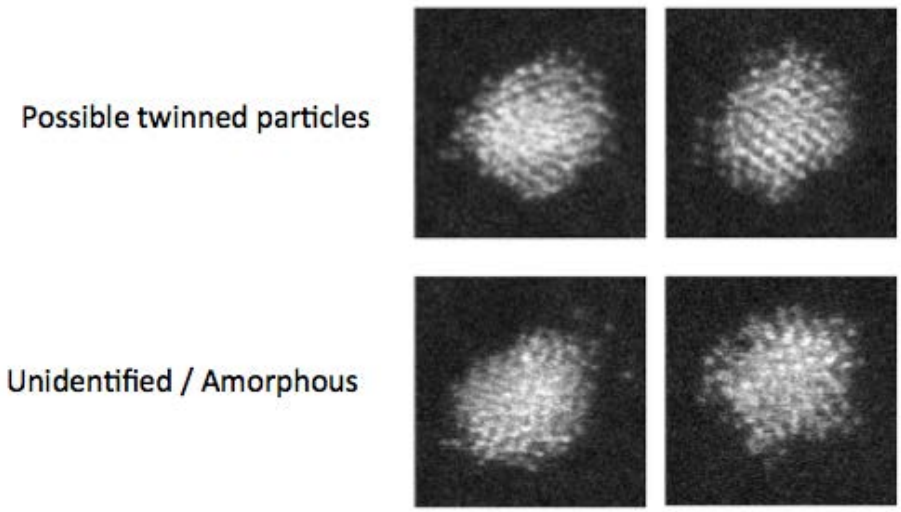

Figure 4.9: Examples of two distinct 309 Pt atom clusters seen in the amorphous / unidentified category. The top row shows the pair of 309 Pt atom clusters that show possible twinned particles, whilst the pair on the bottom row shows two examples of clusters with no distinct structure.

4.3.3 QSTEM Simulations of Clusters with 55 and 147 Atoms

To identify some of the 55 and 147 atom clusters, simulated clusters, found through global optimisation in Section 5.4.5, were used to generate QSTEM atlases. The extra atlases, made from non-perfect structures, give different simulated intensity alases. These new atlases generate more images from the slightly distorted clusters that are more likely to be matched to the real STEM images. To produce these atlases the lowest energy octahedral, decahedral, and icosahedral structure generated by the global optimisation was used for 55 Pt atoms, and the lowest energy octahedral and decahedral structure was used for 147 Pt atoms. The icosahedral motif was not simulated for 147 atoms as the lowest energy structure generated was almost identical to the perfect icosahedral structure. The global optimisations also put the icosahedral structure relatively high in energy when compared with the decahedral and octahedral motifs. The simulation atlases for 55 atoms are shown in Figures 4.10, 4.11, and 4.12. Each motif was rotated in two dimensions between 0° and 90°. As the clusters produced by global optimisation in Section 5.4.5 had an arbitrary rotation, the cluster had to be manually rotated so that the 0°, 0° rotation was symmetric. This minimised the number of angles through which the cluster had to be rotated for QSTEM simulations, as it maximised the number of rotations that had the same QSTEM simulation. A 10° interval was chosen to maximise variation in patterns, whilst minimising the time taken for simulation and matching the QSTEM projections with the real STEM images. The clusters shown top left, top right and bottom left are the clusters for the 0°, 0°, the 90°, 0°, and the 0°, 90° projection respectively.

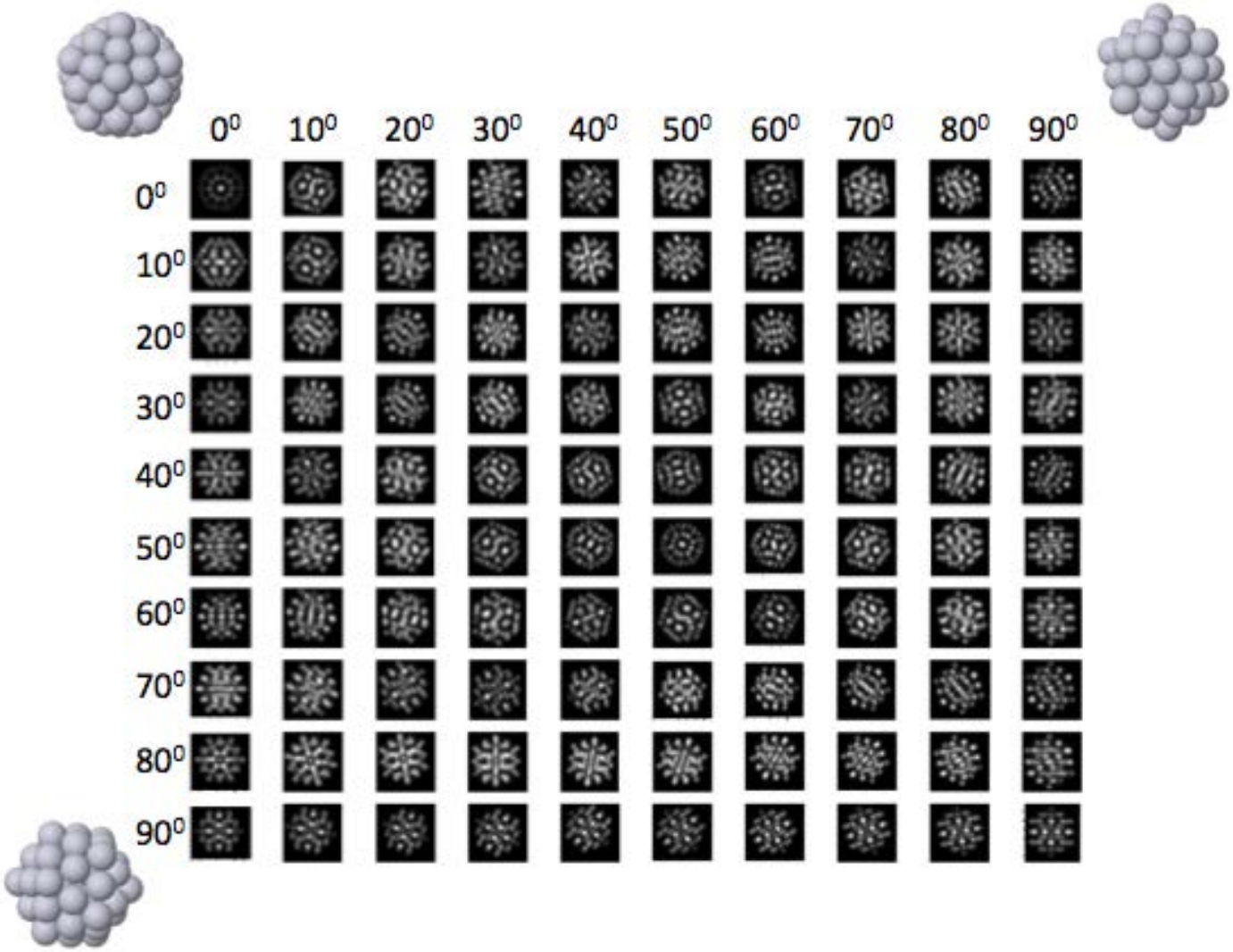

Figure 4.10: QSTEM simulation of lowest icosahedral structure with 55 atoms. The clusters shown top left, top right and bottom left are the clusters for the 0°, 0°, the 90°, 0°, and the 0°, 90° projection respectively.

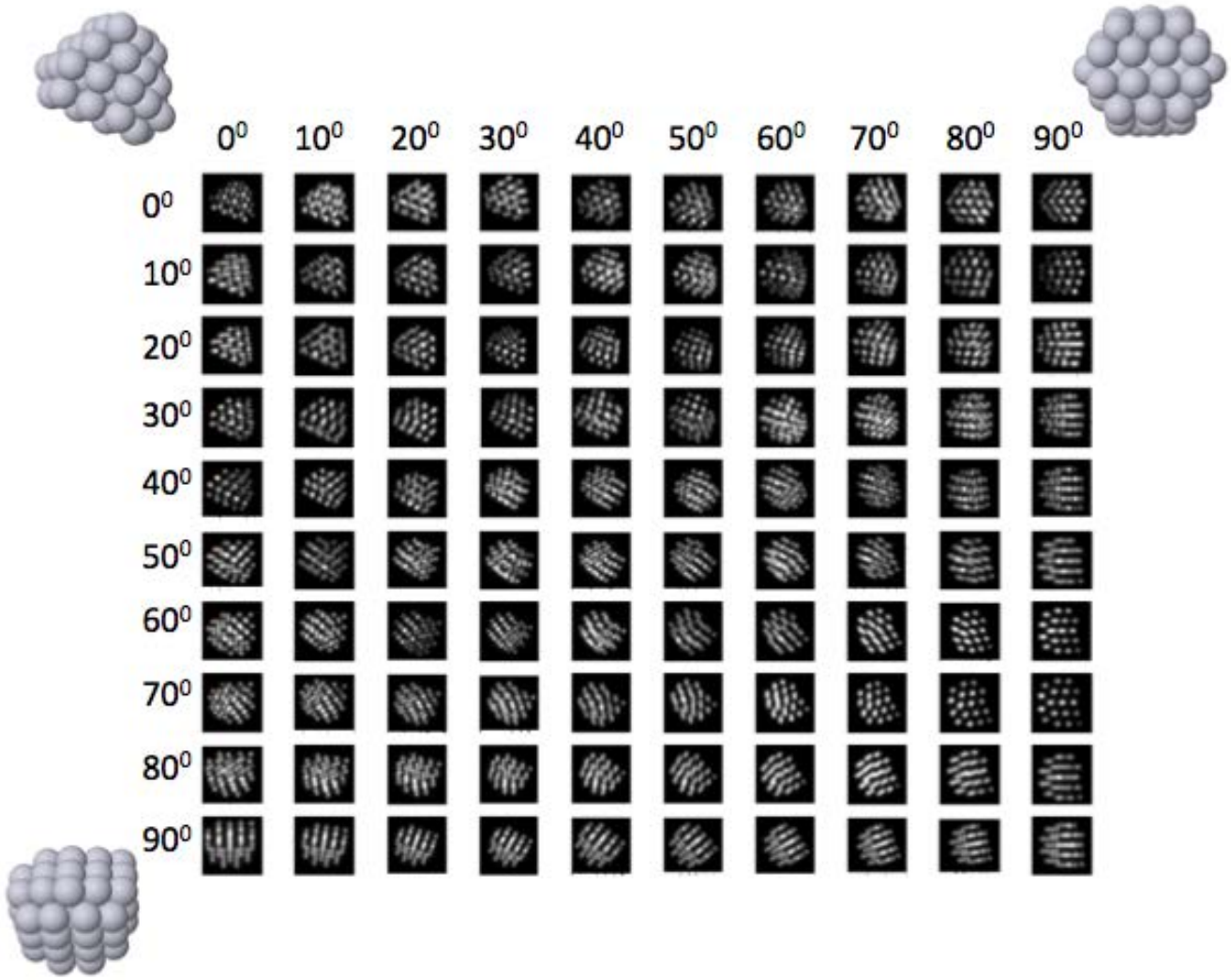

Figure 4.11: QSTEM simulation of lowest decahedral structure with 55 atoms. The clusters shown top left, top right and bottom left are the clusters for the 0°, 0°, the 90°, 0°, and the 0°, 90° projection respectively.

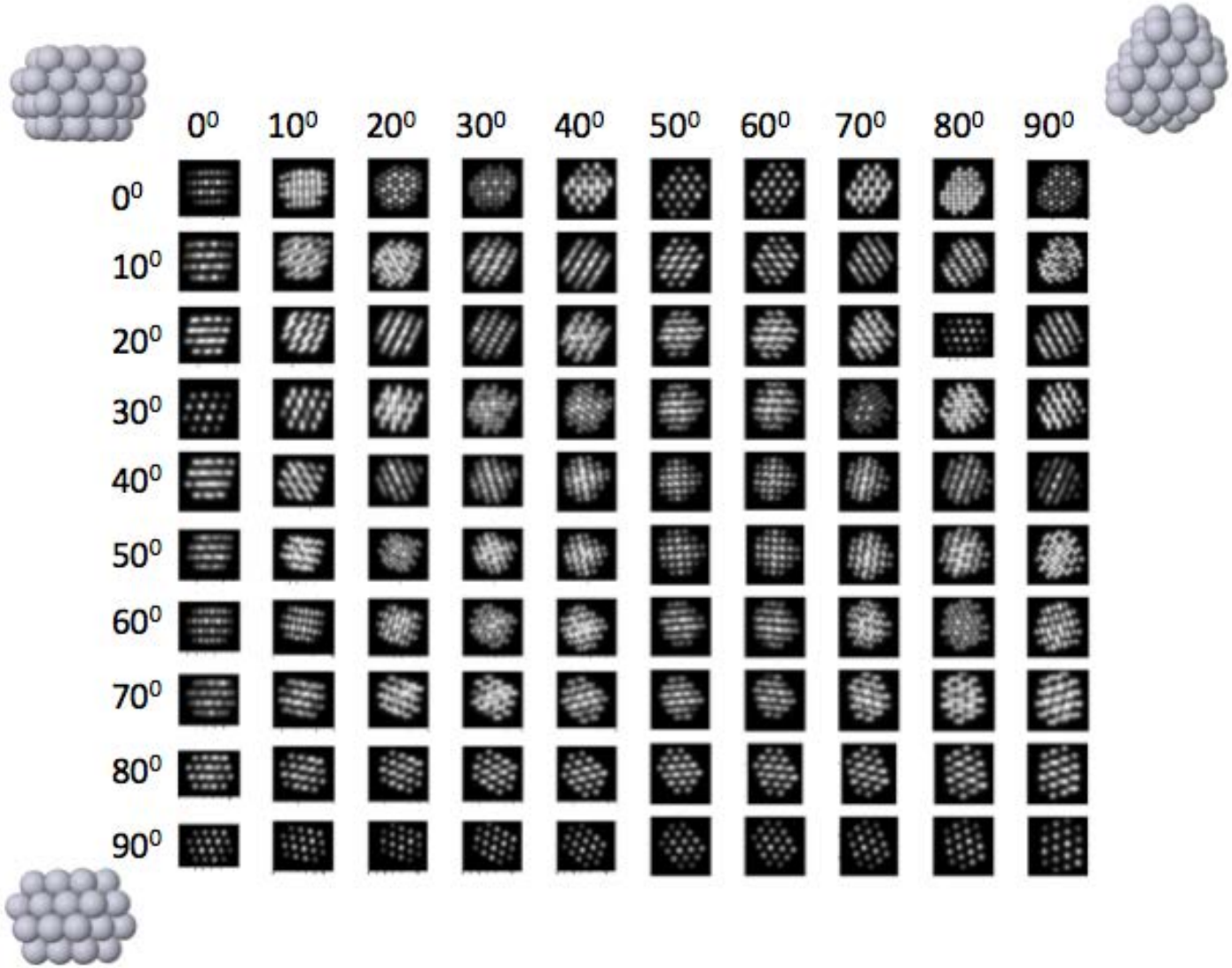

Figure 4.12: QSTEM simulation of lowest octahedral structure with 55 atoms. The clusters shown top left, top right and bottom left are the clusters for the 0°, 0°, the 90°, 0°, and the 0°, 90° projection respectively.

Figure 4.13 shows the six matches for 55 atom clusters with the new icosahedral QSTEM simulation. The STEM image is designated by a blue edge, whilst the QSTEM simulation is shown next to the image rotated to the matching angle. For the icosahedral identification each STEM image and simulation show either a ring, line, or a pair of dots that can be used to match the two images. Figure 4.14 shows the matches between the STEM images, and the new decahedral QSTEM atlas. Four clusters were matched, with the overall shape of the cluster being considered along with the internal pattern. Figure 4.15 shows the five matches between the new octahedral QSTEM atlas and the 55 atom STEM images. These are matched with the parallel plane pattern along with their external shape. The matches seen for these clusters are not perfect, but are the closest match with the simulation atlases, and they show a closer match than the standard octahedral, decahedral, and icosahedral atlases.

Out of the 100 clusters imaged at 55 atoms, 15 have been positively identified with the new QSTEM atlases generated from the global optimisations described in Section 5.4.5. The additional simulation angles, and the fact that each globally optimised structure is slightly different to the perfect magic number structure, has allowed more identifications, but the majority of clusters remain unidentified / amorphous. From this analysis there is no dominant structure at the 55 atom size, as there is an approximately even distribution of motifs. To improve the identification the atlases would need to be simulated with smaller angle changes, but this result implies that the atlases based on the simulations are a better match to experimental results than the standard octahedral, decahedral, and icosahedral atlases.

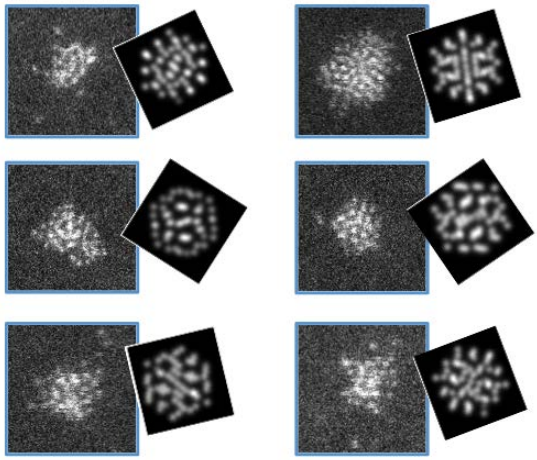

Figure 4.13: STEM images of 55 Pt atom clusters (blue edge) with matching new icosahedral QSTEM simulation. 6 of the 100 clusters were identified as icosahedral in motif.

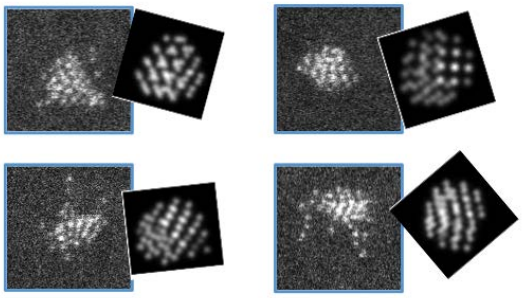

Figure 4.14: STEM images of 55 Pt atom clusters (blue edge) with matching new decahedral QSTEM simulation. 4 of the 100 clusters were identified as decahedral in motif.

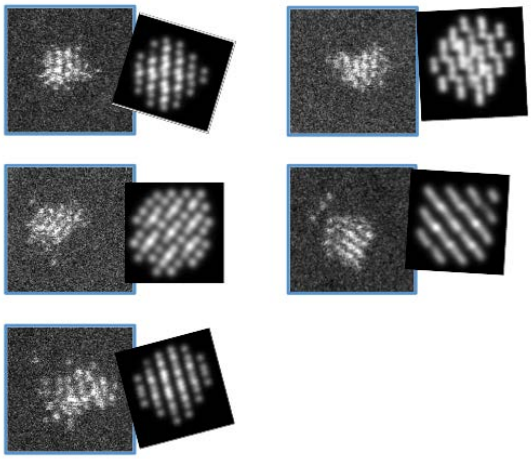

Figure 4.15: STEM images of 55 Pt atom clusters (blue edge) with matching new octahedral QSTEM simulation. 5 of the 100 clusters were identified as octahedral in motif.

The QSTEM atlases for the lowest decahedral and octahedral structure produced from global optimisation for clusters with 147 atoms are shown in Figures 4.16 and 4.17. The octahedral atlas is of particular interest, as the slightly deformed octahedral structure gives rise to twin like cluster simulations. Figure 4.18 shows a larger image of four clusters that have an intensity which each look like a twinned cluster. Twinned clusters are nanoclusters that appear to be made up of two smaller cubic clusters that have joined together [136, 137]. In this case they occur in the simulation atlas as the initial structure is a slightly distorted octahedral structure. In some rotations the intensity appears to be that of a traditional octahedral cluster, but alternative rotations give rise to the twinned cluster intensity pattern. This slightly distorted octahedral cluster offers an alternative production mechanism, rather than two distinct octahedral clusters joining together as explained in Section 4.3.2. No twin examples were seen in the STEM images of the 147 atoms for the Pt clusters, but two have been seen in the 309 amorphous / unidentified clusters.

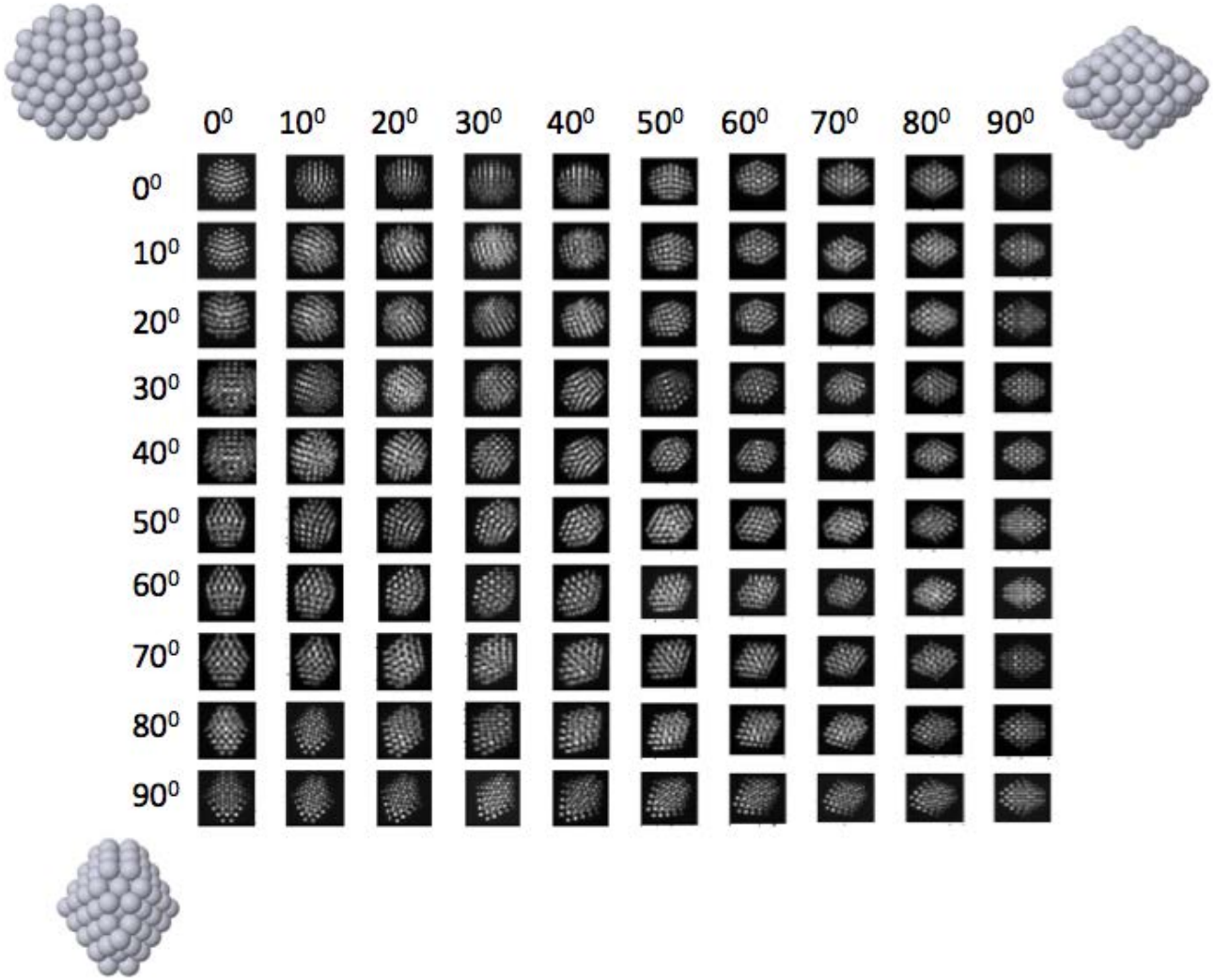

Figure 4.16: QSTEM simulation of lowest decahedral structure with 147 Pt atoms. The clusters shown top left, top right and bottom left are the clusters for the 0°, 0°, the 90°, 0°, and the 0°, 90° projection respectively.

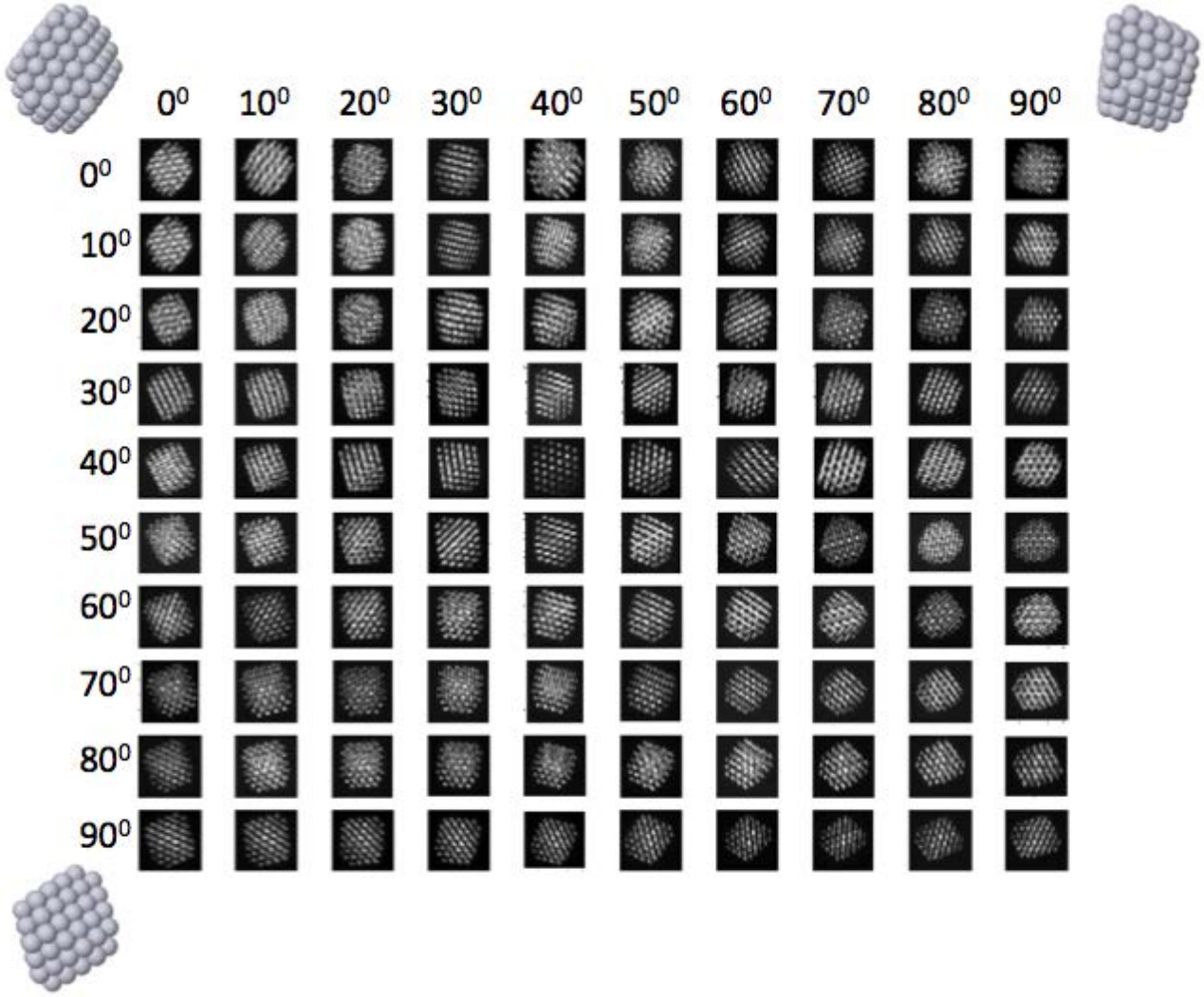

Figure 4.17: QSTEM simulation of lowest octahedral structure with 147 Pt atoms. The clusters shown top left, top right and bottom left are the clusters for the 0°, 0°, the 90°, 0°, and the 0°, 90° projection respectively.

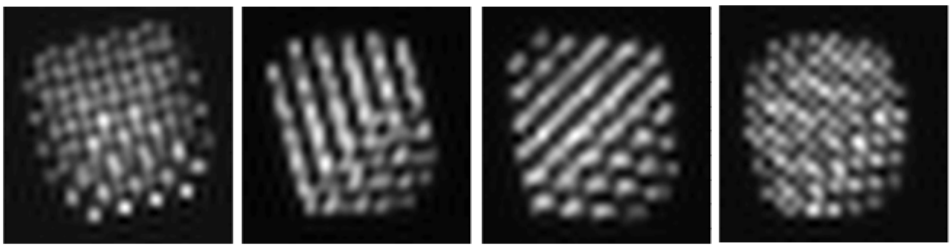

Figure 4.18: Four clusters from the 147 Pt atom octahedral QSTEM atlas (Figure 4.17) that all show features of twinned clusters. Twinned clusters are identified when two areas of the same cluster show different octahedral patterns, for example areas of lines and dots.

Figures 4.19 and 4.20 show the identifications for the 147 atom clusters. The icosahedral motif is not considered here, as it is far higher in energy than the lowest decahedral or octahedral structures, and the globally optimised structure was almost identical to the perfect icosahedral structure. Out of the 100 clusters imaged, six clusters are identified as decahedral, with one being identified as octahedral. This shows that the decahedral motif is the more dominant structure, but only 7 out of the 100 clusters were positively identified with the new QSTEM atlases.

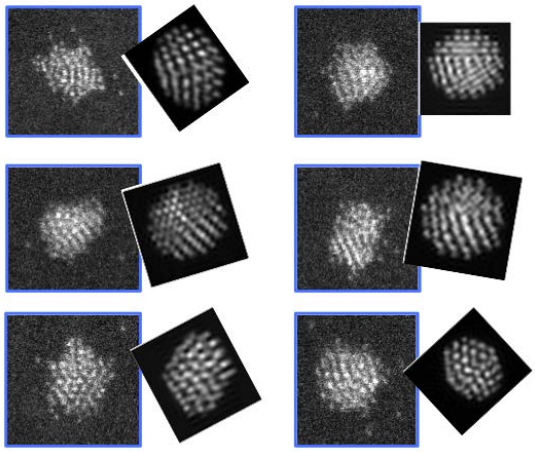

Figure 4.19: STEM images of 147 Pt atom clusters (blue edge) with matching new decahedral QSTEM simulations. 6 of the 100 clusters were identified as decahedral in motif.

The identifications for 55 and 147 Pt atom clusters have been checked by an independent observer who has extensive experience with matching gold and silver clusters of multiple sizes, to QSTEM simulated atlases. This helps reduce false matches.

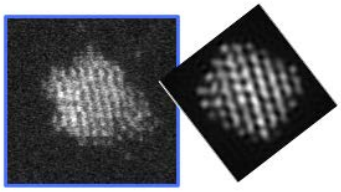

Figure 4.20: STEM image of a 147 Pt atom cluster (blue edge) with matching new octahedral QSTEM simulation. 1 of the 100 clusters were identified as octahedral in motif.

4.4 Electron Beam Heating of the Pt Samples

It is possible that the Pt clusters studied are melting under the STEM electron beam, thus identification of the structural motif is difficult. It is generally accepted that the melting point of a nano material scales as $\frac{1}{radius}$ for particles over 500 atoms [138, 139, 140]. This means that all nanoclusters have a melting point below that of their respective bulk material[141]. For clusters smaller than 500 atoms in size, the relationship between cluster size and melting temperature becomes more complicated as both the geometry and the electronic structure of the cluster impacts upon its melting point [142, 143].

Experiments studying the STEM electron beam heating for a 28 nm cluster were done by Asoro *et al.* [144]. These studies estimated that their STEM was heating the clusters to approximately 100°C. Experimentation with a STEM heating arm preformed by Foster *et al.* at the University of Birmingham showed that gold clusters were being heated to less than 150°C by the electron beam [130]. This estimation was made based upon the study of structural fluctuations of gold clusters under the electron beam. For the fluctuations induced by the electron beam, only octahedral to decahedral motif changes were seen. These results were compared with structural proportions seen when the clusters were imaged on the STEM heating arm that was ramped over multiple temperatures. For heating below 150°C only octahedral to decahedral structural changes were seen, whilst above this temperature decahedral to octahedral structural changes started to occur. This study leads to an upper limit of the heating temperature of the STEM electron beam of 150°C.

A molecular dynamics study on the melting of Pt clusters by Ping *et al.* discusses the temperatures at which the surface of the cluster starts to melt, the temperature that total melting happens, and the temperature at which the cluster solidifies upon cooling [145]. They have shown that for a cluster of 256 atoms, an octahedral cube cluster exhibits surface melting at 600 K (326°C), full melting at 1000 K (726°C) and re-solidifies on cooling at between 900 - 1000 K (626 - 726°C). Experiential work by Wang *et al.* demonstrates surface and total melting for a Pt cluster with a radius of 4 nm [146]. For

this size the surface begins to melt at 300-450°C and full melting appears at temperatures above 600°C. These two sets of data are reasonably consistent in approximating the surface melting temperature to 350°C and full melting occurring at 650°C. The melting temperature for bulk Pt is 1750°C, therefore these melting temperatures are consistent with clusters melting at temperatures far below that of the bulk.

From the comparison of the STEM temperature (150°C) and the surface and total melting temperatures of small Pt clusters (300 - 650°C) it is clear that the 309 atom clusters are most likely solid during imaging. This is consistent with what has been observed, as the 309 atom clusters appeared to remain stable, even when multiple images are taken. For the smaller clusters of 55 and 147 atoms it is quite possible that the melting temperatures (particularly the surface melting temperature) for these clusters is below the temperature to which the STEM electron beam heats. The surface melting temperature is also likely to be more influential on these smaller clusters, as the surface area is larger. If the surface atoms of these small clusters have melted, and thus move positions, the STEM image is unlikely to match any of the QSTEM simulations, as a very large percentage of the cluster's atoms will be distorted within the image. This could lead to the very low identification percentage seen in the 55 and 147 Pt atom cluster results.

4.5 Comparison Between Experimental and Theoretical Pt Magic Number Clusters

The above results can be contrasted with the results found from the theoretical calculations performed in Chapter 5.

From the above results it is clear that for sizes above 250 atoms the dominant structure is the octahedral motif, whilst below this size the structure is classed as amorphous / unidentified. The magic number results from the experimental data show that the 309 structure is dominant as 66% of the clusters were identified as octahedral. This is consistent with the results found through global optimisation (Section 5.4.5) which showed

that for the size range of 303 - 315 Pt atoms, 76% of the lowest structures found were octahedral (10 out of the 13 sizes). The theory predicted that the other 24% would be decahedral, but experimentally no clusters of this size have been positively identified as decahedral. This may be due to the decahedral motif being inherently harder to identify as the patterns seen are less distinct.

For the 147 atom clusters 6 of the 100 are identified as being decahedral in motif, with 1 being identified as octahedral. Although these numbers are very low, they match favourably with the theoretical calculations which show a decahedral dominance in the size range of 144 - 150 Pt atoms. The theory also shows that the octahedral motif is very close in energy to the decahedral, thus is likely to be second in dominance. This matches well with the decahedral structure being identified more than the octahedral.

For the 55 Pt atom experimental data, clusters from all motifs have been identified with reasonably equally occurrence, thus no single motif is most dominant. From the theoretical data the icosahedral motif is dominant for clusters of 54 and 55 atoms, whilst the decahedral motif is dominant for 56 atoms. From the theoretical data for 54 - 56 atom Pt clusters it can be seen that the three motifs are particularly close in energy. For all sizes, an example of each structural motif can be seen within 0.32 eV of the lowest energy structure. This closeness in energy would lead to a higher probability of structures which are not the absolutely lowest in energy being found, especially if the beam is heating the clusters and causing them to switch between low energy structures prior to melting.

These results show that there is some agreement between the theoretical and the experimental results, but the results are limited by the low number of experimental clusters that have been positively identified. If the clusters that have been identified at 55 and 147 atoms are representative of all of the experimental cluster results then the data has reasonably good agreement, but further identification may vastly change the trends of the experimental data at these two sizes. To positively identify more clusters further QSTEM simulation atlases may be useful, particularly for clusters that are not magic number in size.

4.6 Conclusion and Further Work for Platinum Clusters

From the experimental work, it can be seen that for clusters with more than 250 Pt atoms they display a cubic structure. This is consistent with the bulk structure of Pt, identifying 250 atoms as the point where Pt clusters start representing bulk FCC Pt in structure. Below this size, the motifs remain mostly unidentified / amorphous.

The use of extra QSTEM simulation atlases and further simulation rotation angles has made it possible to identify a small proportion of the unidentified / amorphous clusters for both 55 and 147 atom clusters. These extra identifications match 55 Pt atom clusters to non-perfect octahedral, decahedral and icosahedral clusters, whilst for 147 Pt atom clusters most of the matches have been made to the decahedral motif.

For the smallest clusters (10 - 250 atoms) further investigation into the melting temperatures of these clusters could be done. This would involve using a STEM heating arm to experimentally investigate the temperature at which these clusters melt. It would be useful to investigate the smallest structure which does not melt under the STEM beam as this would give information about the structural motif of this smallest, stable cluster. Further investigation into melting could be used to investigate the loss of cubic dominance below 250 atoms. This would clarify whether the loss of cubic identification is due to melting or if there is a motif switch between cubic and a different structure as predicted theoretically.

Further work within this area should focus upon identifying more clusters below 250 atoms by producing further QSTEM simulations. These could include the creation of more atlases for extra globally optimised structures at the magic number sizes, or looking at the simulations for intermediate sizes. Above 250 atoms, further Pt clusters could be produced to identify the size at which all clusters show the bulk structure of Pt.

Chapter 5

Platinum Theory

5.1 Introduction

This thesis chapter will address the theoretical modelling of pure platinum clusters. This work will complement the work undertaken in Chapter 4, as structures identified herein are matched to the experimentally produced and STEM imaged clusters.

Within this chapter, we will use both local and global optimisation techniques to investigate the relative energies of different structures and motifs of Pt clusters. In particular, we will be investigating which structural motif is theoretically dominant for a wide range of cluster sizes (55 - 10,000 atoms), followed by the explicit calculation of energies for the magic number sized clusters (55, 147, and 309 atoms) within a 2% size range. Along the way, comparisons between different empirical potentials used to describe the Pt-Pt interactions will be performed.

Theoretical modelling of Pt clusters will allow us to investigate the clusters in more detail than experimental methods alone. We are able to examine a wider range of sizes theoretically than we are experimentally, due to the time it takes to produce and then image many clusters for a given level of statistical accuracy. The wider range of sizes also allows for a broader interpretation of the data, identifying trends that may not be apparent in smaller experimental datasets. The explicit calculations for magic number sized cluster

allows comparison between the theoretical and experimental data, as these are the sizes that the experimental data focusses upon. The theoretical modelling can also give more information, than STEM imaging alone, with regards to the atomic arrangement of each cluster.

5.2 Computational Details

To specify each cluster, a set of indices are used that uniquely defines the cluster. For icosahedral clusters, i is used to indicate the number of shells, with $i = 1$ being a single atom. For octahedral clusters, the index i is used to specify the edge length of the corresponding complete octahedral cluster, while j indicates the depth of the truncation at the corners of the octahedron. For decahedral clusters, p, q, and r are used. p and q specify the size of the (100) facet perpendicular and parallel to the principle axis of rotation, respectively. r specifies the depth of the re-entrant corner. Examples of these are shown in Figure 5.1. These indices are limited to certain ranges, to produce clusters that are approximately spherical . For example, in decahedral clusters q is limited between 1 and $p+3$ which prevents unstable rod style clusters being produced, which would occur when q is much greater than p. For the octahedral clusters, the truncation (j) is related to the edge length, so that it ranges from 0 to $[(i-1)/2]$ when i is odd, and $[i/2-1]$ when i is even. Only indices that produce clusters with 10,000 atoms or less are included within this study. Some examples of various truncations are shown in Figures 5.5 and 5.6.

Two different computational approaches will be used to investigate the clusters, and to calculate the energy of each cluster. These calculations will be hereafter referred to as simple and explicit calculations.

In the simple calculations, the interactions between atoms are described using a particular functional form, as opposed to describing the electronic structure of the system. The parameters of these so-called empirical potentials are obtained by fitting the function to real world measurements of a material, i.e. the potentials function is calibrated using

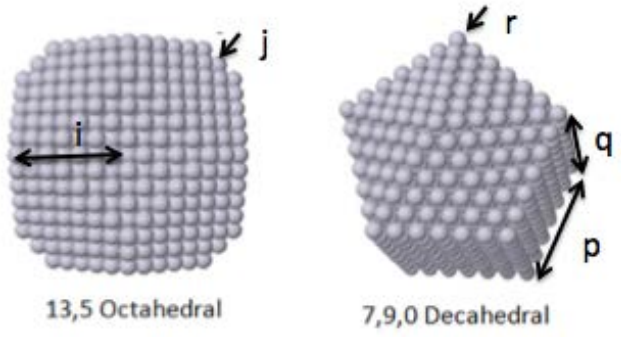

Figure 5.1: Schematic of clusters indicating where the (i,j) and (p,q,r) values are measured against.

the experimentally measured specific heat capacity of the material. This fast approach to modelling a system is often utilised for clusters [147], and as such will be used to calculate the energies of clusters for the wide size range of 55 - 10,000 atoms. The two potentials explored here will be the Gupta potential [148] and the Effective Medium Theory (EMT) potential [149]. The Gupta potential was first used in the 1980s to describe the interactions between atoms within transition metals [148]. It is a widely used potential for FCC materials, particularly for nanoclusters [150, 56, 151, 152, 25]. The EMT potential is also used to calculate the energies of FCC materials [149], often for Pt [153, 154]. The differences between the two potentials are described in Section 5.3.3. Alternative potentials that are suitable for FCC bulk materials would be the Embedded Atom Model (EAM) [155, 156, 157] or the Sutton-Chen potential [158, 159], but further investigation of these potentials was beyond the scope of this work.

Explicit calculations refer to two types of calculations that either explicitly explore the Potential Energy Surface (PES) (using global optimisation techniques) or explicitly describe the electronic structure (using DFT) [160]. Global optimisation will be used to look in-depth at the smaller size ranges around the magic number clusters at 55, 147, and 309 atoms. The Global Optimisation Using Saddle Traversal (GOUST) (Section 5.4.5) algorithm will be applied to low energy structures identified by the simple calculations,

and will explore the PES in more detail by traversing saddle points. Future work will look at using DFT to explicitly calculate the energies of these clusters.

All of the cluster structures are generated using the Atomic Simulation Environment (ASE) version 3.9.1 [161]. The simple calculations (using the Gupta and EMT potentials) are performed with As Soon As Possible (ASAP) version 3.8.4 [162]. The global optimisations are performed using the EON software package revision 2310 [163] with the GOUST algorithm [164, 165].

For the analysis of cluster stability, we define two values: Excess energy per atom in eV, E_{ex}, and Delta, Δ. E_{ex} is defined by Equation 5.1, where E_{tot} is the energy of the cluster, E_{coh} is the cohesive energy of the bulk, and N is the number of atoms within the cluster. This means that the absolute stability of clusters of different sizes can be directly compared.

$$E_{ex} = (E_{tot} - NE_{coh})/N \tag{5.1}$$

Δ is defined by Equation 5.2, and is used to represent excess energy per atom once the surface area to volume ratio has been removed. This allows for a detailed comparison of structural stability.

$$\Delta = (E_{tot} - NE_{coh})/N^{2/3} \tag{5.2}$$

5.3 Motif Dominance of Pt Clusters Between 55 and 10,000 Atoms

To achieve a broad overview of the Pt cluster morphology, we investigate the motif dominance of clusters across a large size range for both symmetric and asymmetric clusters. Symmetric clusters are those which are defined by the indices i, j, p, q, and r,where as asymmetric clusters are not as the have non-complete facets. Symmetric clusters are

those where all exposed facets of the cluster are the same size and complete (with no missing atoms). Figure 5.2A shows a symmetric octahedral cluster with indices (5,2) with some of the corner atoms marked for reference. Asymmetric closed shell clusters are those where the exposed facets are of different sizes, but all are complete. Figure 5.2B highlights atoms that would have to be removed from Figure 5.2A to form an asymmetric closed shell cluster. This is because all of the atoms from a facet need to be removed to form an asymmetrical cluster. Asymmetric open shell clusters are those where there are incomplete facets. Figure 5.2C shows the atoms which could be removed to form an asymmetric open shell cluster.

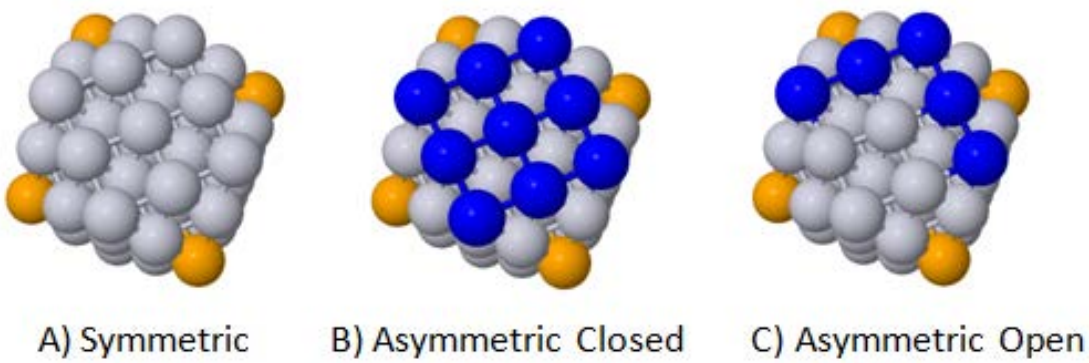

Figure 5.2: A) A symmetric cluster with some of the corner atoms marked in orange for reference. B) and C) A example of atoms (blue) which could be removed to form an asymmetric closed or open shell cluster, respectively.

The energies of a large size range (55 - 10,000 atoms) of symmetric clusters will be calculated to allow an initial assessment of which motifs are dominant within each size region. This will allow us to identify 'crossover' sizes where the most stable cluster motif changes. To investigate the stability of asymmetric clusters, an interpolation scheme will be used (Section 5.3.2). This will give a more accurate estimate of which motif dominates at which size range, but negates the need to explicitly calculate each and every asymmetric cluster, as this process would be very time consuming.

5.3.1 Symmetric Clusters

Symmetric Pt clusters are generated for all combinations of structure indices (i, i, j, p, q, and r) defined in Section 5.2. The energy of each of these clusters is calculated by performing a local minimisation where the Pt-Pt interactions are described by an empirical potential. In this section, only calculations with the Gupta potential are shown, with a comparison between the Gupta and EMT potentials made in Section 5.3.3.

Figure 5.3 shows the excess energy (E_{ex}) of symmetric clusters plotted against cluster size for the three motifs, icosahedral, octahedral, and decahedral. It shows that for all motifs, as the cluster gets larger the energy decreases. This is due to the surface area to volume ratio decreasing, increasing cluster stability. To identify the most stable clusters, a minimum energy front is constructed. A cluster belongs to the minimum energy front if it has a lower energy than all smaller clusters. This is done separately for each motif. It is then possible to compare which minimum energy front (i.e. icosahedral, decahedral, or octahedral) is lower within a given size range. This information is displayed in the colour bar shown below each plot. Red indicates that the decahedral minimum energy front is lowest in energy, whilst blue indicates that the octahedral minimum energy front is lowest. The colour bar indicates which structure should be the more dominant motif in a given size range, and thus is the one which we are most likely to find experimentally.

To be able to inspect the difference between the motifs more closely, a plot of Δ against cluster size is shown in Figure 5.4. Figures 5.3 and 5.4 effectively show the same data. The minimum energy front (shown by a solid line) for each motif is calculated using excess energy per atom, so the same clusters are connected in both figures, therefore the two colour bars are identical. These figures also highlight the magic number clusters using square boxes.

Figure 5.4 shows that the icosahedral structure is never dominant, as it is always far above the octahedral and decahedral minimum energy fronts. This is consistent with work that shows icosahedral motifs to be only stable at small sizes [166]. It also shows

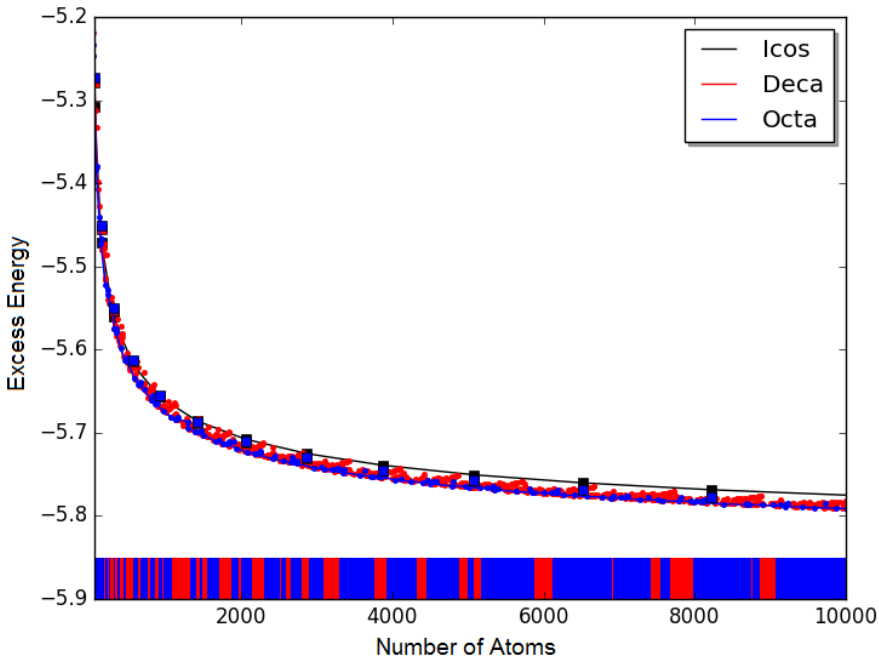

Figure 5.3: Plot of the excess energy of symmetric Pt clusters calculated with the Gupta potential for 55 - 10,000 atom clusters. It shows that the icosahedral motif is higher in energy than the decahedral or octahedral motif. The colour bar indicates the most stable motif at each size. Magic number clusters are denoted by large squares.

that the magic number structures are relatively unstable when compared with the lowest energy fronts, as they sit high up on the Δ scale. The colour bar shows that, initially, decahedral (red) and octahedral (blue) clusters are reasonably equal in dominance, but as the size increases the octahedral motif becomes more favoured. This is logical, as the bulk structure of Pt is FCC cubic and the octahedral clusters are simply truncations of the FCC crystal. This figure also highlights the fact that the two structures, decahedral and octahedral, are both similar in energy, with constant motif switching, although the frequency of the switching begins to decrease after 5,000 atoms.

These results are in contrast to a paper published in 2002 by Baletto *et al.*, [147] which reports a crossover in dominance from icosahedral to decahedral at clusters with < 100 atoms, and a crossover from decahedral to octahedral at 6,500 atoms. The paper does show some consistency with our results: The icosahedral motif being non-dominant, and

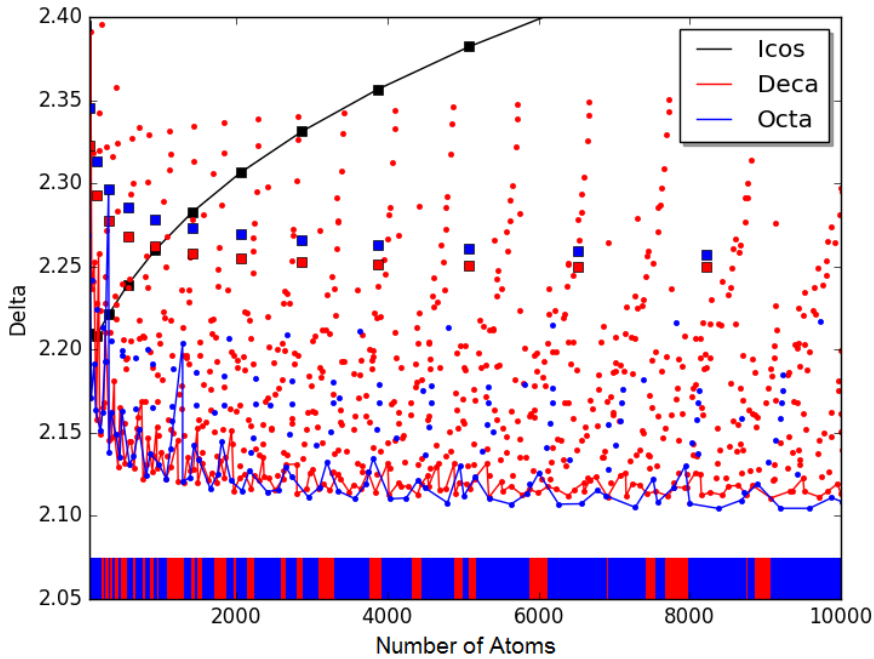

Figure 5.4: Plot of delta values for symmetric Pt clusters calculated with the Gupta potential for 55 - 10,000 atom clusters. It shows that the icosahedral motif is higher in energy than the decahedral or octahedral motif. The colour bar indicates the most stable motif at each size. This figure shows the same data as Figure 5.3, but on a delta scale rather than excess energy. Magic number clusters are denoted by large squares.

the octahedral motif being dominant at far larger sizes. However, here we show that there is multiple switching between motifs, rather than two discrete crossover sizes. Although the results contrast with ours, which show multiple motif switching, the results published by Baletto *et al.*, [147] may not have modelled as many cluster sizes, thus being too course to see the intricacies of the motif swapping.

The minimum energy front in Figures 5.3 and 5.4 simply connects low energy clusters, rather than representing energies of clusters at intermediate sizes (asymmetric clusters). This limits its usefulness, thus to improve this, we need to connect the clusters in a more meaningful way. We turn our attention to asymmetric clusters to obtain an estimate of the energies of intermediate sized clusters. In Section 5.3.2 we detail a method of interpolation that allows us to estimate the energy of the asymmetric clusters. The asymmetric cluster predicted energies are then added to Figure 5.4 to give a more detailed overview of the

55 - 10,000 atom size range.

5.3.2 Asymmetric Clusters

In order to try and connect the minimum energy fronts from Figure 5.3 in a more physical way, investigations of the energies of a selection of asymmetric closed and open shell clusters are performed for the decahedral and octahedral motifs. It is hoped that the energies of asymmetric clusters can be estimated based upon the energy of symmetric clusters, as explicitly constructing and calculating each cluster's energy would be very time consuming. Intermediate icosahedral structures are not investigated as they already have very high excess energies. To make a sensible selection of asymmetric clusters that represent the most stable clusters we first investigate the feature of asymmetric clusters that tend towards stability. The first step involves investigating the order of removing whole planes of atoms that yield the most stable asymmetric closed shell cluster. This is followed by investigation of the individual atom removal orders yielding the most stable asymmetric open shell clusters. Using this information, investigation into how to estimate the energies of low energy asymmetric clusters, will be performed.

Successive removal of all planes of a cluster represents a transition between two symmetric clusters. Figure 5.5 shows the transition of an octahedral cluster from (13,4) to either (13,5) or (11,3) depending upon whether planes are removed from the (100) or (111) facets. Figure 5.6 shows a decahedral cluster of (8,8,0) in which planes are removed from the (100), (111) or the corner giving either a (7,9,0), (8,6,0), or (6,8,1) decahedral cluster. Several of each type of facet are present on a single cluster, thus there are many orders in which these planes can be removed. The order of removal impacts the excess energy of the asymmetric closed shell clusters, thus, we investigate the order of plane removal that results in the most stable intermediate asymmetric closed shell clusters.

The energies of the clusters generated by different removal orders are shown in Figures 5.7, 5.8, and 5.9. Each figure shows multiple panels, corresponding to the different removal

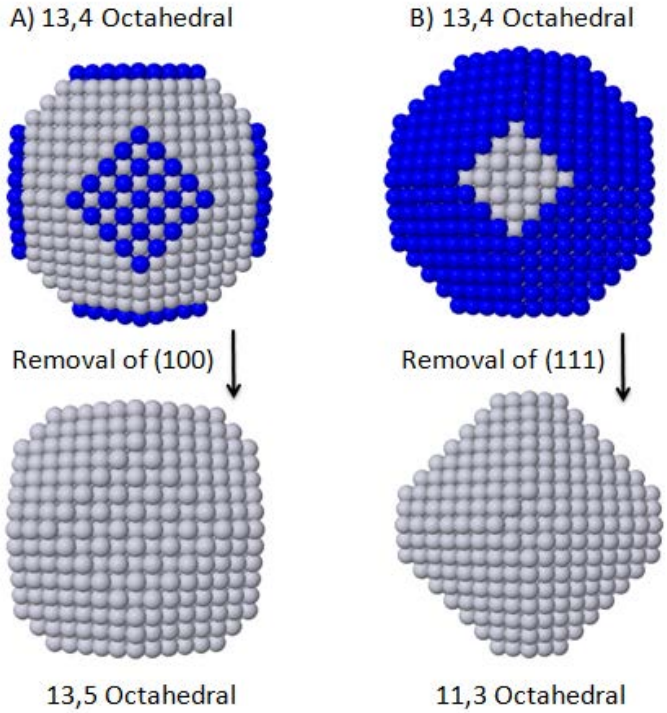

Figure 5.5: A) and B): Atoms that are removed (blue) to transition from a (13,4) octahedral cluster to a (13,5) or (11,3) octahedral cluster by the (100) or (111) removal mechanisms, respectively.

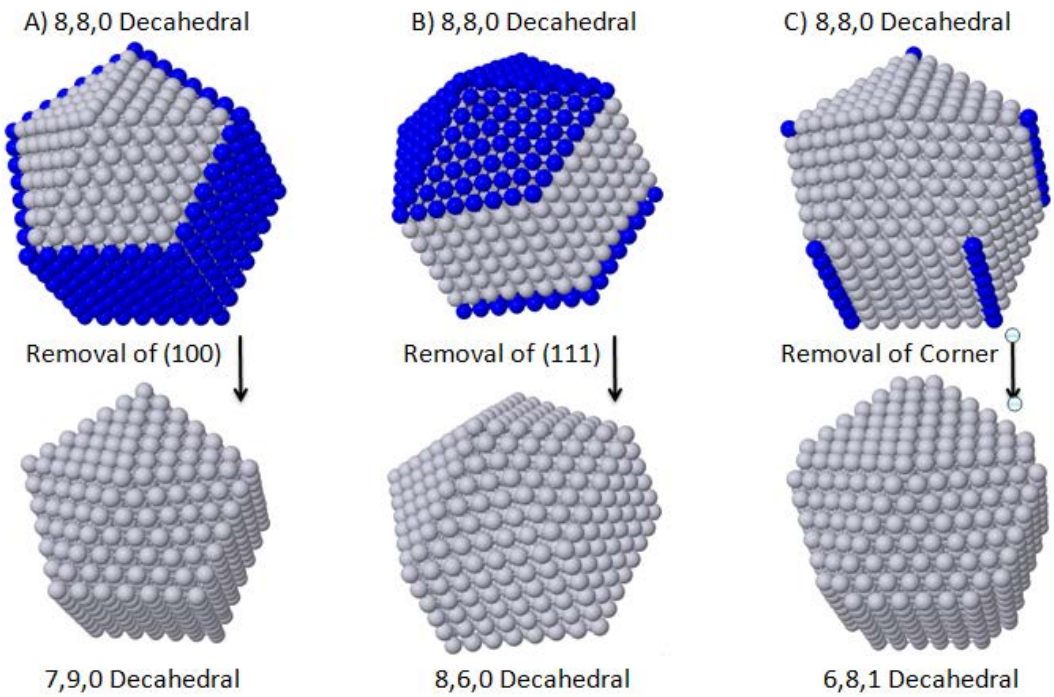

Figure 5.6: A), B) and C): Atoms that are removed (blue) to transition from a (8,8,0) decahedral cluster to a (7,9,0), (8,6,0), or (6,8,1) decahedral cluster by the (100), (111) or corner removal mechanisms, respectively.

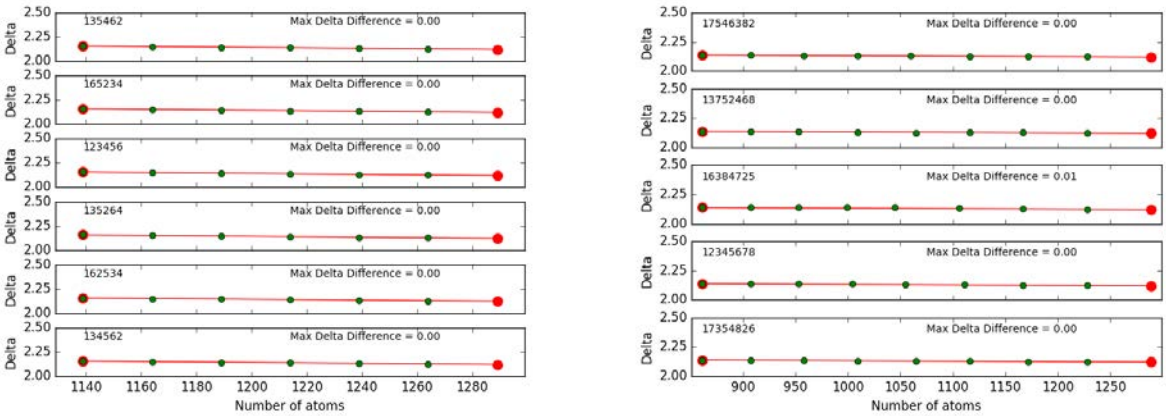

(A) Plane removal of (100) planes (B) Plane removal of (111) planes

Figure 5.7: Multiple plane removal orders are shown for the removal mechanisms from the (100) and (111) facets from an octahedral (13,4) cluster. A smaller max delta difference implies a better, lower energy plane removal order.

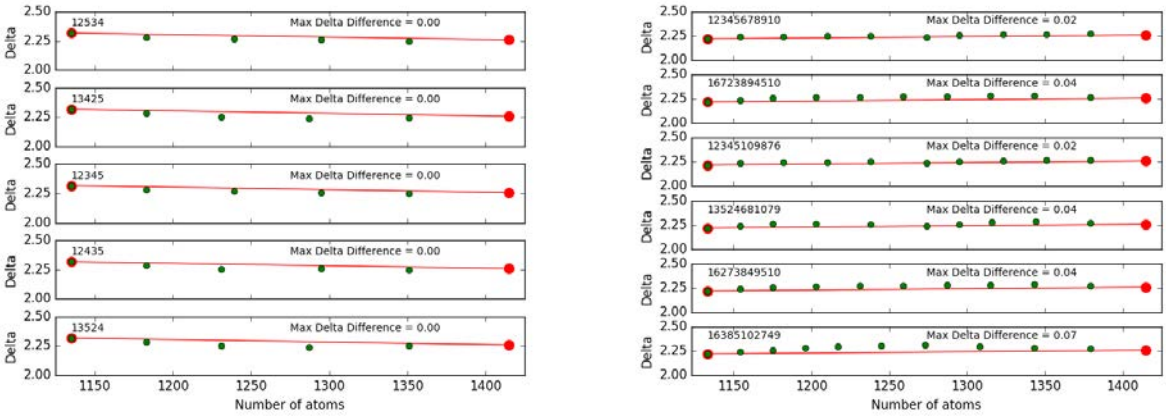

(A) Plane removal of (100) planes (B) Plane removal of (111) planes

Figure 5.8: Multiple plane removal orders are shown for the removal mechanisms from the (100) and (111) facets from a decahedral (8,8,0) cluster. A smaller max delta difference implies a better, lower energy plane removal order.

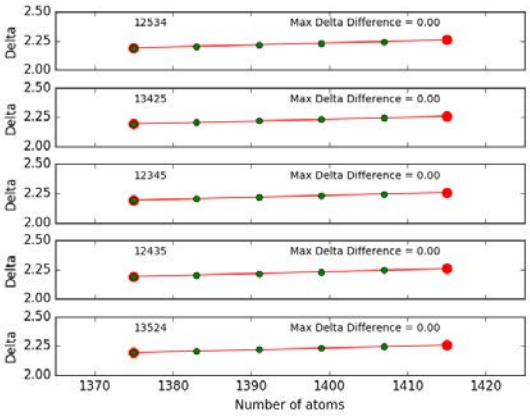

Figure 5.9: Removal of corner planes from a decahedral (8,8,0) cluster. A smaller max delta difference implies a better, lower energy plane removal order.

orders of the planes, indicated by the numbers seen in the top left of the panel. The larger starting symmetric cluster is on the right-hand side of each panel, and the final smaller symmetric cluster is on the left-hand side. The large red dots are the symmetric clusters, while the green dots indicate the energy of the cluster where a plane has been removed. Each structure has been manually generated and then minimised to calculate the energy. All unique combinations of plane removal orders have been calculated. A straight line has been used to connect the symmetric clusters. The difference between the line and the green points is used to calculate the max Δ difference of the asymmetric clusters above the line. This value is displayed in the top right-hand corner of each panel. A value of zero means that all of the asymmetric closed shell clusters fall on or below the symmetric-symmetric line. The best removal order will minimise the Δ of the closed shell asymmetric clusters, as it produces the lowest energy configuration for the clusters. For the octahedral clusters, there are six plane removals for the (100) facet (Figure 5.7A), as there are six (100) facets in a truncated octahedral cluster. Similarly, for the (111) removal order (Figure 5.7B) there are 8 points as there are 8 (111) facets in an octahedral cluster. For the decahedral cluster, there are 5 (100) facets, 10 (111), facets and 5 corners which can have planes removed.

For the octahedral clusters, the removal order for the (100) planes is inconsequential. This is because the energy of all of the clusters falls on the symmetric-symmetric line, as the max Δ for all removal orders is zero. For the (111) planes, almost any removal order is acceptable. The slight exception to this is the 16384725 removal order, which represents non-touching facets being removed. For the decahedral cluster, the removal order of the (100) facets is again unimportant, but for the (111) facet, removal of one side (plane numbers 1 - 5) before the second side (plane numbers 6 - 10) is preferential, giving a max Δ difference value of 0.02. From the figures, it can be seen that in general, the removal order does not influence the energy of the cluster if the facets are not initially connected. For facets that are initially connected, removal from one area first is associated with a lower energy than removal of opposing or unconnected facets. This is because the

removal of opposing facets leads to more exposed edge sites being formed.

A similar process was used for the asymmetric open shell clusters, where the removal order of the atoms from one plane is investigated. Figures 5.10, 5.11, and 5.12 illustrate how removing atoms in various orders from one plane impacts the energy of the cluster. The red dot shows the starting symmetric cluster on the right-hand side, and the green dot shows the asymmetric closed shell final structure with one plane removed on the left-hand side of each panel. The black dots indicate where a single atom has been removed and the energy calculated. The red line connects the symmetric-symmetric cluster, with the smaller symmetric cluster not seen in the figures, whilst the max Δ difference is a measure of the maximum energy above the line an asymmetric open shell cluster is. The word in the top left-hand corner describes the order of atom removal. For example the spiral removal starts removing atoms from an external edge, in a circular manner.

From the figures, it can be seen that randomly removing atoms from a facet generates a cluster with a high energy. This is expected, as removing an atom from the centre of a facet, which has a large coordination number, is likely to increase the excess energy. Removing atoms with low coordination numbers is thus preferential, implying that removal in an spiralling manner from the outside inwards generates clusters with lower energies. This holds in most cases, except with the decahedral (8,8,0) where parallel lines of atoms removed from the edge of the cluster towards the point yields a slightly lower max Δ difference and thus excess energy.

From the investigation of the best removal orders for both planes and atoms, we know that removal of connected planes first, and removing atoms in a spiral manner, typically keeps the energy of the asymmetric cluster low. This is important information, as the main goal of the project was to identify stable clusters. We will use these removal orders to generate a test suite of clusters from which we will investigate ways in which the energy can be estimated.

Using starting octahedral clusters of (13,0) and (13,3), we create asymmetric clusters by removing atoms one by one from the (100) facet and calculating the energy (Figure

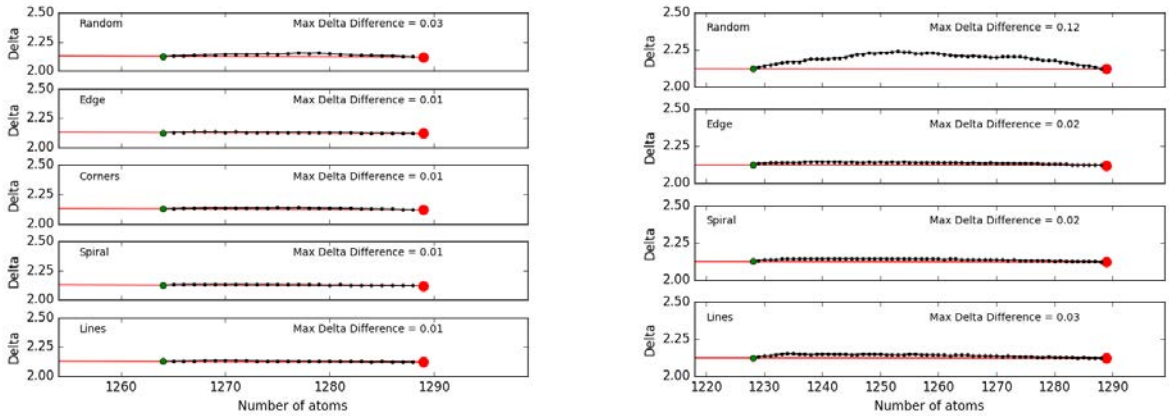

(A) Atom removal off (100) plane (B) Atom removal off (111) plane

Figure 5.10: Removal mechanisms (100) and (111) from an octahedral (13,4) cluster. A smaller max delta difference implies a better, lower energy atom removal order.

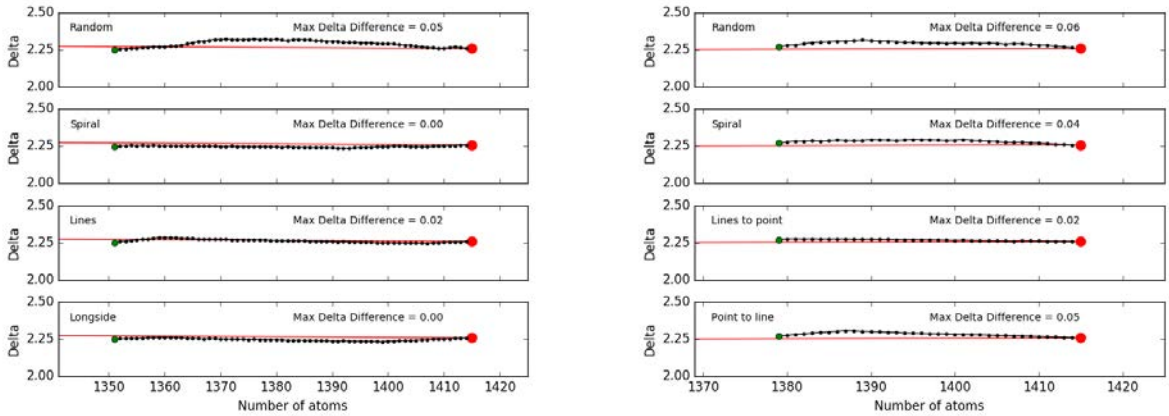

(A) Atom removal off (100) plane (B) Atom removal off (111) plane

Figure 5.11: Removal mechanisms (100) and (111) from a decahedral (8,8,0) cluster. A smaller max delta difference implies a better, lower energy atom removal order.

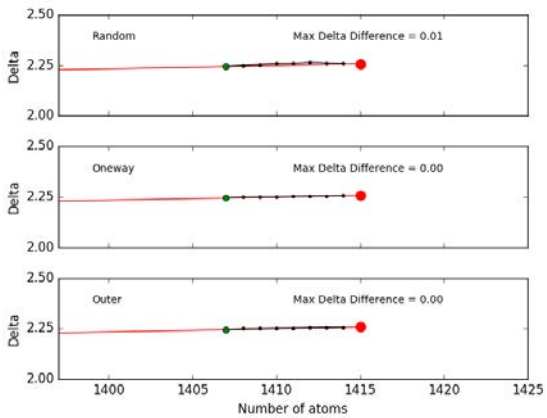

Figure 5.12: Removal of corner atoms from a decahedral (8,8,0) cluster. A smaller max delta difference implies a better, lower energy atom removal order.

5.13, green). The same was done for the (111) facet (Figure 5.13, blue). For the decahedral cluster we started with three clusters, (8,8,0), (7,5,1), and (6,3,2). We then remove the (100) (green), (111) (blue) and the corner atoms (pink) shown in Figure 5.14. The clusters get smaller as atoms are removed from right to left. The large dots are the symmetric clusters, the small dots are asymmetric closed shell clusters, and the shaped line connects the atom removals for each plane, removed in a spiral manner. Atoms from all initially exposed facets of a given type are removed, eventually producing a different symmetric cluster. A linear interpolation of the energy of these clusters is made, shown in Figures 5.13 and 5.14.

Considering first the asymmetric closed shell clusters (large dots on Figures 5.13 and 5.14), the energies of most of these clusters lie reasonably close to the interpolation lines and would thus be approximated moderately well by points evenly spaced between two symmetric clusters, for both the octahedral and the decahedral motifs. There are two notable exceptions. Firstly, the removal of the decahedral (111) facets (Figure 5.14 blue), shows higher energies than the interpolation line due to the exposure of twin boundaries, which are high in energy. This is seen in the figure where the cluster blue line is always above the straight line connecting the two clusters. Removing only some of the (111) facets results in a none symmetrical cluster that is high in energy. Secondly, removal of the (100) facets from the (p,q,0) decahedral clusters results in energies significantly lower than the interpolation line for clusters between the magic number sizes. This is because unfavorable corners of the ino-decahedral are truncated into a more Marks decahedral type corner, and a less balanced cluster. Figure 5.6 demonstrates the atoms that would be removed in removing the (100) planes. However, as these clusters are always high in energy, the poor fit is inconsequential.

The energies of the asymmetric open shell clusters are more complex, as although the energies of the (100) and corner removal mechanisms are approximated reasonably well by the interpolation (green and pink), the interpolation poorly represents the energies of the (111) removal mechanism (blue). To this end, it is only appropriate to use the

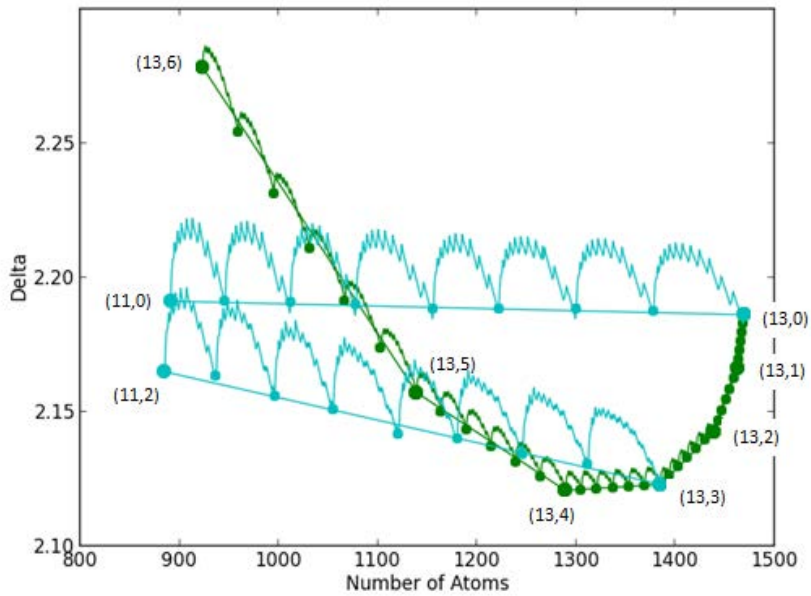

Figure 5.13: A plot showing the energies of clusters generated by removing atoms, and thus planes, from octahedral clusters in the optimal way. Green indicates the energy of the removals from the (100) facets, whilst blue indicates the energy for the (111) removal mechanism.

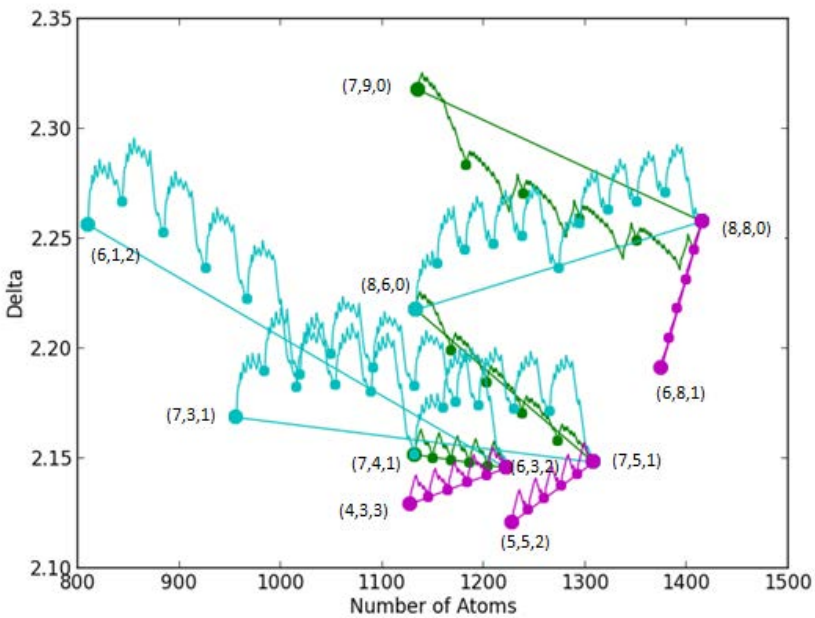

Figure 5.14: A plot showing the energies of clusters generated by removing atoms, and thus planes, from decahedral clusters in the optimal way. Green indicates the energy of the removals from the (100) facets, blue indicates the energy for the (111) removal mechanism and pink indicates the corner removal mechanism.

interpolation for the (100) and corner removal from symmetric clusters.

The ability to use the interpolation scheme to estimate the energies of the asymmetric clusters produced by the (100) and corner removal mechanisms, allows the energies of many more clusters to be included within the motif dominance study. This will allow us to plot a more accurate minimum energy front, and thus produce a more representative colour bar for motif dominance. Asymmetric open shell clusters, where the (111) facets have been removed, are not included in the interpolation, and hence the minimum energy front and colour bar.

To apply the interpolation method to Figure 5.4, a list of relations needed to be derived to correctly connect symmetric clusters, as removal of one plane from one specific symmetric cluster generates a new symmetric cluster with specific indices. For example, removing the (111) facets from a decahedral (5,1,2) cluster produces a (7,1,0) cluster [(p, q, r) goes to ($p+2$, q, $r-2$)] whilst the same removal from a decahedral (5,2,2) results in a cluster defined by (6,1,1) [(p, q, r) goes to ($p+1$, $q-1$, $r-1$)]. In the interest of brevity, not all relations are listed but to eliminate any errors in index matching, many examples were tested for both octahedral and decahedral clusters, before the connections were made.

A secondary use of Figures 5.13 and 5.14 is to identify structural features that yield particularly stable clusters. For the (100) removal mechanism from the octahedral cluster, it can be seen that no truncation of the corner (13,0) is less stable (higher in energy) than any degree of truncation e.g. (13,3) or (13,4). For decahedral clusters, the same can be seen for the re-entrant corner e.g. changing from (8,8,0) to (6,8,1) or from (7,5,1) to (5,5,2) the energy reduces. These types of structure has been seen as a stable structure in previous studies [147]. These are useful to note in order to see if the globally optimised structures examined later show any of these features.

For now, the interpolation is limited to removing a single type of facet of atoms, as well as removing a single external layer from the cluster at a time. Future work with this interpolation method could investigate removing two stacked planes instead of one,

creating greater asymmetry or removing atoms from multiple facets at the same time. Both of these may produce clusters with a lower energy.

Figure 5.15 shows Figure 5.4 with the interpolation scheme, including points for the energies of asymmetric cluster produced using the (111) removal mechanism and lines for energies of asymmetric clusters produced using the (100) and corner removal mechanisms. The colour bar again looks at the most stable structure for each size, taking into account the asymmetric cluster line connections, but excludes the points for the (111) removal. The figure looks similar to Figure 5.4, but the octahedral dominance appears earlier. It also shows a clearer decahedral dominance between 55 and 2,000 atoms, with small pockets of octahedral dominance. The figure also shows a more regular trend in the switching between motif dominance.

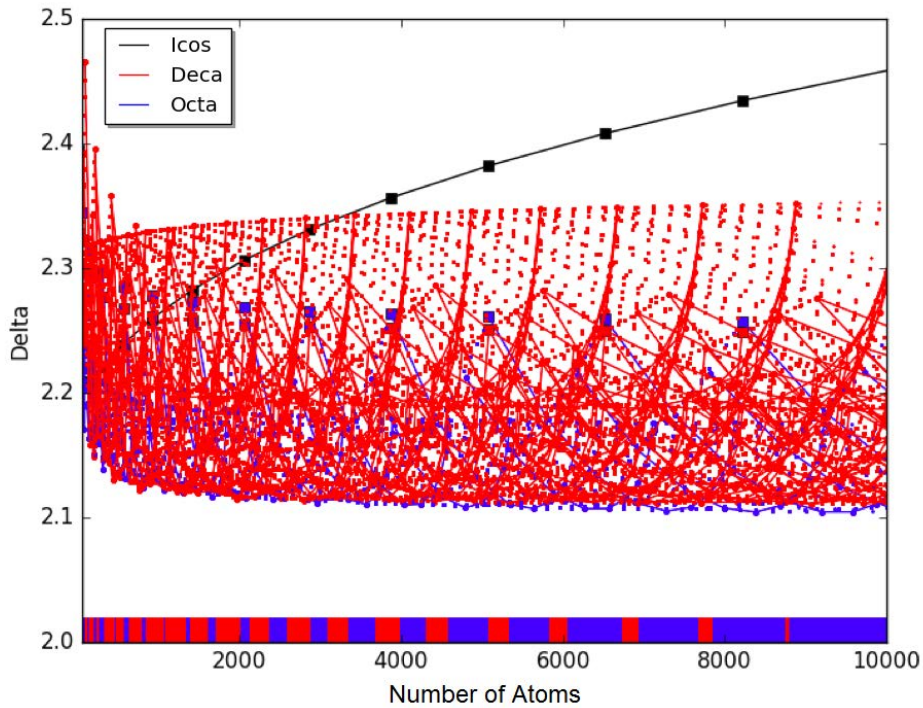

Figure 5.15: Plot of delta values for symmetric and interpolated asymmetric Pt clusters calculated with the Gupta potential for 55 - 10,000 atom clusters. It shows that the icosahedral motif is higher in energy than the decahedral or octahedral motif. The colour bar indicates the most stable motif at each size. Magic number clusters are denoted by large squares.

5.3.3 Influence of the Interaction Potential

To investigate the generality of the interpolation scheme, all steps in the above sections have been repeated using the EMT potential, allowing for comparison with the Gupta potential.

The Gupta potential is a simple model used to simulate FCC metals using the second moment approximation. It is based upon the following functional form [148]:

$$E = A\Big(\sum_j{}' \exp(-2q(R_j - R_0))\Big)^{\frac{1}{2}} - \frac{A}{\sqrt{N}}\frac{q}{p}\Big(\sum_j{}' \exp(-p(R_j - R_0))\Big), \tag{5.3}$$

where N is the number of nearest neighbours, R_j - R_0 is the distance between atom j and the minimum in the interaction potential, whilst p and q describe the short distance repulsive and attractive ranges respectively.

The EMT potential determines the energy of a system by calculating the energy of a known reference system (the effective medium, typically FCC) and applying a small correction to mimic the real system being modelled. The potential has the form [149]:

$$E = \sum_i (E_i(n_i) + \Delta E_{as}(i)), \tag{5.4}$$

where E_i is the energy of the atom embedded within an FCC crystal with electron density n_i, and ΔE_{as} is the atomic sphere correction. This correction is the difference in energy between the real and reference system.

The parameters used for the Gupta potential were p=10.710, q=3.845, a=0.277443, Xi=2.6209 and $r0$=2.77 [167]. For the EMT potential the parameters were $E0$=-5.82286, $S0$=1.55073, $V0$=2.69717, $E2$=2.41957, K=3.86730, L=4.02350 and $n0$=0.05412 [161].

These two potentials were chosen as they have both been carefully parametrised for transition metals and used for clusters [147, 168]. Additionally, the difference in functional forms means that any structural bias can be identified.

Figure 5.16 shows the results obtained for Pt clusters calculated with each potential.

The overall trends were found to be the same, but the absolute energies between the two potentials differ. For this work, identification of the dominant motif within each size range is the overarching concern, thus the relative energies between motifs is key. This absolute energy deviation is due to the differences between the two potential forms. The icosahedral structure is shown by both potentials to be highly unstable at large cluster sizes. The decahedral and octahedral motifs alternate in dominance, with an octahedral dominance at larger sizes, and a decahedral dominance in the smaller size range. The two colour bars, showing the most dominant structure at each size, are also very similar, demonstrating consistency between the potentials. There is slight variation in the size of the decahedral dominance windows, with the Gupta potential showing slightly larger decahedral dominance windows. The differences in the results from these two potentials are minimal, and the success is that they both show the same trends. There are no studies that conclusively show that one potential is better than the other, and thus both are used in conjunction to check consistency. Being that the differences between the two potentials is very small it is impossible to say which would fit the experimental data better.

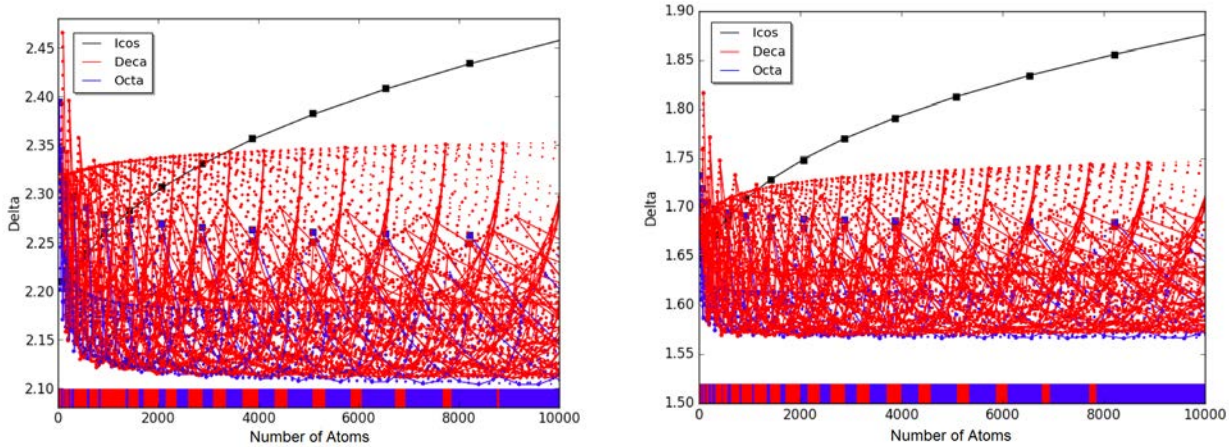

(a) Gupta (b) EMT

Figure 5.16: Comparison of motif dominance for Pt clusters as calculated using the Gupta and EMT potentials for 55 - 10,000 atoms. Red is decahedral, blue is octahedral and black is icosahedral. The colour bar indicates which motif is most stable at each size. Magic number clusters are denoted by large squares.

5.4 Explicit Modelling of Magic Number Clusters

To investigate the magic number sized structures in more detail, focus is placed upon the 55, 147, and 309 atom clusters. A global optimisation algorithm will be utilised to identify, for each size, low energy structures with the aim of identifying the most stable structure. The interpolation method, developed in Section 5.3, will be used to generate the clusters from which to initiate the global optimisation algorithm. Clusters within a 2% size range will be used to replicate experimental precision, thus for 147 atoms clusters of 144 - 150 atoms will be studied. Global optimisation is often performed for small nanoclusters (typically 10 - 150 atoms), as they are small enough systems to be modelled [25, 79]. In principle, the lowest energy structure should be able to be located from a number of unique stating guesses, however, even the clusters considered here have a very complex PES so we introduce a large number of starting guesses to obtain a confident estimate of the most stable cluster for each motif. The 309 atom clusters are classed as large clusters for global optimisation, thus there is a limit to the PES that can be studied. Even with many starting guesses, it is not always possible to identify the absolute lowest energy cluster for each motif.

5.4.1 The Global Optimisation Problem

To find the lowest energy structure, we need to examine the PES associated with each cluster. Each cluster size has a unique PES that is made up of peaks (maximum energy areas) and troughs (minimum energy areas). The troughs, known as minima, may appear in groups on the PES, forming funnels which are areas with many similar minima. The art of finding the lowest minima upon the PES is known as global optimisation. For clusters of hundreds of atoms it is computationally very difficult, so many types of optimisation algorithms exist. It is impossible to visit all minima on a PES, so the optimisation methods aim to maximise the probability of finding the global minimum, whist using the

smallest amount of computing resources. Once a minima has been reached, a decision as to whether this minima is the global minimum has to be made. It is impossible to know if the minima found is the global minimum of the system; it can only be compared with previously found minima. Each time the optimisation is run it may find different minima, due to the statistical nature of the methods.

For clusters, there are a number of common global optimisation methods, including basin hopping, simulated annealing, and genetic algorithms. These are all discussed with specific reference to clusters in Section 5.4.2. For the clusters investigated in this thesis, a new algorithm will be used, called Global Optimisation Using Saddle Traversals (GOUST), developed by A. Pedersen and H. Jonsson [164, 165], and implemented through the EON software.

5.4.2 Global Optimisation Methods for Clusters

For clusters in the size region of interest within this work, the PES tends to be very detailed with many minima. For example, for a cluster of 147 atoms there are in the order of 10^{60} minima [169, 170]. The minima tend to cluster on the PES as funnels, as variations based upon each motif. This can lead to optimisations becoming 'stuck' in a single motif funnel, or allow the optimisation to totally skip past a motif. This means that some optimisation methods are better suited to this style of problem than others. For clusters, basin hopping, simulated annealing, and genetic algorithms are often used [171].

Basin hopping [170, 134, 172] is a method of optimisation that involves passing from one minimum to another minimum that is expected to be lower. It is done by deforming the PES to form an approximation that is easier to identify a minimum from. A local minimisation is performed after each step to identify low energy structures. This is shown in Figure 5.17. This optimisation method is good for investigating the more immediate PES, but it is difficult to induce a large structural change, which may be necessary for clusters to swap between motifs.

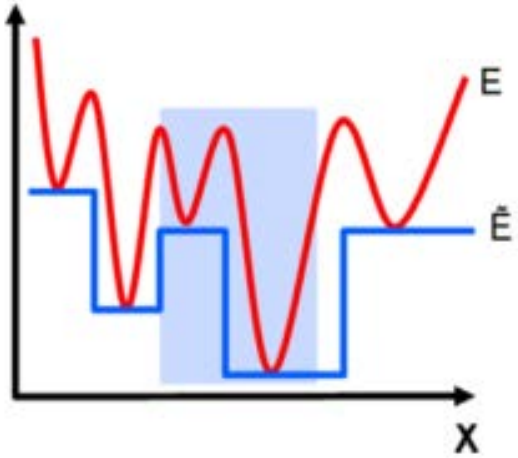

Figure 5.17: An example of the basin hopping algorithm that smooths the PES. The initial PES is shown with a red line, and the final is shown by the blue. Reproduced from [172].

Simulated annealing [173, 174] is a method of increasing the energy of the system in order to change and smooth the PES. This makes it easier to find minima, which when cooled, theoretically fall to low minima. This has the advantage of being reasonably easy to do, but does cause searches to become stuck in minima that are preferential at higher temperatures. It is not guaranteed that minima at high temperatures fall to minima at low temperatures. The lowering of the energy of the system has to be performed slowly to reduce the probability of it becoming stuck in a high energy minima, thus this algorithm requires very long simulation times.

Genetic algorithms [150, 172, 25] are a method of taking two structures that have 'good' characteristics (low energy in the case of finding the most stable cluster) and 'mating' them to form a new cluster with, in theory, even better characteristics (lower energy). This is typically combined with local minimisation to find low energy structures. This method would increase the chance of generating clusters with very varied structures. This algorithm can easily move between funnels, but does not study the local minima particularly well. It is highly dependent upon the initial structures 'mated'. In addition to low energy, further definitions of good characteristics for clusters could be the size of

truncation, and the completeness of facets, however if two very different structures were mated, e.g. an octahedral and an icosahedral, the final structure is likely to be very high in energy and very unstable. Genetic algorithms can be computationally intensive and time consuming, as the number of possible mating combinations is very large, thus only some mates are made, but is comparable in efficiency to basin hopping when both are coupled with local minimisation.

We have chosen to use the GOUST algorithm as it has all the benefits of basin hopping, as it chooses moves based upon low minima, but locates these minima by finding saddle points. This has been shown to enable multiple atom transitions, dramatically changing the structure and thus motif of a cluster. This helps to prevent the optimisation becoming stuck in a single funnel or motif [175].

5.4.3 GOUST Algorithm

The GOUST algorithm is based on an Adaptive Kinetic Monte Carlo (AKMC) algorithm, with a few variations to favour finding minima for clusters. In AKMC, saddle points are located on the fly, and from these nearby minima can be reached. A key feature of GOUST is that although the saddle points are used to explore the PES, new minima are selected based upon the system energy of the minima, without the energy of the saddle point being used. For global optimisation with GOUST, there are a number of parameters that can be varied, detailed later in this section. Each optimisation procedure for a cluster takes many hours (on current high performance desktop computers), so optimizing the parameters and reducing the number of repeats is key to generating the maximum amount of useful data with limited resources.

The first step of the GOUST algorithm is to randomly displace the system from the minimum. This is done by sampling a displacement value from a Gaussian distribution, the standard deviation of which is specified by an input parameter. The larger the displacement value, the further from the current minima the optimisation starts, thus the

greater the chance of leaving the current minimum or funnel. This input parameter is hence forth refereed to as the 'kick'. A kick of 0.15 is taken as the default value, and tends to favour local investigation of the PES. For this work, additional values of 1.00 and 1.50 were used to encourage funnel hopping and major structural changes.

Once the displacement has been generated, the program starts saddle searching. This is where it 'climbs' to the saddle point and investigates reachable minima from the saddle. The program performs four saddle searches before choosing which minima to proceed to. The choice of minima to proceed to is selected based upon the relative energies of the minima. If the new minimum is lower in energy than the system minimum it is chosen. If all minima are higher in energy than the system, it moves on with a probability based upon Boltzmann statistics. This is the main difference between GOUST and AKMC, as AKMC would use a low saddle point as the driving force for moving, rather than minimum comparisons.

The Boltzmann statistics lead to an important feature implemented within GOUST: The algorithm has the ability to remain in a funnel when few minima have been found, but it is encouraged to move to a new funnel when many minima in the funnel have been explored. This is done by incorporating a 'fill' factor which modifies the probability of moving to a new area. This is a ratio based on the current minimum value and the lowest one already found in the funnel. The larger the difference, the larger the fill factor. This means that there is a higher the probability exploring a different funnel, as most minima within the current funnel will have already been explored. When the difference is low, or the new minimum is below a previously found minimum, the ratio favours remaining in the funnel, as more low lying minima can probably be found.

As mentioned previously, the cluster sizes investigated here are large, thus full global optimisation is difficult. As such, to further improve the GOUST algorithm and explore more of the PES, the interpolation scheme will be used to generate a wide selection of predicted low lying structures. These will be used as starting guesses for the algorithm to explore from. This will give the GOUST algorithm the best chance of minimising at least

one of the structures to the lowest energy structure. The main concern with this is the possibility of using two starting guesses that are structurally very similar. To reduce the occurrence of these, the local minimisation energies can be used to identify any clusters with very similar energies, those which may have very similar structures, always leaving the lower of the two options. However, caution has to be exercised, with each removal manually checked, as octahedral and decahedral clusters can show very similar energies whilst still having very unique structures. The starting guesses also allow us to investigate each motif separately.

5.4.4 Generation of the Low Energy Starting Guesses

To generate the initial starting guesses for the GOUST algorithm, the interpolation method detailed in Section 5.3.2 is used. For each size, possible asymmetric clusters are first identified by the interpolation scheme. For example, for a given size there may exist a (100) removal line connecting a larger and smaller symmetric cluster. The clusters at each size upon this line are then explicitly constructed, using the optimal order of atom and plane removal as identified in Section 5.3.2. A local minimisation is then performed. This allows us to generate structures across all sizes within the 2% size ranges which are likely to have a low energy.

Figure 5.18 shows the interpolation lines, with (100) removals as solid lines and the (111) removal as dotted lines. The value of Δ from the local minimisation has been overlaid. The figures show that the interpolation method estimates the (100) removal very well (panels A, C, and E), as the dots lie close to the lines. It is not as accurate for the (111) and corner removal mechanisms seen in panels B, D, and F, in accordance with Section 5.3.2. To maximise the chances of finding the global minimum for each size, all of the interpolation lines will be used to generate the starting guesses, independent of how close the interpolation and minimisation energies are.

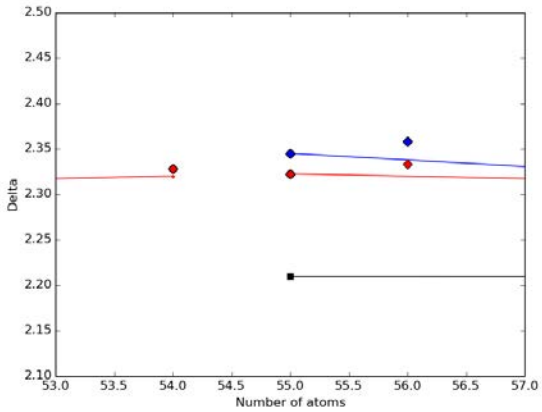

(A) (100) plane removal for 55 Pt atoms

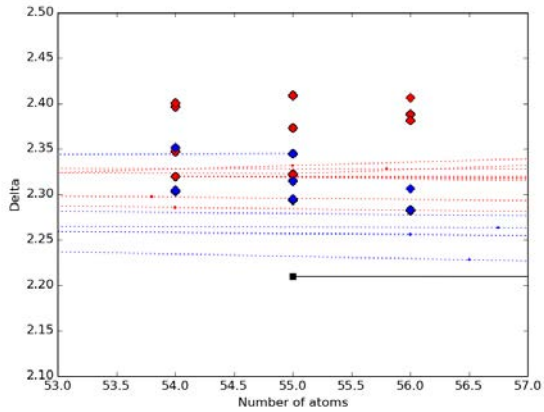

(B) (111) plane removal for 55 Pt atoms

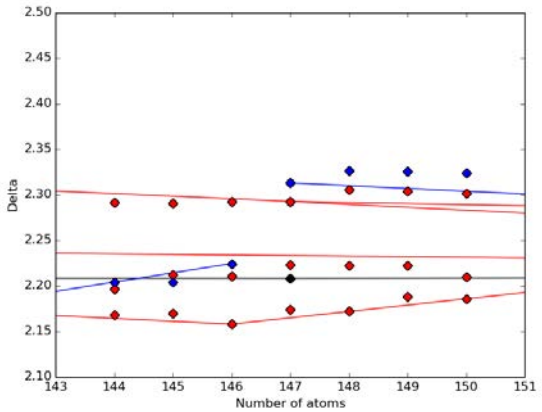

(C) (100) plane removal for 147 Pt atoms

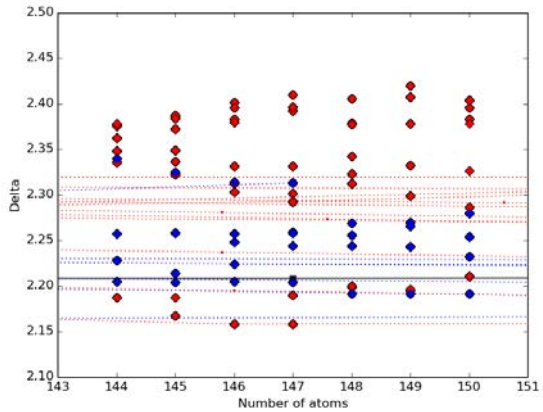

(D) (111) plane removal for 147 Pt atoms

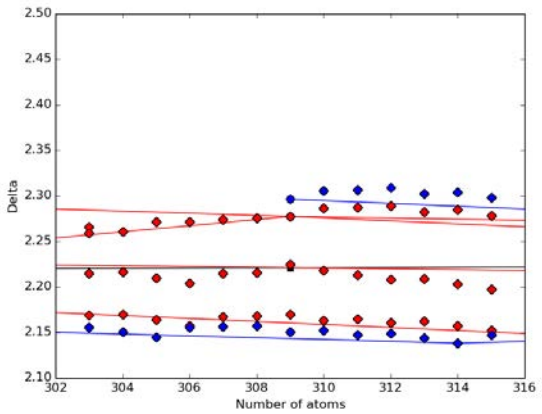

(E) (100) plane removal for 309 Pt atoms

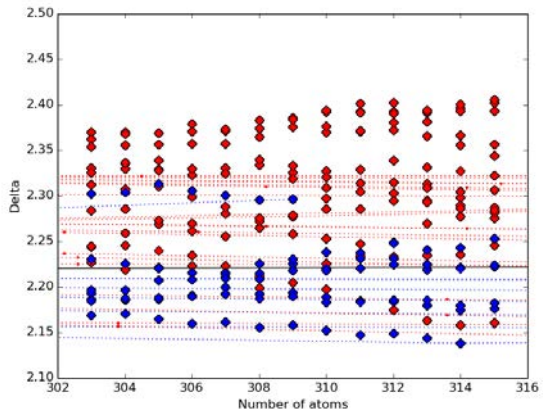

(F) (111) plane removal for 309 Pt atoms

Figure 5.18: These graphs show zoomed versions' of Figure 5.15 in the regions of 54 - 56, 144 - 150 and 303 - 315 atoms. Figures on the left-hand side show the (100) removals with solid lines, whilst figures on the right-hand side show the (111) and corner removal mechanisms with dotted lines. The lines (solid or dotted) show the predicted Δ from the interpolation scheme, whilst the solid circles show the Δ from local minimisation. Red denotes decahedral clusters, whilst blue denotes octahedral clusters. The black lines are the icosahedral motif for reference.

5.4.5 GOUST Results

For small clusters, it is possible to use all of the starting guesses, generated by the interpolation method, for the global optimisation simulations. Therefore, for 54, 55, and 56 atom clusters all of the starting guesses will be optimised. For these sizes there were eight starting guesses. Due to the computing time taken to calculate larger clusters, it is not feasible to run the global optimisations for all starting guess clusters because there are more guesses and each simulation is much slower. For the magic number sizes, 147 and 309, all of the possible starting guesses will be used, but for the 2% size ranges, 144 - 146, 148 - 150, 303 - 308, and 310 - 315 atoms, only some of the starting guesses will be used. The ones chosen will be those with the lowest energy, as obtained from the local optimisation, described in further detail below.

55 Atom Clusters

To investigate the structural dominance near 55 atoms, 54, 55, and 56 atom clusters were optimised with the GOUST algorithm. This represents the 2% size range for a cluster with 55 atoms. Initially, the focus is on the magic number sized cluster with 55 atoms.

For the 55 atom clusters, eight starting guesses were used, with kicks of 0.15, 1.00 and 1.50, for each. Figure 5.19 shows the initial (crossed) and final (circle) energy of each of the starting clusters, where the initial energy is from the local minimisation, and the final energy is obtained from GOUST. Red crosses are decahedral starting clusters, and blue crosses are octahedral. The black dots are final states that are icosahedral in structure, whilst the green dots are assigned to clusters significantly higher in energy than the global minimum, investigated further in Figure 5.21. 0 eV has been set as the energy of the lowest state found. The clusters in each panel have been ordered from left to right with increasing initial energy. It can be seen that for almost all starting guesses and kicks the same structure has been found, thus this indicates that a successful global optimisation has been performed. Figure 5.20 shows the lowest energy structure found,

at two different rotations. It is a structure similar to the typical icosahedral cluster.

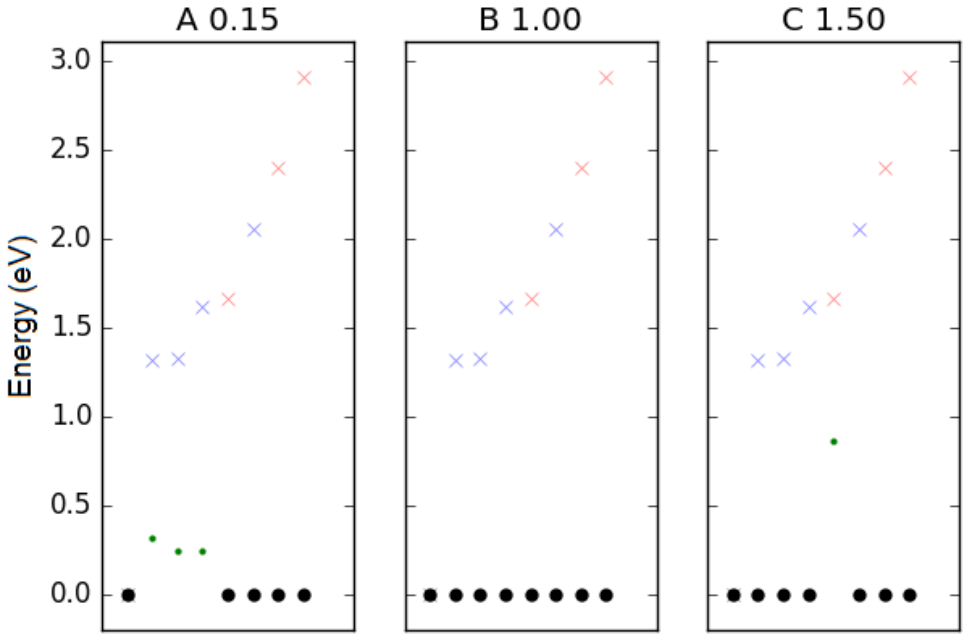

Figure 5.19: Initial (crosses) to final (dots) energies of the 55 atom clusters with each kick size. Red is decahedral, blue is octahedral, and black is icosahedral. Green dots show high energy final states.

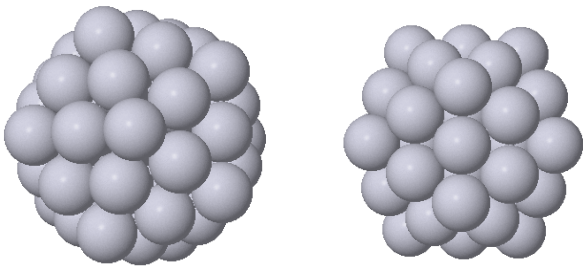

Figure 5.20: Two rotations of the lowest globally optimised energy structure found for 55 atoms.

To investigate other structures which have low energies, but are not the absolute lowest energy structure, all data produced during the global optimisations can be analysed. Taking all kicks, and all states for all of the starting clusters, the clusters with energies up to 0.5 eV are analysed. These are shown in Figure 5.21, and include the structures of the green dots seen in Figure 5.19. After the icosahedral structure, a decahedral structure is

next lowest (0.25 eV higher) in energy. This decahedral, and the most stable octahedral cluster (0.32 eV), give some indication of structural features that are more sable. For the decahedral (0.25 eV) cluster, the facets are complete. The octahedral (0.32 eV) cluster also shows complete facets, with some of them being truncated. These are used for the QSTEM simulations seen in Section 4.3.3. The higher energy icosahedral structures seen in Figure 5.21 are non-standard structures (e.g. the 0.49 eV cluster is a standard icosahedral motif with an atom missing from the centre and placed externally).

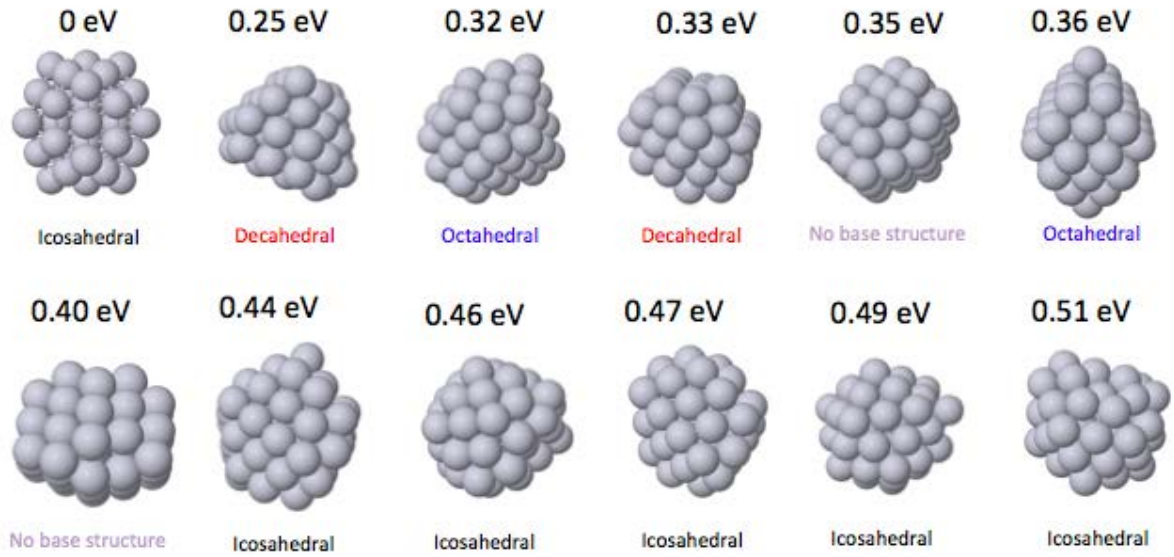

Figure 5.21: Low energy clusters found during global optimisation for 55 atoms. They have been categorised, by visual inspection, based upon the base shape of the structure. No base structure means that the structure does not fit in either the decahedral, octahedral, or icosahedral motif.

Figures 5.22 and 5.23 show the lowest energy structures seen for 54 and 56 atoms respectively. For 54 atoms, the lowest structure has an icosahedral motif with the central atom missing, which has been seen in previous studies [132]. The decahedral structure seen is based upon the decahedral seen for 55 atoms. For 56 atoms, the icosahedral motif becomes unstable, as a single atom added to the 55 atom icosahedral would make it particularly high in energy. The lowest energy icosahedral for 56 atoms is at 0.22 eV which is an approximately half of an icosahedron with an additional shell. The lowest structure seen is the decahedral motif common across all of the cluster sizes.

This analysis of the motif dominance at each size shows that different structures can be dominant within a very small size range. For 54 and 55, the icosahedral motif is expected, whilst for 56 atoms the decahedral motif is energetically most stable. Another key result is that the lowest decahedral and octahedral motif for 54, 55, and 56 atoms are very close in energy, thus almost equally stable. This fits very well with the motif switching seen in the earlier results.

147 and 309 Atom Clusters

For 147 and 309 atom clusters, including the 2% ranges, it is impractical to use all of the starting guesses as the computation time is too high. To further reduce the computation time, it is also practical to limit the number of kicks. The test case for this will be the 147 atom clusters: All starting guesses and kicks will be investigated for this data set, but all subsequent data will be limited in terms of starting guesses and kick sizes.

The three kicks used are the same as for 55 atom clusters, 0.15, 1.00, and 1.50. The results for 147 atom clusters are shown in Figure 5.24 where initial energies, from local minimisation (crosses), are refined to a final energy obtained from GOUST (solid). The initial starting guess clusters were 9 decahedral, 5 octahedral, and 1 icosahedral clusters. The filled shapes are the final energies, with red being decahedral, blue being octahedral, and black being icosahedral. The shape gives the specific structure which is visualised in Figure 5.25. The green dots are cluster with energy of more than 1 eV above the lowest energy cluster. The first point to note is that the lowest energy cluster is only located in 11 of the 39 GOUST runs. This indicates that the algorithm is not performing as well for these larger clusters when compared with the 55 atom clusters. Additionally in the majority of cases, the initial structure of the clusters are preserved, indicating that the GOUST algorithm does not enable hoping between motif funnels. It can also be seen that the final energies are always equal to, or lower than, the initial energy, indicating favourable refinements to the structure which have been made using GOUST. There also appears to be some success in identifying the lowest energy structure for each motif. With

the decahedral motif the lowest energy structure was found 11 out of 22 runs, whilst within the octahedral motif the lowest energy structure was found 4 out of 9 times. The three kicks are large enough to explore the funnel of the starting motif, but are not large enough to climb into a funnel of another motif on the PES.

The structure of the low energy 147 atom clusters are shown in Figure 5.25, categorised by motif where small variations in each motif are classed as a single structure. The lowest energy shape found is the decahedral D1, thus all energies are normalised to this cluster. The decahedral clusters, D1 to D4, are all based upon the (3,2,1) cluster with varying numbers of external atoms moved. D5 is a taller cluster loosely based upon the (2,4,1) cluster, with a closed shell as all facets are complete. For the octahedral clusters, the O1 structures are the typical octahedral motif, but have some planes displaced with respect to the standard positioning. O2 and O3 are the standard octahedral clusters with varying truncations, with O2 having larger truncations, sometimes accompanied by missing atoms. The only icosahedral structure present is the standard 147 atom icosahedral, I1.

These results can be compared with the results seen for the 54, 55, and 56 atom clusters. It is clear that the icosahedral dominance for 54 and 55 atoms is not seen for 147 atoms as the icosahedral cluster is high in energy. This agrees with previous results that show that the icosahedral motif is only favoured at small sizes. In terms of decahedral motif, complete facets are less preferential for the 147 atom clusters, but a rentrant corner of 1 atom occurs frequently. For the octahedral clusters complete facets are a still preferable.

Using the results for the 147 atom clusters, areas for computational time savings can be identified: Reducing the number of kicks calculated, or reducing the number of starting structures used. Firstly, considering the kick size, the 0.15 kick is classed as the standard kick size, used to study the more immediate PES, so a choice between the 1.00 and 1.50 kicks has to be made. Both of the kicks find the lowest energy for decahedral, octahedral, and icosahedral (filled circles), but the 1.00 kick finds more distinct structures than the 1.50 kick (7 compared with 5), so it is sensible to take the 0.15 and 1.00 kick for future

calculations.

To further reduce the number of calculations, the higher energy starting clusters can be removed, e.g. optimising only the lowest 3 or 4 decahedral and octahedral clusters would reduce the number of starting guesses by approximately 50%. A choice between 3 and 4 starting guess can be made based upon the starting energies for each cluster size, maximising the chance of finding the ground state. When the third and fourth decahedral or octahedral clusters are very similar in energy, both will be used for global optimisation.

For all further calculations, only the 0.15 and 1.00 kick sizes, and the 3 or 4 lowest energy starting guesses will be used to reduce the computational cost. The results for the 144 - 150 and 303 - 315 atom clusters are discussed within the rest of this section.

To investigate the 144 - 150 range, 3 or 4 starting structures for both the decahedral and octahedral motif at each size have been taken and optimised using GOUST. The results are shown in Figures 5.26 and 5.27. These each show the initial (crosses) to final (circles) energy of the clusters. The images below each figure are the structures of the low energy clusters, with the top row being decahedral, the second octahedral, and the third icosahedral (only applicable for 146 and 147 atoms). This allows for comparison of the structure types across the size range.

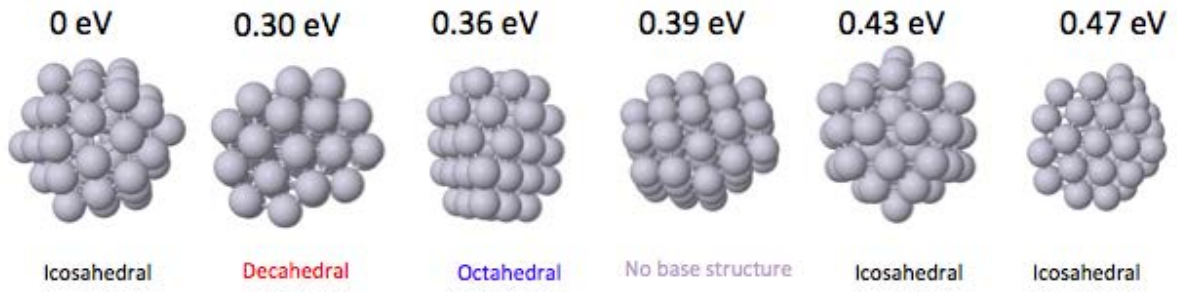

Figure 5.22: Low energy clusters found during global optimisation for 54 atoms. They have been categorised, with visual inspection, based upon the base shape of the structure. No base structure means that the structure does not fit in either the decahedral, octahedral, or icosahedral motif.

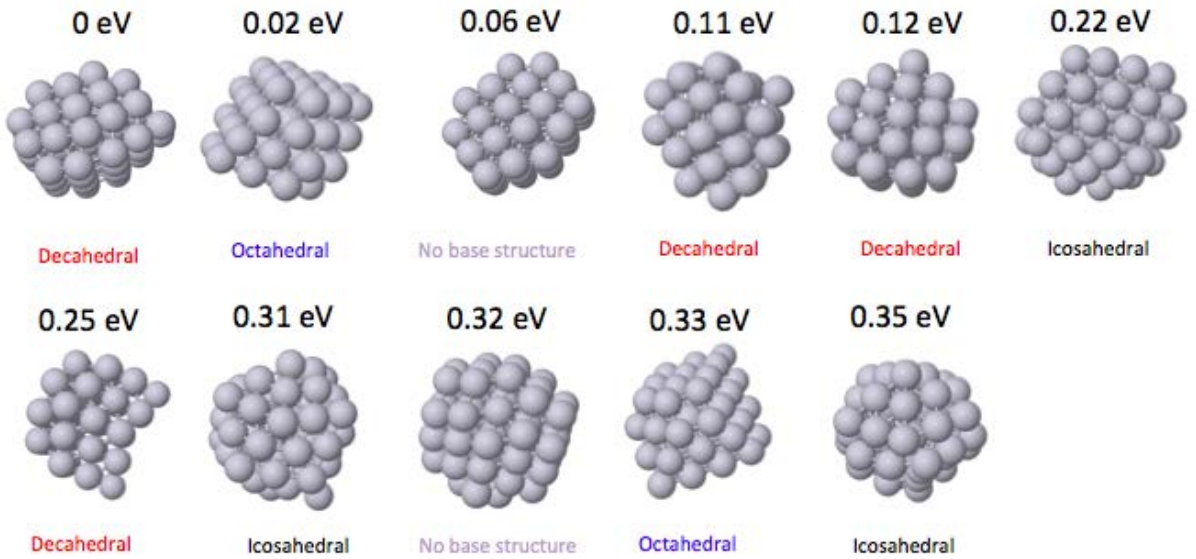

Figure 5.23: Low energy clusters found during global optimisation for 56 atoms. They have been categorised, with visual inspection, based upon the base shape of the structure. No base structure means that the structure does not fit in either the decahedral, octahedral, or icosahedral motif.

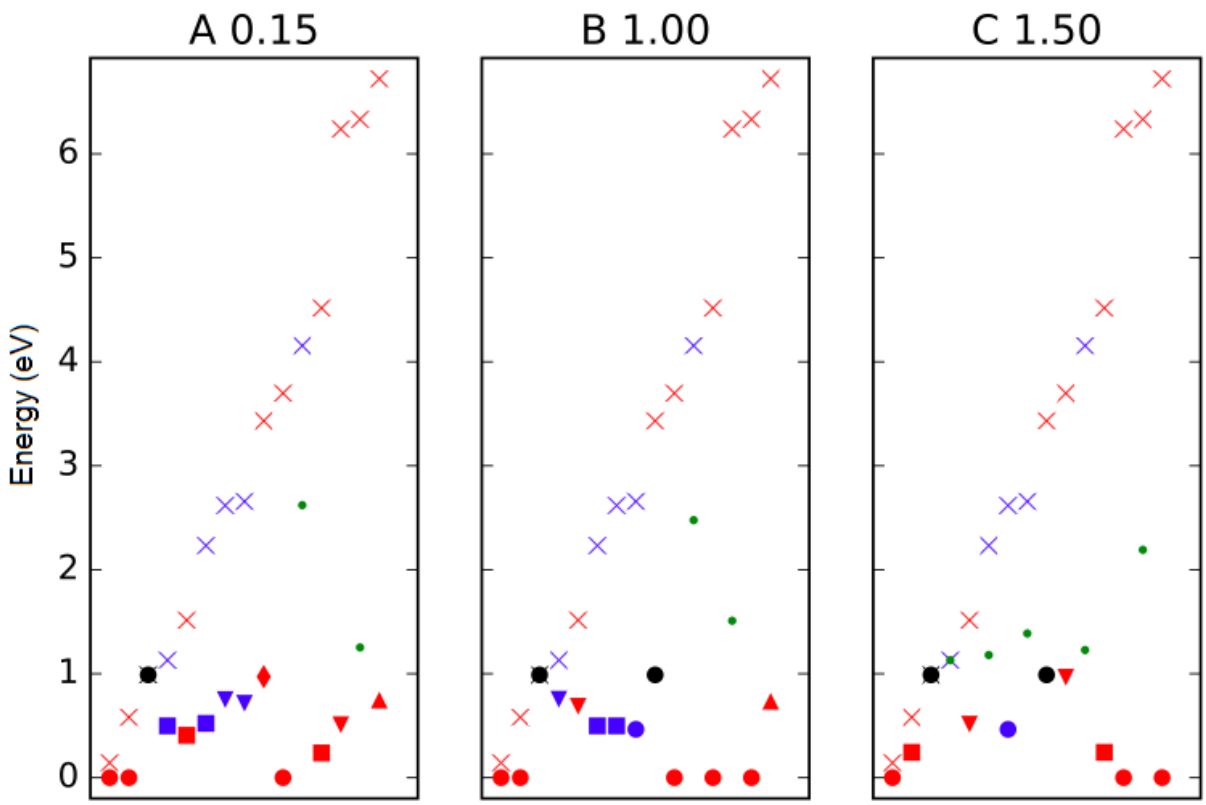

Figure 5.24: Initial (crosses) to final (filled shapes) energies of the 147 atom clusters with kicks of 0.15 (A), 1.00 (B), and 1.50 (C). Red is decahedral, blue is octahedral, and black is icosahedral. The various shapes are used to identify the different styles of each motif, explained in Figure 5.25. Green dots show high energy final states; those more than 1 eV above the ground state.

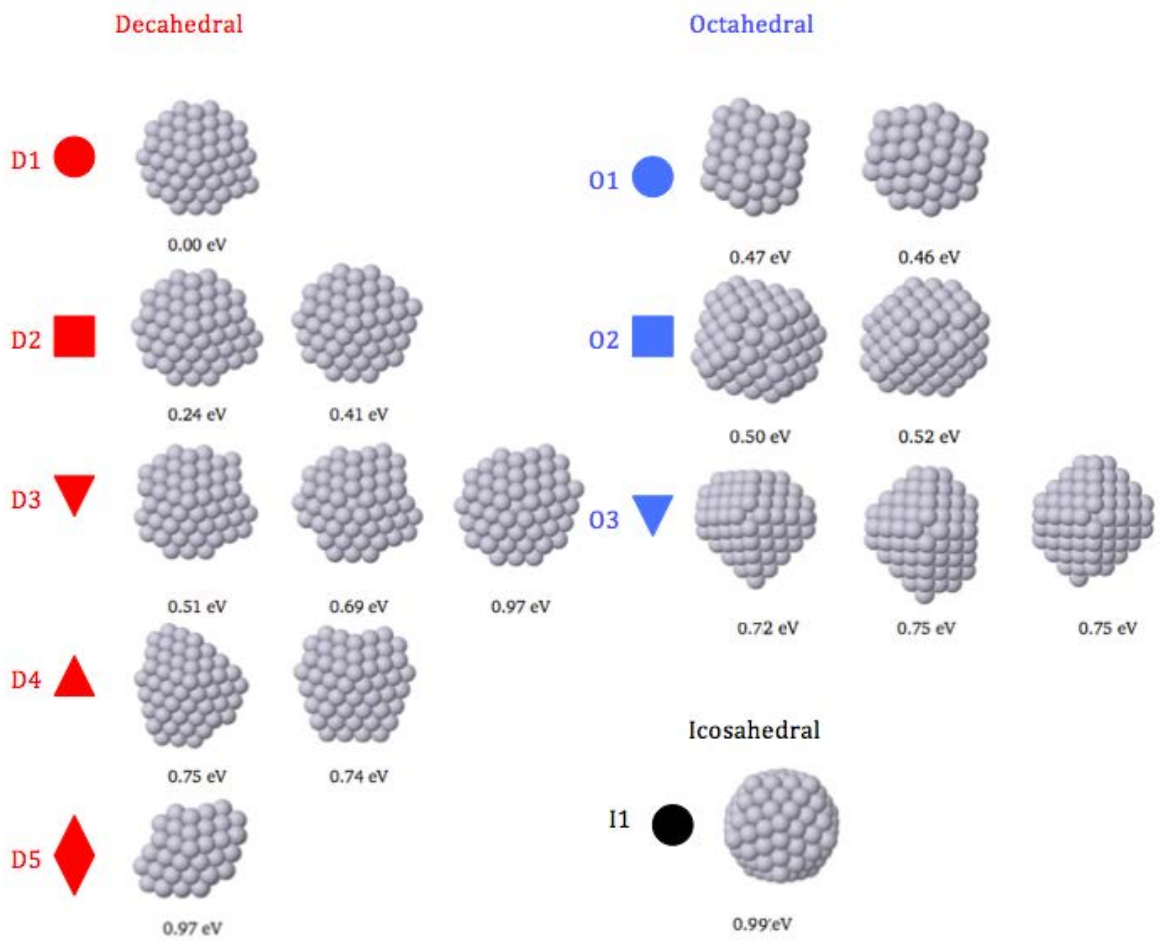

Figure 5.25: Schematic showing the variation between final energy structures, grouped by similarities. 0 eV is set to be the lowest structure, D1.

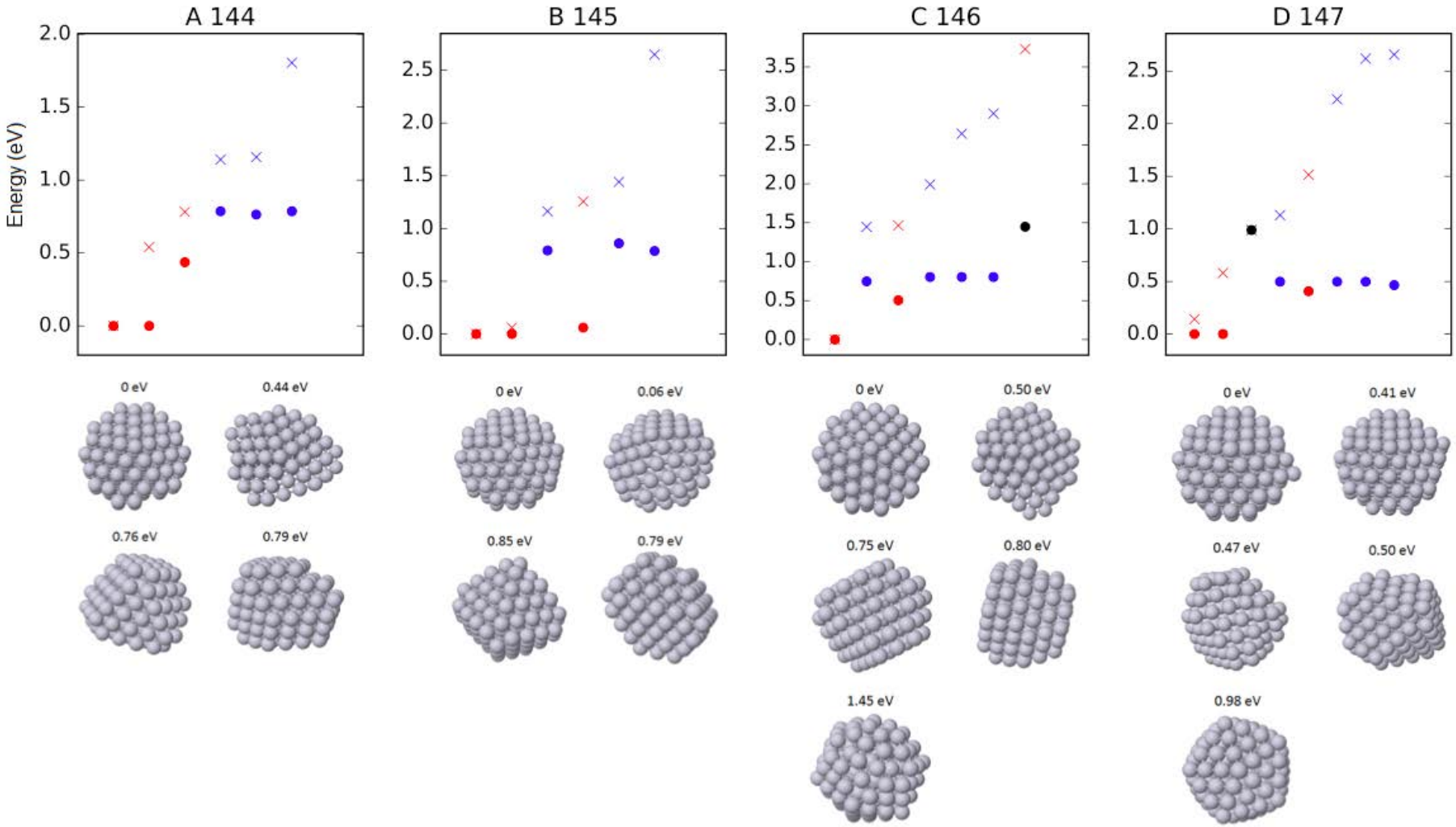

Figure 5.26: The upper part of the figure shows the initial (crosses) and final (solid circles) energies for each cluster size between 144 and 147 atoms. Red is decahedral, blue is octahedral, and black is icosahedral. The images below each graph show the unique structures generated. The energy in eV is in comparison to the lowest minima found for each size.

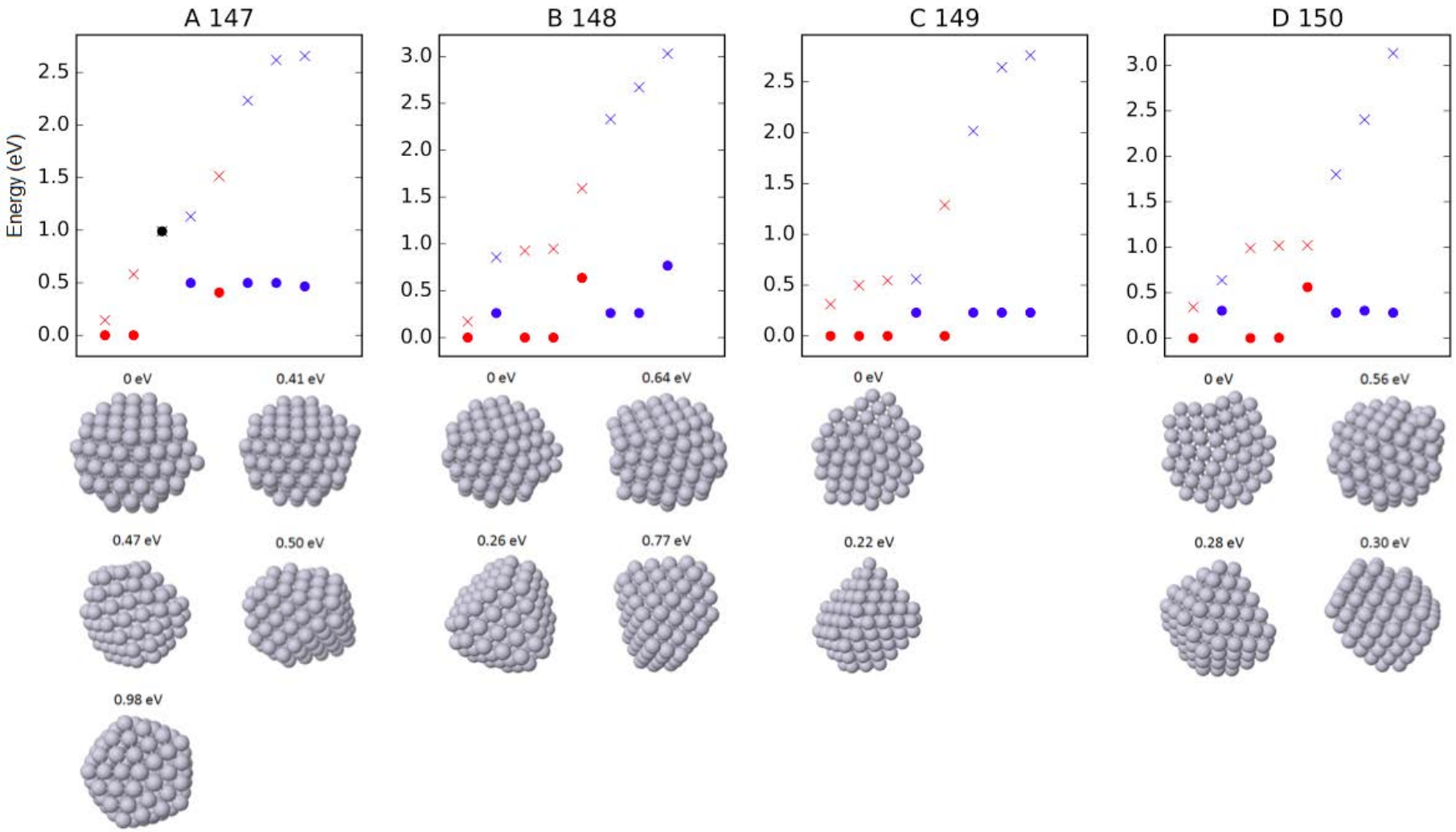

Figure 5.27: The upper part of the figure shows the initial (crosses) and final (solid circles) energies for each cluster size between 147 and 150 atoms. Red is decahedral, blue is octahedral, and black is icosahedral. The images below each graph show the unique structures generated. The energy in eV is in comparison to the lowest minima found for each size.

Looking at the structures found, the decahedral structure based upon the (3,2,1) decahedron is in all cases most stable. It is a perfect structure at 146 atoms, thus smaller sizes lose atoms, either from the edge or the vertex where (111) planes meet. For sizes larger than 146 atoms the decahedral (3,2,1) is seen with extra atoms either on the (100) facet or at corner sites, preventing some re-entrant corners.

For octahedral clusters, the structures found have mostly complete facets and tend towards spherical clusters. The majority of clusters also show large truncations at the corners, with the only exception being the octahedral seen at 149 atoms.

The icosahedral structure seen in at 147 atoms is the standard structure, and for 146 atoms the outer most shell is missing an atom, which has allowed for a small rearrangement of the surface.

For the 309 data, a similar procedure was used as for the 147 Pt atom data. Initially the clusters within the 309 atom bracket (303 - 315) were built from the interpolation scheme. This generated a selection of structures that were all locally minimised. For 309 Pt atoms only, all of the structures found from the interpolation scheme were optimised using GOUST. The lowest few (minimum of 3) for each of the decahedral and octahedral structures were optimised using GOUST for the 303 - 308 and 310 - 315 Pt atom ranges. For all clusters within the 309 bracket, the 0.15 and the 1.00 kick were used, with the lowest energy structure generated from these two kicks displayed.

The results for all of the starting guesses for 309 atoms are shown in Figure 5.28. It shows consistency with the 147 results that all of the final globally optimised energies are equal to or smaller than the initial local minimisation energies, thus the clusters have rearranged to new, more stable, configurations. This figure also helps to justify again only using a few of the lowest locally minimised clusters, as the lowest decahedral and octahedral structure found are generated from low energy locally minimised structures. The clusters that have a high locally minimised energy tend to fall to higher globally minimised energies. It is difficult to know whether the global optimised has been found for these clusters as although they all fall to a lower energy structure, the lowest energy

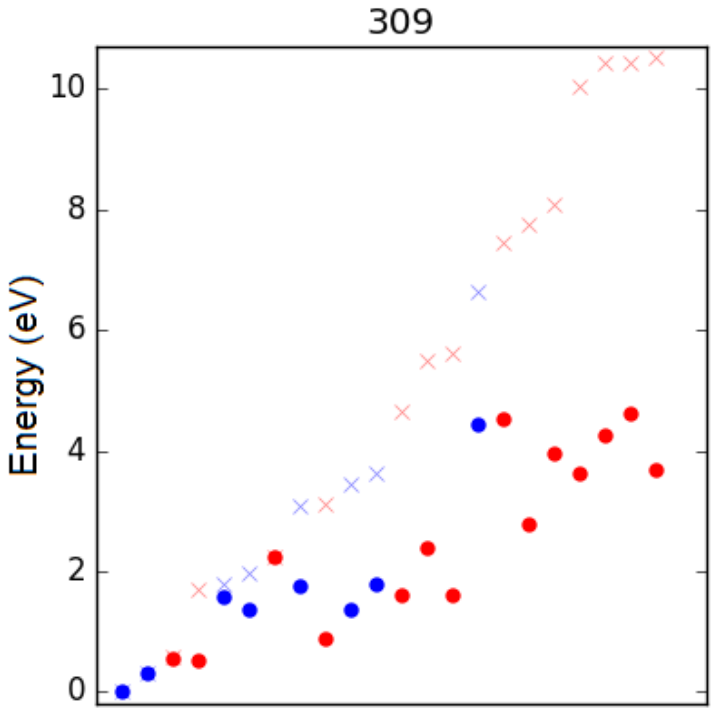

Figure 5.28: This figure shows the initial (crosses) and final (solid circles) energies for each cluster with 309 Pt atoms. Red indicates the decahedral motif, whilst blue indicates the octahedral motif.

structure observed only occurs once, for both the octahedral and decahedral motif. This is unsurprising as the 309 atom clusters are very large for global optimisation calculations. The lowest motif found for 309 Pt atom clusters is an octahedral structure, shown in Figure 5.34.

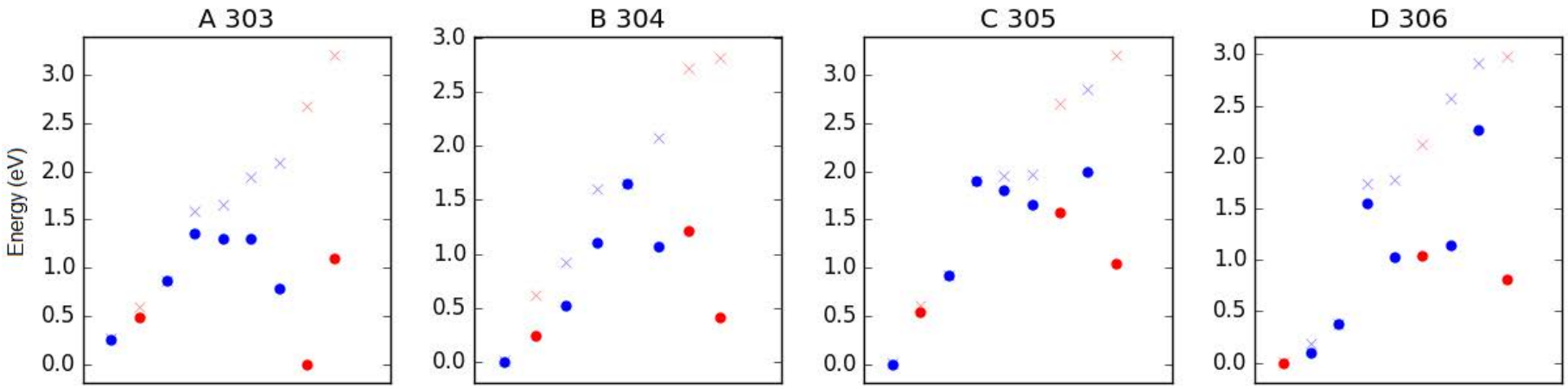

Figure 5.29: These figures show the initial (crosses) and final (solid circles) energies for each cluster size between 303 and 306 atoms. The energy in eV is in comparison to the lowest minima found for each size. Red indicates the decahedral motif, whilst blue indicates the octahedral motif.

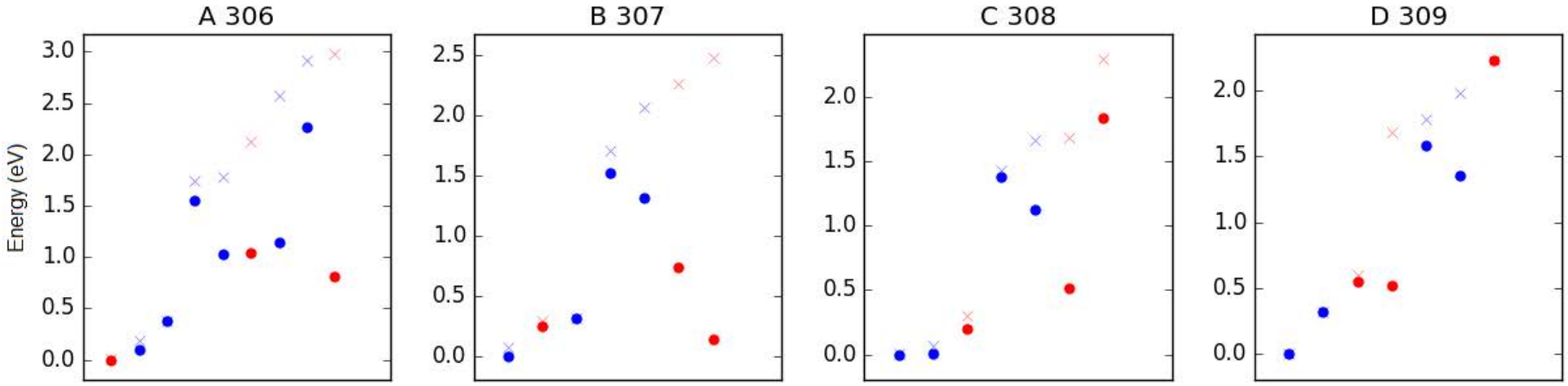

Figure 5.30: These figures show the initial (crosses) and final (solid circles) energies for each cluster size between 306 and 309 atoms. The energy in eV is in comparison to the lowest minima found for each size. Red indicates the decahedral motif, whilst blue indicates the octahedral motif.

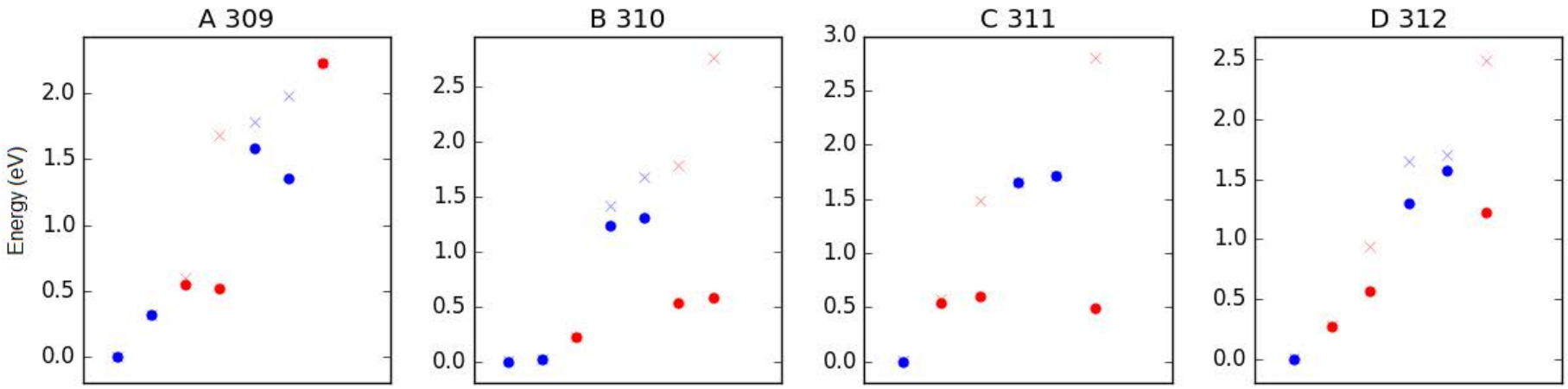

Figure 5.31: These figures show the initial (crosses) and final (solid circles) energies for each cluster size between 309 and 312 atoms. The energy in eV is in comparison to the lowest minima found for each size. Red indicates the decahedral motif, whilst blue indicates the octahedral motif.

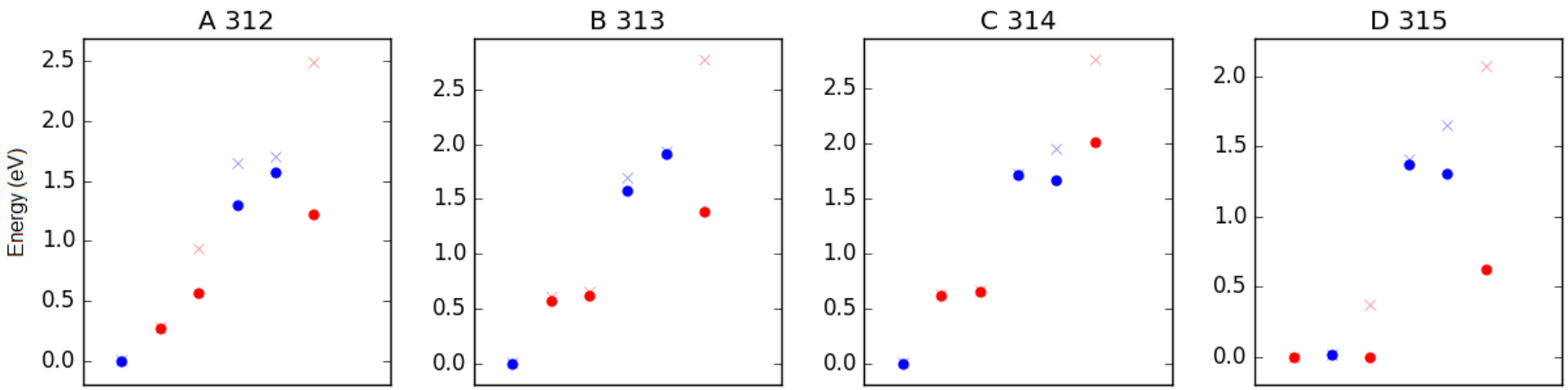

Figure 5.32: These figures show the initial (crosses) and final (solid circles) energies for each cluster size between 312 and 315 atoms. The energy in eV is in comparison to the lowest minima found for each size. Red indicates the decahedral motif, whilst blue indicates the octahedral motif.

The results in Figures 5.29, 5.30, 5.31, and 5.32 show that the final energy calculated by global optimisation is always lower than or equal to the local minimisation for each of the starting guess clusters. They also show that for the octahedral clusters, the lowest locally minimised structure always falls to the lowest globally optimised structure. For the decahedral clusters this happens 9 times out of the 13 sizes studied. There is switching in dominance between the octahedral and the decahedral motif, with the octahedral motif being dominant in at 10 sizes and decahedral at 3 sizes (303, 306 and 315). The data also shows that the energy gap between the two motifs is always small (< 0.62 eV). The lowest decahedral and octahedral motifs are shown in Figures 5.33 and 5.34 respectively. The number of Pt atoms within each cluster is shown, along with the globally optimised energy of each cluster relative to the lowest structure found. If the energy is 0.0 eV, it is the lowest energy structure found. For all sizes the decahedral clusters are all based upon the (4,3,1) decahedral cluster with some displaced atoms. All of the octahedral clusters are based upon the (8,2) octahedral structure with atoms removed (303 - 313 atoms) or added (315 atoms).

It is clear from the decahedral structure seen that the re-entrant corner is preferable for low energy structures, as it is a very common feature of clusters at all sizes. For the octahedral clusters, stable clusters are formed when the facets are complete, which is seen twice in these results, once for the cluster with 305 atoms and a second time for a cluster with 314 atoms. This means that the clusters one atom larger than each of these sizes are particularly unstable and high in energy. This gives rise to the decahedral motif being the most stable structure for the sizes of 306 and 315 atoms.

The results for the 309 bracket show that the octahedral motif is dominant for the majority of the sizes, but that the decahedral motif is very close in energy at most sizes. As the 303 - 315 atom clusters are very large, we may not be examining the PES in as much detail as we would ideally like to. This means that we may not find the absolute lowest energy structure, but the starting guesses definitely help improve the number of low lying structures found.

In summary, the 54 and 55 atom Pt clusters form with an icosahedral base structure. The 54 atom cluster is missing its central atom, making it more stable. For 56 atom clusters, the dominant motif is decahedral. For the 144 - 150 Pt atom size range, the dominant motif is always decahedral. For the 303 - 315 size range, most of the dominant structures are octahedral in motif, but when the octahedral is unstable due to the addition of a single atom to a symmetric cluster, the decahedral motif becomes dominant. We have identified for 55 atoms clusters that the traditional magic number cluster for the icosahedral motif, where $i = 3$, is present. For the decahedral and the octahedral motifs, the magic number sized clusters have formed as non-magic shapes. The decahedral has typically presented as a flatter, wider version, whilst the octahedral motif typically exhibits truncations of varying degrees. This means that the traditional magic number cluster shapes are unstable.

The most stable structures have been formed when the decahedral clusters are flat, and exhibit re-entrant corners. For the icosahedral motif, complete shells, including or excluding the central atom appear to be favoured. For octahedral clusters, complete facets, and some truncation, has led to high stability clusters.

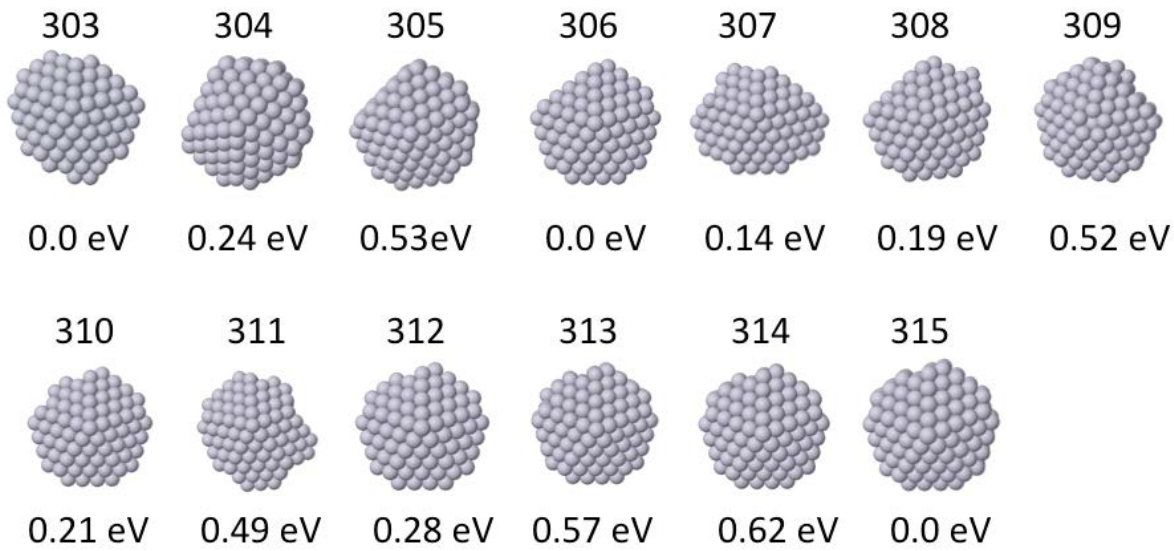

Figure 5.33: The lowest energy structure for the decahedral motif for clusters size between 303 and 315 Pt atoms. The energy is 0.0 eV if it is the lowest globally optimised structure found, and greater than 0.0 eV if the lowest octahedral structure was lower in energy.

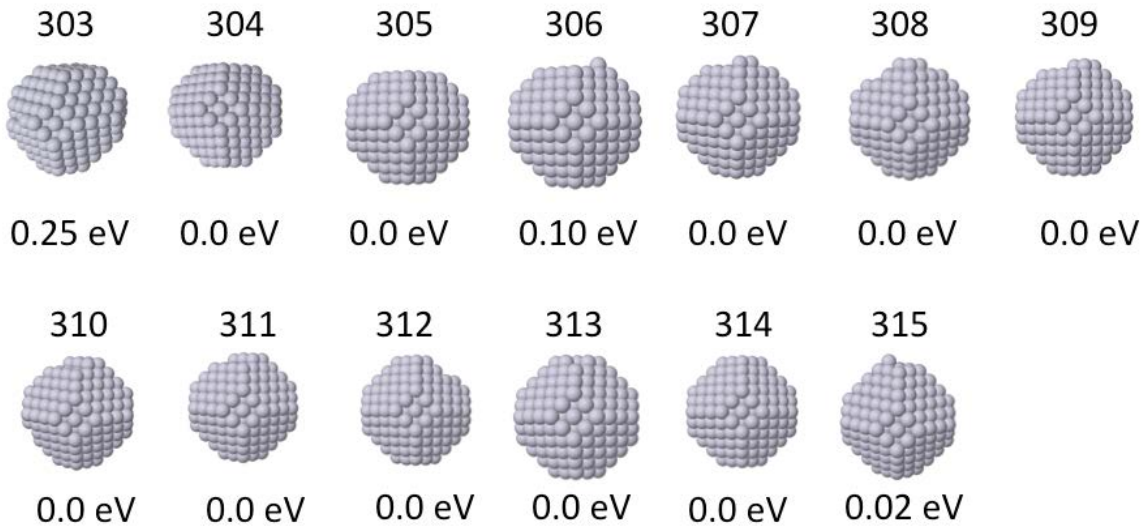

Figure 5.34: The lowest energy structure for the octahedral motif for clusters size between 303 and 315 Pt atoms. The energy is 0.0 eV if it is the lowest globally optimised structure found, and greater than 0.0 eV if the lowest decahedral structure was lower in energy.

5.5 Conclusions and Further Work for Platinum Theory

The work within this chapter has identified that for a size range of 55 - 10,000 atoms, the motif dominance swaps between decahedral and octahedral. The decahedral motif is more dominant at the smaller size, with the octahedral being dominant at larger sizes, which is consistent with the fact that bulk Pt is FCC in nature. The motif dominance constantly switches between the two motifs, which is in contrast to a paper by Baletto [147] which stated that there was a crossover between the decahedral and the octahedral motif at 6,500 atoms. From the overview of structures the icosahedral motif is never the dominant structure for Pt, which contrasts with other metals like silver or copper where the motif is expected to be icosahedral at small sizes,and decahedral at medium sizes, before becoming octahedral at larger clusters sizes.

The interpolation scheme investigated is good for predicting the energy of asymmetric clusters, especially when the (100) facet is being removed. This approach enables more information to be gained from the calculation of the symmetric clusters, without many hours being spent manually generating each cluster. This method is limited to the removal of a single shell from a cluster. It may be possible to investigate how the energy of the clusters are impacted when multiple layers from one facet of a cluster are removed, making very unbalanced clusters. This could be particularly important when looking at octahedral clusters and the re-entrant corner, as the clusters that have been found via global optimisation are not always balanced, with a single cluster often containing very varying degrees of corner truncations. Further work could look at building more test cases for larger truncations, looking for non-spherical clusters. Including these would improve the knowledge of motif dominance at different sizes.

Further work comparing more potentials may also be useful, as although the trends are the same, different potentials would place the relative energies between different motifs at

different values. This may have an impact upon the crossover sizes between the decahedral and octahedral motifs, with the octahedral motif becoming more dominant earlier or later in cluster size.

The global optimisation has allowed for an in-depth look at the motifs that are dominant around the magic number sized clusters. For the 55 atom cluster bracket, the 54 and 55 atom clusters show an icosahedral motif, whilst the 56 atom show a decahedral motif being most stable. For the 147 atom cluster bracket, the decahedral motif is always most stable. For the 309 atom cluster bracket, 3 out of 13 sizes have a decahedral dominance, but 10 out of 13 sizes have a octahedral dominance. Comparisons on this data with the experimental results are made in Section 4.5.

The GOUST optimisations has generated clusters which are low lying in energy, giving the approximate energy relations between the icosahedral, decahedral and octahedral motifs, but this algorithm still has limitations. Future work would include verifying the relationship between these motifs using DFT simulations. This would be done by taking the globally optimised structures and performing DFT simulations to calculate a more accurate energy for each structure. This would enable a check of the relative energies to be made, as a slight shift in the energy of one motif with reference to another could change the dominant structure at each cluster size.

References

[1] J. P. Hansen, P. A. Narbel, and D. L. Aksnes. Limits to growth in the renewable energy sector. *Renew. Sustain. Energy Rev.*, 70(October 2016):769–774, 2017.

[2] D. Brugge, J. L. Durant, and C. Rioux. Near-highway pollutants in motor vehicle exhaust: A review of epidemiologic evidence of cardiac and pulmonary health risks. *Environ. Heal. A Glob. Access Sci. Source*, 6:23, 2007.

[3] TFL Hydrogen Buses - http://tfl.gov.uk/campaign/bus-investment. Accessed: 2016-08-13.

[4] J. D. Holladay, J. Hu, D. L. King, and Y. Wang. An overview of hydrogen production technologies. *Catal. Today*, 139(4):244–260, 2009.

[5] J. H. Hirschenhofer, D. B. Stauffer, P. R. Engleman, and M. G. Klett. *Fuel Cell Handbook*. Parsons Corporation, Reading, PA, 4th edition, 1998.

[6] M. Dokiya. SOFC system and technology.pdf. 153:383–392, 2002.

[7] K. Alanne, A. Saari, V. I. Ugursal, and J. Good. The financial viability of an SOFC cogeneration system in single-family dwellings. *J. Power Sources*, 158(1):403–416, 2006.

[8] PEM Fuel Cells - http://electrochem.cwru.edu/encycl/art-f04-fuel-cells-pem.htm. Accessed: 2016-08-13.

[9] Electrolysis Figure - http://www.alternative-energy-tutorials.com/energy-articles/hydrogen-energy.html. Accessed: 2016-08-13.

[10] M. Gratzel. Photo-electrochemical cells. *Nature*, 414:338–344, 2001.

[11] A. Fujishima and K. Honda. Electrochemical photolysis of water at a semiconductor electrode. *Nature*, 238, 1972.

[12] J. Tang, S. Dai, and J. A. Darr. Recent Developments in Solar Energy Harvesting and Photocatalysis. *Int. J. Photoenergy*, 2012:1–2, 2012.

[13] Y. Tachibana, L. Vayssieres, and J. R. Durrant. Artificial photosynthesis for solar water-splitting. *Nat. Photonics*, 6:511–518, 2012.

[14] H. Ahmad, S.K. Kamarudin, L.J. Minggu, and M. Kassim. Hydrogen from photocatalytic water splitting process: A review. *Renew. Sustain. Energy Rev.*, 43:599–610, 2015.

[15] Cost of Metals - http://infomine.com/investment/base-metals/. Accessed: 2017-06-20.

[16] S. E. Cross, B. Innes, M. S. Roberts, T. Tsuzuki, T. A. Robertson, and P. McCormick. Human skin penetration of sunscreen nanoparticles: In-vitro assessment of a novel micronized zinc oxide formulation. *Skin Pharmacol. Physiol.*, 20(3):148–154, 2007.

[17] A. W. Harrison and M. R. Walton. Radiative cooling of TiO2 white paint. *Sol. Energy*, 20(2):185–188, 1978.

[18] S. M. Gupta and M. Tripathi. A review of TiO2 nanoparticles. *Chinese Sci. Bull.*, 56(16):1639–1657, 2011.

[19] A. Zaleska. Doped-TiO 2 : A Review. *Recent Patents Eng.*, 2(1):157–164, 2008.

[20] S. Gupta and M. Tripathi. A review on the synthesis of TiO2 nanoparticles by solution route. *Open Chem.*, 10(2), 2012.

[21] M. Saurat and S. Bringezu. Platinum group metal flows of Europe, part I: Global supply, use in industry, and shifting of environmental impacts. *J. Ind. Ecol.*, 12(5-6):754–767, 2008.

[22] K. Pyrzyska. Recent advances in solid-phase extraction of platinum and palladium. *Talanta*, 47(4):841–848, 1998.

[23] V. Kumar and Y. Kawazoe. Evolution of atomic and electronic structure of Pt clusters: Planar, layered, pyramidal, cage, cubic, and octahedral growth. *Phys. Rev. B*, 77(20):205418, 2008.

[24] A. Chen and P. Holt-Hindle. Platinum-based nanostructured materials: synthesis, properties, and applications. *Chem. Rev.*, 110(6):3767–804, 2010.

[25] R. Ferrando, J. Jellinek, and R. L. Johnston. Nanoalloys: from theory to applications of alloy clusters and nanoparticles. *Chem. Rev.*, 108(3):845–910, 2008.

[26] B. C. Steele and A. Heinzel. Materials for fuel-cell technologies. *Nature*, 414(6861):345–352, 2001.

[27] A. F. Ghenciu. Review of fuel processing catalysts for hydrogen production in PEM fuel cell systems. *Curr. Opin. Solid State Mater. Sci.*, 6(5):389–399, 2002.

[28] Y. Zhou, K. Neyerlin, T. S. Olson, S. Pylypenko, J. Bult, H. N. Dinh, T. Gennett, Z. Shao, and R. O'Hayre. Enhancement of Pt and Pt-alloy fuel cell catalyst activity and durability via nitrogen-modified carbon supports. *Energy Environ. Sci.*, 3(10):1437, 2010.

[29] R. Borup, J. Meyers, and B. Pivovar. Scientific Aspects of Polymer Electrolyte Fuel Cell Durability and Degradation. *Chem. Rev.*, 107(10):3904–3951, 2007.

[30] J. K. Nørskov, J. Rossmeisl, A. Logadottir, L. Lindqvist, J. R. Kitchin, T. Bligaard, and H. Jónsson. Origin of the Overpotential for Oxygen Reduction at a Fuel-Cell Cathode. *J. Phys. Chem. B*, 108(46):17886–17892, 2004.

[31] J. Greeley, J. Rossmeisl, A. Hellman, and J. K. Nørskov. Theoretical Trends in Particle Size Effects for the Oxygen Reduction Reaction. *Zeitschrift für Phys. Chemie*, 221:1209–1220, 2007.

[32] J. Greeley and N. M. Marković. The road from animal electricity to green energy: combining experiment and theory in electrocatalysis. *Energy Environ. Sci.*, 5(11):9246, 2012.

[33] C. J. Zhong, J. Luo, B. Fang, B. N. Wanjala, P. N. Njoki, R. Loukrakpam, and J. Yin. Nanostructured catalysts in fuel cells. *Nanotechnology*, 21(6):062001, 2010.

[34] M. T. M. Koper. Structure sensitivity and nanoscale effects in electrocatalysis. *Nanoscale*, 3(5):2054–73, 2011.

[35] E. F. Holby, W. Sheng, Y. Shao-Horn, and D. Morgan. Pt nanoparticle stability in PEM fuel cells: influence of particle size distribution and crossover hydrogen. *Energy Environ. Sci*, 2(8):865, 2009.

[36] P. C. Jennings, B. G. Pollet, and R. L. Johnston. Theoretical studies of Pt-Ti nanoparticles for potential use as PEMFC electrocatalysts. *Phys. Chem. Chem. Phys.*, 14(9):3134–9, 2012.

[37] P. C. Jennings, B. G. Pollet, and R. L. Johnston. Electronic Properties of PtTi Nanoalloys and the Effect on Reactivity for Use in PEMFCs. *J. Phys. Chem. C*, 116(29):15241–15250, 2012.

[38] M. Ni, M. K. H. Leung, D. Y. C. Leung, and K. Sumathy. A review and recent developments in photocatalytic water-splitting using TiO2 for hydrogen production. *Renew. Sustain. Energy Rev.*, 11(3):401–425, 2007.

[39] G. R. Bamwenda, S. Tsubota, T. Nakamura, and M. Haruta. Photoassisted hydrogen production from a water-ethanol solution: a comparison of activities of AuTiO2 and PtTiO2. *J. Photochem. Photobiol. A Chem.*, 89(2):177–189, 1995.

[40] V. Subramanian, E. E. Wolf, and P. V. Kamat. Influence of Metal/Metal Ion Concentration on the Photocatalytic Activity of TiO2Au Composite Nanoparticles. *Langmuir*, 19(2):469–474, 2003.

[41] H. Li, Z. Bian, J. Zhu, Y. Huo, H. Li, and Y. Lu. Mesoporous Au/TiO2 nanocomposites with enhanced photocatalytic activity. *J. Am. Chem. Soc.*, 129(15):4538–4539, 2007.

[42] S. K. Mohapatra, N. Kondamudi, S. Banerjee, and M. Misra. Functionalization of Self-Organized TiO2 Nanotubes with Pd Nanoparticles for Photocatalytic Decomposition of Dyes under Solar Light Illumination. *Langmuir*, 24(19):11276–11281, 2008.

[43] F. Solymosi and I. Tombacz. Photocatalytic reaction of H2O + CO2 over pure and doped Rh/TiO2. *Catal. Letters*, 27(1-2):61–65, 1994.

[44] N. Rajalakshmi, N. Lakshmi, and K. S. Dhathathreyan. Nano titanium oxide catalyst support for proton exchange membrane fuel cells. *Int. J. Hydrogen Energy*, 33(24):7521–7526, 2008.

[45] Y. Li, W. N. Wang, Z. Zhan, M. N. Woo, C. Y. Wu, and P. Biswas. Photocatalytic reduction of CO2 with H2O on mesoporous silica supported Cu/TiO2 catalysts. *Appl. Catal. B Environ.*, 100(1-2):386–392, 2010.

[46] P. D. Cozzoli, E. Fanizza, R. Comparelli, M. L. Curri, A. Agostiano, and D. Laub. Role of metal nanoparticles in TiO2/Ag nanocomposite-based microheterogeneous photocatalysis. *J. Phys. Chem. B*, 108(28):9623–9630, 2004.

[47] R. Abe, K. Sayama, and H. Arakawa. Significant effect of iodide addition on water splitting into H2 and O2 over Pt-loaded TiO2 photocatalyst: Suppression of backward reaction. *Chem. Phys. Lett.*, 371(3-4):360–364, 2003.

[48] A. Galin and J. Walendziewski. Photocatalytic Water Splitting over Pt-TiO2 in the Presence of Sacrificial Reagents. *Am. Chem. Soc.*, 19(16):1143–1147, 2005.

[49] J. Yu, L. Qi, and M. Jaroniec. Hydrogen production by photocatalytic water splitting over Pt/TiO2 nanosheets with exposed (001) facets. *J. Phys. Chem. C*, 114(001):13118–13125, 2010.

[50] S. K. Mohapatra, M. Misra, V. K. Mahajan, and K. S. Raja. Design of a Highly Efficient Photoelectrolytic Cell for Hydrogen Generation by Water Splitting: Application of TiO2-xCx Nanotubes as a Photoanode and Pt/TiO2 Nanotubes as a Cathode. *J. Phys. Chem. C*, 111(24):8677–8685, 2007.

[51] A. Sanchez, S. Abbet, U. Heiz, W. D. Schneider, H. Häkkinen, R. N. Barnett, and U. Landman. When Gold Is Not Noble: Nanoscale Gold Catalysts. *J. Phys. Chem. A*, 103(48):9573–9578, 1999.

[52] M. B. Cortie and E. Van Der Lingen. Catalytic gold nano-particles. *Mater. Forum*, 26(2002):1–14, 2002.

[53] E. Skúlason, A. A. Faraj, L. Kristinsdóttir, J. Hussain, A. L. Garden, and H. Jónsson. Catalytic activity of Pt nano-particles for H2 formation. *Top. Catal.*, 57(1-4):273–281, 2014.

[54] D. W. Galbraith. Magic nanoclusters of gold. *J. Cereal Sci.*, 2(May):3–4, 2007.

[55] L. D. Marks. Experimental studies of small particle structures. *Reports Prog. Phys.*, 57(6):603, 1994.

[56] A. M. Angulo and C. Noguez. Atomic Structure of Small and Intermediate-Size Silver Nanoclusters. *J. Phys. Chem. A*, 112:5834–5838, 2008.

[57] D. Bochicchio and R. Ferrando. Morphological instability of core-shell metallic nanoparticles. *Phys. Rev. B*, 87(16):165435, 2013.

[58] Y. Chan, R. Schrock, and R. Cohen. Synthesis of single nanoclusters within spherical microdomains in block copolymer films. *J. Am. Chem. Soc.*, 114(10):7295–7296, 1992.

[59] W. Wang, Z. H. Jin, T. l. Li, H. Zhang, and S. Gao. Preparation of spherical iron nanoclusters in ethanol-water solution for nitrate removal. *Chemosphere*, 65(8):1396–1404, 2006.

[60] X. Duan and C. M. Lieber. General synthesis of compound semiconductor nanowires. *Adv. Mater.*, 12(4):298–302, 2000.

[61] M. J. Cuddy, K. P. Arkill, Z. W. Wang, H. P. Komsa, A. V. Krasheninnikov, and R. E. Palmer. Fabrication and atomic structure of size-selected, layered MoS2 clusters for catalysis. *Nanoscale*, 6(21):12463–12469, 2014.

[62] A. W. Castleman. From elements to clusters: The periodic table revisited. *J. Phys. Chem. Lett.*, 2(9):1062–1069, 2011.

[63] L. D. Marks and L. Peng. Nanoparticle shape, thermodynamics and kinetics. *J. Phys. Condens. Matter*, 28(5):053001, 2016.

[64] R. E. Palmer, L. Cao, and F. Yin. Note: Proof of principle of a new type of cluster beam source with potential for scale-up. *Rev. Sci. Instrum.*, 87(4):046103, 2016.

[65] B. L. Cushing, V. L. Kolesnichenko, and C. J. O'Connor. Recent advances in the liquid-phase syntheses of inorganic nanoparticles. *Chem. Rev.*, 104(9):3893–3946, 2004.

[66] C. W. Scheeren, G. Machado, J. Dupont, P. F. P. Fichtner, and S. R. Texeira. Nanoscale Pt(0) particles prepared in imidazolium room temperature ionic liquids: synthesis from an organometallic precursor, characterization, and catalytic properties in hydrogenation reactions. *Inorg. Chem.*, 42(15):4738–4742, 2003.

[67] J. Belloni. Nucleation, growth and properties of nanoclusters studied by radiation chemistry: Application to catalysis. *Catal. Today*, 113(3-4):141–156, 2006.

[68] Y. Wang, Y. Li, C. Rong, and J. P. Liu. Sm-Co hard magnetic nanoparticles prepared by surfactant-assisted ball milling. *Nanotechnology*, 18(46):465701, 2007.

[69] V. M. Chakka, B. Altuncevahir, Z. Q. Jin, Y. Li, and J. P. Liu. Magnetic nanoparticles produced by surfactant-assisted ball milling. *J. Appl. Phys.*, 99(8):2005–2007, 2006.

[70] W. A. De Heer. The physics of simple metal clusters: Experimental aspects and simple models. *Rev. Mod. Phys.*, 65(3):611–676, 1993.

[71] O. F. Hagena. Cluster Formation in Expanding Supersonic Jets: Effect of Pressure, Temperature, Nozzle Size, and Test Gas. *J. Chem. Phys.*, 56(5):1793, 1972.

[72] C. Binns. Nanoclusters deposited on surfaces. *Surf. Sci. Rep.*, 44(1-2):1–49, 2001.

[73] B. Wrenger and K. H. Meiwes-Broer. The application of a Wien filter to mass analysis of heavy clusters from a pulsed supersonic nozzle source. *Rev. Sci. Instrum.*, 68(5):2027, 1997.

[74] W. Marine, L. Patrone, B. Luk'Yanchuk, and M. Sentis. Strategy of nanocluster and nanostructure synthesis by conventional pulsed laser ablation. *Appl. Surf. Sci.*, 154:345–352, 2000.

[75] A. M. Morales and C. M. Lieber. A Laser Ablation Method for the Synthesis of Crystalline Semiconductor Nanowires. *Science (80-.).*, 279(5348):208–211, 1998.

[76] O. Polonskyi, P. Sola, O. Kylián, M. Drábik, A. Artemenko, J. Kousal, J. Hanuš, J. Pešička, I. Matolínová, E. Kolíbalová, D. Slavínská, and H. Biederman. Nanocomposite metal/plasma polymer films prepared by means of gas aggregation cluster source. *Thin Solid Films*, 520(12):4155–4162, 2012.

[77] F. Frank, W. Schulze, B. Tesche, J. Urban, and B. Winter. Formation of metal clusters and molecules by means of the gas aggregation technique and characterisation of size distribution. *Surf. Sci.*, 156(PART 1):90–99, 1985.

[78] M. Drábik, A. Serov, O. Kylián, A. Choukourov, A. Artemenko, J. Kousal, O. Polonskyi, and H. Biederman. Deposition of Pt nanoclusters by means of gas aggregation cluster source. *Plasma Process. Polym.*, 9(4):390–397, 2012.

[79] D. M. Wells, G. Rossi, R. Ferrando, and R. E. Palmer. Metastability of the atomic structures of size-selected gold nanoparticles. *Nanoscale*, 7(15):6498–6503, 2015.

[80] N. Jian and R. E. Palmer. Variation of the Core Atomic Structure of Thiolated (Au x Ag 1 x) 31255 Nanoclusters with Composition from Aberration-Corrected HAADF STEM. *J. Phys. Chem. C*, 119(20):11114–11119, 2015.

[81] S. R. Plant, L. Cao, and R. E. Palmer. Atomic Structure Control of Size-Selected Gold Nanoclusters during Formation. *J. Am. Chem. Soc.*, 136:7559–7562, 2014.

[82] S. R. Plant, L. Cao, F. Yin, Z. W. Wang, and R. E. Palmer. Size-dependent propagation of Au nanoclusters through few-layer graphene. *Nanoscale*, 6(3):1258–1263, 2014.

[83] K. J. Hu, S. R. Plant, P. R. Ellis, C. M. Brown, P. T. Bishop, and R. E. Palmer. Atomic Resolution Observation of a Size-Dependent Change in the Ripening Modes of Mass-Selected Au Nanoclusters Involved in CO Oxidation. *J. Am. Chem. Soc.*, 137(48):15161–15168, 2015.

[84] K. J. Hu, S. R. Plant, P. R. Ellis, C. M. Brown, P. T. Bishop, and R. E. Palmer. The effects of 1-pentyne hydrogenation on the atomic structures of size-selected Au N and Pd N (N = 923 and 2057) nanoclusters. *Phys. Chem. Chem. Phys.*, 16(48):26631–26637, 2014.

[85] C. E. Blackmore, N. V. Rees, and R. E. Palmer. Modular construction of size-selected multiple-core PtTiO2 nanoclusters for electro-catalysis. *Phys. Chem. Chem. Phys.*, 17(42):28005–28009, 2015.

[86] L. D. Menard, S. P. Gao, H. Xu, R. D. Twesten, A. S. Harper, Y. Song, G. Wang, A. D. Douglas, J. C. Yang, A. I. Frenkel, R. G. Nuzzo, and R. W. Murray. Sub-nanometer Au monolayer-protected clusters exhibiting molecule-like electronic behavior: Quantitative high-angle annular dark-field scanning transmission electron microscopy and electrochemical characterization of clusters with precise atomic stoichiom. *J. Phys. Chem. B*, 110(26):12874–12883, 2006.

[87] H. S. Al Qahtani, K. Kimoto, T. Bennett, J. F. Alvino, G. G. Andersson, G. F. Metha, V. B. Golovko, T. Sasaki, and T. Nakayama. Atomically resolved structure of ligand-protected Au9 clusters on TiO2 nanosheets using aberration-corrected STEM. *J. Chem. Phys.*, 144(11):114703, 2016.

[88] S. Van Aert, K. J. Batenburg, M. D. Rossell, R. Erni, and G. Van Tendeloo. Three-dimensional atomic imaging of crystalline nanoparticles. *Nature*, 470(7334):374–7, 2011.

[89] N. D. Browning, M. F. Chisholm, and S. J. Pennycook. Atomic-resolution chemical analysis using a scanning transmission electron microscope. *Nature*, 366(6451):143–146, 1993.

[90] N. D. Browning, D. J. Wallis, P. D. Nellist, and S. J. Pennycook. EELS in the STEM: Determination of materials properties on the atomic scale. *Micron*, 28(5):333–348, 1997.

[91] S. Privitera, G. Bersuker, B. Butcher, A. Kalantarian, S. Lombardo, C. Bongiorno, R. Geer, D. C. Gilmer, and P. D. Kirsch. Microscopy study of the conductive filament in HfO2 resistive switching memory devices. *Microelectron. Eng.*, 109:75–78, 2013.

[92] J. M. Triscone, J. Mannhart, N. Reyren, S. Thiel, and D. A. Muller. Superconducting Interfaces Between Insulating Oxides. *Science (80-.).*, 317(1):1196, 2007.

[93] Super Stem - http://superstem.coml/. Accessed: 2017-06-21.

[94] F. Yin, Z. W. Wang, and R. E. Palmer. Ageing of mass-selected Cu/Au and Au/Cu core/shell clusters probed with atomic resolution. *J. Exp. Nanosci.*, 7(6):703 – 710, 2012.

[95] F. Yin, Z. W. Wang, and R. E. Palmer. Controlled formation of mass-selected Cu-Au core-shell cluster beams. *J. Am. Chem. Soc.*, 133(27):10325–7, 2011.

[96] A. I. Ayesh, H. A. Ahmed, F. Awwad, S. I. Abu-Eishah, and S. T. Mahmood. Mechanisms of Ti nanocluster formation by inert gas condensation. *J. Mater. Res.*, 28(18):2622–2628, 2013.

[97] Z. W. Wang and R. E. Palmer. Intensity calibration and atomic imaging of size-selected Au and Pd clusters in aberration-corrected HAADF-STEM. *J. Phys. Conf. Ser.*, 371:012010, 2012.

[98] I. M. Goldby, B. von Issendorff, L. Kuipers, and R. E. Palmer. Gas condensation source for production and deposition of size-selected metal clusters. *Rev. Sci. Instrum.*, 68(9):3327, 1997.

[99] B. von Issendorff and R. E. Palmer. A new high transmission infinite range mass selector for cluster and nanoparticle beams. *Rev. Sci. Instrum.*, 70(12):4497–4500, 1999.

[100] S. Pratontep, S. J. Carroll, C. Xirouchaki, M. Streun, and R. E. Palmer. Size-selected cluster beam source based on radio frequency magnetron plasma sputtering and gas condensation. *Rev. Sci. Instrum.*, 76(4):1–8, 2005.

[101] PI KEM - Cluster Source Target Supplier - http://pi-kem.co.uk/. Accessed: 2016-08-13.

[102] V. N. Popok, I. Barke, E. E. B. Campbell, and K. H. Meiwes-Broer. Clustersurface interaction: From soft landing to implantation. *Surf. Sci. Rep.*, 66(10):347–377, 2011.

[103] Agar Scientific - Supplier of TEM Grids - http://www.agarscientific.com. Accessed: 2016-08-13.

[104] JEOL Microscope Supplier - http://www.jeoluk.com/. Accessed: 2016-08-13.

[105] D. B. Williams and C. B. Carter. *Transmission Electron Microscopy.* Springer, New York, 2009.

[106] Image of CS corrector program - http://ceos-gmbh.de/English/products/residualsCEXCOR.html/. Accessed: 2017-06-21.

[107] H. Okamoto and T. B. Massalski. The AuPd (Gold-Palladium) system. *Bull. Alloy Phase Diagrams*, 6(3):229–235, 1985.

[108] JDigital Micrograph Software - http://www.gatan.com/. Accessed: 2016-08-13.

[109] Z. W. Wang, Z. Y. Li, S. J. Park, A. Abdela, D. Tang, and R. E. Palmer. Quantitative Z-contrast imaging in the scanning transmission electron microscope with size-selected clusters. *Phys. Rev. B*, 84(7):073408, 2011.

[110] J. M. Lebeau, S. D. Findlay, L. J. Allen, and S. Stemmer. Standardless atom counting in scanning transmission electron microscopy. *Nano Lett.*, 10(11):4405–4408, 2010.

[111] N. P. Young, Z. Y. Li, Y. Chen, S. Palomba, M. Di Vece, and R. E. Palmer. Weighing supported nanoparticles: Size-selected clusters as mass standards in nanometrology. *Phys. Rev. Lett.*, 101(24):28–31, 2008.

[112] Z. W. Wang, O. Toikkanen, F. Yin, Z. Y. Li, B. M. Quinn, and R. E. Palmer. Counting the atoms in supported, monolayer-protected gold clusters. *J. Am. Chem. Soc.*, 132(9):2854–2855, 2010.

[113] J. M. Lebeau, S. D. Findlay, L. J. Allen, and S. Stemmer. Quantitative atomic resolution scanning transmission electron microscopy. *Phys. Rev. Lett.*, 100(20):1–4, 2008.

[114] W. D. Pyrz, S. Park, D. A. Blom, D. J. Buttrey, and T. Vogt. High-angle annular dark-field scanning transmission electron microscopy investigations of bimetallic nickel bismuth nanomaterials created by electron-beam-induced fragmentation. *J. Phys. Chem. C*, 114(6):2538–2543, 2010.

[115] S. D. Findlay and J. M. Lebeau. Detector non-uniformity in scanning transmission electron microscopy. *Ultramicroscopy*, 124:52–60, 2013.

[116] W. Van den Broek, A. Rosenauer, B. Goris, G. T. Martinez, S. Bals, S. Van Aert, and D. Van Dyck. Correction of non-linear thickness effects in HAADF STEM electron tomography. *Ultramicroscopy*, 116:8–12, 2012.

[117] A. De Backer, G. T. Martinez, A. Rosenauer, and S. Van Aert. Atom counting in HAADF STEM using a statistical model-based approach: Methodology, possibilities, and inherent limitations. *Ultramicroscopy*, 134:23–33, 2013.

[118] L. Ackermann and R. Bergman. A Highly Reactive Titanium Precatalyst for Intramolecular Hydroamination Reactions. 148(4):825–832, 2008.

[119] J. A. Lee, K. C. Krogman, M. Ma, R. M. Hill, P. T. Hammond, and G. C. Rutledge. Highly reactive multilayer-assembled TiO2 coating on electrospun polymer nanofibers. *Adv. Mater.*, 21(12):1252–1256, 2009.

[120] Keith McKenna's Group University of York. Personal Communication June 2016.

[121] G. Marletta, S. M. Catalano, and S. Pignataro. Chemical Reactions Induced in Polymers by keV Ions, Electrons and Photons. 16:407–411, 1990.

[122] Metrohm - http://metrohm.com/en-gb/. Accessed: 2017-07-21.

[123] S. Bals, S. Van Aert, C. P. Romero, K. Lauwaet, M. J. Van Bael, B. Schoeters, B. Partoens, E. Yücelen, P. Lievens, and G. Van Tendeloo. Atomic scale dynamics of ultrasmall germanium clusters. *Nat. Commun.*, 3(May):897, jan 2012.

[124] S. Zhao, Y. Zhou, K. Zhao, Z. Liu, P. Han, S. Wang, W. Xiang, Z. Chen, H. Lü, B. Cheng, and G. Yang. Violet luminescence emitted from Ag-nanocluster doped ZnO thin films grown on fused quartz substrates by pulsed laser deposition. *Phys. B Condens. Matter*, 373(1):154–156, 2006.

[125] L. Ding, D. Yuan, and J. Liu. Growth of high-density parallel arrays of long single-walled carbon nanotubes on quartz substrates. *J. Am. Chem. Soc.*, 130(16):5428–5429, 2008.

[126] QSTEM Software - http://qstem.org. Accessed: 2016-08-13.

[127] Z. W. Wang and R. E. Palmer. Determination of the Ground-State Atomic Structures of Size-Selected Au Nanoclusters by Electron-Beam-Induced Transformation. *Phys. Rev. Lett.*, 108(24):245502, 2012.

[128] J. P. O'Neill, I. M. Ross, A. G. Cullis, T. Wang, and P. J. Parbrook. Electron-beam-induced segregation in InGaN/GaN multiple-quantum wells. *Appl. Phys. Lett.*, 83(10):1965–1967, 2003.

[129] K. A. Mkhoyan and J. Silcox. Electron-beam-induced damage in wurtzite InN. *Appl. Phys. Lett.*, 82(6):859–861, 2003.

[130] Dawn Foster University of Birmingham. Personal Communication August 2016.

[131] Alex Pattison University of Birmingham. Personal Communication June/July 2015.

[132] Y. Wang, S. Teitel, and C. Dellago. Melting of icosahedral gold nanoclusters from molecular dynamics simulations. *J. Chem. Phys.*, 122(21):1–40, 2005.

[133] M. José-Yacamán, M. Marin-Almazo, and J. A. Ascencio. High resolution TEM studies on palladium nanoparticles. *J. Mol. Catal. A Chem.*, 173:61–74, 2001.

[134] K. Bao, S. Goedecker, K. Koga, F. Lançon, and A. Neelov. Structure of large gold clusters obtained by global optimization using the minima hopping method. *Phys. Rev. B - Condens. Matter Mater. Phys.*, 79(4):1–4, 2009.

[135] Z. L. Wang. Transmission Electron Microscopy of Shape-Controlled Nanocrystals and Their Assemblies. *J. Phys. Chem. B*, 104(6):1153–1175, 2000.

[136] Y. G. Chushak and L. S. Bartell. Melting and freezing of gold nanoclusters. *J. Phys. Chem. B*, 105(47):11605–11614, 2001.

[137] H. B. Liu, U. Pal, A. Medina, C. Maldonado, and J. A. Ascencio. Structural incoherency and structure reversal in bimetallic Au-Pd nanoclusters. *Phys. Rev. B - Condens. Matter Mater. Phys.*, 71(7):1–6, 2005.

[138] G. A. Breaux, R. C. Benirschke, T. Sugai, B. S. Kinnear, and M. F. Jarrold. Hot and solid gallium clusters: too small to melt. *Phys. Rev. Lett.*, 91(21):215508, 2003.

[139] J. Ross and R. P. Andres. Melting temperature of small clusters. *Surf. Sci.*, 106(1-3):11–17, 1981.

[140] P. Buffat and J. Borel. Size effect on the melting temperature of gold particles. *Phys. Rev. A*, 13(6):2287–2298, 1976.

[141] A. Shvartsburg and M. Jarrold. Solid Clusters above the Bulk Melting Point. *Phys. Rev. Lett.*, 85:2530–2532, 2000.

[142] M. Schmidt, R. Kusche, B. von Issendorff, and H. Haberland. Irregular variations in the melting point of size-selected atomic clusters. *Nature*, 393(May):238, 1998.

[143] J. P. Borel. Thermodynamical size effect and the structure of metallic clusters. *Surf. Sci.*, 106(1-3):1–9, 1981.

[144] M. A. Asoro, D. Kovar, and P. J. Ferreira. In-situ Transmission Electron Microscopy Observations of Sublimation in Silver Nanoparticles. *ACS Nano*, 7(9):7844–7852, 2013.

[145] S. P. Ping and P. B. Balbuena. Platinum nanoclusters on graphite substrates: a molecular dynamics study. *Mol. Phys.*, 100(13):2165–2174, 2002.

[146] Z. L. Wang, J. M. Petroski, T. C. Green, and M. A. El-Sayed. Shape Transformation and Surface Melting of Cubic and Tetrahedral Platinum Nanocrystals. *J. Phys. Chem. B*, 102(32):6145–6151, 1998.

[147] F. Baletto, R. Ferrando, A. Fortunelli, F. Montalenti, and C. Mottet. Crossover among structural motifs in transition and noble-metal clusters. *J. Chem. Phys.*, 116(9):3856, 2002.

[148] R. Gupta. Lattice relaxation at a metal surface. *Phys. Rev. B*, 23(12):6265–6270, 1981.

[149] K. W. Jacobsen, P. Stoltze, and J. K. Nørskov. A semi-empirical effective medium theory for metals and alloys. *Surf. Sci.*, 366:394–402, 1996.

[150] K. Michaelian, N. Rendón, and I. L. Garzón. Structure and energetics of Ni, Ag, and Au nanoclusters. *Phys. Rev. B*, 60(3):2000–2010, 1999.

[151] F. Baletto and R. Ferrando. Structural properties of nanoclusters : Energetic , thermodynamic , and kinetic effects. *Rev. Mod. Phys.*, 77:371–423, 2005.

[152] Z. Y. Li, N. P. Young, M. Di Vece, S. Palomba, R. E. Palmer, A. L. Bleloch, B. C. Curley, R. L. Johnston, J. Jiang, and J. Yuan. Three-dimensional atomic-scale structure of size-selected gold nanoclusters. *Nature*, 451(7174):46–8, 2008.

[153] F. Pauly, M. Dreher, J. K. Viljas, M. Häfner, J. C. Cuevas, and P. Nielaba. Theoretical analysis of the conductance histograms and structural properties of Ag, Pt, and Ni nanocontacts. *Phys. Rev. B - Condens. Matter Mater. Phys.*, 74(23), 2006.

[154] S. R. Bahn and K. W. Jacobsen. Chain Formation of Metal Atoms. *Phys. Rev. Lett.*, 87(26):266101, 2001.

[155] A. F. Voter. Embedded atom method potentials for seven fcc metals: Ni, Pd, Pt, Cu, Ag, Au, and Al. *Los Alamos Unclassif. Tech. Rep.*, (LA-UR 93-2901):1–9, 1993.

[156] M. S. Daw and M. I. Baskes. Embedded-atom method: Derivation and application to impurities, surfaces, and other defects in metals. *Phys. Rev. B*, 29(12):6443–6453, 1984.

[157] S. M. Foiles, M. I. Baskes, and M. S. Daw. Embedded-atom-method functions for the fcc metals Cu, Ag, Au, Ni, Pd, Pt, and their alloys. *Phys. Rev. B*, 33(12):7983–7991, 1986.

[158] A. P. Sutton and J. Chen. Long-Range Finns-Sinclair Potentials. *Philos. Mag. Lett.*, 61(3):139–146, 1990.

[159] J. Doye and D. J. Wales. Global Minima for Transition Metal Clusters Described by Sutton-Chen Potentials. *New J. Chem*, 93(22):16, 1997.

[160] W. Kohn. Nobel Lecture: Electronic structure of matterwave functions and density functionals. *Rev. Mod. Phys.*, 71(5):1253–1266, 1999.

[161] ASE Software - http://wiki.fysik.dtu.dk/ase. Accessed: 2016-08-13.

[162] ASAP Software - http://wiki.fysik.dtu.dk/asap. Accessed: 2016-08-13.

[163] EON Software - http://theory.cm.utexas.edu/eon/. Accessed: 2016-08-13.

[164] G. Henkelman and H. Jonsson. Long time scale kinetic Monte Carlo simulations without lattice approximation and predefined event table. *J. Chem. Phys.*, 115(21):9657–9666, 2001.

[165] M. Plasencia, A. Pedersen, A. Arnaldsson, J. C. Berthet, and H. Jónsson. Geothermal model calibration using a global minimization algorithm based on finding saddle points and minima of the objective function. *Comput. Geosci.*, 65:110–117, 2014.

[166] E. Aprà, F. Baletto, R. Ferrando, and A. Fortunelli. Amorphization mechanism of icosahedral metal nanoclusters. *Phys. Rev. Lett.*, 93(6):10–13, 2004.

[167] F. Baletto, R. Ferrando, A. Fortunelli, F. Montalenti, and C. Mottet. Crossover among structural motifs in transition and noble-metal clusters. *J. Chem. Phys.*, 116(9):3856, 2002.

[168] J. Gavnholt and J. Schiøtz. Structure and reactivity of ruthenium nanoparticles. *Phys. Rev. B - Condens. Matter Mater. Phys.*, 77(3):1–10, 2008.

[169] C. Tsai and K. Jordan. Use of an Eigenmode Method for Locate the Stationary Points on the Potential Energy Surfaces of Selected Argon and Water Clusters. *J. Phys. Chem.*, 97:11227–11237, 1993.

[170] D. J. Wales and J. P. K. Doye. Global Optimization by Basin-Hopping and the Lowest Energy Structures of Lennard-Jones Clusters Containing up to 110 Atoms. *J. Phys. Chem. A*, 101(97):5111–5116, 1997.

[171] E. Fan. Global Optimization of Lennard-Jones Atomic Clusters. 2002.

[172] G. Rossi and R. Ferrando. Searching for low-energy structures of nanoparticles: a comparison of different methods and algorithms. *J. Phys. Condens. Matter*, 21(8):084208, 2009.

[173] W. Cai and X. Shao. A fast annealing evolutionary algorithm for global optimization. *J. Comput. Chem.*, 23(4):427–435, 2002.

[174] T. Gregor and R. Car. Minimization of the potential energy surface of Lennard-Jones clusters by quantum optimization. *Chem. Phys. Lett.*, 412(1-3):125–130, 2005.

[175] A. Pedersen, A. Garden and H. Jonsson. Size and temperature dependence of the atomic structure of Au clusters including 100 to 4000 atoms. Unpublished work, Personal Communication March 2016.